LASER COMMUNICATION EXPERIMENT

DESIGN STUDY REPORT
VOL I PART 2
SPACECRAFT TRANSCEIVER

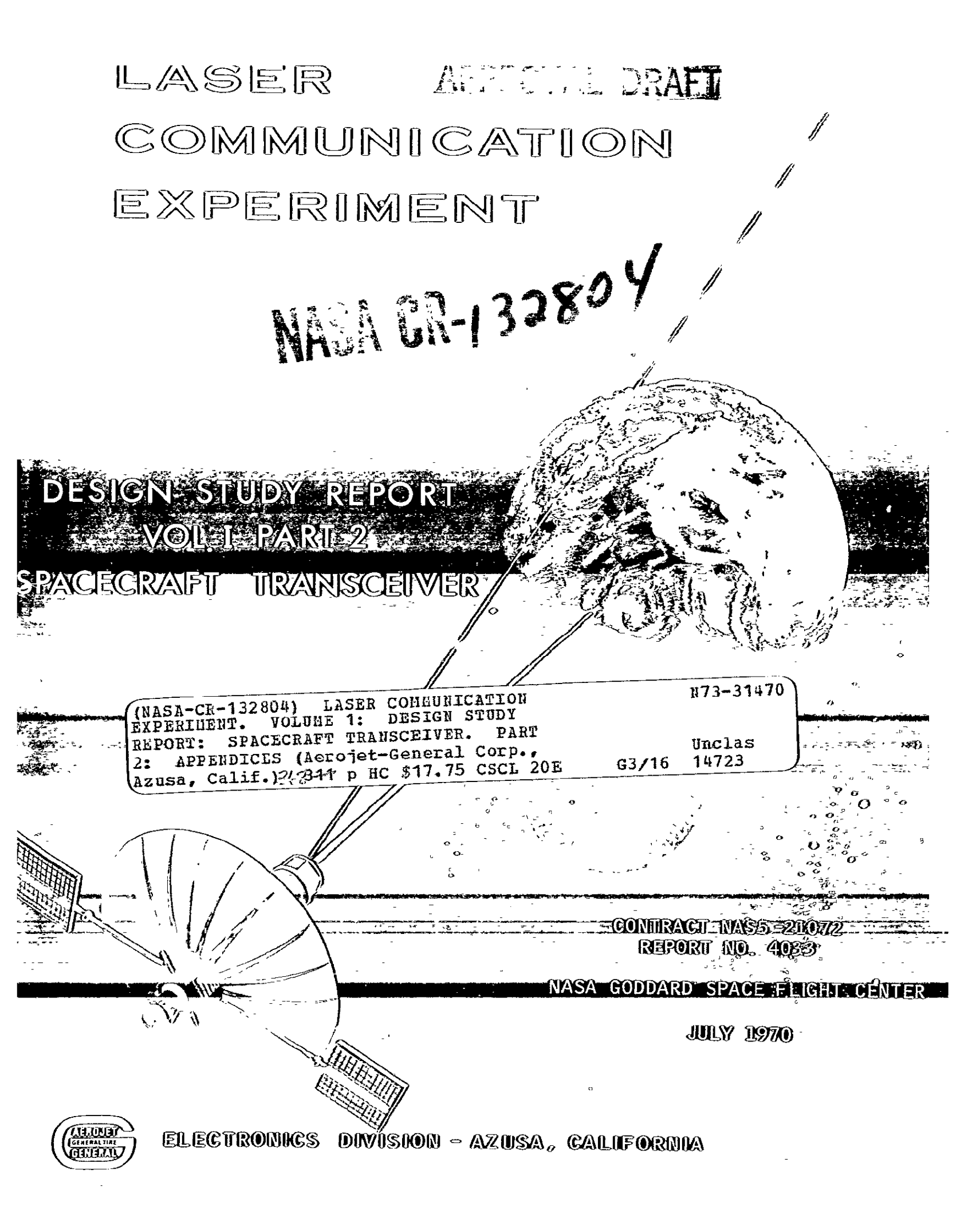

CONTRACT NAS5-21072
REPORT NO. 4033

NASA GODDARD SPACE FLIGHT CENTER

JULY 1970

AEROJET GENERAL TIRE GENERAL

ELECTRONICS DIVISION - AZUSA, CALIFORNIA


OCT 1973
RECEIVED
NASA STI FACILITY
ACQ BRANCH

FOREWORD

This report was prepared in conformance with the requirements of NASA Specification S-460-ATS-19, GSFC's specification pertaining to the ATS-F experiments, design study, and fabrication. Additional requirements are contained in GSFC specification S-524-P-4C, "10.6 Micron Laser Communications Systems Experiment for ATS-F." This is Part 2 of the three-part Volume I of the Design Study Report pertaining to the LCE spacecraft transceiver. It contains the appendices referenced in Part 1, a self-contained report of the transceiver design. Part 3 contains the LCE design specifications.

Volume II, to be delivered in late fall of 1970, will cover the remaining elements of the LCE, including the Operational Ground Equipment, Data Acquisition Plan, and Data Processing, Reduction, and Analysis Plan.

CONTRIBUTORS

The contributors to the Appendix material in this part of Volume I are listed below.

Appendix	Title	Contributors
A	Communications System Analysis	J. V. Cernius
B	Acquisition and Tracking System Design and Analysis	R. Y. Wong
C	LCE Telescope Interface Transfer Study	T. W. Lawson, Jr.
D	Analysis of Discriminator Linearity	AIL
E	The CO_2 Laser Signature Problem	Dr. P. K. Cheo (from Task Force work)
F	Laser Frequency Stabilization	Dr. P. K. Cheo (from Sylvania proposal)
G	Theoretical Model for Laser Power Computation	Dr. P. K. Cheo (from recent Sylvania work)
H	Preliminary Structural Analysis of Radiator Sun Shade and Support	R. Goldie
I	Preliminary Thermal Analysis of the LCE Passive Radiator	C. B. Fischer
J	Technical Meeting with Philco-Ford, Palo Alto, on 22 January 1970	C. B. Fischer
K	Analysis of Wire Grating Polarizer	Dr. C. D. Bass
L	LCE Optical Train Analysis	T. J. Wright
M	Coarse Pointing Mirror Lubrication Techniques	N. N. Richman

TABLE OF CONTENTS

APPENDIXES

Appendix	
A	Communications System Design Analysis
B	Acquisition and Tracking Design and Analysis
C	LCE Telescope Compartment/ATS Spacecraft Interface Heat Transfer Study
D	Analysis of Discriminator Linearity
E	The CO_2 Laser Signature Problem
F	Laser Frequency Stabilization
G	Theoretical Model for Laser Power Computation
H	Preliminary Structural Analysis of Radiator/Sunshade and Support
I	Preliminary Structural Analysis of the LCE Passive Radiator
J	Technical Meeting with Philco Ford, Palo Alto, 22 January 1970
K	Analysis of Wire Grating Polarizer
L	LCE Optical Train Analysis
M	Coarse-Pointing-Mirror Lubricating Techniques

APPENDIX A

COMMUNICATIONS SYSTEM DESIGN AND ANALYSIS

1.0 INTRODUCTION

Attainment of a satisfactory transmission of information via a communications link requires consideration of the following:

a. Predetection carrier-to-noise ratio (calculated in para. 5.1.3 in main text under the Link Analysis).

b. Information spectrum, modulation technique, and the required system filter bandwidth with its amplitude and phase linearity.

Implementation of the design for such a communications link must, necessarily, consider the system constraints such as limited electrical power and weight, and technology constraints such as those imposed by the need to use in-cavity GaAs modulator to frequency-modulate the 10.6-micron carrier.

In this analysis, first the communications system block diagram will be established and its configuration justified. This will be followed by the analysis of the required vestigial sideband filter characteristics, the determination of the required bandwidth for various baseband signal spectral structures, the analysis and the trade-off of FM modulation index (and the required bandwidth) versus FM modulator power required, derivation of the post-detection signal-to-noise ratio as a function of modulation index, and an analysis of the required filter amplitude and phase linearity to keep distortion products at an acceptable level. The analysis will be completed with a summary of the technical requirements of the 10.6-micron communications link.

To assist in keeping track of the mathematics in the sections that follow a summary of the notation used is given.

To distinguish (in the frequency domain) between voltage transforms and power transforms, the voltage transforms are made functions of radian frequency (ω), and the power transforms are made functions of cyclical frequency (f). All lower-case symbols are time-domain functions, and upper-case symbols are the corresponding frequency domain functions. Thus

$g(t)$ = input signal

$\Psi_g(\tau)$ = input signal auto-correlation function
$= E\left\{g(t)\, g(t+\tau)\right\}$

$G(\omega)$ = input signal (voltage) spectrum

$\Psi_g(f)$ = input signal (power) spectrum

$H(\omega)$ = filter transfer function (complex)

$\left|H(f)\right|^2$ = filter power transfer function

Further, the notation of input/output signals associated with various elements of the LCE communications link is shown in Figure A-1.

2.0 COMMUNICATIONS SYSTEM BLOCK DIAGRAM

The simplest approach to implement the communications link is to directly FM the GaAs crystal with the baseband signal in the frequency bandwidth from 30 Hz to 5.0 MHz. However, there are difficulties associated with this approach:

a. The GaAs electro-optic modulators exhibit selective frequency interference arising from resonances within the electro-optic crystal. These resonances occur (Ref. 1) at a frequency of

$$f = \frac{V}{2D} \qquad (1)$$

where V is the velocity of sound in the crystal ($V \simeq 3 \times 10^3$ in./sec) and D is the crystal dimension parallel to the direction of sound propagation. The LCE crystal dimensions are 3 mm, 9.9 mm, and 30 mm, with corresponding transverse resonances at 500 kHz, 150 kHz, and 50 kHz. Therefore, spectral

components of the baseband signal in the vicinity of the crystal resonant frequencies will produce carrier frequency deviation out of proportion with the response to all other baseband spectral components resulting in a distorted signal.

b. The laser carrier frequency stability is highly dependent on the effective laser cavity length. Any mechanical vibration causing mirror separation will result in frequency shift given by

$$\Delta f = -f \frac{\Delta L}{L} \tag{2}$$

where f is the carrier frequency (3×10^{13} Hz) and L is the effective laser cavity length (LCE laser transmitter cavity length is approximately 25 cm). It is easy to see that a change of 1 microinch will result in a frequency shift of 2.5 MHz. Although the laser cavities are designed to be extremely rigid, they are more susceptible to low-frequency FM noise since the spectral distribution of mechanical vibration is predominantely at low frequencies. Figure A-2 shows a typical FM noise spectrum. The second source of low-frequency FM noise is due to the laser current ripple with a scale factor of 1 MHz/ma (Ref. 2).

These factors, especially the lack of a proven approach to dampen the crystal piezoelectric resonances, led Aerojet to conclude that direct frequency modulation should not be considered.

What is required is to up-translate the baseband spectrum to occupy a frequency regime above the piezoelectric resonances of the crystal. The 1.0-MHz frequency has been selected to be the lower frequency of the up-converted baseband signal to ensure that potential crystal resonant frequencies are bypassed.

One approach to accomplish the up-translation is to amplitude-modulate a carrier at 6 MHz with the resulting bandwidth of 10 MHz and then drive the frequency modulator. However, this imposes impractical bandwidth and power requirements on the laser transmitter, modulator, and optical receiver. To

conserve the bandwidth, either single sideband or VSB are the only remaining practical approaches. Ideally, SSB would require least bandwidth covering a range from 1 to 6 MHz. The design of such a modulator is extremely difficult due to the necessity to pass the TV field frequency spectral lines only 60 Hz from the carrier. To completely eliminate energy from the lower sideband (at 1 MHz minus 60 Hz), a high-pass filter would be required which would be extremely difficult to design and costly to implement.

Therefore, our choice is to use VSB modulation to up-translate the baseband spectrum. This is the reason that conventional television transmitters use VSB carrier modulation. In this method, the entire upper sideband and a small segment, or "vestige", of the lower sideband is transmitted. By proper VSB design, it is possible to reconstruct the baseband signal quite readily.

The overall communications block diagram is shown in Figure A-1. It consists of the following segments:

VSB up-translator
FM modulator/laser transmitter
Receiver mixer & preamplifier
FM demodulator
VSB down-translator
Low-pass filter

The key filters, details of which are discussed in subsequent sections, are

VSB up-translator
Receiver noise-limiting filter
VSB down-translator
LPF

3.0 UP-TRANSLATOR/DOWN-TRANSLATOR

This section covers the analysis and specification for the up-translator/down-translator. In order to analyze the FM segment of the communications link, the characteristics of the up-translated baseband signal

must be known, which in turn dictates the need to establish the transfer functions of the up-translator/down-translator stages.

In the analysis, the requirements are examined from the point of view of minimizing the necessary bandwidth, subject to the constraints of maintaining signal distortion at a reasonable level, realizability of modulator design, and ease of VSB (vestigial-sideband) filter design.

The ease with which the baseband signal is recovered depends upon the amount of lower sideband which is transmitted along with the upper sideband. In commercial TV, approximately 17.5% of the lower sideband is transmitted at a modulation of 100%. This has been empirically determined as providing an unobjectionable amount of distortion when demodulated with a conventional envelope detector. This distortion may be reduced by either reducing the percentage modulation or by increasing the width of the VSB. For the LCE, reduction in the percentage modulation is undesirable since it represents a waste of transmitter power, while an increase in the VSB represents a waste of bandwidth and increases modulator driving power.

It is desired to reduce the VSB more than that presently used in commercial TV applications so that a maximum information bandwidth may be obtained in the desired spectral region of 1 to 6 MHz. This can be done by increasing the filter complexity and by requiring that the VSB demodulator be a coherent demodulator, rather than a conventional envelope detector. This is the approach taken in this analysis.

3.1 PEAK-TO-AVERAGE POWER

One of the effects produced by not transmitting one of the sidebands is the increase in the peak-to-average power ratio required for sync signals. To transmit a theoretically perfect square wave using SSB would require a theoretically infinite increase in peak-to-average power over that required to transmit the same square wave using AM. Transmitting a perfect square wave using a 17.5% VSB requires about 7.7 db greater peak-to-average than the same square wave in an AM system. However, the TV sync pulses are not perfect square waves but have a finite rise and fall time. As shown in

Figure A-3, the commercial TV VSB transmission of TV sync pulses requires about 3.5 db greater peak-to-average power than would be required in an AM system. As can be seen from Figure A-3, decreasing the percent of the lower sideband to be transmitted increases the required peak-to-average power for the TV sync pulses, although not appreciably. The problem with the decreasing percent of the transmitted lower sideband is more a factor of tremendously increasing the complexity of the filter design. Therefore, for this application, it is recommended that only a 1-db degradation in peak-to-average power requirement be allowed relative to commercial TV, which would require a VSB of about 4.2% to be transmitted. In this case the peak-to-average power increase of the VSB over the AM is then 4.5 db.

3.2 TRANSMITTED SPECTRUM

The recommendation for a 4.2% lower sideband transmission results in the transmitted spectrum shown in Figure A-4. Here, the 3 db points of the up-translated output are at 1 MHz and 6 MHz. In order to maintain the unattenuated lower sideband at 4.2% of the upper sideband, it is required that about 200 kHz of lower sideband be transmitted unattenuated. This then results in having the picture carrier placed at 1.4 MHz. In this manner, the region from 1.2 to 1.6 MHz can be kept unattenuated in the transmission characteristic, and the vestigial filtering required to reconstruct the signal without distortion accomplished in the receiver, as is standard practice. This results in a total 3-db bandwidth of 5 MHz and an "information" bandwidth (from the carrier frequency to the upper 3-db point) of 4.6 MHz. This information bandwidth is more than sufficient to transmit high quality TV signals, although it is somewhat less than the desired 5 MHz. In Figure A-4, the points where the spectrum goes to zero are assumed to be the 20 db points, as is conventional. Therefore, the information bandwidth with this system is approximately 4.8 MHz between the carrier and the 20-db point.

3.3 VESTIGIAL-SIDEBAND FILTERS

A VSB signal (upper-sideband transmitted) may be written as

$$s(t) = \left[g(t) + g_d(t) \right] \cos \omega_c t - g_q(t) \sin \omega_c t \qquad (3)$$

where

$g(t)$ = the modulation

$g_d(t)$ = an in-phase distortion term

$g_q(t)$ = a quadrature term

ω_c = the carrier frequency

The distortion and quadrature terms depend on the filter used to eliminate the major portion of the lower sideband. Broadly speaking, as the filter widens to include the entire lower sideband, $g_d(t) \longrightarrow 0$ and $g_q(t) \longrightarrow 0$, and as the filter narrows to eliminate the entire lower sideband $g_q(t) \longrightarrow \hat{g}(t)$, the Hilbert transform of $g(t)$, a pure single-sideband signal is generated provided $g_d(t)$ is kept at zero. The requirements to maintain $g_d(t)$ at zero are discussed in a subsequent paragraph.

It is seen from the discussion above that if a perfect reference is used (i.e., a local oscillator at ω_c) and the filter does not produce distortion, then $g(t)$ may be recovered exactly. On the other hand, an envelope detector will produce a term proportional to

$$\sqrt{g^2(t) + g_q^2(t)} \qquad (4)$$

where the residual effects of $g_q(t)$ are a source of distortion. Investigation of the distortion caused by a non-ideal VSB filter is required to determine the filter specifications.

Referring to Figure A-5, showing the VSB modulator and demodulator, it may be written as (to within a constant)

$$S_o(\omega) = G(\omega) \left[H_-(\omega - \omega_c) + H_+(\omega + \omega_c) \right] \qquad (5)$$

where

$S_o(\omega)$ = the output spectrum [signal portion of $V_o(t)$]

$G(\omega)$ = the input (baseband) spectrum

$H_+(\omega)$ = the positive frequency portion of the total (transmitter and receiver) VSB filter

$H_-(\omega)$ = the negative frequency portion of the filter

Then

$$S_o(t) = g(t) + g_d(t) \tag{6}$$

and

$$g_d(t) = \frac{1}{2\pi} \int_{-\infty}^{\infty} G(\omega) \left[H_-(\omega - \omega_c) + H_+(\omega + \omega_c) - 1 \right] e^{j\omega t} \, d\omega \tag{7}$$

The distortion will therefore be zero if

$$H_-(\omega - \omega_c) + H_+(\omega + \omega_c) \equiv 1$$

for all ω of interest. Bearing in mind that $H(\omega)$ is complex, it is possible then to estimate the amplitude and phase requirements of the VSB filter, $H(\omega)$.

The best approximation to use expands the filter in a Fourier series around the (positive and negative) carriers. This expansion is valid only in the region around the carrier and will therefore define these requirements for the receiver filter since the transmitter filter will be flat over this region.

The analysis shows that the major filter amplitude requirement in the vestige region is not for linearity but rather for odd symmetry around the carrier. This requires that the filter be 6 db down at the carrier. It may be shown that the signal distortion is related to the peak deviation, δ_{pk}, from odd symmetry by

$$\left[\frac{(g_d)_{rms}}{(g(t))_{rms}} \right] \underset{\text{Ampl.}}{\approx} \sqrt{2} \left| \delta_{pk} \right| \tag{8}$$

Therefore, to keep the distortion below about -26 db, the peak error in symmetry must be less than 0.3 db, and for -30 db max distortion, the peak error must not exceed 0.2 db.

The error caused by phase nonlinearities in the region around the carrier may be shown to be

$$\left[\frac{(g_d)_{rms}}{(g)_{rms}}\right]_{\phi} \approx \sqrt{2} \left|\phi_{pk}\right| \text{ (radians)} \tag{9}$$

Therefore, for -26 db distortion, $\left|\phi_{pk}\right| < 2^{\circ}$, and for -30 db distortion, $\left|\phi_{pk}\right| < 1.5^{\circ}$.

In the area outside the carrier region, the amplitude deviation from a flat transmission characteristic may be specified as a maximum gain-slope. Approximating the baseband TV signal as a triangular power spectrum gives for the relationship between gain-slope and distortion:

$$\left|H(\omega)\right| \approx .08 \frac{(g_d)_{rms}}{(g)_{rms}} \text{ per MHz} \tag{10}$$

For -26 db distortion, the gain-slope must be less than .035 db/MHz, and for -30 db the gain-slope should be less than .02 db/MHz.

The phase characteristic outside the carrier region may be shown to provide a relationship between phase linearity and distortion of

$$\left|\phi_{pk}\right| \leq 10.0 \frac{(g_d)_{rms}}{(g)_{rms}} \text{ degrees} \tag{11}$$

Therefore, for -26 db distortion, $\left|\phi_{pk}\right| < 5^{\circ}$, and for -30 db distortion, $\left|\phi_{pk}\right| < 3^{\circ}$.

Summary specifications for the filters are given in later sections.

3.4 UP-TRANSLATION EQUIPMENT

The up-translator block diagram is shown in Figure A-6. Double conversion is required to retain the spectral distribution in the 1.4- to 6.0-Mhz band identical to spectral distribution in the 30-Hz to 4.6-MHz band. This is important since most signals (such as TV) contain most of this energy in the lower spectral region. With one conversion, the inversion of such a spectrum would result in a considerable increase in modulator power requirements.

The choice of the two conversion frequencies depends on

a. The necessary frequency separation so that harmonic distortion products fall outside the desired band

b. The ease with which the two frequencies may track to eliminate frequency uncertainty

c. Tradeoffs between the weight and the ease of implementation of the VSB filter which favor higher frequencies while b. (above) decreases at high frequencies.

A 14-MHz local oscillator has been selected. The tracking VCO is then 15.4 MHz, and tracking is accomplished through dividing by 10 and dividing by 11 networks to derive the 1.4-MHz carrier.

If it presents an implementation problem to provide the VSB filtering at 14 MHz, the circuit can easily be redesigned for operation at a higher frequency, such as at 70 MHz, as shown in Figure A-7.

This frequency selection is also sufficient to keep the distortion introduced by the sidebands of the harmonics negligible.

The summary specifications of the 9- to 14-MHz filter are

Attenuation:

3 db down at 9.4 MHz
3 db down at 14.4 MHz
20 db down at 9.2 MHz
20 db down at 14.6 MHz

The gain-slope and phase linearity requirements are specified in Section 6.5.

3.5 DOWN-TRANSLATION EQUIPMENT

The down-translator block diagram for the 14-MHz VSB filter is shown in Figure A-8. The first VCO is at 15.4 MHz and the second at 14.0 MHz. The summary specifications for the VSB filter are

Attenuation:

Odd symmetry within $\pm$0.3 db around 14 $\pm$0.2 MHz
6 db down at 14 MHz
0 $\pm$0.1 db at 13.8 MHz
-20 $\pm$0.1 db at 14.2 MHz
-20 db at 9.2 MHz

Again, the gain-slope and phase linearity requirements are specified in Section 6.5.

4.0 REQUIRED SPECTRAL BANDWIDTH

In this section, the required spectral occupancy of a single modulating frequency, an average television signal which is vestigial-sideband modulated and then frequency-modulated, and finally a signal having a uniform spectral distribution are derived.

4.1 SINGLE FREQUENCY MODULATION SPECTRUM

For a given peak frequency deviation, the highest modulating frequency determines the bandwidth. This is because as the modulating frequency decreases, even if the index of modulation increases thereby increasing the number of sidebands, the sideband spacing on both of the sides of the carrier decreases at a higher rate than the increase of the significant sidebands (1 percent or higher amplitude). In Figure A-9, the amplitudes of the second and third sidebands are plotted for a 6-MHz modulating sinusoid as a function of peak frequency deviation.

4.2 VIDEO SPECTRUM

The video spectrum of an interlaced TV signal has been shown by many authors to consist of lines at harmonics of the line-scan frequency (15,750 Hz) with each of these harmonics modulated by the harmonics of the field repetition frequency (60 Hz). The width of each of these lines is related to the line-to-line and frame-to-frame picture correlation. The amplitude of the lines rolls off with an amplitude characteristic which depends on the element-to-element correlation along each scan line.

Following the analysis of Franks (Ref. 1) the 3-db line widths of the 60-Hz line harmonics were computed as functions of the frame-to-frame correlation (ρ_t) and the line-to-line correlation (ρ_v). The results are plotted in Figure A-10. From the figure it is seen that for the expected high correlations ($\rho_t > 0.8$ and $\rho_v > 0.8$) the lines are very narrow and may therefore be thought of as representing sine waves with some degree of phase randomness to account for the non-zero line width. This significantly simplifies the analysis to follow.

The remaining question has to do with the characteristic of the envelope rolloff. Franks' model considers a random video signal and derives a single-pole rolloff characteristic which appears to be quite representative of actual spectra. A plot of the 3-db and 10-db bandwidths of the envelope as a function of element-to-element correlation is shown in Figure A-11. It then remains to choose a representative value for the correlation ρ_h to complete the video spectrum representation. Using empirical data from Kretzmer (Ref. 2) we find that ρ_h is between 0.75 and 0.99. We use the worst case value of 0.75, which gives a 3-db bandwidth of 570 kHz, a 10-db bandwidth of 1.7 MHz, and a 20-db bandwidth of 5.7 MHz. This TV spectral envelope is plotted as $\overline{W}_1(f)$ in (a) of Figure A-12.

Before proceeding further we must consider the nature of the line spectrum. Ignoring the field lines (the 60-Hz harmonics at multiples of 15.75 kHz), which we will consider as contributing to the phase randomness of the scan harmonics, it is seen that the envelope in (a) of Figure A-12 will contain some 360 harmonics of 15.75 kHz.

4.2.1 VSB Spectrum

As seen in (b) of Figure A-12, the original TV spectrum is shifted 1.4 MHz and then filtered by the VSB transmit filter $H_t(\omega)$. This leaves the new signal spectrum (to be FM-modulated), shown in Figure A-13. Note that there are some 390 spectral lines within this envelope. This large number of lines is the basis for the approximate analysis which follows.

4.2.2 Random Signal Model

It is well known that the amplitude of the sum of a large number of randomly phased sine waves approaches a Gaussian distribution. Although the envelope of Figure A-13 shows that the amplitudes of the sine waves are not equal, we will consider the number of spectral components to be so large that the Gaussian condition is sufficiently met. This allows us to operate on the envelope of Figure A-13 to derive the required transmitted spectrum.

Consider the transmitted signal

$$v(t) = A_c \cos\left[\omega_c t + \theta(t)\right] \tag{11}$$

with $\theta(t) = b\int s(t)\,dt$

and $\dot{\theta}(t) = b\,s(t)$

and where b = constant

$s(t)$ = signal of spectrum $\Psi_s(f)$ (Figure A-13)

Then the following may be derived.

$$\overline{\dot{\theta}^2} = \Psi_{\dot{\theta}}(0) = \int_{-\infty}^{\infty} \Psi_{\dot{\theta}}(f)\,df \tag{12}$$

$$\overline{(\dot{\theta})^2} \triangleq (\Delta\omega)^2 = \int_{-\infty}^{\infty} \Psi_{\dot{\theta}}(f)\,df = 4\pi^2 \int_{-\infty}^{\infty} f^2\,\Psi_{\theta}(f)\,df$$

$$= b^2 \int_{-\infty}^{\infty} \Psi_s(f)\,df \tag{13}$$

Note that $\Delta\omega \equiv 2\pi\Delta f$ is the rms frequency deviation of ω_c due to $\theta(t)$. We also define the rms frequency bandwidth, $B_{\dot{\theta}}$, as

$$(B_{\dot{\theta}})^2 = \frac{\int_{-\infty}^{\infty} f^2 \Psi_{\dot{\theta}}(f)\, df}{\int_{-\infty}^{\infty} \Psi_{\dot{\theta}}(f)\, df} = \frac{\int_{-\infty}^{\infty} f^2 \Psi_s(f)\, df}{\int_{-\infty}^{\infty} \Psi_s(f)\, df} \tag{14}$$

and the rms phase bandwidth, B_θ, as

$$(B_\theta)^2 = \frac{\int_{-\infty}^{\infty} f^2 \Psi_\theta(f)\, df}{\int_{-\infty}^{\infty} \Psi_\theta(f)\, df} = \frac{\frac{b^2}{4\pi^2} \int_{-\infty}^{\infty} \Psi_s(f)\, df}{\Psi_\theta(0)} = \frac{(\Delta f)^2}{\Psi_\theta(0)} \tag{15}$$

It is then possible to define the rms modulation index, β, as

$$\beta^2 \triangleq \left(\frac{\Delta f}{B_{\dot{\theta}}}\right)^2 = \frac{b^2}{4\pi^2} \frac{\left[\int_{-\infty}^{\infty} \Psi_s(f)\, df\right]^2}{\int_{-\infty}^{\infty} f^2 \Psi_s(f)\, df} \tag{16}$$

We are interested in the spectrum $\Psi_v(f)$ of the transmitted signal, $v(t)$, which may be derived as follows.

$$\begin{aligned} v(t) &= \mathrm{Re}\left[A_c\, e^{j\omega_c t}\, e^{j\theta(t)}\right] \\ &= \mathrm{Re}\left[V(t)\, e^{j\omega_c t}\right] \end{aligned} \tag{17}$$

where

$$V(t) = A_c\, e^{j\theta(t)}$$

The autocorrelation function of V(t) is then

$$\Psi_v(\tau) = E\left\{v(t)\, v(t+\tau)\right\} = \mathrm{Re}\; E\left[V(t)\, V^{*}(t+\tau)\, e^{-j\omega_c \tau}\right]$$

$$= \frac{A_c^2}{2}\,\mathrm{Re}\left\{e^{-j\omega_c\tau}\, E\left[e^{j\theta(t)}\, e^{-j\theta(t+\tau)}\right]\right\} \qquad (18)$$

But, letting $\theta(t) = \theta$, and $\theta(t+\tau) = \theta_2$

$$E\left[e^{j\theta_1 X_1}\, e^{j\theta_2 X_2}\right] = \int_{-\infty}^{\infty}\int_{-\infty}^{\infty} e^{j(X_1\theta_1 + X_2\theta_2)}\, p(\theta_1,\theta_2)\, d\theta, d\theta_2$$

$$= M_\theta\,(jX_1,\, jX_2) \qquad (19)$$

M_θ = 2-dimensional moment generating function of θ.

For the Gaussian distribution of θ it is known that

$$M_\theta\,(jX_1,\, jX_2) = \exp\left[-\frac{1}{2}\left(\mu_{11} X_1^2 + \mu_{22} X_2^2 + 2\mu_{12} X_1 X_2\right)\right]$$

where μ_{ij} = the moments of θ and are

$$\mu_{11} = \mu_{22} = \Psi_\theta(0)$$

$$\mu_{12} = \Psi_\theta(\tau)$$

Hence

$$E\left[e^{j\theta_1}\, e^{-j\theta_2}\right] = M_\theta\,(1,\,-1) = e^{-\left[\Psi_\theta(0) - \Psi_\theta(\tau)\right]} \qquad (20)$$

and Equation (18) evaluates to be

$$\Psi_v(\tau) = \frac{A_c^2}{2} e^{-\Psi_\theta(0)} e^{\Psi_\theta(\tau)} \cos \omega_c \tau \tag{21}$$

The desired spectrum of v(t) is

$$\Psi_v(f) = \widetilde{f}\left\{\Psi_v(\tau)\right\} = \frac{1}{2}\Psi_0(f - f_c) + \frac{1}{2}\Psi_0(f + f_c) \tag{22}$$

where

$$\Psi_0(f) = \frac{A_c^2}{2} e^{-\Psi_\theta(0)} \widetilde{f}\left[e^{\Psi_\theta(\tau)}\right] \tag{23}$$

Equation (23) cannot be evaluated for a general $\Psi_\theta(\tau)$, but for the special condition of low modulation index used in the LCE, evaluation is straightforward.

From Equations (14) and (15) we write

$$\left(\frac{B_\theta}{B_{\dot\theta}}\right)^2 = \frac{\left[\int_{-\infty}^{\infty} f^2 \Psi_\theta(f)\, df\right]^2}{\left[\int_{-\infty}^{\infty} f^4 \Psi_\theta(f)\, df\right]\left[\int_{-\infty}^{\infty} \Psi_\theta(f)\, df\right]} \tag{24}$$

Which, by the Schwartz inequality may be shown to give

$$\left(\frac{B_\theta}{B_{\dot\theta}}\right)^2 \leq 1 \tag{25}$$

But, from Equations (12), (14), (15), (16) and (25)

$$\Psi_\theta(0) = \left(\frac{\Delta f}{B_\theta}\right)^2 = \left(\frac{\Delta f}{B_{\dot\theta}}\right)^2\left(\frac{B_{\dot\theta}}{B_\theta}\right)^2 = \beta^2\left(\frac{B_{\dot\theta}}{B_\theta}\right)^2 \geq \beta^2$$

Therefore, the low modulation index requirement for $\beta^2 \ll 1$ is always satisfied if $\Psi_\theta(0) \ll 1$. The actual value of $\Psi_\theta(0)$ to be used will be discussed in a subsequent paragraph. Therefore, since $\Psi_\theta(\tau) \leq \Psi_\theta(0)$ expanding the exponential in Equation (23) and dropping all terms of order higher than one gives

$$\Psi_0(f) = \frac{A_c^2}{2}\left[1 - \Psi_\theta(0)\right] \; \tilde{f}\left[1 + \Psi_\theta(\tau)\right] \tag{26}$$

$$= \frac{A_c^2}{2}\left[1 - \Psi_\theta(0)\right]\left[\delta(f) + \Psi_\theta(f)\right]$$

Combining all the previous results gives, finally

$$\Psi_\theta(f) = \frac{A_c^2}{4}\left[1 - \Psi_\theta(0)\right]\left\{\delta\,(f - f_o) + \frac{b^2}{4\pi^2}\,\frac{\Psi_s\,(f - f_o)}{(f - f_o)^2}\right.$$

$$\left. + \delta\,(f + f_o) + \frac{b^2}{4\pi^2}\,\frac{\Psi_s\,(f + f_o)}{(f + f_o)^2}\right\} \tag{27}$$

Figure A-14 shows the spectrum of $\Psi_s(f)/f^2$ derived from Figure A-13, and Figure A-15 shows the modulated spectrum of Equation (27). From Figures A-14 and A-15 it may be seen that the transmitted FM wave has a 3-db bandwidth of 3.4 MHz, a 10-db bandwidth of 4.4 MHz and a 20-db bandwidth of about 8 MHz.

4.2.3 Frequency Deviation

To derive the required frequency deviation it is necessary first to evaluate the constant b in Equation (13). This may be done by choosing the maximum value of $\Psi_\theta(0)$ which will not violate the constraint that $\Psi_\theta(0) \ll 1$. Choosing $\Psi_\theta(0) \equiv 0.1$, gives

$$\Psi_\theta(0) = 0.1 = \int_{-\infty}^{\infty} \Psi_\theta(f)\,df = \frac{b^2}{4\pi^2}\int_{-\infty}^{\infty} \frac{\Psi_s(f)}{f^2}\,df,$$

which may be graphically integrated from Figure A-15 to give

$$\frac{b}{2\pi} = \sqrt{\frac{0.1}{0.9}} = 0.33$$

A graphical integration of Figure A-14 gives

$$\int_{-\infty}^{\infty} \Psi_s(f)\, df = 2.3$$

So that, from Equation (13)

$$\Delta f = \frac{b}{2\pi}\sqrt{\int_{-\infty}^{\infty} \Psi_s(f)\, df} = 0.33\ \sqrt{2.3} = 0.50 \text{ MHz rms frequency deviation}$$

Since for a Gaussian process the peak-to-rms may be taken as 4 (negligibly small probability of exceeding 4 standard deviations), we have, approximately

$$f_o = \text{peak frequency deviation}$$

$$\approx 2.0 \text{ MHz.}$$

Equation (26) represents only the first two terms of an expansion for the exponential $e^{-\Psi_\theta(\tau)}$. If the third term is considered, so that a better bound on $\Psi_\theta(0)$ may be obtained, it will be seen in Section 4.3 that the added term will be less than -20 db at the 8 MHz bandwidth with $\Psi_\theta(0) = 0.4$, and $f_D = 4$ MHz. Under this circumstance, evaluation of Equation (16) shows that

$$\Psi_\theta(0) = 0.4$$

$$f_D = 4 \text{ MHz peak}$$

$$\Delta f = 1 \text{ MHz rms}$$

$$\beta = 0.465$$

Since an acceptable rule of thumb is to define low index frequency modulation as $\beta \leq 0.5$, a peak frequency deviation of 4 MHz is seen from all considerations to be acceptable and is chosen for system design.

4.3 UNIFORMLY DISTRIBUTED SPECTRUM

Many baseband signals such as multiplex telephony occupy essentially a flat spectrum. Therefore, in this section, the bandwidth requirements for various frequency deviations based upon a uniformly distributed signal spectrum between 1 and 6 MHz are examined. The results show that for peak frequency deviations as great as 4 MHz, the required IF bandwidth does not exceed 12 MHz.

Using the results of Section 4.2.2, we have for a uniform spectrum,

$$\int_{-\infty}^{\infty} \Psi_s(f)\, df = 2 \int_{1}^{6} df = 10$$

$$\int_{-\infty}^{\infty} f^2\, \Psi_s(f)\, df = 2 \int_{1}^{6} f^2\, df = 430/3$$

$$\int_{-\infty}^{\infty} \frac{\Psi_s(f)}{f^2}\, df = 2 \int_{1}^{6} f^{-2}\, df = 5/3$$

The rms frequency deviation from Equation (13) is

$$(\Delta f)^2 = \left(\frac{b}{2\pi}\right)^2 \int_{-\infty}^{\infty} \Psi_s(f)\, df = \left(\frac{b}{2\pi}\right)^2 \quad (10)$$

From Section 4.2.3 we have

$$\Psi_\theta(0) = \left(\frac{b}{2\pi}\right)^2 \int_{-\infty}^{\infty} \Psi_s(f) \frac{df}{f^2} = \frac{5}{3}\left(\frac{b}{2\pi}\right)^2$$

Therefore

$$\Psi_\theta(0) = (\Delta f)^2/6$$

and since $f_D \approx 4\ \Delta f$ (i.e., the peak deviation $\approx$ 4 times the rms deviation)

$$\Psi_\theta(0) = \frac{(f_D)^2}{96} \tag{28}$$

The low frequency equivalent of the transmitted autocorrelation can be written as

$$\Psi_0(\tau) = e^{\Psi_\theta(\tau)} = 1 + \Psi_\theta(\tau) + \frac{1}{2!}\Psi_\theta{}^2(\tau) + \frac{1}{3!}\Psi_\theta{}^3(\tau) + \ldots \tag{29}$$

giving a low-frequency spectrum of

$$\Psi_0(f) = \delta(f) + \Psi_\theta(f) + \frac{1}{2}\Psi_\theta{}^{(2)}(f) + \frac{1}{3!}\Psi_\theta{}^{(3)}(f) + \ldots \tag{30}$$

where $\Psi_\theta{}^{(n)}(f)$ = n-fold convolution of $\Psi_\theta(f)$. The first and second order spectra are shown in Figure A-16.

If $\Psi_\theta(0) \ll 1$ then the higher order terms $\Psi_0{}^n(\tau)$ may be neglected, and the IF bandwidth is just twice the bandwidth of $\Psi_0(f)$, or

$$BW = 2\ \Psi_0(f) \doteq 2\ \Psi_\theta(f) = 12\ \text{MHz}$$

The conditions under which this is valid, and an approximate evaluation of the full bandwidth is the subject of what follows.

The higher order terms are insignificant for

$$\frac{\Psi_0^{\,2}(\tau)}{2\Psi_\theta(\tau)} = \frac{\Psi_\theta(\tau)}{2} \ll 1$$

Hence, for $\Psi_\theta(0) \leq 0.2$, the sensible bandwidth is 12 MHz. From Equation (28) this corresponds to

$$f_D \leq \sqrt{96\ \Psi_\theta(0)}$$

or

$$f_D \leq 4.3 \text{ MHz}$$

Hence, the approximation of 12 MHz bandwidth holds out to the 4.0 MHz peak frequency deviation chosen before. The actual spread beyond ± 6 MHz may be computed by performing the convolution.

It may be shown that

$$\left[\frac{\Psi_s(f)}{f^2}\right]^{(2)} = \begin{cases} \frac{2}{f^2}\left(\frac{f-2}{f-1}\right) + \frac{4}{f^3}\ln(f-1) & 5 \leq f \leq 7 \\ \frac{1}{3f^2}\frac{(12-f)}{(f-6)} + \frac{4}{f^3}\ln\left(\frac{6}{f-6}\right) & 7 \leq f \leq 12 \\ 0 & f > 12 \end{cases}$$

The relative contribution of $\frac{1}{2}\Psi_\theta^{(2)}(f)$ may be determined by comparing it to the peak of $\Psi_\theta(f)$ for several values of frequency and frequency deviation.

$$\text{Relative Contribution} = \frac{\frac{1}{2}\Psi_\theta^{(2)}(f)}{\left|\Psi_\theta(f)\right|_{pk}}$$

$$= \frac{f_D^{\,2}}{320}\left[\frac{\Psi_s(f)}{f^2}\right]^2$$

which is plotted in Figure A-17, for f_D = 3 MHz, f_D = 4 MHz and f_D = 5 MHz. The figure shows that even for f_D as great at 5 MHz the contribution from the second-order term at $f_{carrier} \pm 6$ MHz is more than 20 db below the peak value of the spectrum.

It is also seen that at $f_{carrier} \pm 4$ MHz the contribution of the second-order term is less than 20 db below the peak signal, which validates the use of 4 MHz for peak frequency deviation of the TV signal.

4.4 MODULATOR POWER REQUIREMENTS

In order to make the decision on the peak frequency deviation to be used in the system, the modulator power must be considered. The modulator equivalent circuit is shown in Figure A-18. Normally

$$R_m \gg R_\ell \text{ and}$$

$$C_t = C_\ell + C_m$$

The total load impedance is then

$$Z_{eq} = \frac{X_c^2 R_\ell}{R_\ell^2 + X_c^2} + j \frac{R_\ell^2 X_c}{R_\ell^2 + X_c^2}$$

If $R_\ell \ll X_c$

$$Z_{eq} = R_\ell + j \frac{R_\ell^2}{X_c} .$$

Normally R_ℓ is chosen to equal X_c at the maximum modulating frequency, therefore,

$$R_\ell = \frac{1}{2\pi f_{mod_{max}} C_t}$$

and

$$Z_{eq} = \frac{X_c}{2} + j\,\frac{X_c}{2}$$

or

$$R_{eq} = \frac{X_c}{2} = \frac{1}{4\pi f_{mod_{max}}\, C_t}$$

The power consumed in the modulator driver amplifier may be expressed as

$$P = \frac{1}{M} \times K_1 \times \frac{(V_p)^2}{R_{eq}} + P_q = \frac{1}{M} K_1 \left(2\pi f_{mod_m}\, C_t\right)\left(\frac{\Delta F_p}{K_2}\right)^2 + P_q$$

when

P_q = quiescent power

K_1 = average power to peak power factor

M = amplifier efficiency

$$K_2 = F_p = \frac{\Delta F_p}{V_p}$$

ΔF_p = peak frequency deviation in MHz

V_p = peak modulator voltage

In Figure A-19 the computed average power is given for a uniformly distributed spectrum of random phase as a function of peak frequency deviation. The following constants are used:

$P_q = 2$ watts

$C_t = 20 \times 10^{-12}$ farads

$M = 0.9$

$K_2 = 1.87 \times 10^{-2}$ MHz/volt

$f_{mod_{max}} = 6.0$ MHz

From Figure A-19, it is to be noted that at peak frequency deviation of 4 MHz the power consumption is computed at 11.0 watts.

4.5 POST-DETECTION PEAK SIGNAL-TO-NOISE RATIO

In order to analyze the post-detection peak signal-to-noise ratio for the LCE, it is necessary to consider the full double-modulation (VSB/FM) system, rather than merely the FM portion. Thus, this summary analysis derives deviation requirements, bandwidth utilization requirements, and pre-emphasis/de-emphasis gains based on the block diagram of Figure A-1(a) and (b).

4.5.1 FM Equations

The FM signal may be written as

$$v_1(t) = \mathrm{Re}\left\{ A_c\, e^{j\theta(t)}\, e^{j\omega_c t} \right\}$$

where

$$\theta(t) = b \int s\,(t)\, dt$$

The noise may be written as:

$$n_1(t) = \mathrm{Re}\left\{ r(t)\, e^{j\phi(t)}\, e^{j\omega_c t} \right\} = R_e \left\{ \left[x(t) + jy(t) \right] e^{j\omega_c t} \right\}$$

where

$r(t)$ = noise envelope

$\phi(t)$ = noise phase

$x(t), y(t)$ = low-pass equivalent in-phase and quadrature-phase noise components

Therefore, the signal into the FM demodulator is

$$v_1(t) = v(t) + n_1(t) = \mathrm{Re}\left\{ v(t)\, e^{j\alpha(t)}\, e^{j\omega_c t} \right\}$$

where

$v_1(t)$ = composite envelope

$\alpha(t)$ = composite phase

The output of the FM demodulator, $v_2(t)$, is proportional to the rate of change of $\alpha(t)$. Thus, it may be shown that

$$v_2(t) = \alpha'(t) = N/D$$

$$N = A_c^2\,\theta'(t) + \left[x(t)\,y'(t) - y(t)\,x'(t)\right] + A_c\theta'(t)\left[x(t)\cos\theta(t) + y(t)\sin\theta(t)\right] + A_c\left[y'(t)\cos\theta(t) - x'(t)\sin\theta(t)\right]$$

$$D = A_c^2 + r^2(t) + 2r(t)\,A_c\cos\left[\theta(t) - \phi(t)\right]$$

For the high SNRs required for TV transmission, the terms involving the signal and noise cross products are insignificant, and the signal and noise may be considered separately. Thus

$$s_2(t) = \alpha'(t)\Big|_{r(t)=0} \approx \theta'(t) = b\,s(t) = \text{signal portion of } v_2(t)$$

$$n_2(t) = \alpha'(t)\Big|_{\theta(t)=0} \approx y'(t)/A_c = \text{noise portion of } v_2(t)$$

Thus, the signal out of the FM demodulator is equal to the signal into the modulator, times a constant, the peak (radian) frequency deviation.

For completeness, we add that the output noise-autocorrelation function and spectral density are

$$\Psi_{n_2}(\tau) = \frac{1}{A_c^2}\ \Psi_{y'}(\tau) = \frac{1}{A_c^2}\left[-\frac{d^2}{d\tau^2}\ \Psi_y(\tau)\right]$$

$$\Psi_{n_2}(f) = \frac{1}{A_c^2}\ \Psi_{y'}(f) = \frac{4\pi^2 f^2}{A_c^2}\ \Psi_y(f)$$

4.5.2 Overall Transfer Function

It has been shown in Section 3.0 that the signal output from the VSB demodulator is equal to the input information, g(t). In the previous section it was shown that the signal transmission through the FM portion of the system may be represented by a constant, b. Thus, as before

$$S_o(\omega) = b\ G(\omega)\left[H_+(\omega + \omega_o) + H_-(\omega - \omega_o)\right]$$

$$= b\ G(\omega) \text{ for proper choice of } H_T(\omega)\ H_R(\omega)$$

To account for the pre-emphasis/de-emphasis characteristic, it is only necessary to add the filter characteristics. Therefore,

$$S_o(\omega) = b\ H_P(\omega)\ H_d(\omega)\ G(\omega)\ H_{LP}(\omega) \tag{31}$$

and

$$\Psi_{s_o}(f) = 4\pi^2 f^2 \left|H_P(f)\right|^2 \left|H_d(f)\right|^2 \left|H_{LP}(f)\right|^2 \Psi_g(f)$$

For the noise we write

$$\Psi_{n_o}(f) = \left|H_{LP}(f)\right|^2 \left|H_d(f)\right|^2 \left[\Psi_{n_2}(f + f_o)\left|H_R(f + f_o)\right|^2 + \Psi_{n_2}(f + f_o)\left|H_R(f - f_o)\right|^2\right]$$

$$= \frac{4\pi^2}{A_c^2}\left|H_{LP}(f)\right|^2 \left|H_d(f)\right|^2 \left\{(f + f_o)^2\left|H_R(f + f_o)\right|^2 \Psi_y(f + f_o) + (f - f_o)^2\left|H_R(f - f_o)\right|^2 \Psi_y(f - f_o)\right\}$$

Since all the vestigial filtering in the 1.4 MHz carrier region is accomplished on the ground,

$$\left| H_R(f + f_o) \right|^2 = \left| H_+(f + f_o) \right|^2$$

and

$$\left| H_R(f - f_o) \right|^2 = \left| H_-(f - f_o) \right|^2$$

Also, if the input noise may be considered white, the output noise spectral density is also white, and

$$\Psi_y(f) = n_o = \frac{N_{RF}}{B_{RF}} \text{ watts/Hz}$$

Therefore

$$\Psi_{n_o}(f) = \frac{4\pi^2 n_o}{A_c^2} \left| H_{LP}(f) \right|^2 \left| H_d(f) \right|^2 \left\{ (f + f_o)^2 \left| H_+(f + f_o) \right|^2 + (f - f_o)^2 \left| H_-(f - f_o) \right|^2 \right\}$$

which may be shown to be

$$\Psi_{n_o}(f) = \frac{4\pi^2 n_o}{A_c^2} \left| H_{LP}(f) \right|^2 \left| H_d(f) \right|^2 (f^2 + f_o^2) \qquad (32)$$

4.5 SIGNAL-TO-NOISE RATIO WITHOUT PRE-EMPHASIS

Without pre-emphasis/de-emphasis, Equation (31) gives

$$\Psi_{s_o}(f) = 4\pi^2 b^2 \Psi_g(f) \left| H_{LP}(f) \right|^2$$

Taking the low-pass filter as being flat out to the required video bandwidth, B_v (=4.6 MHz), which will encompass the total signal, the output signal power is

$$s_o = \int_{-\infty}^{\infty} \Psi_{s_o}(f)\, df = 4\pi^2 b^2 \int_{-B_v}^{B_v} \Psi_g(f)\, df$$

$$= 4\pi^2 b^2 \overline{g^2(t)}$$

where

$\overline{g^2(t)}$ = the mean-square input signal

The noise output is

$$n_o = \int_{-\infty}^{\infty} \Psi_{n_o}(f)\, df = \frac{4\pi^2 n_o}{A_c^2} \cdot 2 \int_{o}^{B_v} (f^2 + f_o^2)\, df$$

$$= \frac{4\pi^2 n_o}{A_c^2\, 2} \left[\frac{B_v^3}{3} + f_o^2\, B_v \right]$$

$$= \frac{4\pi^2 n_o}{3C}\, B_v^3 \left[1 + 3 \left(\frac{f_o}{B_v} \right)^2 \right]$$

where

C = the total signal power

Note that the vestigial sideband conversion has offset the frequency of minimum noise from 0 to f_o MHz, thereby increasing the output noise power over ideal FM by

$$1 + 3\left(\frac{f_o}{B_v}\right)^2 = 1 + 3\left(\frac{1.4}{4.6}\right)^2 = 1.278 = 1.07 \text{ db}$$

The output SNR is

$$\frac{S_o}{n_o} = \frac{3\overline{g^2(t)}}{B_v^3}\left(\frac{b}{2\pi}\right)^2\left(\frac{C}{n_o}\right)\frac{1}{1+3\,(f_o\,B_v)^2} \tag{33}$$

$$= 3\overline{g^2(t)}\left(\frac{b}{2\pi B_v}\right)^2\left(\frac{C}{n}\right)_{RF}\left(\frac{B_{IF}}{B_v}\right)\frac{1}{1+3\,(f_o\,B_v)^2} \tag{34}$$

Equation (34) is the generally recognized form for an FM system. The output SNR is improved over the input CNR by an amount proportional to the square of the modulation index and the bandwidth ratio (B_{IF}/B_v) so long as the CNR exceeds the minimum (threshold) requirement, which is also a function of the modulation index.

Based on the analysis of section 4.3

$$B_{IF} \approx 2\,(B_v + f_o) + B_u$$

for low index FM

where

B_u = an additional bandwidth required by frequency instabilities, doppler spreads, etc.

The use of these parameters and their effect on the choice of frequency deviation may be seen by incorporating the above into Equation (34) recognizing that

$$p_o = \left(\frac{b}{2\pi}\right)^2\left|g(t)\right|_{pk}^2 = \left(\frac{b}{2\pi}\right)^2 = f_D^2 \text{ for } g(t) \text{ normalized to unity}$$

and $$s_o = \left(\frac{b}{2\pi}\right)^2\overline{g^2(t)}$$

so that $$p_o = \frac{s_o}{\overline{g^2(t)}} = \text{peak output power}$$

Therefore

$$\frac{p_o}{n_o} = \frac{6}{1 + 3\left(\frac{f_o}{B_v}\right)^2}\left(\frac{f_D}{B_v}\right)^2\left(\frac{C}{N}\right)_{RF}\left(\frac{f_o + B_v + B_u}{B_v}\right)^2$$

Using the values

$$f_o = 1.4 \text{ MHz}$$

$$B_v = 4.6 \text{ MHz}$$

$$\frac{p_o}{n_o} = 23 \text{ db}$$

gives the curve shown in Figure A-20 for (CNR) versus f_D. The spread of the curve is due to the uncertainty bandwidth, B_u. This has the effect of requiring somewhat less peak frequency deviation, f_D, for the same above-threshold CNR. The plotted value of threshold CNR is taken, with some changes in notation, from Heitzman (Ref. 3).

From Figure A-18 it is seen that, for an output SNR of 23 db (pk/rms), optimum modulation efficiency (operation just above threshold) is achieved with a frequency deviation of about 6 MHz, which approaches high index FM and gives an RF bandwidth of greater than 12 MHz.

With a frequency deviation of 4 MHz ($B_{IF} \approx 12$ MHz), Figure A-18 shows that for a 23 db output SNR, 4.5 db greater carrier power is required (operation at 4.5 db above threshold). Therefore, in order to maintain the operation at somewhat above threshold, so that some signal loss will not drop the output below threshold; the specified deviation of 4 MHz is a reasonable choice.

4.5.4 Signal-to-Noise Ratio With Pre-emphasis

The rolloff of the envelope of a typical TV spectrum at frequencies greater than about 200 kHz is due to lack of high-frequency content in the signal - i.e., slow transitions (over many data element widths) from black to

white. This allows for the possibility of inteoducing pre-emphasis/de-emphasis to enhance the output SNR.

Standard TV pre-emphasis ("predistortion") characteristics are

$$\left| H_p(f) \right|^2 = \frac{1 + (f/f_1)^2}{1 + (f/f_2)^2}$$

$$\left| H_d(f) \right|^2 = \frac{1}{1 + (f/f_1)^2}$$

where $f_1 \approx 200$ kHz, to coincide with the standard TV predistortion characteristic

and $f_2 \approx 800$ kHz

Taking

$$\Psi_g(f) = \frac{\overline{g^2(t)}}{10^7}, \quad 1 \text{ MHz} \leq \left| f \right| \leq 6 \text{ MHz}$$

so that

$$\int_{-\infty}^{\infty} \Psi_g(f)\, df \equiv \overline{g^2(t)}$$

it may be shown that

$$\gamma_D = \frac{B_v f_2}{3 f_1^2} \; \frac{1 + 3\left(\frac{f_o}{B_v}\right)^2}{1 + \frac{\pi}{2}\frac{f_o^2}{f_1 B_v}} \; \tan^{-1}\left(\frac{B_v}{f_2}\right) \approx 11 \text{ db}$$

Therefore, there is a theoretical improvement of 11 db. This is the total noise-power improvement, averaged over the entire band, but achieved through a reduction in the higher-frequency noise content. However, in black-and-white TV, the high-frequency noise is less objectionable than the noise at lower frequencies, so that the improvement in actual performance is

much less than that given above. This is the reason why pre-emphasis was introduced only for color TV transmission, where the color carrier may be immersed in the high-frequency noise (Ref. 4). Thus, for the LCE system, pre-emphasis is not required.

4.6 DISTORTION ANALYSIS

In this section the transmission deviations, modulator/demodulator linearity requirements, carrier drift effects, phase tracking error, and up-translator/down-translator filter requirements are analyzed to keep the total distortion well below the specified post-detection peak signal-to-noise ratio requirement of 23 db.

4.6.1 Transmission Deviations - RF and IF Requirements

One of the principle sources of distortion in FM systems arises from the generation of unwanted sideband energy through transmission deviations (nonlinear phase and nonuniform gain). These deviations result in unwanted amplitude and phase modulation which interfere with the desired modulating signal and produce signal distortions. Although in theory the resulting amplitude modulation can be completely removed by limiting in the receiver, in practice the phase characteristic of the receiver is always somewhat dependent on the instantaneous signal amplitude. This AM-to-PM conversion converts some of the amplitude distortion into phase distortion and the residual AM due to the transmission deviations must be accounted for and held to a minimum. A general analysis of these distortions is not possible, but an approximate analysis may be used with excellent results to derive the RF and IF requirements necessary to maintain the distortion within reasonable levels.

Figure A-21 shows the system to be analyzed, with $s(t)$ being the signal from the translator and $s_o(t)$ the signal to the down-translator. Using complex notation we make the following observations:

$$v_1(t) = A_c\, e^{j\theta(t)}\, e^{j\omega_c t} \tag{35a}$$

$$V_1(\omega) = \tilde{f}\left\{v_1(t)\right\} \tag{35b}$$

$$V_2(\omega) = H(\omega)\, V_1(\omega) \tag{35c}$$

$$v_2(t) = \tilde{f}^{-1}\left[H(\omega)\, V_1(\omega)\right] \tag{35d}$$

$$s_o(t) = \arg\left[v_2(t)\right] = s(t) + s_o(t) \tag{35e}$$

where

$$\theta(t) = b\int s(t)\, dt$$

and

$s_D(t)$ = distortion term

Expanding $H(\omega)$ in a power series around ω_c gives,

$$H(\omega) \equiv \left[1 + g_1\,(\omega - \omega_c) + g_2\,(\omega - \omega_c)^2 + g_3\,(\omega - \omega_c)^3 + \ldots\right] \cdot e^{j\left[b_2\,(\omega - \omega_c)^2 + b_3\,(\omega - \omega_c)^3 + \ldots\right]} \tag{36}$$

Note that the linear phase term, b_1, has been omitted, since it may be shown to introduce only delay, but no distortion.

After some manipulation, it may be shown that

$$v_2(t) = A_c\, e^{j\omega_c t}\ \tilde{f}^{-1}\left\{H\,(\omega + \omega_c)\ \tilde{f}\left[e^{j\theta(t)}\right]\right\} \tag{37}$$

For a narrow-band process, we may ignore all components of $H(\omega)$ which are not in the vicinity of $\omega = \omega_c$ and use the zero frequency representation

$$H\,(\omega + \omega_c) \equiv (1 + g_1\,\omega + g_2\,\omega^2 + \ldots)\, e^{j(b_2\omega^2 + b_3\omega^3 + \ldots)}$$

Expanding the exponential and retaining only terms up to the fourth power of ω, gives

$$H(\omega + \omega_c) \approx (1 + g_1\omega + g_2\omega^2 + g_3\omega^3 + g_4\omega^4)\left[\left(1 - \frac{b_2^2\,\omega^4}{2}\right) + j(b_2\omega^2 + b_3\omega^3 + b_4\omega^4)\right] = 1 + g_1\omega + (g_2 + jb_2)\omega^2 + \left[g_3 + j(b_3 + g_1b_2)\right]\omega^3 + \left[g_4 - \frac{b_2^2}{2} + j(b_4 + b_3g_1 + b_2g_2)\right]\omega^4 \tag{38}$$

Substituting Equation (38) into (37) results in

$$v_2(t) = \sqrt{\left[1 + P(t)\right]^2 + Q^2(t)}\ \cos\left[\omega_c t + \theta(t) + \theta_D(t)\right] \tag{39}$$

where

$$\theta_D(t) = \tan^{-1}\frac{Q(t)}{1 + P(t)}$$

and

$$P(t) = g_1\dot{\theta} + g_2\dot{\theta}^2 + b_2\ddot{\theta} + 3(b_3 + g_1b_2)\,\dot{\theta}\,\ddot{\theta} + g_3\,(\dot{\theta}^3 - \dddot{\theta}) + \left(g_4 - \frac{b_2^2}{2}\right)(-4\,\dddot{\theta}\,\dot{\theta} - 3\ddot{\theta}^2) + (b_4 + b_3g_1 + b_2g_2)(6\dot{\theta}^2\,\ddot{\theta} - \ddot{\theta}) \tag{40}$$

$$Q(t) = -g_2\ddot{\theta} + b_2\dot{\theta}^2 + (b_3 + g_1b_2)\,(\dot{\theta}^3 - \ddot{\theta}) - 3g_3\,\dot{\theta}\,\ddot{\theta} + (b_4 + b_3g_1 + b_2g_2)(-4\,\dddot{\theta}\,\dot{\theta} - 3\ddot{\theta}^2) + \left(g_4 - \frac{b_2^2}{2}\right)(\ddddot{\theta} - 6\dot{\theta}^2\,\ddot{\theta}) \tag{41}$$

For $P(t) \ll 1$ and $Q(t) \ll 1$, which is the case, Equation (39) becomes, approximately,

$$v_2(t) \approx \left[1 + P(t)\right] \cos \left\{\omega_c t + \theta(t) + Q(t)\left[1 - P(t)\right]\right\} \qquad (42)$$

Some of the distortion terms (linear terms such as $\dot{\theta}$, $\ddot{\theta}$, $\dddot{\theta}$, etc.) fall without frequency translation directly on the modulating signal causing them. These are directly equalizable at baseband since their effect is only to change baseband gain and not to cause interference by generating new frequencies. This is because the linearity introduces no new frequencies, but preferentially amplifies certain frequencies in a predictable manner. However, the remaining terms generate new frequencies and therefore represent nonequalizable distortion and hence must be considered in the specification of the allowable transmission deviations.

The analysis is quite cumbersome and tedious, and will not be included here in all its detail. Instead, only an example of the deviation of one of the terms of the result will be included as an illustration of the technique.

Consider only the second term of Equation (41) as being the phase distortion term. That is

$$\theta_o(t) = b_2 \left[\dot{\theta}(t)\right]^2$$

Then, the distortion term is

$$s_D(t) = b\dot{\theta}_D(t) = b\, b_2 \frac{d}{dt}\left[\dot{\theta}(t)\right]^2 = b\, b_2 \frac{d}{dt}\left[s(t)\right]^2$$

It is well known that the autocorrelation of $s^2(t)$ is (when $s(t)$ is Gaussian)

$$\Psi_{s^2}(\tau) = \Psi_s{}^2(o) + 2\,\Psi_s{}^2(\tau)$$

and therefore its spectrum is

$$\Psi_{s^2}(f) = \Psi_s{}^2(o)\,\delta(f) + 2\,\Psi_s{}^{(2)}(f)$$

Since the derivative in Equation (43) is equivalent to multiplying the spectrum by $\omega^2 = 4\pi^2 f^2$, we have, after ignoring the dc term as not contributing to the distortion

$$D_{\phi}(f) = 2b^2 \, b_2^{\,2} \, (4\pi^2 f^2) \, \Psi_s^{(2)}(f) \tag{44}$$

Performing the same type of analysis on the remainder of the non-equalizable distortion terms of Equations (40) and (41) and retaining only the most significant terms to the third order gives

$$D_{\phi}(f) = 2b^2 \left[b_2^{\,2} \, (4\pi^2 f^2) + \left(\frac{3g_3}{2} \right)^2 (16\pi^4 f^4) \right] \Psi_s^{(2)}(f)$$

$$+ b \, b^4 \, b_3^{\,2} \, (4\pi^2 f^2) \, \Psi_s^{(3)}(f) \tag{45}$$

Before deriving the amplitude distortion spectrum, we must define terminology regarding AM/PM conversion. From Equation (42) the amplitude of the distorted carrier is $1 + P(t)$, approximately, or, in db,

$$20 \log \left[1 + P(t) \right] \approx 8.686 \, P(t) \qquad P(t) \ll 1$$

AM/PM conversion is usually expressed as a conversion constant Φ, in degrees/db. Hence, the resulting phase distortion due to the conversion of the amplitude distortion into phase variations and changing degrees to radians is

$$\theta_{D_{AM/PM}}(t) = \Phi \frac{\pi}{180} \times 8.686 \, P(t) = 0.1516 \, \Phi \, P(t) \tag{46}$$

Continuing as with the results of Equation (45) for the amplitude terms gives

$$D_{AM/PM} = (.1516\ \Phi)\left\{2b^2\left[\frac{1}{4}g_1^4\,(4\pi^2f^2) + g_2^2\,(4\pi^2f^2) + \left(\frac{3b_3}{2}\right)^2(16\pi^4f^4)\right]\Psi_s^{(2)}(f) + 6b^4\,g_3^2\,(4\pi^2f^4)\,\Psi_s^{(3)}(f)\right\} \qquad (47)$$

The approach taken to evaluate g_1, g_2, g_3, b_2, b_3, and Φ will be to (1) assume a spectrum for $\Psi_s(f)$; (2) perform the required convolutions, $\Psi_s^{(2)}(f)$ and $\Psi_s^{(3)}(f)$; (3) evaluate Equation (45) by integrating over the baseband of interest (1-6 MHz), (4) choose an allowable distortion-to-signal ratio; (5) evaluate b_2, g_3, and b_3 from Equation (46); and (6) evaluate g_1 and g_2 from Equation (47) for several possible values of Φ.

To simplify the analysis, we assume a flat spectrum for $\Psi_s(f)$, which is the worst case of video transmission. This is shown in (a) of Figure A-22, where η is the spectral density in watts/Hz. Inset (b) of Figure A-22 shows the spectrum of the convolution of $\Psi_s(f)$ with itself; and Figure A-23 shows $\Psi_s^{(3)}(f)$. The other needed spectra are

$f^2\,\Psi_s^{(2)}(f)$ - Figure A-24(a)

$f^4\,\Psi_s^{(2)'}(f)$ - Figure A-24(b)

$f^2\,\Psi_s^{(3)}(f)$ - Figure A-25(a)

$f^4\,\Psi_s^{(3)}(f)$ - Figure A-25(b)

Graphically integrating the above over the desired baseband region $(1\ \text{MHz} \le |f| \le 6\ \text{MHz})$ gives

$$2\int_{1\ \text{MHz}}^{6\ \text{MHz}} f^2\,\Psi_s^{(2)}(f)\,df = 6 \times 10^{26}\,\eta^2$$

$$2\int_{1\ \mathrm{MHz}}^{6\ \mathrm{MHz}} f^4\,\Psi_s^{(2)}(f)\,df = 13.5 \times 10^{39}\,\eta^2$$

$$2\int_{1\ \mathrm{MHz}}^{6\ \mathrm{MHz}} f^2\,\Psi_s^{(3)}(f)\,df = 7.7 \times 10^{33}\,\eta^3$$

$$2\int_{1\ \mathrm{MHz}}^{6\ \mathrm{MHz}} f^4\,\Psi_s^{(3)}(f)\,df = 18 \times 10^{46}\,\eta^3$$

Since the peak frequency duration for the assumed Gaussian signal is 4 times the rms frequency deviation, and since, from section 4.2.2

$$b^2 = 4\pi^2(\Delta f)^2 \Big/ \int \Psi_s(f)\,df$$

we find that

$$b^2 = \frac{\pi^2}{4\eta} \times 10^{-7}\,f_D^{\,2} \tag{48}$$

Also,

$$S = \int \Psi_s(f)\,df = 10^7\eta$$

so that, finally

$$\left(\frac{D}{S}\right)_{\phi} = 12\pi^2 \times 10^{12}\,b_2^{\,2}\,f_D^{\,2} + 243\pi^2 \times 10^{25}\,g_3^{\,2}\,f_D^{\,2} + 11.55\pi^6\,b_3^{\,2}\,f_D^{\,4} \tag{49}$$

and

$$\left(\frac{D}{S}\right)_{AM/PM} = (.1516\ \Phi)^2 \left\{ 3\pi^4 \times 10^{12}\ g_1^4\ f_D^2 + 12\ \pi^4 \times 10^{12}\ g_2^2\ f_D^2 + 243\pi^6 \times 10^{25}\ b_3^2\ f_D^2 + 11.55 \times 10^{12}\ g_3^2\ f_D^4 \right\} \quad (50)$$

Note that in Equations (49) and (50), the distortion-to-signal ratios are seen to increase with increasing frequency deviation. This is to be expected, since the greater the deviation the more the transmitted spectrum is spread over the IF bandwidth, and the distortion increases for constant phase and gain parameters.

The evaluation of Equation (49) is straightforward. Letting $\left(\frac{D}{S}\right)_{\phi} \leq -36$ db and apportioning the distortion equally among the three terms gives

$$b_2 = \frac{0.6}{f_{D_{MHz}}} \cdot \text{deg/MHz}^2 = \frac{1.67}{f_{D_{MHz}}} \text{ nsec/MHz}$$

$$b_3 = \frac{1.23}{f_{D_{MHz}}^2} \text{ deg/MHz}^3 = \frac{3.41}{f_{D_{MHz}}^2} \text{ nsec/MHz}^2$$

$$g_3 = \frac{1.48 \times 10^{-3}}{f_{D_{MHz}}} (\text{MHz})^{-1}$$

Using these values where applicable in Equation (49), letting $\left(\frac{D}{S}\right)_{AM/PM} \leq -36$ db, and apportioning the remaining distortion equally between the first two terms shows that g_1 and g_2 are very dependent on Φ, the AM/PM conversion constant. For small Φ, g_1, and g_2 may be relatively large, but as

Φ increases, g_1 and g_2 must decrease. If Φ is too large (greater than about 2.5°/db) g_1 and g_2 must vanish, and practical filter design becomes impossible. Since good limiter design will limit Φ to less than 0.5°/db, this should not be a problem if the laser transmitter does not have a conversion factor greater than 2°/db. All the required parameter values for $\left(\frac{D}{S}\right)_\phi = \left(\frac{D}{S}\right)_{AM/PM} = -36$ db and for $f_D = 4$ MHz are given below.

$$b_2 = \text{parabolic phase} = 0.15^\circ/\text{MHz}^2 = 0.416 \text{ nsec/MHz}$$

$$b_3 = \text{cubic phase} = 0.047^\circ/\text{MHz}^3 = 0.213 \text{ nsec/MHz}^2$$

	0.1°/db	0.5°/db	1.0°/db	2.0°/db
g_1 = gain slope (db/MHz)	6.7	3.6	2.7	1.5
g_2 = parabolic gain (db/MHz^2)	1.7	0.4	0.15	.005
g_3 = cubic gain (db/MHz^3)	.003	.003	.003	.003

Curve-fitting the 30-MHz filter design curves for delay shows that the filter will easily meet the required delay performance.

4.6.2 Modulator Linearity.

A nonlinear amplitude-to-frequency or frequency-to-amplitude conversion will result in a distorted output signal. The effects of this distortion may be analyzed by considering the first two nonlinear terms of the conversion characteristic. Thus

$$2\pi f(t) = 2\pi\left[bs(t) + a_2 b^2 s^2(t) + a_3 b^3 s^3(t)\right] \tag{51}$$

The error is then

$$f_\epsilon(t) = a_2 b^2 s^2(t) + a_3 b^3 s^3(t)$$

with autocorrelation function

$$\Psi_\varepsilon(\tau) = a_2^2 b^4 \left[\Psi_s^2(o) + 2\Psi_s^2(\tau)\right] + a_3^2 b^6 \left[\Psi_s^2(o)\,\Psi_s(\tau) + 2\Psi_s^3(\tau)\right]$$

with a spectrum of

$$\Psi_\varepsilon(f) = a_3^2 b^6\, \Psi_s^2(o)\, \Psi_s(f) + 2a_2^2 b^4\, \Psi_s^{(2)}(f) + 2a_3^2 b^6\, \Psi_s^{(3)}(f) \qquad (52)$$

Evaluating Equation (52) by a graphical convolution and making the same substitution for b as in Equation (48) gives

$$D_{MOD} = \frac{\pi^6}{32} a_3^2 f_D^6 + \frac{2\pi^4}{25} f_D^4$$

The signal power is

$$S_{MOD} = \frac{\pi^2}{4} f_D^2 \qquad (53)$$

so that

$$\left(\frac{D}{S}\right)_{MOD} = \frac{8\pi^2}{25} f_D^2 a_2^2 + \frac{\pi^4}{8} f_D^4 a_3^2 \qquad (53)$$

Letting $\left(\frac{D}{S}\right)_{MOD} \leq -36$ db and apportioning the distortion equally as before, gives, at $f_D = 4$ MHz

$$a_2 \leq .003 \text{ MHz/MHz}^2$$

$$a_3 \leq .0034 \text{ MHz/MHz}^3$$

These coefficients may be related to linearity by finding the best (in the minimum mean-square sense) straight-line fit to Equation (51) and evaluating the peak deviation over the bandwidth. Performing the required mathematics, assuming a Gaussian distribution for s(t) gives a maximum deviation from linearity of $\pm$ 175 kHz over the input frequency deviation swing of $\pm$ 4 MHz, which is not a very stringent requirement.

4.6.3 Effects of Carrier Drift

It may be shown that the effect of a passband characteristic not centered at the carrier will be an increase in linear envelope delay distortion. In a previous section the phase was written as

$$\theta(\omega - \omega_c) = b_1 (\omega - \omega_c) + b_2 (\omega - \omega_c)^2 + b_3 (\omega - \omega_c)^3$$

and the values of b_2 and b_3 were evaluated. Differentiating $\theta(\omega)$ with respect to ω gives the envelope delay distortion

$$\text{EDD} = \frac{d\theta}{dw} = b_1 + 2b_2 (\omega - \omega_c) + 3b_3 (\omega - \omega_c)^2$$

Using the values previously determined gives

$$\text{linear EDD} = 2b_2 = 0.83 \text{ nsec/MHz}$$

$$\text{parabolic EDD} = 3b_3 = 0.64 \text{ nsec/MHz}^2$$

If the expansion is not centered at ω_c but rather at $\omega_1 = \omega_c - \delta\omega$, then a new linear term emerges

$$\text{EDD} = b_1 + 2b_2 (\omega - \omega_c) + 6b_3 \Delta\omega(\omega - \omega_c) + 3b_3 (\omega - \omega_c)^2$$

For the specified frequency stability, an rms computation gives

$$\sqrt{\overline{(\Delta f)^2}} = 18.5 \text{ kHz}$$

so that

$$f_D = .074 \text{ MHz} = 4\Delta f_{rms}$$

Hence, the added linear EDD is

$$6(.213)(.074) = .095 \text{ nsec/MHz}$$

or about an 11% increase over the perfectly stable carrier case.

4.6.4 Effects of Phase Tracking Error Between Up and Down Converters

It was shown previously that for the vestigial filter, properly chosen so that the distortion part in the in-phase term is zero, the signal can be written as

$$s(t) = g(t) \cos \omega_c t - g_q(t) \sin \omega_c t$$

If the detector is perfectly in phase with the cosine term, then no quadrature distortion will result. Due to imperfect tracking between receiver and transmitter, there will be a random phase error the mean-square value of which is inversely proportional to the signal-to-noise ratio in the phase-lock loop. Then,

$$\begin{aligned} s_o(t) &= s(t) \left\{ 2 \cos \left[\omega_c t + \phi(t) \right] \right\} \\ &= g(t) \cos \phi(t) - g_q(t) \sin \phi(t) \end{aligned}$$

For $\phi(t)$ small (usually the case when tracking)

$$s_o(t) \approx g(t) \left[1 - \frac{\phi^2(t)}{2} \right] - \phi(t)\, g_q(t) \qquad (55)$$

The error is

$$\begin{aligned} \epsilon_\phi(t) &= g(t) - s_o(t) \\ &= \frac{\phi^2(t)}{2}\, g(t) + \phi(t)\, g_q(t) \end{aligned}$$

The mean-square error is

$$\overline{\epsilon_\phi^2(t)} = \frac{1}{4}\ \overline{\phi^4(t)}\ \overline{g^2(t)} + \overline{\phi^2(t)}\ \overline{g_q^2(t)} + \overline{\phi^3(t)}\ \overline{g(t)\ g_q(t)}$$

Although $g_q(t)$ and $g(t)$ are correlated, for the zero mean-phase error generated by a locked loop $\overline{\phi^3(t)} = 0$, so that

$$\overline{\epsilon_\phi^2(t)} = \frac{1}{4}\ \overline{\phi^4(t)}\ \overline{g^2(t)} + \overline{\phi^2(t)}\ \overline{g_q^2(t)}$$

Assuming a Gaussian distribution for ϕ, which is normally the case when the loop is in lock, we find

$$\overline{\phi^4} = 3\sigma^4$$

$$\overline{\phi^2} = \sigma^2$$

so that

$$\left(\frac{D}{S}\right)_{track} = \frac{\overline{\epsilon^2}}{\overline{g^2}} = \frac{3}{4}\sigma^4 + \sigma^2\left(\frac{\overline{g_q^2}}{\overline{g^2}}\right)$$

It may be shown that

$$\Psi_{g_q}(f) = \Psi_g(f)\ \left|H_q(f)\right|^2$$

where

$$\left|H_q(f)\right|^2 = \begin{cases} \left|1 - 2\left|H - (f - f_c)\right|\right|^2 & |f| \le B_v \\ 1 & |f| > B_v \end{cases}$$

Therefore, assuming a linear vestige characteristic between f = 0 and f = 200 kHz, and a flat response from f = 200 kHz to f = 4.6 MHz, gives

$$\overline{g_q^2(t)} = \overline{2g^2}\left[\frac{1}{2}(1 \times .2) + (4.4 \times 1)\right] \times 10^6 = 9 \times 10^6$$

while

$$\overline{g^2(t)} = 9.2 \times 10^6$$

so that

$$\left(\frac{D}{S}\right)_{VSB} = .75\,\sigma^4 + .98\sigma^2 \qquad (56)$$

The value of $\sigma^2 = \overline{\phi^2(t)}$ is related to the loop bandwidth which must be chosen not only for minimum phase jitter (σ^2) but also with regard to the dynamic performance requirements. With a loop at or near lock the jitter is inversely proportional to the signal-to-noise ratio in the loop,

$$\overline{\phi^2} = \sigma^2 = \frac{1}{2(S/N)_L} \quad \text{for} \left(\frac{S}{N}\right)_L > 10$$

and $\left(\frac{S}{N}\right)_L = \left(\frac{S}{N}\right)_{in}\left(\frac{B_{in}}{2B_L}\right)$ which is significantly greater than 10.

Therefore

$$\left(\frac{S}{N}\right)_L \geq \frac{0.245}{(D/S)_{VSB}} \pm \sqrt{\frac{.188}{(D/S)_{VSB}} + \frac{.06}{(D/S)^2_{VSB}}}$$

or

$$\left(\frac{S}{N}\right)_L \geq \frac{0.49}{(D/S)_{VSB}} = 39.1 \text{ for} \left(\frac{D}{S}\right)_{VSB} \leq -36 \text{ db}$$

4.6.5 Vestigial Filter

It now remains necessary to examine the vestigial filter requirements in light of the overall distortion budget. Examining all the terms previously considered gives

$$\left(\frac{D}{S}\right)_{TOTAL} = \left(\frac{D}{S}\right)_{\phi} + \left(\frac{D}{S}\right)_{AM/PM} + \left(\frac{D}{S}\right)_{MOD} + \left(\frac{D}{S}\right)_{track}$$

$$= -30 \text{ db for each term equal to } -36 \text{ db}$$

Therefore the distortion introduced by the vestigial filters should be about -27 db, so that the total distortion will be less than -25 db. Then, using Equation (38), with $\frac{b}{2\pi} = f_D = 4$ MHz, gives for the output signal-to-noise ratio

$$\frac{P_o}{n_o} = \frac{3 f_D^2}{B_v^3}\left(\frac{C}{n_o}\right) \frac{1}{1 + 3 (f_o/B_v)^2} = 28.9 \text{ db}$$

Hence the total signal-to-noise plus distortion will be

$$\frac{s}{n_{total}} = 10^{2.89} + 10^{2.5} = 10^{2.37} = 23.7 \text{ db}$$

which exceeds the 23 db requirement.

The -27 db VSB distortion is equally divided among the four contributing terms so that each will be specified at -33 db.

Using the results of Task III gives as new specifications (changes only shown)

Up Converter

Gain Slope: ≤ 0.012 db/MHz for $f > f_o - 0.2$ MHz

Phase Linearity: $\leq \pm 0.7^{\circ}$ deviation from linearity for

$f = f_o \pm 0.2$ MHz

$\leq \pm 1.8^{\circ}$ deviation from linearity for

$f > f_o + 0.2$ MHz

Down Converter

Gain Slope: $\leq .012$ db/MHz for $f > f_o + 0.2$ MHz

Attenuation: Odd symmetry within $\pm$ 0.1 db around subcarrier

Phase Linearity: $\leq \pm 0.7^{\circ}$ deviation from linearity for

$f = f_o \pm 0.2$ MHz

$\leq \pm 1.8^{\circ}$ deviation from linearity for

$f > f_o + 0.2$ MHz

4.7 SUMMARY

4.7.1 Error Budget

Error Source	Signal-to-Distortion (db)		
Random noise		32.7	(f_D = 4 MHz)
Transmission deviations	33	34.6	
Frequency effects 36			
Amplitude effects 36			
Modulator/demodulator linearity		36	
Phase tracking error		36	
Vestigial filter		27	
Total		23.7 db	

4.7.2 Specifications

(a) RF/IF Characteristics

parabolic phase $\leq 0.15^{o}/MHz^{2}$ (0.416 nsec/MHz)

cubic phase $\leq 0.047^{o}/MHz^{3}$ (0.213 nsec/MHz^{2})

linear EDD = 0.83 nsec/MHz (+0.095 nsec/MHz due to carrier instability)

parabolic EDD = 0.64 nsec/MHz^{2}

Requirement \ AM/PM Conv. Factor	0.1^{o}/db	0.2^{o}/db	1.0^{o}/db	2.0^{o}/db
Gain Slope (db/MHz)	6.7	3.6	2.7	1.5
Parabolic Gain (db/MHz^{2})	1.7	0.4	0.15	0.005
Cubic Gain (db/MHz^{3})	0.003			

(b) Frequency Modulator Characteristic

parabolic $\leq .003$ MHz/MHz^{2}

cubic $\leq .0034$ MHz/MHz^{3}

linearity: $\pm$175 kHz maximum deviation from linearity for output frequency deviation of $\pm$ 4 MHz

(c) Phase Tracking (Up/Converter - Down/Converter)

Signal-to-noise ratio (tracking loop) $\geq$ 39 db

(d) Vestigial Filters

Up Converter

Gain Slope:	$\leq .012$ db/MHz	$f > f_o + .2$ MHz
Phase:	$\leq \pm 0.7^{o}$ deviation from linearity	$f \leq f_o \pm 0.2$ MHz
	$\leq \pm 1.8^{o}$ deviation from linearity	$f > f_o + .2$ MHz

Down Converter

Attenuation: Odd symmetry within $\pm$ 0.1 db
$f_s \leq f_o \pm 0.2$ MHz

Gain Slope: $\leq .012$ db/MHz

Phase: $\leq \pm 0.7^\circ$ deviation from linearity
$f \leq f_o \pm 0.2$ MHz

$\leq \pm 1.8^\circ$ deviation from linearity
$f > f_o + 0.2$ MHz

References

1. L. E. Franks, "A Model for the Random Video Process," BSTJ, April 1960, pp. 609-630.

2. E. R. Kretzmer, "Statistics of Television Signals," BSTJ, July 1952, pp. 751-763.

3. R. E. Heitzman, IRE Trans. on Space Electronics and Telem., SET-8, December 1962.

4. Transmission Systems for Communications, Bell Telephone Labs, 1964.

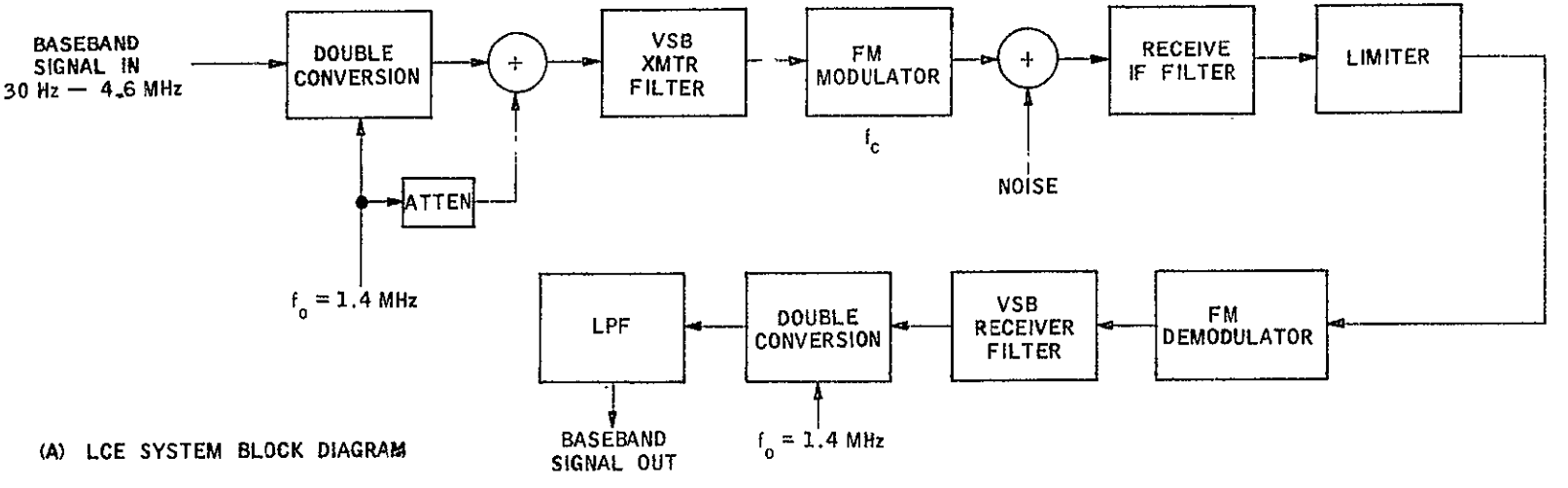

(A) LCE SYSTEM BLOCK DIAGRAM

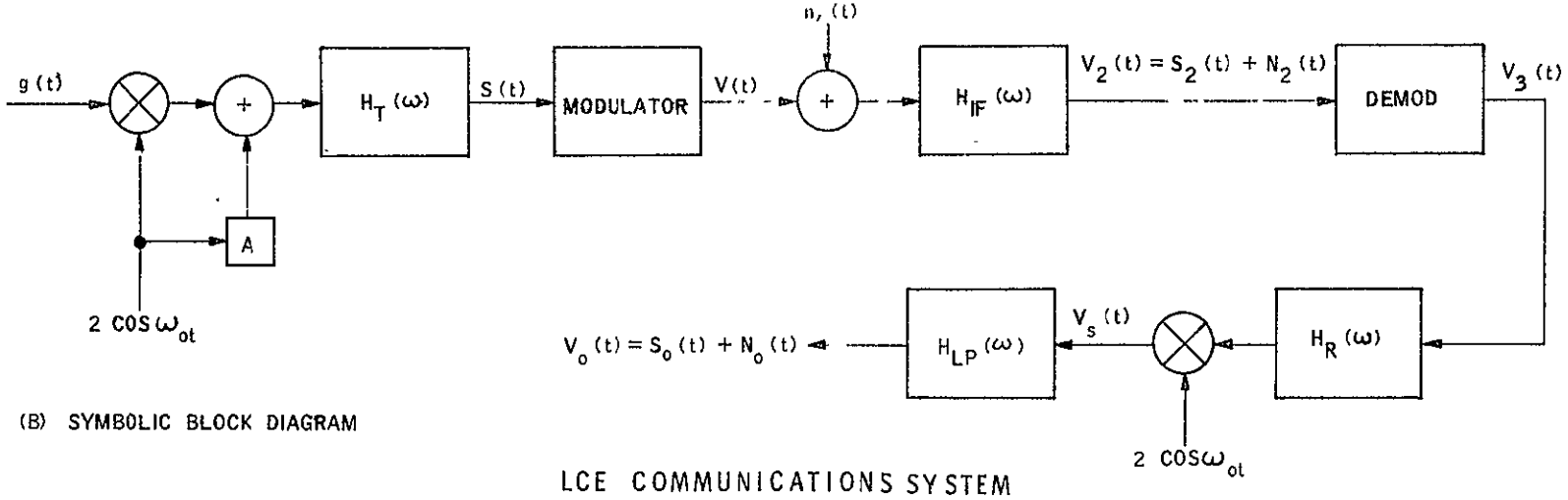

(B) SYMBOLIC BLOCK DIAGRAM

LCE COMMUNICATIONS SYSTEM

Figure A-1

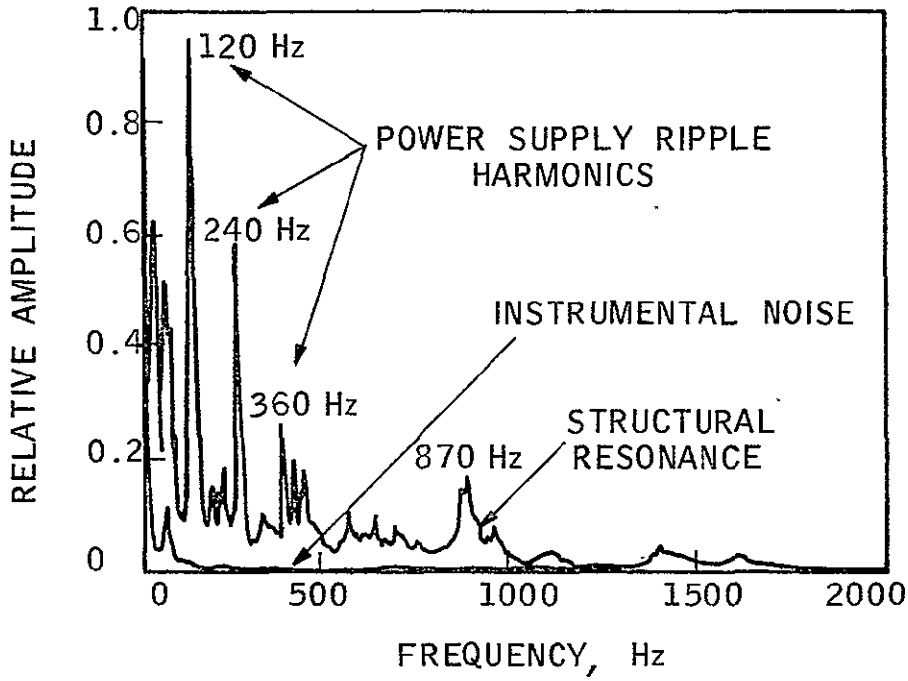

TYPICAL LASER FM NOISE SPECTRUM

Figure A-2

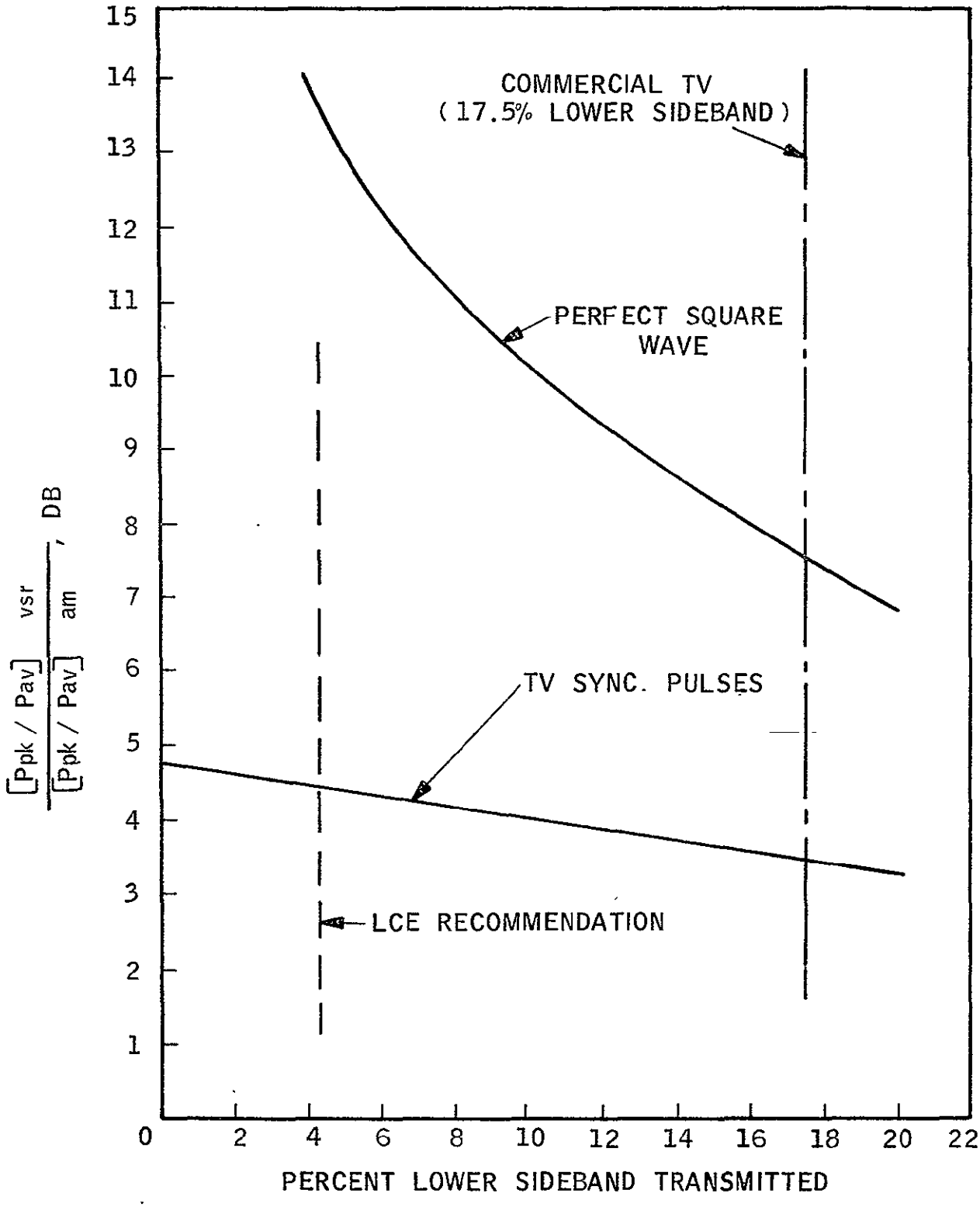

PEAK-TO-AVERAGE POWER RATIO AS A FUNCTION OF PERCENT LOWER SIDEBAND TRANSMITTED

Figure A-3

TOTAL BANDWIDTH: 50 MHz (3 db)

"INFORMATION" BANDWIDTH: 4.6 MHz (3 db)

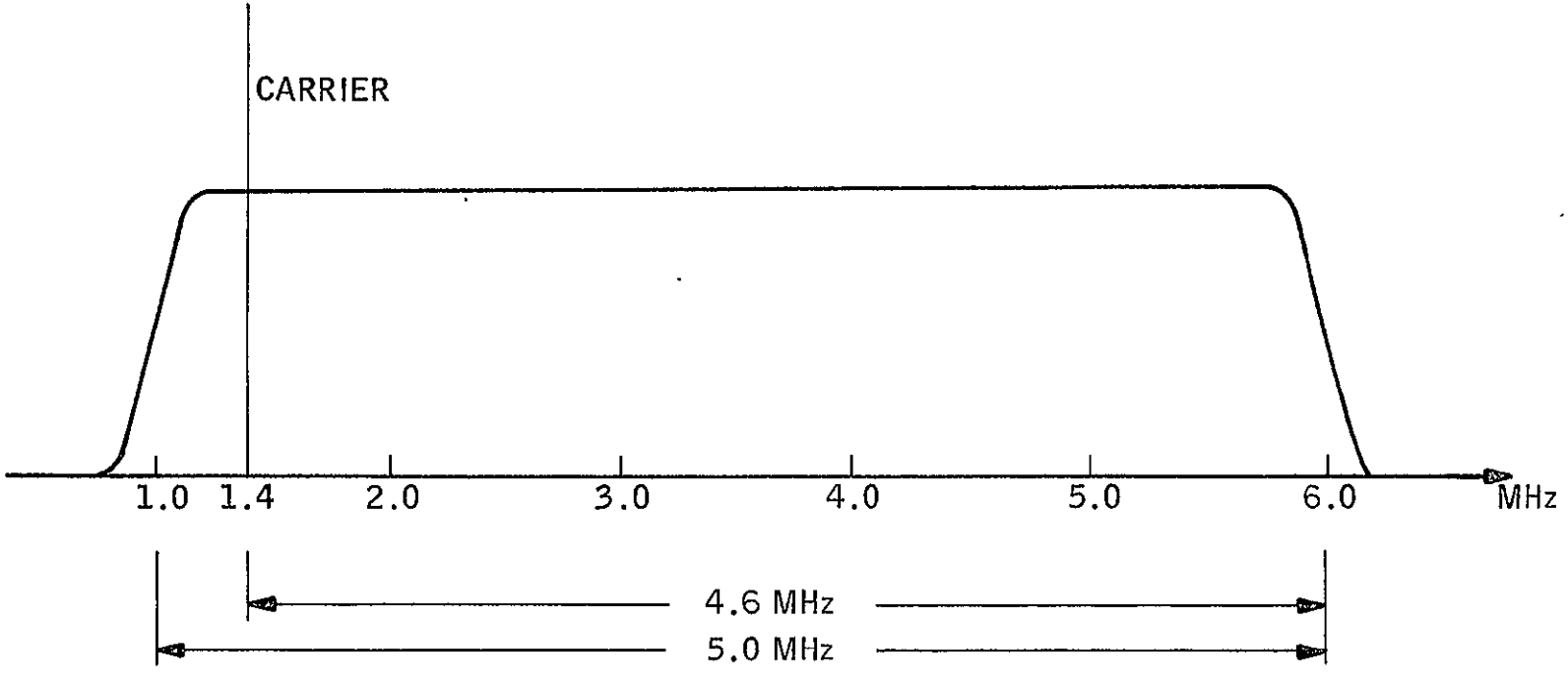

UP CONVERTER OUTPUT FILTER

Figure A-4

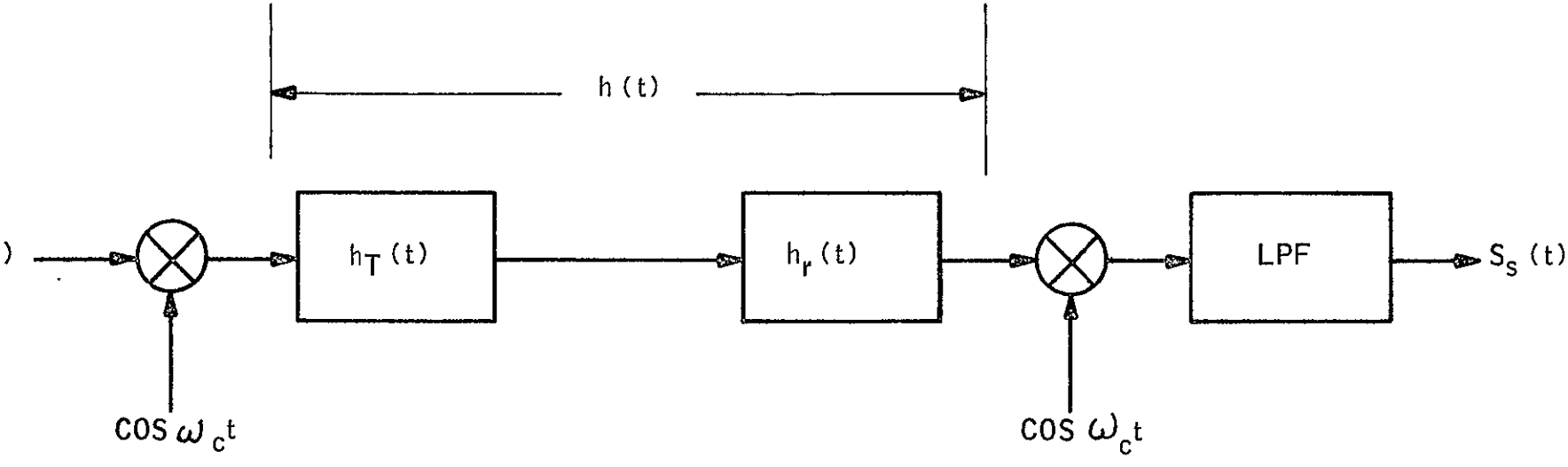

Figure A-5

VESTIGIAL SIDEBAND SYSTEM

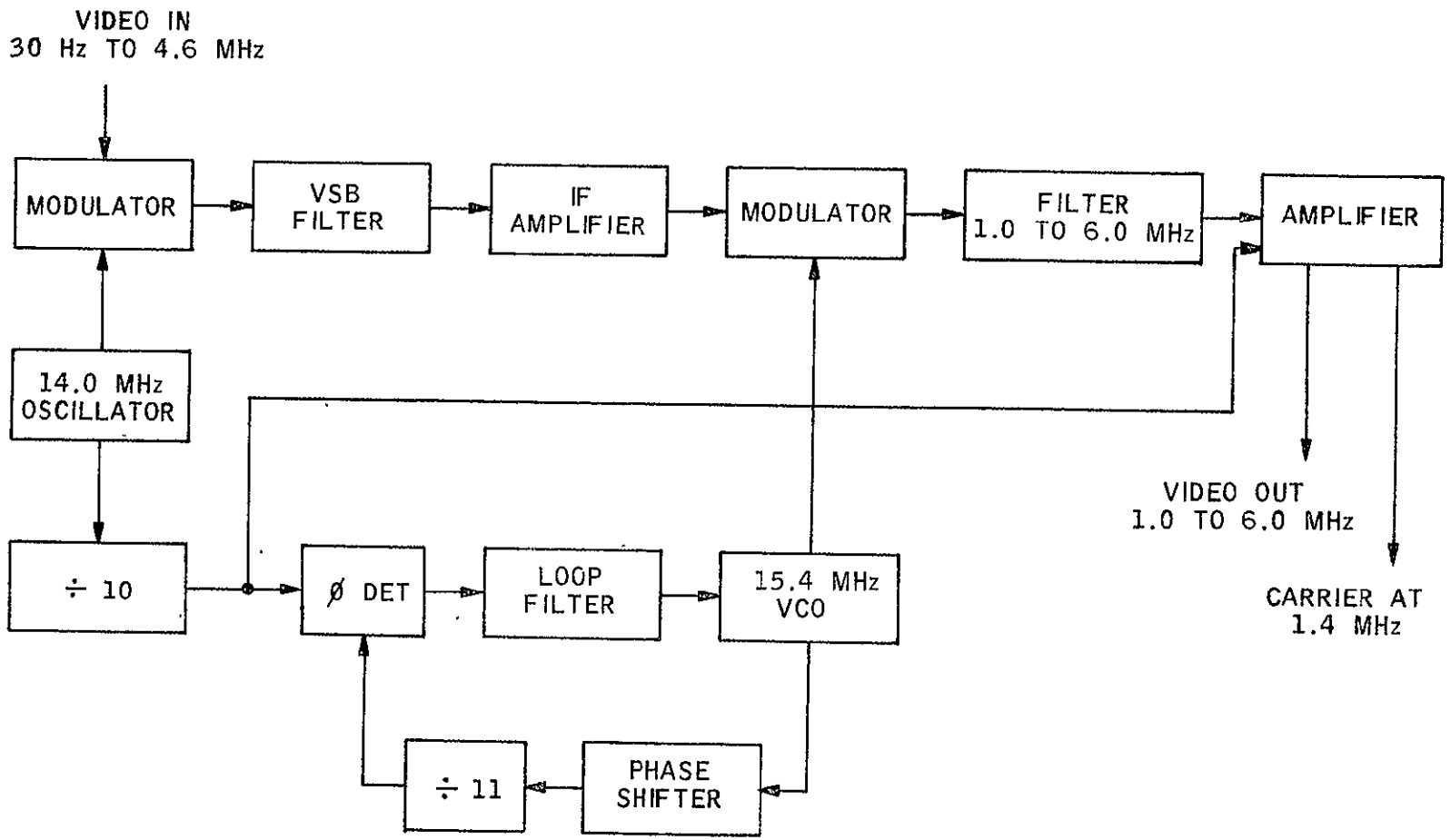

UP-TRANSLATION EQUIPMENT BLOCK DIAGRAM

Figure A-6

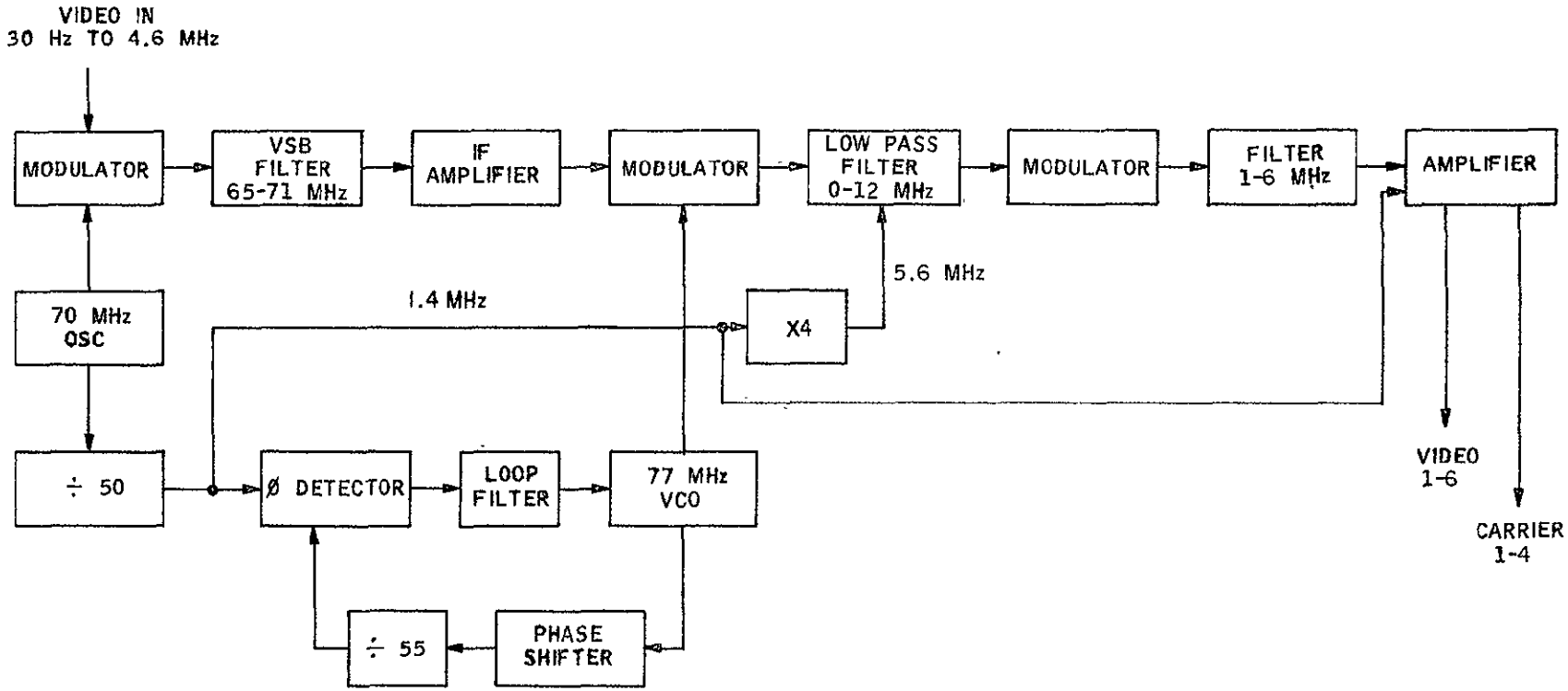

Figure A-7

UP-TRANSLATION WITH FILTERING AT 70 MHz

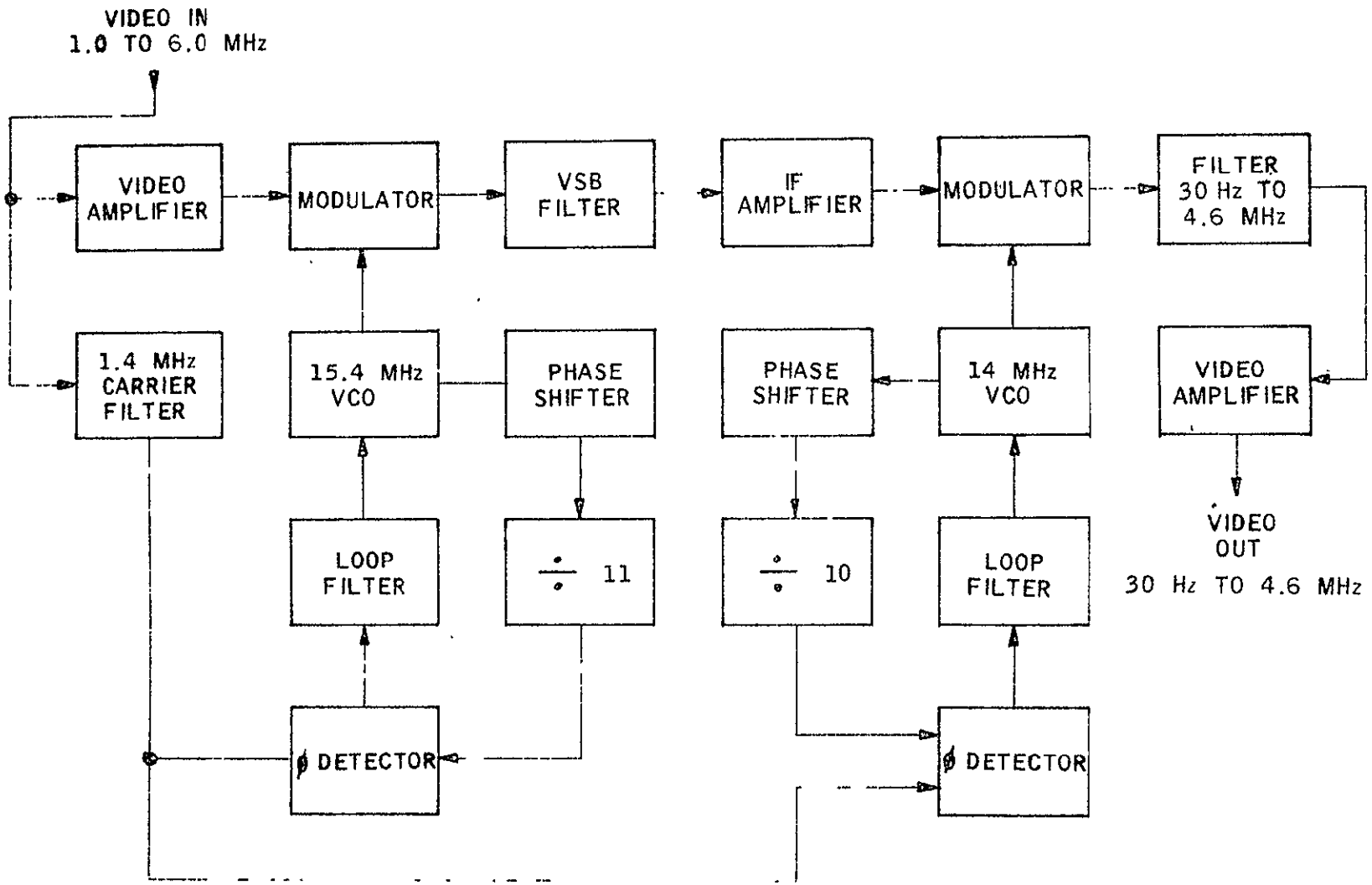

Figure A-8

DOWN TRANSLATION EQUIPMENT BLOCK DIAGRAM

PLOT

ABSCISSA	ORDINATE	
△F	CURVE 1	CURVE 2
0.6	.0012	
1.2	.0049	1.6×10^{-4}
1.8	.0111	
2.4	.0197	1.3×10^{-3}
3.0	.0306	
4.2	.0587	
4.8	.0758	1.0×10^{-2}
5.4	.0945	
6.0	.1149	2.0×10^{-2}

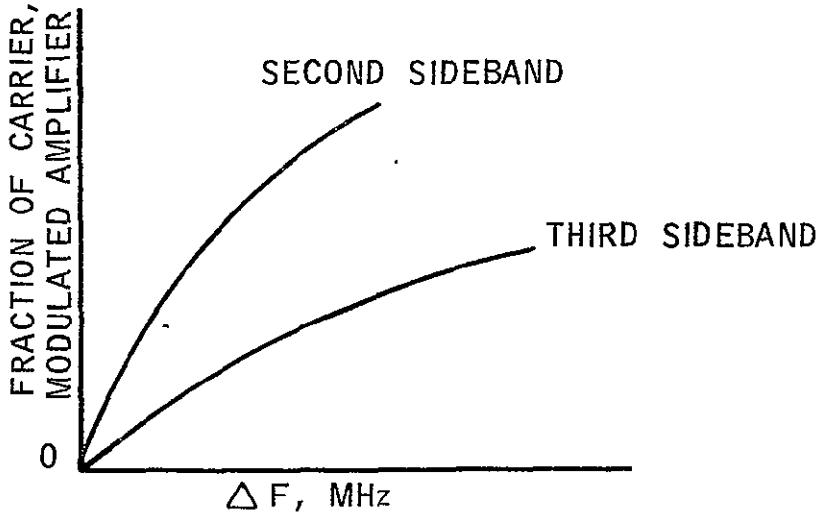

BANDWIDTH REQUIREMENTS OF SINGLE SINUSOID (6 MHz). MODULATION AS A FUNCTION OF PEAK FREQUENCY DEVIATION

Figure A-9

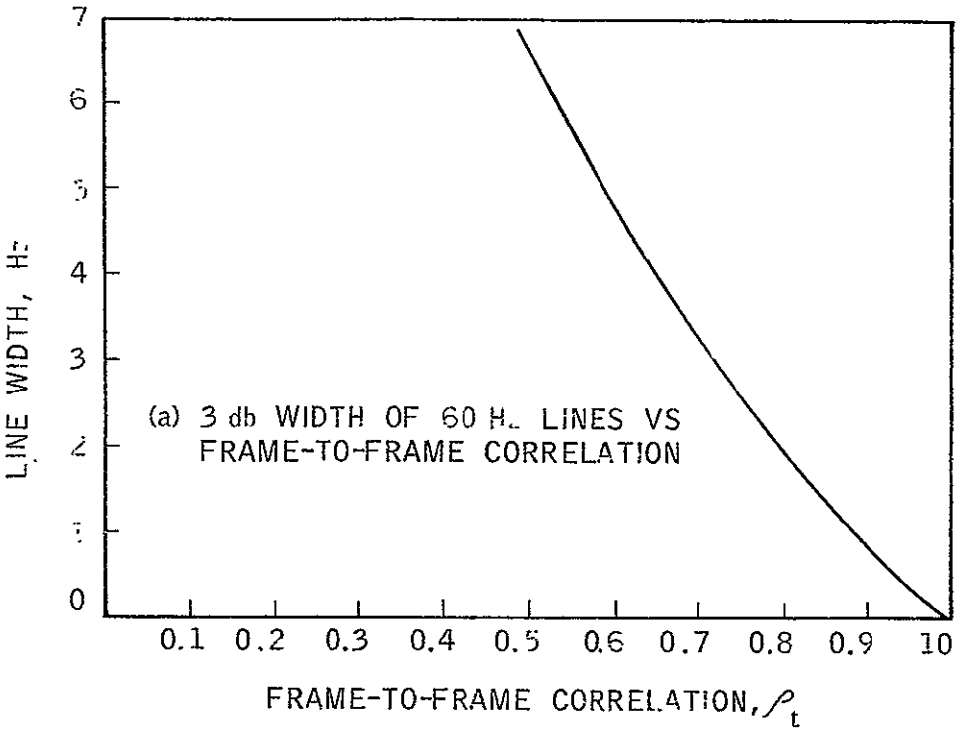

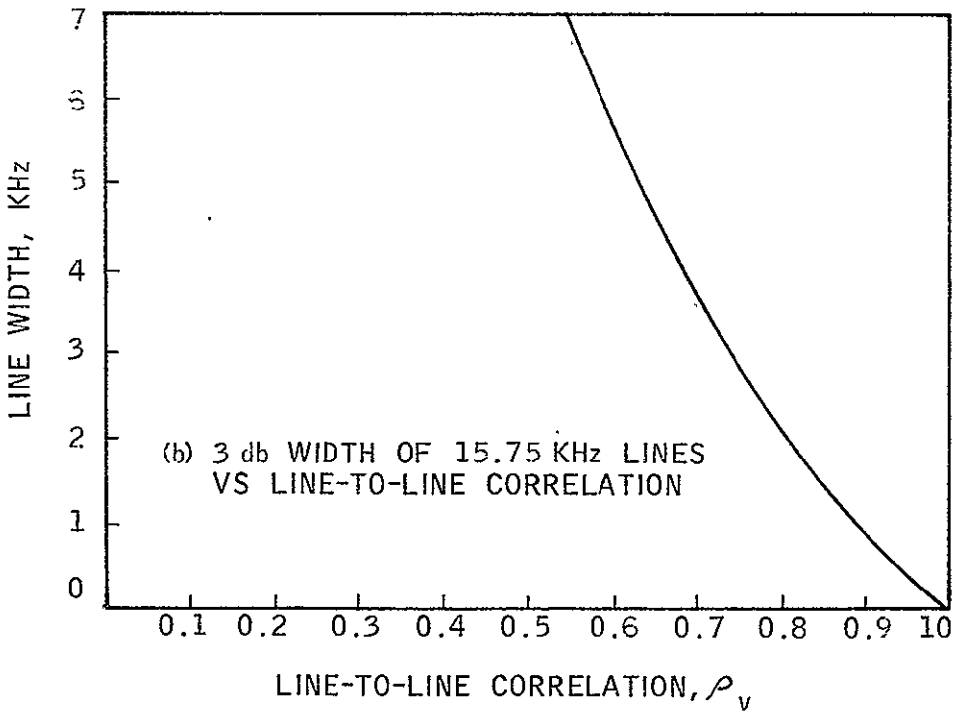

TV VIDEO FRAME AND LINE
SPECTRAL COMPONENT CORRELATION

Figure A-10

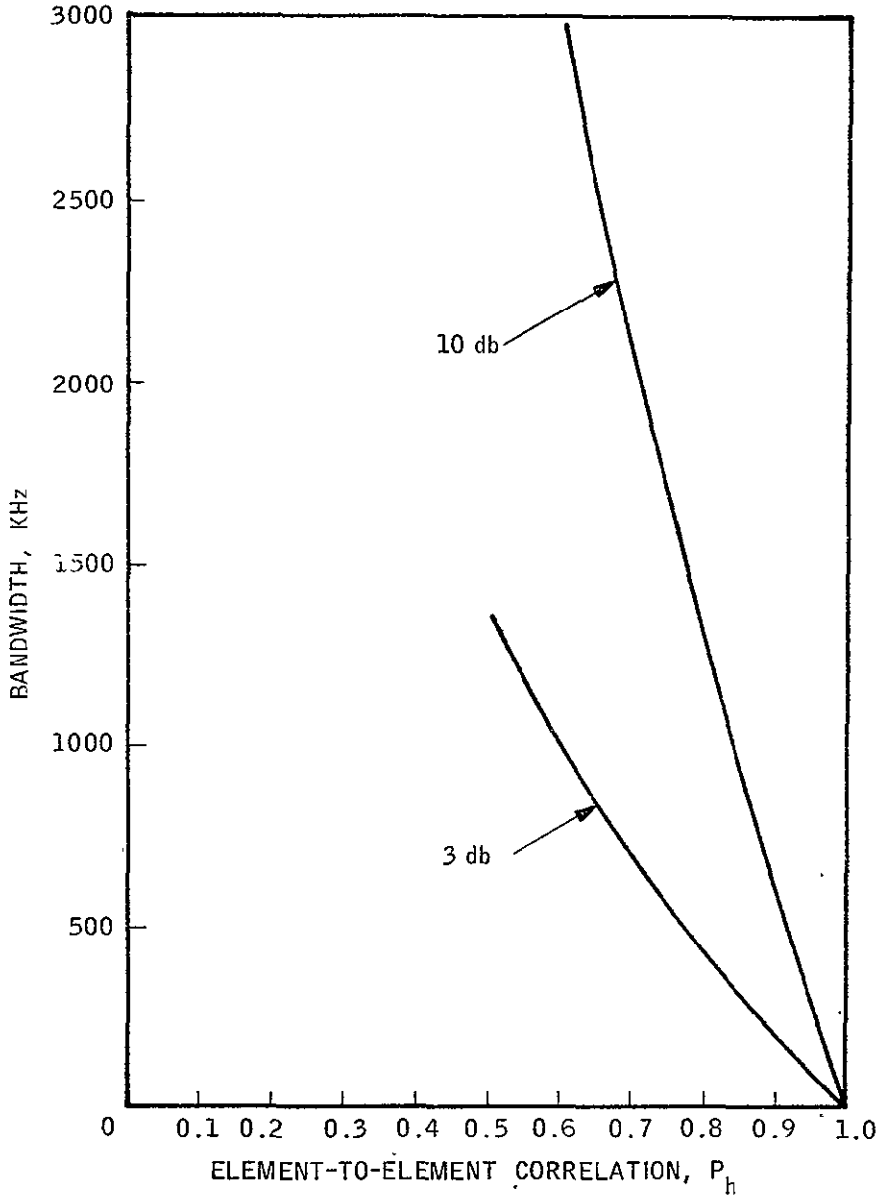

TV BANDWIDTH VS ELEMENT-TO-ELEMENT CORRELATION

Figure A-11

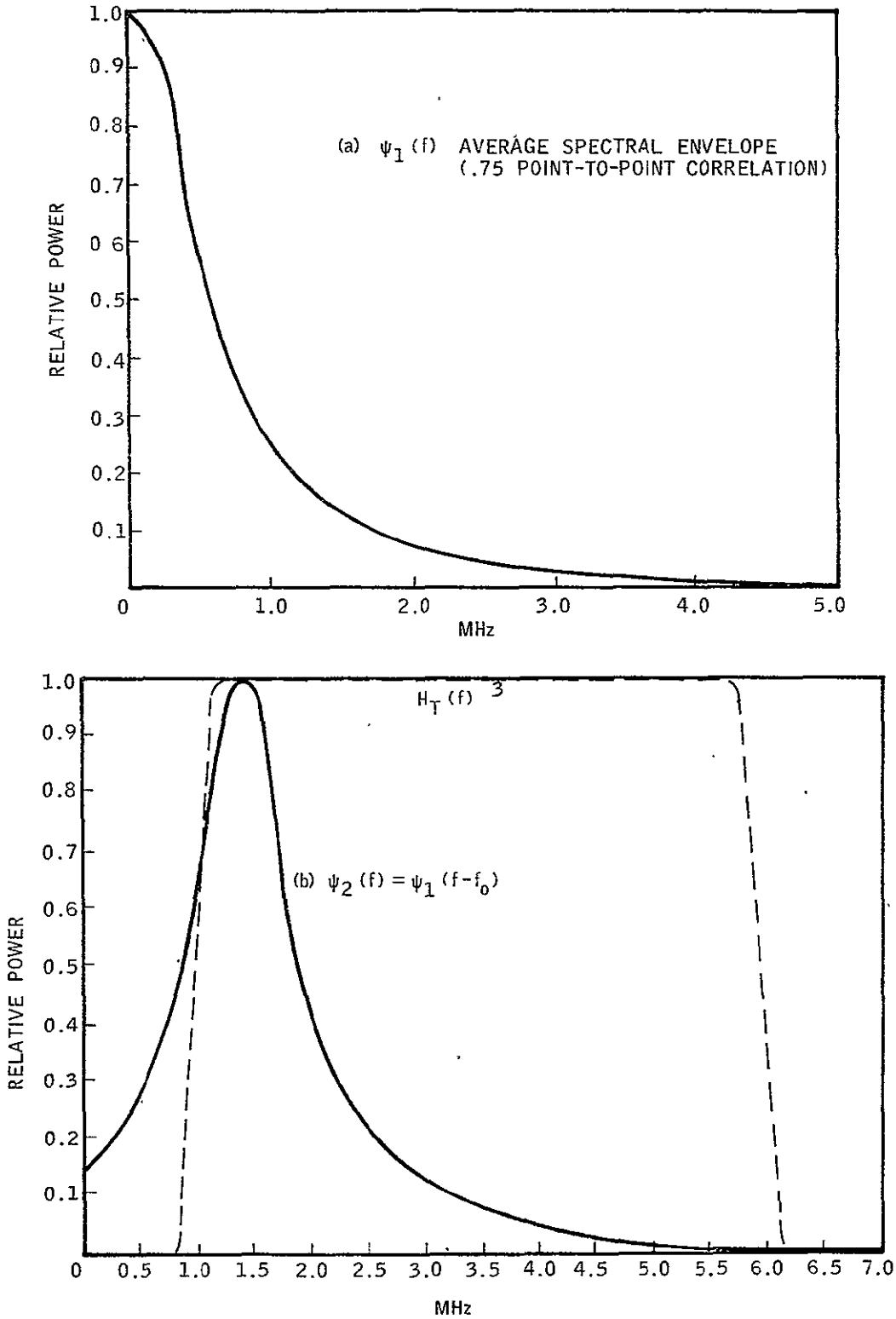

TV AND VESTIGIAL UP-TRANSLATOR FILTER SPECTRUM

Figure A-12

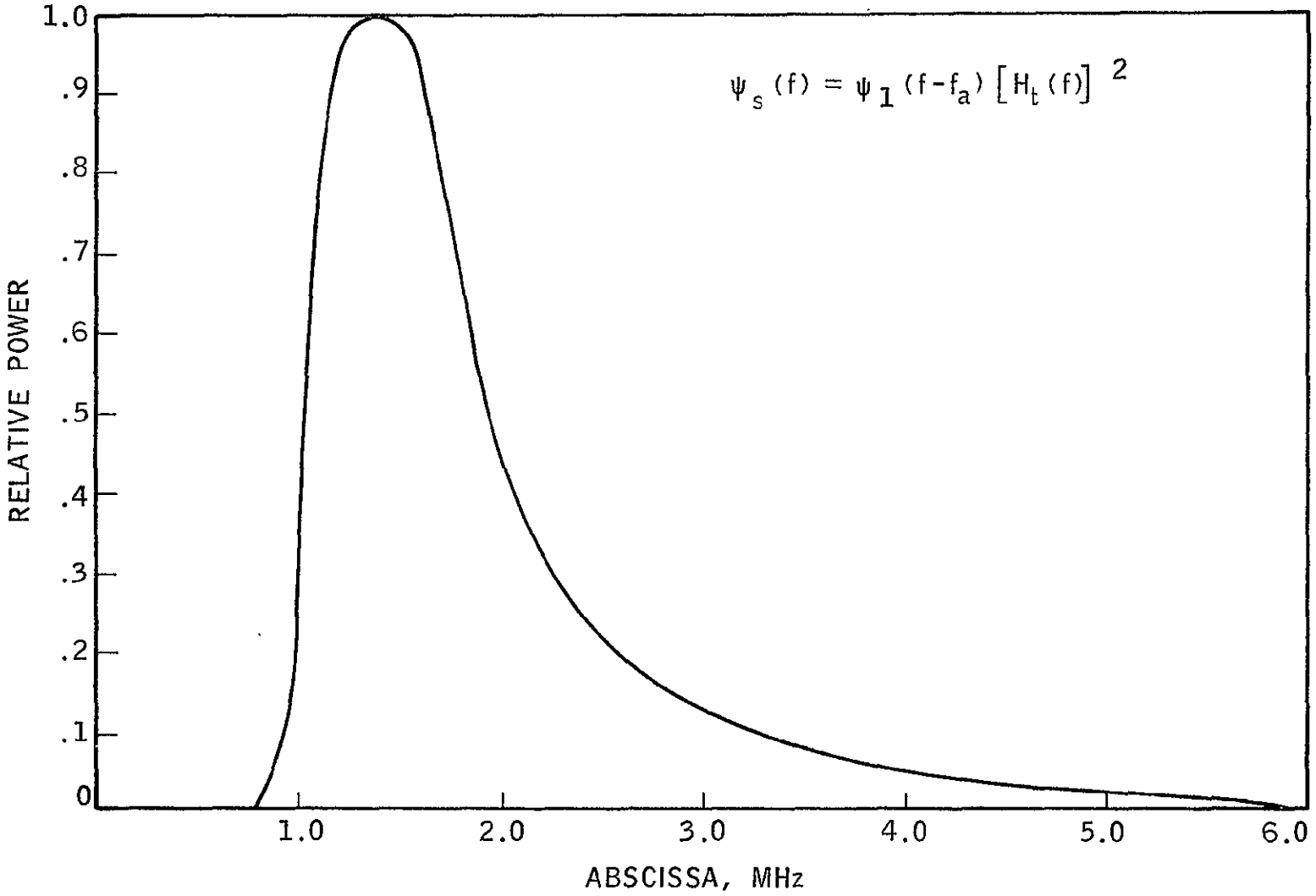

VESTIGIAL SIDEBAND SPECTRUM

Figure A-13

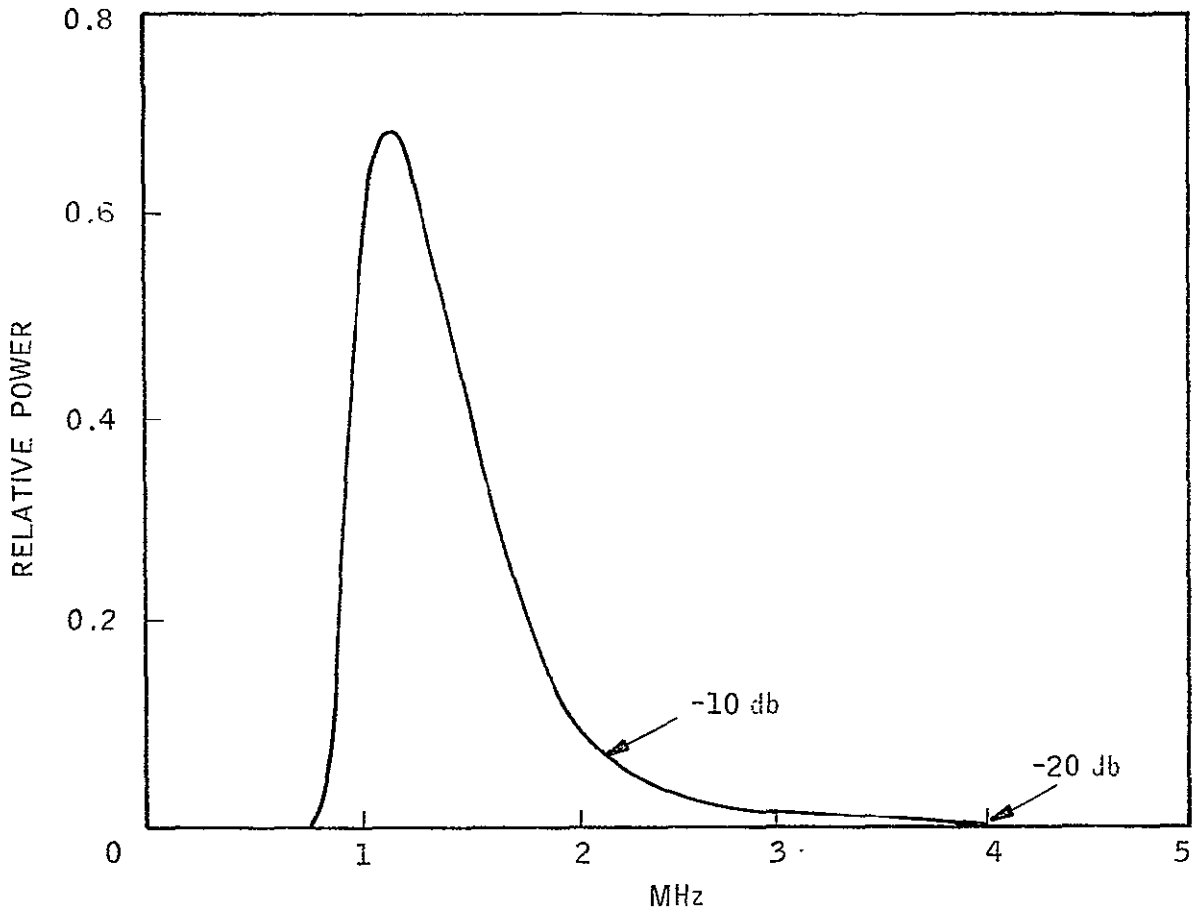

SPECTRUM OF $\psi_s(f) / f^2$

Figure A-14

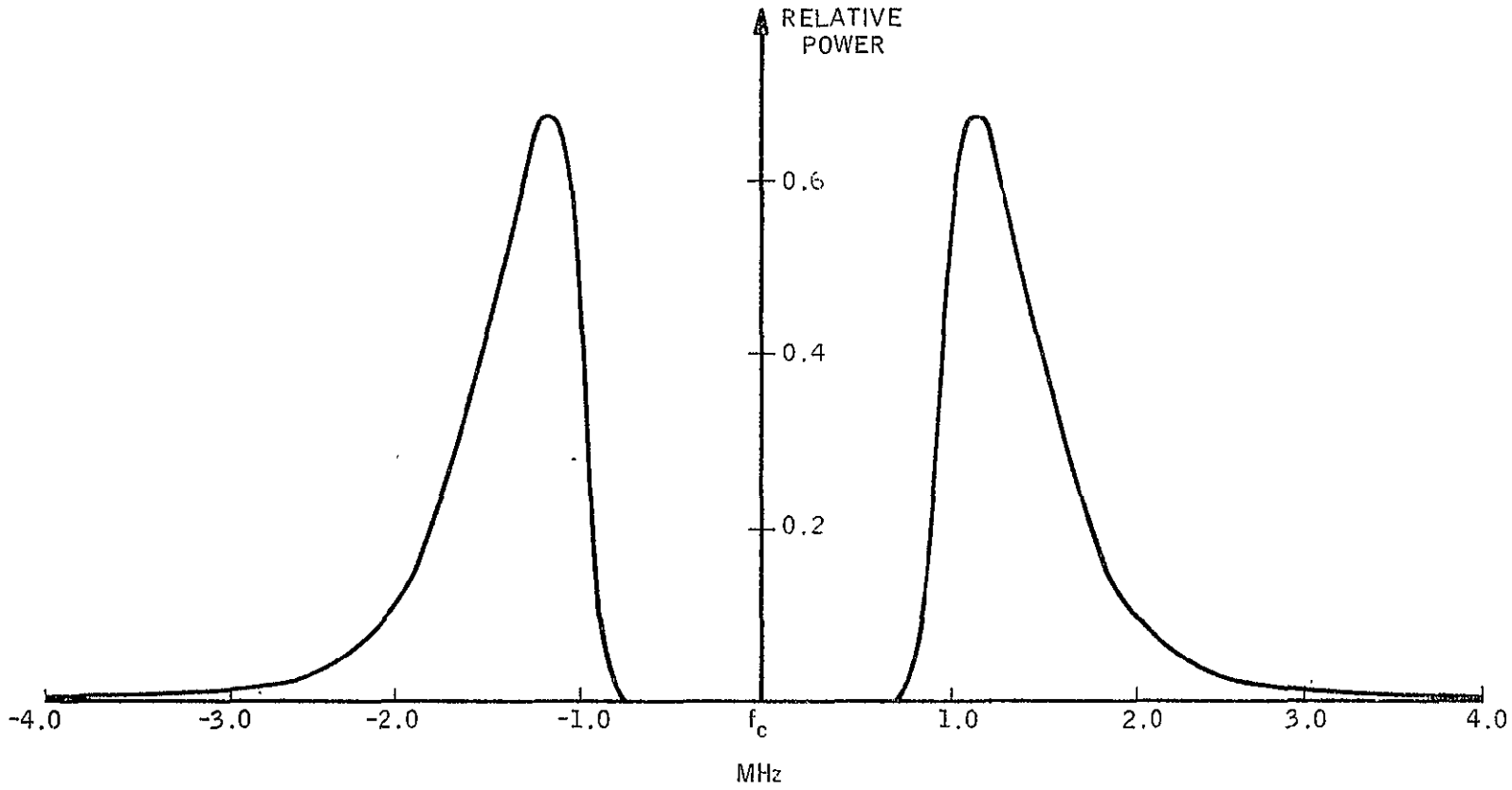

TRANSMITTED SPECTRUM

Figure A-15

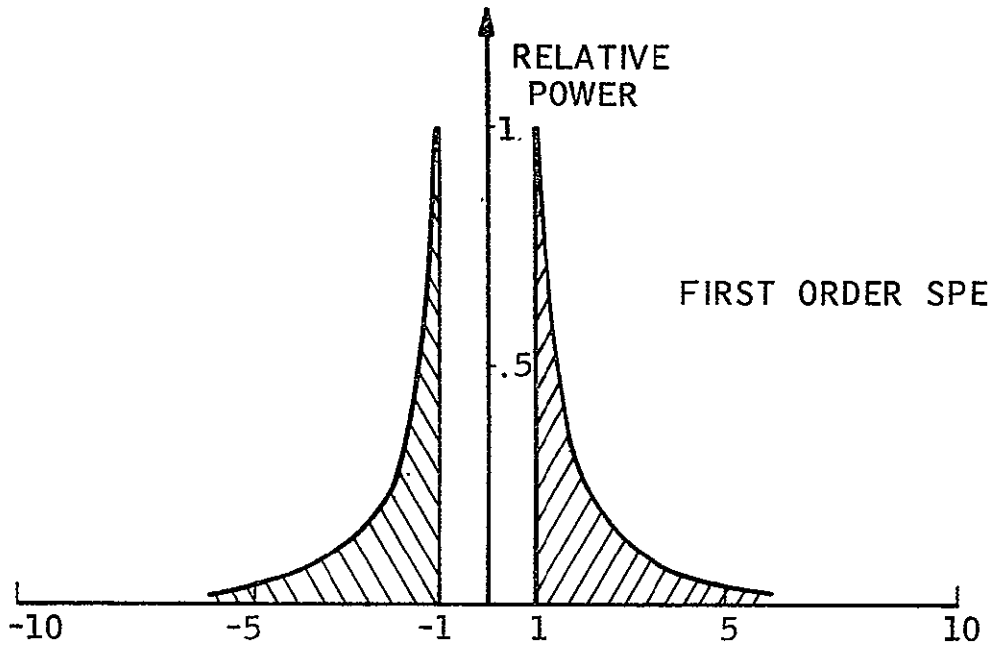

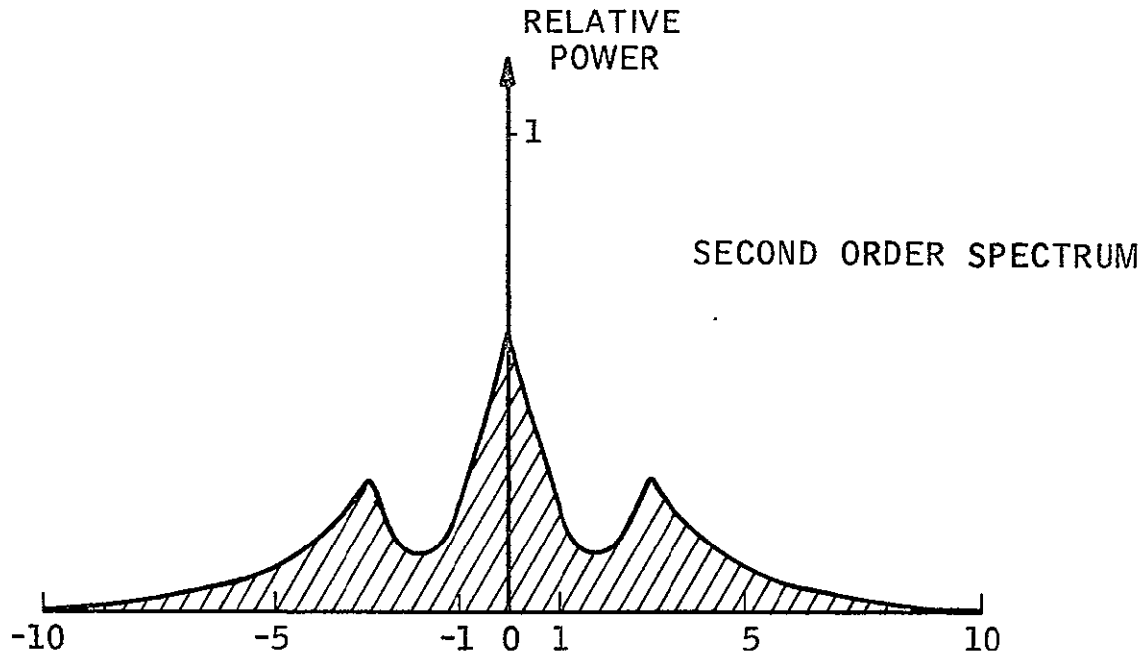

SPECTRA OF ψ_θ (f) ASSUMING ψ (f) TO BE UNIFORM

Figure A-16

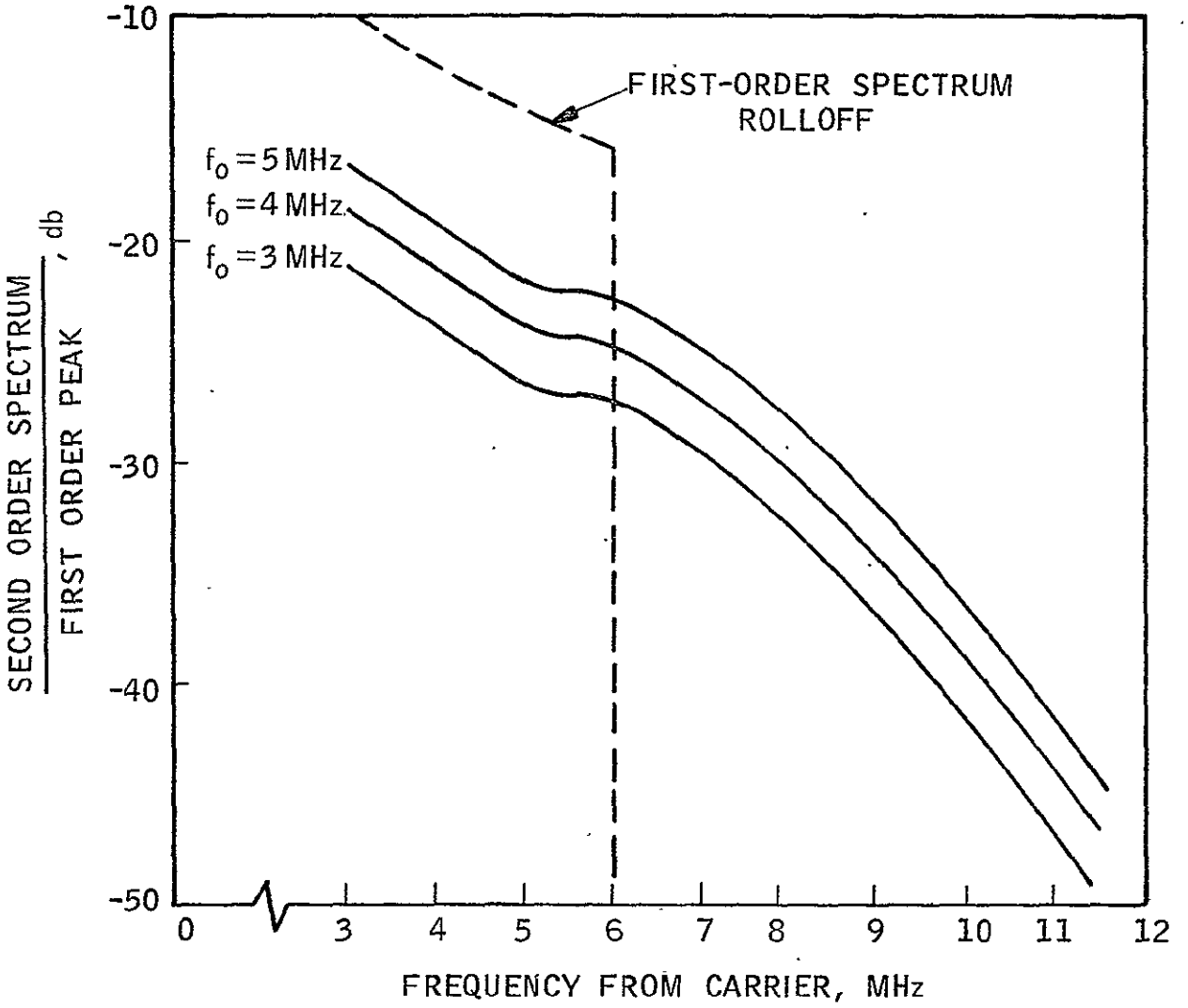

SECOND ORDER SPECTRUM EFFECTS

Figure A-17

C_{mod} = MODULATOR CRYSTAL CAPACITANCE

R_m = MODULATOR CRYSTAL IMPEDANCE

C_ℓ = LEAKAGE CAPACITANCE

R_ℓ = DRIVER OUTPUT RESISTANCE

$$R_\ell << R_m$$

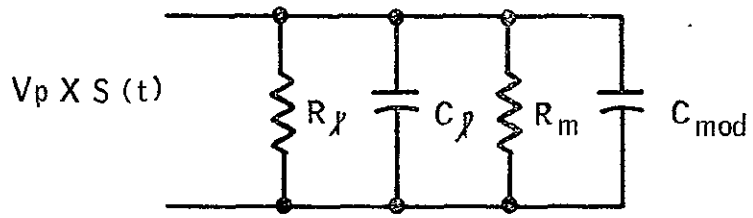

WHEN $S(t)_{max} = 1$

EQUIVALENT CIRCUIT OF FM MODULATOR

Figure A-18

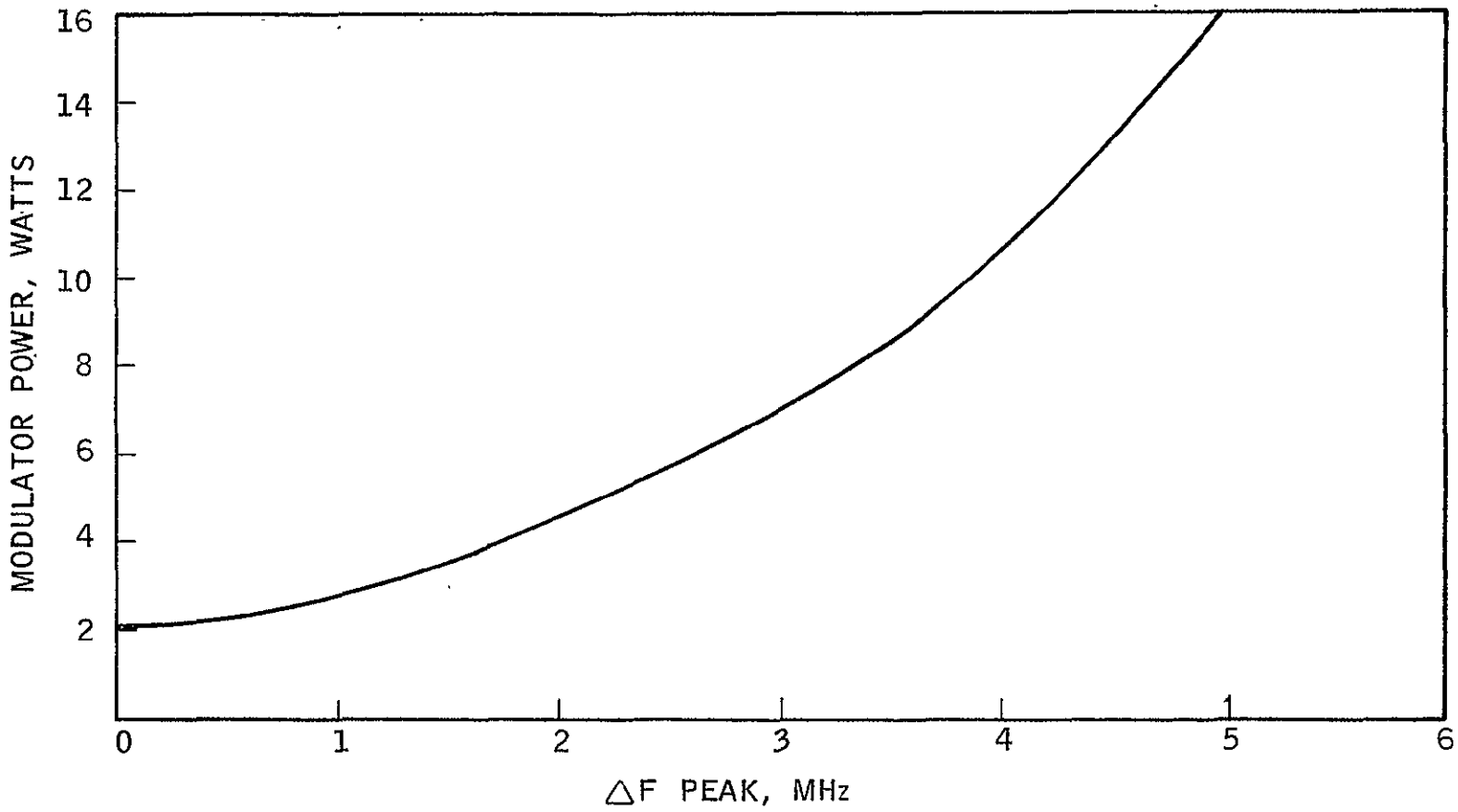

AVERAGE MODULATOR POWER VS PEAK FREQUENCY DEVIATION

Figure A-19

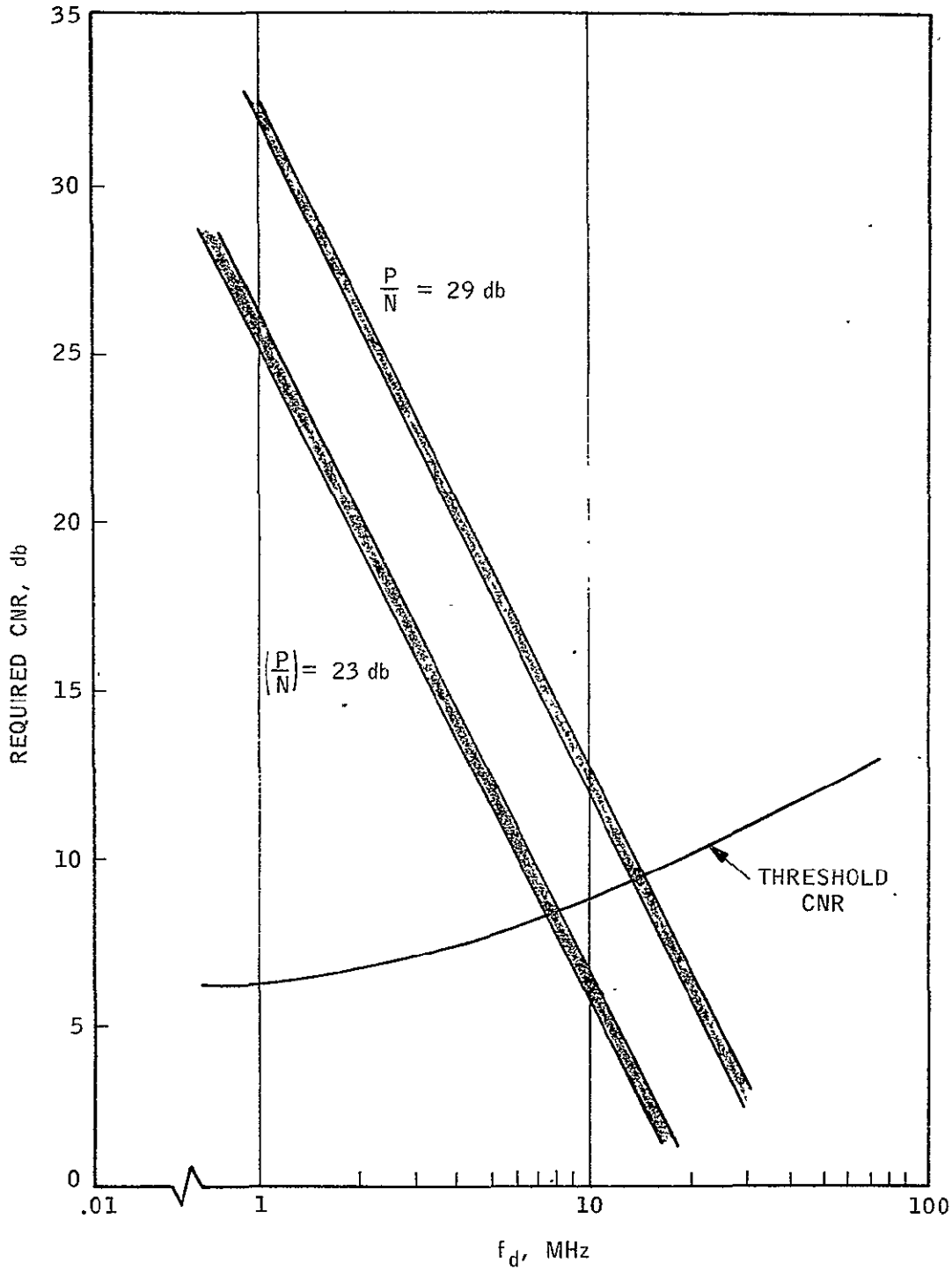

CNR VERSUS PEAK FREQUENCY DEVIATION

Figure A-20

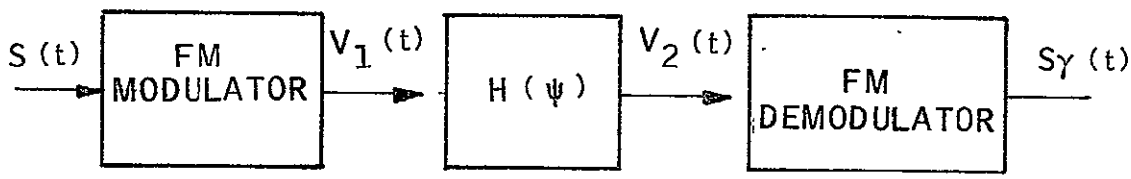

FM SYSTEM FOR SPECIFICATION OF H (ψ)

Figure A-21

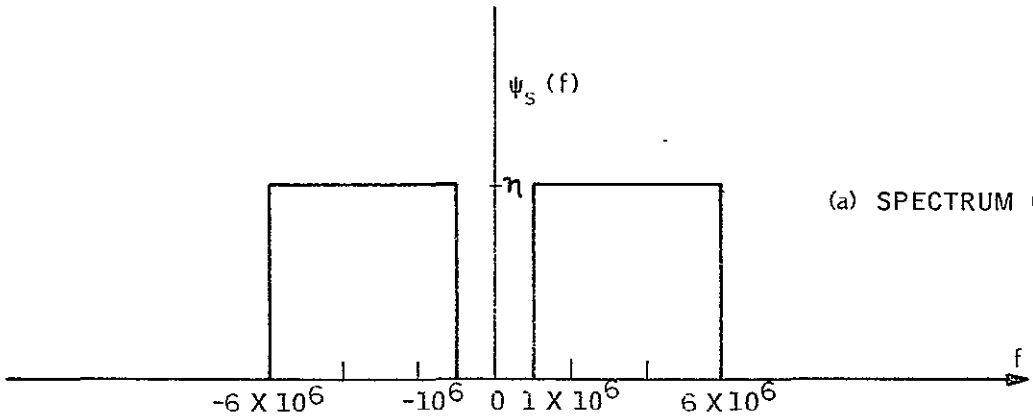

(a) SPECTRUM OF $\psi_s(\tau)$

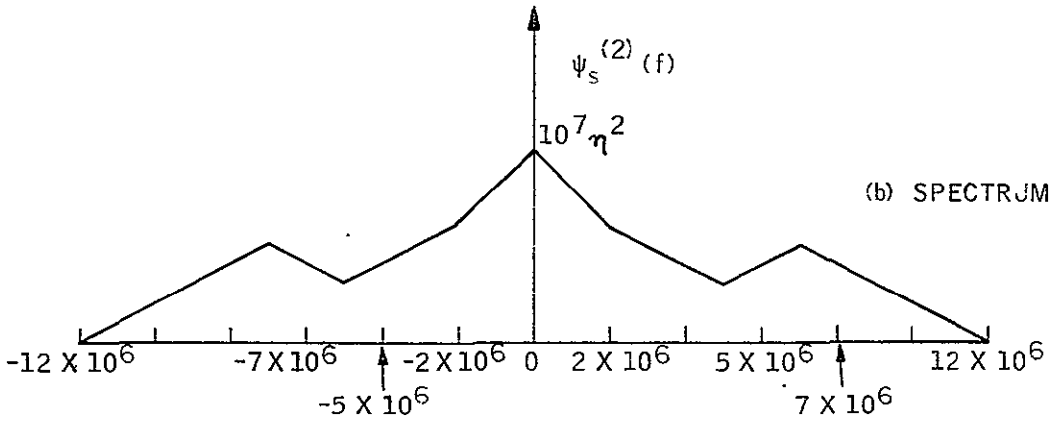

(b) SPECTRUM OF $\psi_s^2(\tau)$

ANALYSIS OF $\psi_s(\tau)$ AND $\psi_s^2(\tau)$ SPECTRA

Figure A-22

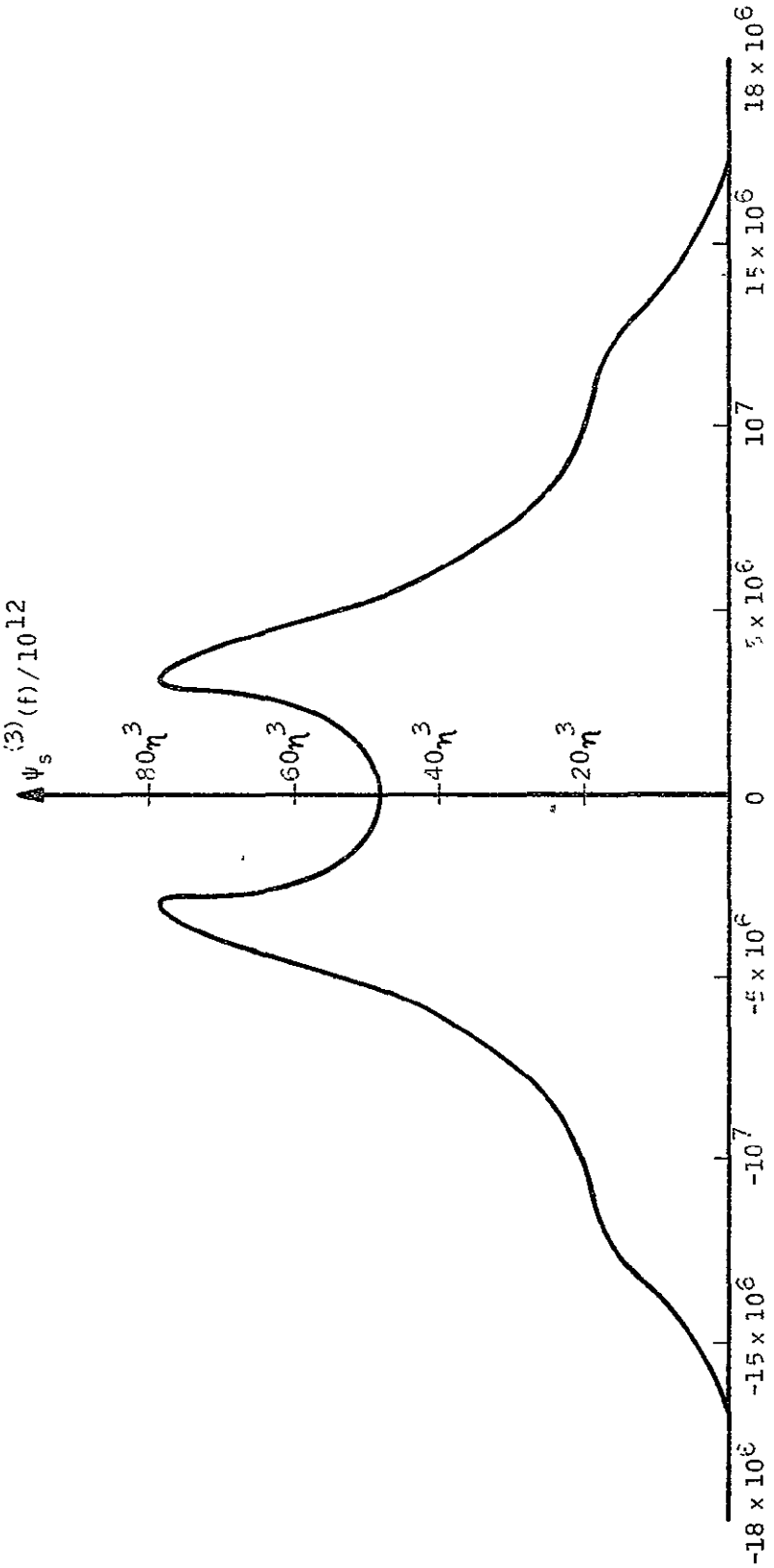

THIRD-ORDER CONVOLUTION ψ_s (f)

Figure A-23

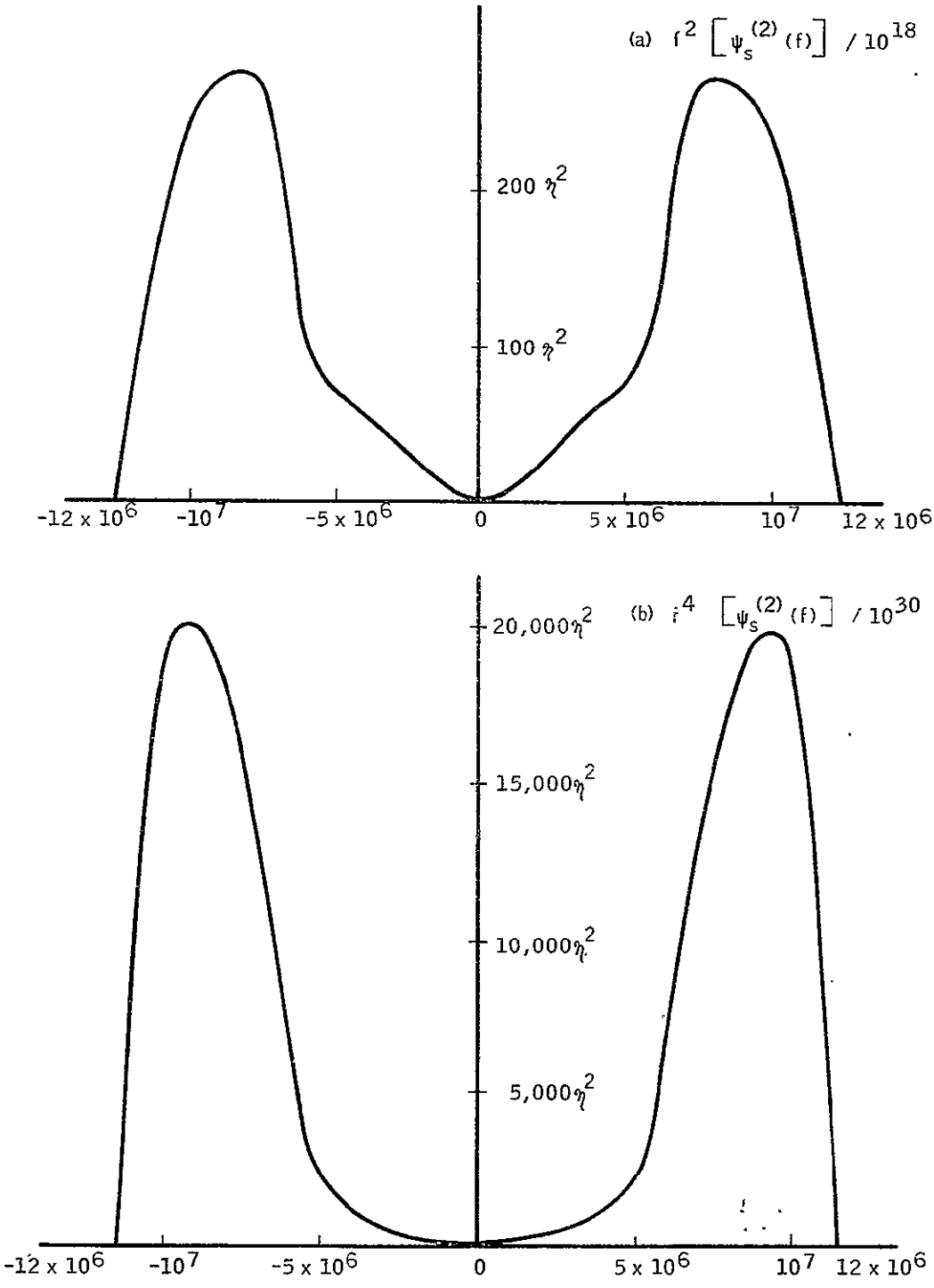

SECOND-ORDER SPECTRA

Figure A-24

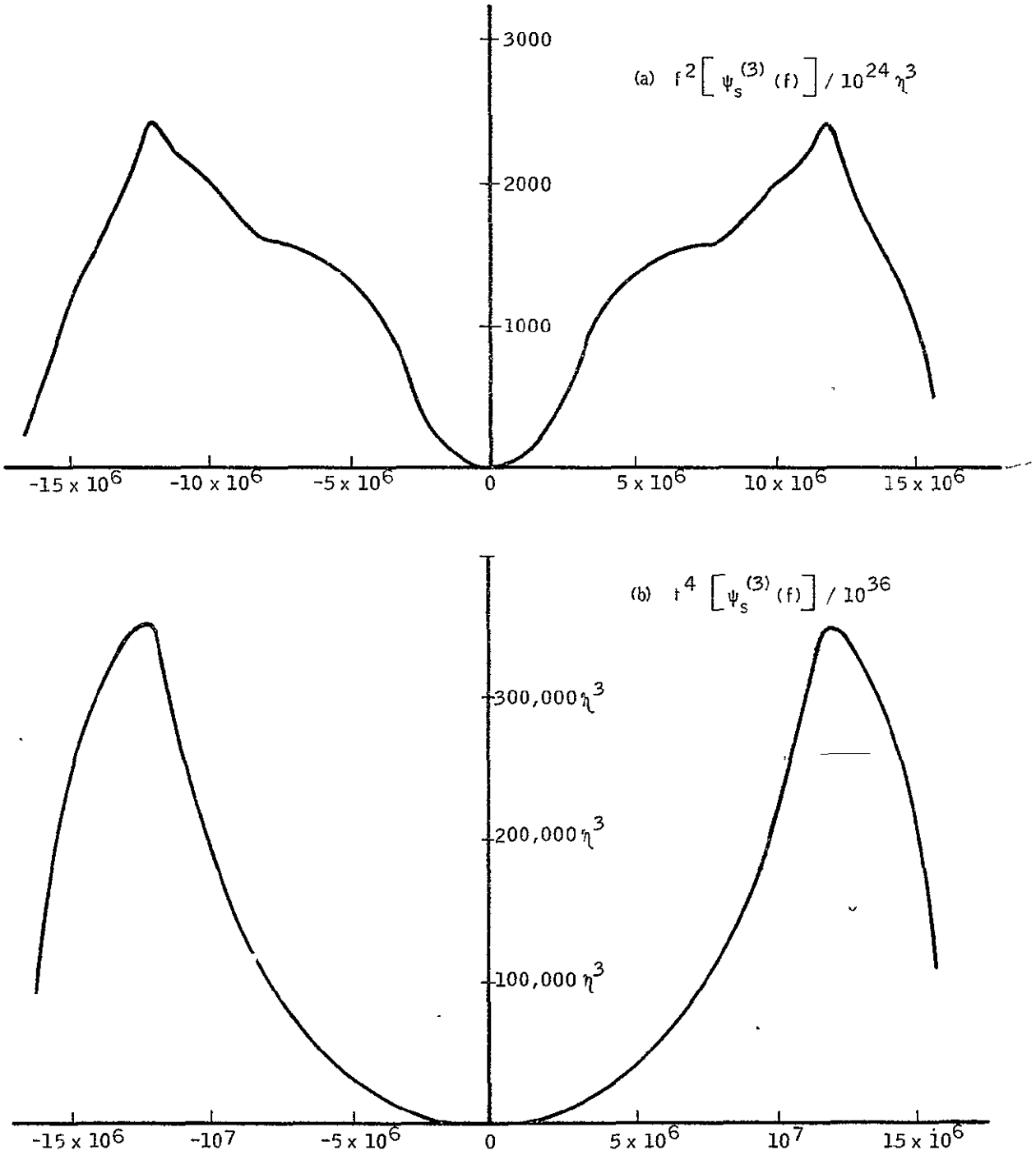

THIRD-ORDER SPECTRA

Figure A-25

APPENDIX B

ACQUISITION AND TRACKING DESIGN AND ANALYSIS

1.0 ACQUISITION DESIGN AND ANALYSIS

A two-station spatial-scan technique is incorporated in the acquisition of the transmitter beam of one station by the receiver of the other station. The transmitter beams of both stations are broadened, and the receivers of both stations are spatially scanned simultaneously. Both receivers are scanned in a rectangular search pattern, with a scan retrace at the end of each horizontal scan line. Acquisition is considered completed when both receivers have acquired their respective transmitter beams and the acquisition and tracking subsystems are tracking the transmitter beams.

The various system-design parameters were established by analyses. The following major parameters were considered in the system-performance analysis.

Target-location uncertainty
Spacecraft-drift rate
Local-oscillator stability
Background noise
Acquisition probability
False-alarm probability
Carrier-to-noise ratio
Signal-to-noise ratio (S/N)
Intermediate-frequency (IF) filter bandwidth
Post-detection filter bandwidth
Transmitter-beamwidth expansion
Search angle
Acquisition time
Design margin.

1.1 SYSTEM PERFORMANCE SUMMARY

Figure B-1 presents a functional block diagram of the acquisition subsystem. The system-parameter values were selected to optimize the acquisition probability and the S/N of the acquisition signal. The methods used in evaluating system performance and in selecting the values for system parameters are described below.

Figure B-2 shows system performance in terms of acquisition time as a function of spacecraft roll rate, with the local-oscillator stability as a parameter. It also specifies conditions under which the curves are generated. Because the amplitude stability of the local oscillator is critical in determining acquisition time, this parameter is used in generating the curves. The curves indicate that for a given value of local-oscillator stability, the acquisition time decreases as the spacecraft roll rate decreases. By specifying the local-oscillator stability of 0.3% (the present design goal) and a maximum spacecraft roll rate of 0.001°/sec, the acquisition time is determined to be 220 sec. The system performance is summarized as follows:

Target-location uncertainty	$\pm 0.2^{\circ}$
Acquisition probability	0.9
False-alarm time	1100 sec (one per five-scan frame)
Acquisition time	220 sec
Design S/N margin	5.6 db 4.9 db (including filter losses)

To accomplish the performance objectives, the following operating conditions and system design parameters are specified:

Maximum spacecraft-drift rate	0.001°/sec
Local-oscillator amplitude stability	0.3% (5 to 45 Hz)
Carrier-to-noise ratio at IF-filter output	-15.4 db
IF-filter noise-equivalent bandwidth	8.5 MHz
Post-detection filter bandwidth	2 to 14 Hz
Expanded transmitter beamwidth	0.177°
Receiver beamwidth	30 arc sec
Search angle	$\pm 0.208^{\circ}$
Search time	220 sec per scan frame

Figure B-3 shows the relative position of the expanded transmitter beam with respect to the position of the receiver beam at the time of acquisition. Acquisition is expected to occur at a point 4.36 db below the transmitter's peak energy level and 1.0 db below the receiver's peak energy level. The received energy is therefore reduced 5.36 db from the peak energy level of the expanded transmitter beam.

1.2 RECEIVED SIGNAL-TO-NOISE RATIO AT TIME OF ACQUISITION

During acquisition, the transmitters of both stations are broadened and the receivers are spatially scanned simultaneously. It is assumed that the transmitted energy and the receiver gain are such that the received energy at the time of acquisition has a carrier-to-noise ratio of C/N at the IF-filter output. Fubini and Johnson (Reference 1) have shown that for $(C/N) \ll 1$, the post-detection S/N is given by

$$\frac{S}{N} = \frac{C}{N}\left(\frac{\beta_I}{2\beta_a}\right)^{1/2} \qquad (1)$$

where

$\frac{S}{N}$ = post-detection signal-to-noise ratio at time of acquisition

$\frac{C}{N}$ = carrier-to-noise ratio at IF-filter output

β_I = equivalent noise bandwidth of IF filter

β_a = post-detection or acquisition signal bandwidth

To determine S/N, two other noise sources are to be considered: (a) background noises received from the sun or earth, as the receiver beam is scanning across the sun or earth, and (b) variations in the local-oscillator output energy falling in the acquisition-signal bandwidth, β_a. Detailed analyses of these two noise sources are described in paragraph 1.6. Let σ_b be the background noise in watts received from the sun or earth falling in the

acquisition-signal bandwidth, β_a. Expressed in fractional form, this noise component is σ_b/N. If α_o is the percentage of local-oscillator (LO) output-power fluctuation in the bandwidth of Δf, the LO output fluctuation, α, falling in the acquisition signal bandwidth, β_a, is

$$\alpha = \alpha_o \frac{\beta_a}{\Delta f} \tag{2}$$

Equation (2) is formulated for a case of $\Delta f > \beta_a$ and the noise spectrum is considered to be uniformly distributed over the acquisition bandwidth of β_a. Taking the two noise sources into consideration, Equation (1) becomes

$$\frac{S}{N} = \left(\frac{C}{N}\right) \frac{1}{\left[\frac{2\beta_a}{\beta_I} + \alpha^2 + \left(\frac{\sigma_b}{N}\right)^2\right]^{1/2}} \tag{3}$$

The transmitter and receiver beamwidth and the search scanning rate are such that the dwell time on a given search position in the scan is t_p. The scan dwell time, t_p, can be related to the acquisition-signal bandwidth by

$$\beta_a = \frac{1}{2t_p} \tag{4}$$

Substituting Equations (2) and (4) into Equation (3);

$$\frac{S}{N} = \frac{C}{N} \frac{1}{\left[\frac{1}{\beta_I t_p} + \left(\frac{\alpha_o \beta_a}{\Delta f}\right)^2 + \left(\frac{\sigma_b}{N}\right)^2\right]^{1/2}} \tag{5}$$

1.3 SELECTION OF IF-FILTER BANDWIDTH

Equation (5) indicated that to optimize the acquisition-signal S/N, the IF bandwidth, β_I, should be made as small as allowable by the frequency uncertainty between the transmitter of one station and the local oscillator of the other. To determine worst-case frequency uncertainty, the following factors are to be considered: (a) transmitter-frequency uncertainty, (b) LO-frequency uncertainty, (c) LO dithering-frequency deviation, and (d) Doppler shift.

During the acquisition period, communication between the two stations has not yet been established; therefore, the transmitter frequency of one station and the LO frequency of the other are controlled independently. The local oscillator performs a frequency dithering to locate its center line frequency. The dithering amplitude produces a frequency deviation of ± 0.6 MHz about its center line. An additional frequency uncertainty of ± 1.1 MHz is produced when the LO frequency is offset from its center line. The IF frequency uncertainty with the various factors taken into consideration is as follows:

	MHz
Transmitter-frequency uncertainty	0.2
LO frequency uncertainty	2.2
LO dithering-frequency deviation	1.2
Doppler shift	0.4
	4.0

The minimum IF bandwidth is selected to be ± 2.0 MHz about the center IF frequency of 30 MHz. The IF-filter transfer characteristic, H(W), is

$$H(W) = \frac{KS^n}{(S-W_1)^n (S-W_2)^n} \qquad (6)$$

where

K = filter constant

$W_1 = 2\pi f_1$

$W_2 = 2\pi f_2$

f_1 = filter's lower-cutoff frequency

f_2 = filter's upper-cutoff frequency

n = number of filter poles

The characteristics of a filter with n=4 are shown in Figure B-4. This filter provides an attenuation of not more than 0.5 db at $\pm$2.0 MHz.

The equivalent noise bandwidth of the filter, β_I, is

$$\beta_I = \frac{\int_{-\infty}^{\infty} |H(W)|^2 \, dW}{|H(W)|^2} \tag{7}$$

A value of β_I = 8.5 MHz is obtained by numerical integration of the filter characteristics shown in Figure B-4.

1.4 OPTIMIZATION OF RECEIVED POWER

Equation (5) indicates that the C/N of the received energy at the time of acquisition must be optimized in order to optimize the acquisition-signal S/N. Let

$$\frac{C}{N} = \frac{P}{(NEP)(\beta_I)}$$

or

$$P = \left(\frac{C}{N}\right)(NEP)(\beta_I) \tag{8}$$

where

$\frac{C}{N}$ = carrier-to-noise ratio of received energy at IF-filter output with a nominal carrier frequency, f_c, of 30 MHz

β_I = equivalent noise bandwidth of IF filter

NEP = receiver NEP

P = received energy, in watts

To maximize P, the following design parameters are to be considered: (a) expanded transmitter beamwidth, (b) scanning angle, and (c) scan-line overlap.

The optimum width of the expanded transmitter beam as a function of the target-uncertainty angle will now be determined. Let

$\pm\theta_1$ = target-uncertainty angle

$P(\theta)$ = expanded-beam power density at off-axis angle θ

$P(0)$ = on-axis power density (peak power density) of expanded beam

P_t = total transmitted power

θ_d = angle defining the beamwidth

Then

$$P(\theta) = P(0) \exp\left(-\frac{\theta^2}{2\theta d^2}\right) \tag{9}$$

$$P_t = \int_0^\infty 2\pi\theta_t \, P(\theta) \, d\theta$$

$$= 2\pi P(0)\theta_d^{\,2} \tag{10}$$

Substituting P(0) from Equation (10) into Equation (9),

$$P(\theta) = \frac{P_t}{2\pi\theta_d^2} \exp\left(-\frac{\theta^2}{2\theta_d^2}\right) \tag{11}$$

To obtain a maximum value for $P(\theta)$, Equation (11) is differentiated with respect to θ_d and is set equal to zero:

$$\frac{dP(\theta)}{d\theta_d} = \frac{\theta^2}{2\theta_d^2} - 1 = 0$$

$$\theta = \sqrt{2}\ \theta_d \tag{12}$$

The maximum value for $P(\theta)$ of Equations (9) and (11) occurs at $\theta = \sqrt{2}\ \theta_d$. Setting $\theta_o = \theta = \sqrt{2}\ \theta_d$, Equation (9) becomes

$$P(\theta_o) = \frac{P(0)}{e} \tag{13}$$

The power density at $\theta = \theta_o$ is down 1/e or -4.36 db from the on-axis peak. The target uncertainty angle, θ_1, is now set to equal θ_o: i.e., $\theta_1 = \theta_o$.

During acquisition, the receiver beams of both stations are scanning in a rectangular pattern, with a scan retrace at the end of each horizontal scan line. To compensate for target motion, some overlapping of the scan line is required. The ensuing analysis is undertaken to optimize the amount of overlapping, with the receiver scanning parameters and target motions considered. The receiver-beam power gain, $G(\theta)$, as a function of the on-axis power gain, $G(0)$, is

$$G(\theta) = G(0) \exp\frac{\theta^2}{2\beta_o^2} \tag{14}$$

where β_o is the angle defining the receiver beamwidth. If the scanning rate is $\dot{u}$, the received energy, E_N, is

$$E_N = \int_{-\infty}^{\infty} G(0) \exp\left(-\frac{\dot{u}^2}{2\beta_o^2}\right) dt$$

$$= \frac{\sqrt{2\pi}\,\beta_o}{\dot{u}}\, G(0) \tag{15}$$

The dwell time relating to E_N is

$$t_p = \frac{E_N}{G(0)} = \frac{\sqrt{2\pi}\,\beta_o}{\dot{u}} \tag{16}$$

If the time for each scan line including line retrace is t_L and the active scan portion of the line is p,

$$\dot{u} = \frac{2\theta_\gamma}{pt_L} \tag{17}$$

where θ_γ is the search angle. With respect to the target, the angular motion of the receiver beam per scan line is

$$\gamma_m = \gamma_L + \gamma_v = (\dot{\gamma} + \dot{\theta})\, t_L \tag{18}$$

where

γ_m = angular motion of receiver beam per scan line

γ_L = angular motion due to frame-scan velocity of $\dot{\gamma}$

$\gamma_L = \dot{\gamma} t_L$

γ_v = angular motion due to spacecraft rolling at a rate of $\pm\dot{\theta}$

$\gamma_v = \dot{\theta} t_L$

If δ is the scan-line overlap, the overlap angle, γ_m, is

$$\gamma_m = \delta\beta_o \tag{19}$$

Setting Equation (18) equal to Equation (19),

$$\delta\beta_o = (\dot{\gamma} + \dot{\theta})\, t_L \tag{20}$$

Let the search time equal T_f, which can be related to the search angle by

$$T_f\dot{\gamma} = 2\theta_\gamma \tag{21}$$

Substituting t_L from Equation (17) and $\dot{\gamma}$ from Equation (21 into Equation (20),

$$\delta\beta_o = \left(\frac{2\theta_\gamma}{T_f} + \dot{\theta}\right)\frac{2\theta_\gamma}{p\dot{u}} \tag{22}$$

Substituting $\dot{u}$ of Equation (16) into Equation (22),

$$t_p = \frac{\sqrt{2\pi}\, T_f\, \delta\, \beta_o^{\,2}\, p}{2\theta_\gamma\,(2\dot{\theta}_\gamma + \dot{\theta}\, T_f)} \tag{23}$$

From Equation (14), the receiver-beam power gain, $G(\theta)$, as a function of the on-axis power gain, $G(0)$, is

$$G(\theta) = G(0)\exp\left(-\frac{\theta^2}{2\beta_o^{\,2}}\right)$$

The receiver power gain at the overlap angle, γ_m, is

$$G(\gamma_m) = G(0) \exp\left(-\frac{\gamma_m^2}{2\beta_o^2}\right)$$

$$= G(0) \exp\left(-\frac{\delta^2 \beta_o^2}{2\beta_o^2}\right), \text{ for } \gamma_m = \delta\beta_o \text{ [Equation (19)]}$$

$$= G(0) \exp\left(-\frac{\delta^2}{2}\right) \tag{24}$$

Assuming

$$\frac{1}{\beta_I t_p} > \alpha^2 + \frac{\sigma_b^2}{N^2}$$

the S/N of Equation (5) becomes

$$\frac{S}{N} = \frac{C}{N} (\beta_I t_p)^{1/2} \tag{25}$$

Substituting C/N from Equation (8) into Equation (25),

$$\frac{S}{N} = KP(t_p)^{1/2}$$

where K is a system constant. Normalizing the received S/N at the overlap angle γ_m,

$$\frac{S}{N} = KP(t_p)^{1/2} = KG(\gamma_m)(t_p)^{1/2} \tag{26}$$

Substituting $G(\gamma_m)$ from Equation (24) and t_p from Equation (23) into Equation (26),

$$\frac{S}{N} = K_1 \sqrt{\delta} \exp\left(-\frac{\delta^2}{2}\right) \tag{27}$$

where

$$K_1 = K\,G(0)\left[\frac{\sqrt{2\pi}\,T_f\,\beta_o^{\,2}\,p}{2\theta_\gamma\,(2\theta_\gamma + \dot{\theta}T_f)}\right]^{1/2}$$

The optimum value for the overlap δ to produce the maximum acquisition S/N can be determined by differentiating Equation (27) with respect to δ and setting the result equal to zero:

$$\frac{d\left(\frac{S}{N}\right)}{d\delta} = K_1\left[\frac{1}{2\sqrt{\delta}}\exp\left(-\frac{\delta^2}{2}\right) - \delta^{3/2}\exp\left(-\frac{\delta^2}{2}\right)\right] = 0$$

$$\delta = \frac{1}{\sqrt{2}} \tag{28}$$

The S/N of Equation (27) has a maximum value at $\delta = 1/\sqrt{2}$. Equation (24) becomes

$$G(\gamma_m) = \frac{G(0)}{e^{0.25}} \tag{29}$$

At the point of optimum overlapping, the receiver gain is down $1/e^{0.25}$ or -1.0 db from the peak. Equations (13) and (29) indicate that the maximum received power, P, is $1/e \cdot e^{0.25}$ or -5.36 db down from the on-axis power density of the expanded transmitter peak, or

$$P = P(\theta_o)\, G(\gamma_m)$$

$$= \frac{P(0)\, G(0)}{e \cdot e^{0.25}} \qquad (30)$$

Normalizing Equation (30) by letting $G(0) = 1$,

$$P = \frac{P(0)}{e^{1.25}}$$

$$P = 0.285\, P(0)$$

If P_t is the carrier power (in watts) present on the peak of the narrow transmitter beam (which has a beamwidth of θ_t), the carrier power in watts for the expanded transmitter beam of θ is

$$P = \frac{0.285\, P_t \theta_t^{\,2}}{\theta^2} \qquad (31)$$

P_t can be related to $(C/N)_t$ by an expression similar to that of Equation (8):

$$P_t = \left(\frac{C}{N}\right)_t (NEP)\, (\beta_I) \qquad (32)$$

Substituting P_t of Equation (32) into Equation (31) and substituting the results into Equation (8),

$$\frac{C}{N} = \frac{0.285 \left(\frac{C}{N}\right)_t (\theta_t)^2}{\theta^2} \qquad (33)$$

The narrow transmitter beam and the expanded transmitter beam are formed by different optical paths. A beam expander is used to form the expanded

beam, thus bypassing the primary mirror and eliminating beam blockage by the secondary mirror. To account for the difference in transmission efficiency of the two optical paths, a constant K is added to Equation (33):

$$\frac{C}{N} = \frac{0.285\ K \left(\frac{C}{N}\right)_t\ \theta_t^{\,2}}{\theta^2} \tag{34a}$$

1.5 FURTHER CONSIDERATION OF EXPANDED TRANSMITTER BEAMWIDTH, SCANNING ANGLE, AND ANGLE OF TARGET UNCERTAINTY

Results of the analysis in paragraph 1.4 indicated that the received carrier energy, P, and the acquisition-signal S/N are optimized when the target-uncertainty angle, θ_1, is made equal to the search scanning angle, θ_γ. The transmitter beam is expanded to an amount equal to the scanning angle.

During acquisition, transmitter beams of both stations are expanded and receiver beams of both stations scan. Because acquisition depends on having both receivers cover the transmitters of other stations, advantage is achieved by making the transmitter beam smaller than the scan angle. Let the transmitter beam, θ_o, decrease by a factor α_s:

$$\theta_o = \theta_1 \alpha_s \tag{34b}$$

where

θ_1 = target-uncertainty angle (3σ value) associated with a standard deviation at θ_ρ

For the case in which $\theta = \theta_o = \theta_\gamma = \theta_1$, the acquisition-signal S/N as a function of θ_o and θ_γ can be determined by substituting t_p of Equation (23) and P of Equation (31) into Equation (26):

$$\frac{S}{N} = \frac{0.285\ \ P_t \theta_t^{\,2}}{\theta_o^{\,2}} \left[\frac{\sqrt{2\pi}\ T_f\ \delta\ \beta_o^{\,2}\ p}{2\theta_\gamma\ (2\theta_\gamma + \dot{\theta}\ T_f)}\right]^{1/2} \tag{35}$$

Let

$$K_2 = 0.285 \quad P_t \theta_t^2 \left[\sqrt{2\pi}\, T_f\, \delta\beta_o^2\, p\right]^{1/2}$$

Equation (35) becomes

$$\frac{S}{N} = \frac{K_2}{\left[\theta_o^4\, 2\theta_\gamma\, (2\theta_\gamma + \dot{\theta} T_f)\right]^{1/2}} \tag{36}$$

Equation (36) indicates that, by maintaining the relationship $\theta_1^6 = \theta_o^4\, \theta_\gamma^2$, an S/N improvement can be achieved by letting $\theta_\gamma = \theta_1/\alpha_s^2$. The derivation of $\theta_\gamma = \theta_1/\alpha_s^2$ is as follows:

$$\theta_1^6 = \theta_o^4\, \theta_\gamma^2$$

$$\theta_\gamma = \left(\frac{\theta_1^6}{\theta_o^4}\right)^{1/2} \tag{37}$$

Substituting θ_1 from Equation (34b) into Equation (37),

$$\theta_\gamma = \frac{\theta_1}{\alpha_s^2} \tag{38}$$

The optimum value of α_s is now evaluated. If the angular uncertainty is pointing, the station has a normal probability distribution with a standard deviation of θ_ρ in two orthogonal directions and the probability density function for the total angle off-axis is given by

$$P(\theta) = \frac{\theta \exp\left(-\frac{\theta^2}{2\theta_\rho^2}\right)}{\theta_\rho^2}$$

With the transmitter beam spread to θ_o, the probability that it will illuminate the other transmitter is

$$P_X = \int_0^{\theta_o} \frac{\theta \exp\left(-\frac{\theta^2}{2\theta_\rho^2}\right) d\theta}{\theta_\rho^2} = 1 - \exp\left(-\frac{\theta_o^2}{2\theta_\rho}\right) \qquad (39)$$

Similarly, if the receiver scans to θ_γ, the probability a receiver will scan the other station is given by

$$P_R = 1 - \exp\left(-\frac{\theta_\gamma^2}{2\theta_\rho^2}\right) \qquad (40)$$

Acquisition will occur where one of the following three mutually exclusive conditions exists:

a. Both stations are pointed within θ_o.

b. Station 1 is pointed within θ_o and Station 2 is pointed between θ_o and θ_γ.

c. Station 2 is pointed within θ_o and Station 1 is pointed between θ_o and θ_γ.

The probability of Condition a is given by

$$P_{C1} = P_X^2 \qquad (41)$$

The probability of Conditions b and c are

$$P_{C2} = P_{C3} = P_X (P_R - P_X) \tag{42}$$

$$P_A = P_{C1} + P_{C2} + P_{C3} \tag{43}$$

From Equations (41), (42), and (43),

$$P_A = P_X + 2 P_X (P_R - P_X) = P_X (2 P_R - P_X) \tag{44}$$

Substituting from Equations (34b), (38), (39), and (40) into Equation (44),

$$P_A = \left[1 - \exp\left(-\frac{\theta_1^2 \alpha_s^2}{2\theta_\rho^2}\right)\right]\left[1 + \exp\left(-\frac{\theta_1^2 \alpha_s^2}{2\theta_\rho^2}\right) - 2 \exp\left(-\frac{\theta_1^2}{2\theta_\rho^2 \alpha_s^4}\right)\right] \tag{45}$$

The values of P_A as a function of α_s at various values of θ_1/θ_ρ are shown in Figure B-5. It is seen that P_A is maximum at $\alpha_s = 0.8$. The values of P_A as a function of θ_1/θ_ρ with $\alpha_s = 0.8$ are shown in Figure B-6. Substituting $\alpha_s = 0.8$ into Equations (34b) and (38),

$$\theta_o = \alpha_s \theta_1 = 0.8\ \theta_1 \tag{46}$$

$$\theta_\gamma = \frac{\theta_1}{\alpha_s^2} = 1.56\ \theta_1 \tag{47}$$

Acquisition probability is optimized when the expanded transmitter beam is 0.8 times the target-uncertainty angle and the search angle is 1.56 times the target-uncertainty angle.

1.6 RECEIVED NOISE

Two major sources of noise received during acquisition are now considered. These are internal noise and background noise from the earth or sun. With the local oscillator as a reference (whose amplitude is much greater than that of the input signal at acquisition), the internal noise is dominated by the variations in the LO output. The amount of LO power fluctuation is associated by the factor α as shown in Equation (2):

$$\alpha = \alpha_o \frac{\beta_a}{\Delta f}$$

where α_o is the percentage of LO output-power variation in the bandwidth of Δf. For small β_a, the noise spectrum is assumed to be uniformly distributed over the acquisition bandwidth of β_a.

The background noise from the earth or sun is associated with the term σ_b/N in Equation (3). The major factors in determining the value of σ_b/N are discussed below.

1.6.1 Self-Emitted Energy Fluctuation from Earth

Earth background energy is received by the detector as the receiver beam is scanned across the earth. The amount of energy received at the IF filter is a function of the earth spectral radiant emittance, E_λ. As the receiver beam scans across the different portions of the earth having a temperature variation of dT, about an average temperature of T, the emittance fluctuates by the amount of dE_λ about an average value of E_λ. From Planck's radiation equation,

$$E_\lambda = C_1 \lambda^{-5} \left(\exp \frac{C_2}{\lambda T} - 1 \right)^{-1} \qquad (48)$$

where

E_λ = spectral radiant emittance in watt-m^{-2}-micron^{-1}

$C_1 = 3.74 \times 10^8$ watt-micron^4-m^{-2}

C-2

$C_2 = 1.44 \times 10^4$ micron-$^\circ$K

λ = radiation wavelength in microns

Because $\exp (C_2/\lambda T) \gg 1$ for T = 300°K and λ = 10.6 microns, Equation (48) becomes

$$E_\lambda = C_1 \lambda^{-5} \left(\exp \frac{C_2}{\lambda T}\right)^{-1} \tag{49}$$

The variation in E_λ as a function of temperature change can be obtained by differentiating Equation (49) with respect to T:

$$\frac{dE_\lambda}{dT} = C_1 \lambda^{-5} \left(\exp \frac{C_2}{\lambda T}\right)^{-1} \left(\frac{C_2}{\lambda T^2}\right)$$

$$dE_\lambda = \frac{E_\lambda C_2 dT}{\lambda T^2} \text{ watt-m}^{-2}\text{-micron}^{-1} \tag{50}$$

With an optical filter having a bandwidth of 1 micron, Equation (50) becomes

$$dE = \frac{E\ C_2\ dT}{\lambda T^2} \text{ watt-m}^{-2} \tag{51}$$

The received power fluctuation, σ_b, is

$$\sigma_b = \frac{(dE)\ A_t\ A_r\ \beta}{R^2} \text{ watts} \tag{52}$$

where

A_r = receiver aperture

A_t = area seen by receiver aperture

R = distance from earth to receiver

β = receiver IF bandwidth = $\frac{\beta_I}{c/d}$

c = speed of light in meters/sec

d = radiation wavelength in meters

Since

$$A_t = \frac{d^2 R^2}{A_r} \tag{53}$$

substituting Equations (51) and (53) into Equation (52) yields

$$\sigma_b = \frac{E\, C_2\, d^3\, \beta_I\, dT}{\lambda\, c\, T^2} \tag{54}$$

Since

$$\frac{\sigma_b}{N} = \frac{\sigma_b}{(NEP)\, \beta_I} \tag{55}$$

substituting Equation (54) into Equation (55) yields

$$\frac{\sigma_b}{N} = \frac{E\, C_2\, d^3\, dT}{\lambda\, c\, (NEP)\, T^2} \tag{56}$$

The maximum temperature variation as the receiver beam scans across the earth with a scan angle of θ_γ is assumed to be 30°K. For a worst-case analysis, it is further assumed that all received energy, σ_b, falls within the acquisition-signal bandwidth. The radiant emittance, E_λ, calculated by Equation (49) for T = 300°K and λ = 10.6 microns is 30.2 watt-m^{-2}-$micron^{-1}$. For an optical filter of 1-micron bandwidth, E = 30.2 watt-m^{-2}. Substituting NEP = 1 x 10^{-19} and the various numerical values into Equation (56),

$$\frac{\sigma_b}{N} = 5.4 \times 10^{-4} \tag{57}$$

Because the receiver is sensitive to only one polarization, this reduces σ_b/N by a factor of 2, and Equations (56) and (57) become

$$\frac{\sigma_b}{N} = \frac{E\, C_2\, d^3\, dT}{2\, \lambda\, C\, (NEP)\, T^2} \tag{58}$$

$$= 2.7 \times 10^{-4} \tag{59}$$

1.6.2 Direct Solar Energy

Solar background energy is received by the detector when the sun is in the scan angle. If the amount of energy received by the detector falling within the IF-filter bandwidth is E, the received energy fluctuates from zero to E as the receiver beam scans from the dark background to the bright solar disk. This is a probable condition, because the angular diameter of the sun and the scan angle of the receiver beam are of the same order of magnitude. The received-energy fluctuation, σ_b, can be now determined by a relationship similar to that shown in Equation (52):

$$\sigma_b = \frac{E\, A_t\, A_r\, \beta_I\, d}{c\, R^2}$$

Since

$$A_t = \frac{d^2 R^2}{A_r}$$

$$\sigma_b = \frac{E \beta_I d^3}{c} \tag{60}$$

Combining Equations (55) and (60),

$$\frac{\sigma_b}{N} = \frac{E d^3}{c (NEP)} \tag{61}$$

Because the receiver is sensitive to only one polarization, this reduces σ_b/N by a factor of 2, and Equation (61) becomes

$$\frac{\sigma_b}{N} = \frac{E d^3}{2c (NEP)} \tag{62}$$

For a worst-case analysis, it is assumed that all received energy falls within the acquisition-signal bandwidth. The spectral radiant emittance of a 6000°K blackbody at 10.6 microns calculated from Equation (48) is 1.10×10^4 watt-m^{-2} for an optical bandwidth of 1 micron. Substituting the appropriate values into Equation (62),

$$\frac{\sigma_b}{N} = 0.218 \tag{63}$$

Acquisition in the presence of such high background energy reduces the acquisition probability to a low value. It is therefore considered impractical to acquire a target in direct sunlight. Once the target is acquired elsewhere, the tracking subsystem is capable of tracking the target in the presence of the sun.

Solar energy reflected from adjacent objects on the spacecraft should also be kept to a minimum. A 0.124% variation in reflected solar energy received by the detector will produce a σ_b/N having the same value as that produced by the self-emitted earth background energy of $\sigma_b/N = 2.7 \times 10^{-4}$.

1.7 ACQUISITION PROBABILITY, FALSE-ALARM PROBABILITY, AND THRESHOLD LEVEL

Statistical-noise theories are used below to obtain expressions for acquisition probability, false-alarm probability, and threshold level.

Acquisition is based on establishing a threshold level at the output of the subsystem. If either the noise alone or the acquisition signal plus noise exceeds the threshold level, the transmitter beam is said to have acquired. The threshold-to-noise ratio therefore determines the false-alarm probability and the required acquisition-signal S/N determines the acquisition probability at a given false-alarm probability.

The probability of noise alone exceeds the threshold as

$$P_{fa} = \exp\left(-\frac{V_T^2}{2N^2}\right) \tag{64}$$

where

P_{fa} = false-alarm probability

V_T = threshold level

N = rms noise voltage

The false-alarm probability is related to the false-alarm time, T_{fa}, and the acquisition-signal bandwidth, β_a, by

$$P_{fa} = \frac{1}{T_{fa}\beta_a} \tag{65}$$

Let the average time between false alarms be $T_{fa} = 5\,T_f$. Then, combining Equations (64) and (65) yields

$$\frac{V_T}{N} = (2\,\ell n\,5\,T_f\,\beta_a)^{1/2} \tag{66}$$

The probability that the acquisition signal plus noise exceeds the threshold level, V_T, is given in Reference 2 as

$$P_d = \frac{1}{2}\left(1 - \operatorname{erf}\frac{V_T-S}{N}\right) + \frac{\exp\left[-\dfrac{(V_T-S)^2}{2N^2}\right]}{2\sqrt{2\pi}\left(\dfrac{S}{N}\right)}\left[1 - \frac{V_T-S}{4S} + \frac{1 + (V_T-S)^2/N^2}{8\left(\dfrac{S}{N}\right)^2} - \ldots\right] \tag{67}$$

where

S = acquisition-signal amplitude

$\frac{S}{N}$ = acquisition signal-to-noise ratio required to produce an acquisition probability of P_d with the threshold set at V_T volts

The overall acquisition probability of the subsystem, P_s, is

$$P_s = P_A\,P_d \tag{68}$$

where

P_A = acquisition probability given by Equation (45)

P_d = acquisition probability given by Equation (67)

1.8 ACQUISITION-SUBSYSTEM DESIGN

The results of the design analysis are now utilized in the design of the subsystem. For a target-uncertainty angle of $\pm 0.2^\circ$ (3σ value), the standard derivation, θ_ρ, is $\frac{0.2}{3} = 0.0667^\circ$ (1σ value). The acquisition-probability curve

of Figure B-6 indicates that a ratio of $\theta_1/\theta_\rho = 2$ is needed for an acquisition probability, P_A, of 0.91. Therefore,

$$\theta_1 = 2\theta_\rho = 2(0.0667)$$

$$= 0.133^\circ$$

The width of the expanded transmitter beam, $\pm\theta_o$, can be determined by Equation (46):

$$\theta_o = \alpha_s \theta_1 = (0.8)(0.133)$$

$$\theta_o = 0.106^\circ \tag{68b}$$

The half-power beamwidth of the expanded transmitter beam, $\pm\theta$, is related to θ_o by Equation (9):

$$\frac{P(\theta)}{P(0)} = \exp \frac{\theta^2}{2\theta_d^2} = 0.5$$

$$\theta = 1.18\ \theta_d$$

The energy received is optimized when $\theta_o = \sqrt{2}\theta_d$ [Equation (12)]:

$$\theta = \frac{1.18\ \theta_o}{\sqrt{2}} = 0.833\ \theta_o \tag{69}$$

Substituting the value of θ_o from Equation (68b) into Equation (69):

$$\theta = 0.833\ \alpha_s \theta_1$$

$$= 0.0885^\circ \tag{70}$$

The half-power beamwidth of the expanded transmitter beam is $2\theta = 0.177^{\circ}$. The scan angle, $\pm\theta_{\gamma}$, according to Equation (47), is

$$\theta_{\gamma} = 1.56\theta_{1} = (1.56)(0.133)$$
$$= 0.208^{\circ} \qquad (71)$$

The total scan angle is $2\theta_{\gamma} = 0.416^{\circ}$.

From Equation (23),

$$t_{p} = \frac{p\, T_{f}\, \delta\, \beta_{o}^{2} \sqrt{2\pi}}{2\, \theta_{\gamma}\, (2\, \theta_{\gamma} + \dot{\theta}\, T_{f})} \qquad (72)$$

Let

$p = 0.9$	Corresponding to 90% of the active scan time
$\delta = 2^{-0.5}$	Value taken from Equation (28)
$\beta_{o} = 3.53 \times 10^{-3}$ degree	Corresponding to the 1σ value of the half-power receiver beamwidth of 8.33×10^{-3} degree (30 arc sec)
$\theta_{\gamma} = 0.208^{\circ}$	Value taken from Equation (71)
$T_{f} = 220$ sec	Value taken from Figure B-2
$\dot{\theta} = 0.001^{\circ}/\text{sec}$	Value taken from Figure B-2

Substituting numerical values into Equation (72),

$$t_{p} = 3.29 \times 10^{-2} \text{ sec} \qquad (73)$$

The corresponding equivalent bandwidth of the acquisition signal is

$$\beta_a = \frac{1}{2\,t_p} = 15.2 \text{ Hz} \tag{74}$$

The acquisition-signal S/N can now be determined from Equation (5):

$$\frac{S}{N} = \frac{C}{N} \frac{1}{\left[\frac{1}{\beta_I t_p} + \left(\frac{\alpha_o \beta_a}{\Delta f}\right)^2 + \left(\frac{\sigma_b}{N}\right)^2\right]^{1/2}} \tag{75}$$

From Equation (34),

$$\frac{C}{N} = \frac{0.285\ K \left(\frac{C}{N}\right)_t \theta_t^{\,2}}{\theta^2} \tag{76}$$

Let

$\left(\frac{C}{N}\right)_t = 235$ — Corresponding to 23.7-db on-axis S/N, narrow transmitter beam with a 8.5-MHz IF bandwidth.

$\theta_t = 1.665 \times 10^{-3}$ degree — Narrow transmitter beamwidth 0.00333° (12 arc sec) at half-power points

$\theta = 0.0885°$ — Expanded transmitter beamwidth, value taken from Equation (70)

$\beta_I = 8.5$ MHz — IF equivalent-noise bandwidth, value taken from Equation (7)

$K = 1.2$

Substituting numerical values into Equation (76),

$$\frac{C}{N} = 2.87 \times 10^{-2} \qquad (77)$$

To evaluate the acquisition-signal S/N, the following numerical values are established:

$t_p = 3.29 \times 10^{-2}$ sec	Value taken from Equation (73)
$\frac{\sigma_b'}{N} = 2.7 \times 10^{-4}$	Value taken from Equation (59)
$\alpha_o = 0.003$	Current estimate for the LO power variations in the bandwidth from dc to 45 Hz, $\Delta f = 45$ Hz
$\alpha = \alpha_o \frac{\beta_a}{\Delta f}$	From Equation (2)
$\alpha = 1.02 \times 10^{-3}$	$\beta_a = 15.2$ Hz [Equation (74)]

Substituting the proper numerical values into Equation (75),

$$\frac{S}{N} = 13.1 \qquad (78)$$

From Equation (66),

$$\frac{V_T}{N} = (2 \ln 5 \, T_f \, \beta_a)^{1/2}$$

With

$T_f = 220$ sec	Acquisition time, value taken from Figure B-2

and

$\beta_a = 15.2$ Acquisition-signal bandwidth, value taken from Equation (74)

$$\frac{V_T}{N} = \left[2 \ln 5(220)(15.2)\right]^{1/2}$$

$$= 4.4$$

To produce an average time between false alarms of 1100 sec (or one per five scan frames), the threshold required is 4.4 times the rms-noise voltage of the subsystem.

The acquisition probability as a function of signal-to-noise ratio is shown in Equation (67). A family of curves of P_d as functions of S/N and T_{fa} were plotted on page 34 of Reference 2 for

$P_d = 0.99$ Representing 99% probability of acquiring the signal

$P_{fa} = \frac{1}{5T_f \beta_a}$ False-alarm probability with $T_f = 220$ sec and $\beta_a = 15.2$ Hz

$$P_{fa} = 6 \times 10^{-5}$$

From curves of Reference 2, the value needed to meet these requirements is

$$\frac{S}{N} = 6.9 \qquad (80)$$

Comparing Equations (78) and (80), the acquisition subsystem has a design margin of 5.6 db, which is a gross system margin. Factors such as signal attenuation of the filters will reduce the margin to a lower value. The analysis in paragraph 1.9 includes the amount of attenuation due to imperfect matching of the acquisition-signal spectrum to the post-detection filter characteristics. From Equation (68),

$$P_s = P_A P_d$$

$$= (0.91)(0.99)$$

$$= 0.9$$

The subsystem has an overall acquisition probability of 0.9.

To illustrate the effects of the various parameters on subsystem performance, curves based on Equation (5) were generated using the acquisition time as a function of the spacecraft roll rate with the LO output stability as a parameter. The curves are shown in Figure B-2. The operating point selected for the subsystem is at T_f = 220 sec, $\dot{\theta} = 0.001^{\circ}$/sec, and $\alpha_o = 0.003$.

1.9 POST-DETECTION MATCH FILTER

To extract the acquisition signal from the carrier, the signal is demodulated by an AM detector. The weak acquisition signal is then extracted by means of a matched filter. For a matched filter, the output is the correlation between the received waveform and the response of the filter. The energy distribution and waveform of the input signal are therefore important parameters determining the ability to extract the weak signal from a carrier having C/N = -15.4 db as calculated from Equation (77).

In the analysis of paragraph 1.4, the receiver beam is assumed to have a Gaussian power-gain distribution. The acquisition signal is therefore also assumed to have a Gaussian shape, with a half-amplitude width equal to the dwell time, t_p, given by Equation (72).

Let the acquisition signal, f(t), have the form of

$$f(t) = \frac{1}{\sqrt{2\pi}\,\sigma} \exp\left(-\frac{t^2}{2\sigma^2}\right)$$

The signal spectral distribution, F(jw), of f(t) is

$$F(jw) = \int_{-\infty}^{\infty} f(t) \exp(jwt)\, dt$$

$$= \frac{1}{\sqrt{2\pi}\,\sigma} \int_{-\infty}^{\infty} \exp\left(-\frac{t^2}{2\sigma^2} + jwt\right) dt$$

$$= \exp(-w^2\sigma^2/2)$$

For a Gaussian signal,

$$\sigma = \frac{0.5\, t_p}{1.2}, \quad t_p = 3.29 \times 10^{-2} \text{ sec}$$

$$F(jw) = \exp\left[-(2\pi f)^2 \frac{\sigma^2}{2}\right]$$

$$= \exp\left[-(3.72 \times 10^{-3})\, f^2\right] \qquad (81)$$

The signal spectrum, F(jw), as a function f is shown in Figure B-7, as are the characteristics of the post-detection filter. For a singly-tuned, two-stage filter, the equivalent noise bandwidth, β_a, is

$$\beta_a = 1.22 \text{ (3-db bandwidth)}$$
$$= 1.22\ (14)$$
$$= 17 \text{ Hz}$$

Substituting $T_f = \frac{1}{2\beta_a}$ into Equation (5), the acquisition-signal S/N is found to be 12.1. In comparison with the value in Equation (78), there is a 0.7-db S/N loss due to filter mismatch. With this loss taken into consideration, the design margin of subsystem decreased from 5.6 db to 4.9 db.

2.0 TRACKING DESIGN AND ANALYSIS

To compensate for spacecraft motion and to maintain the proper optical alignment between the transmitter of one station and the receiver of another, target tracking is to be performed by both stations. A functional block diagram of the tracking subsystem is presented in Figure B-8. The subsystem performs position sampling by rotating the received beam over the detector. When the beam is not centered on the detector, the IF carrier signal is amplitude-modulated and the phase and depth of the modulation indicate the misalignment direction and magnitude. North-south and east-west axis error signals are generated by (a) detecting the AM signal from the IF carrier, and (b) phase-detecting the AM signal, with the two nutation-drive signals as reference. The two error signals are then employed to actuate and control the servo system in centering the received beam on the detector.

The tracking subsystem has two modes of operation - acquisition tracking and operational tracking.

Acquisition tracking is performed to maintain pointing during acquisition after only one station has acquired the other station. Because the transmitter beam is expanded, the power density is low. The radius of nutation for acquisition tracking must be large enough to produce a tracking-error signal of sufficiently high S/N to control the servo system.

An acquisition-confirm signal is produced during acquisition tracking. It is used to verify that the transmitter beam has acquired and the subsystem is tracking the beam; in its absence, the subsystem reverts to the search operation. The acquisition-confirm signal is generated by driving the nutator with an additional signal having a frequency approximately twice that of the tracking-nutation frequency. This driving signal will apply to one axis of nutation. The acquisition-confirm signal is synchronously detected from the IF carrier, with the new nutator-drive signal as reference.

Operational tracking employs electronics used in the acquisition tracking. To compensate for the difference in received power density, the radius of nutation and the error-signal amplification are decreased for normal operation.

Analyses were performed to establish the various system design parameters. System performances were then analyzed with the following major parameters taken into consideration:

Spacecraft roll rate
Radius of nutation
Nutating frequency
Carrier-to-noise ratio
Tracking-error signal-to-noise ratio
Tracking-subsystem bandwidth
Tracking error
Carrier attenuation at maximum tracking error
Acquisition-tracking confirm capability
Acquisition-confirm signal-to-noise ratio.

2.1 SYSTEM PERFORMANCE SUMMARY

The values of the various system parameters were selected to achieve good tracking accuracy and to minimize the amount of hardware required for implementation. Succeeding pages describe the methods used in parameter selection and system-performance evaluation. System performance is summarized as follows:

Tracking	± 3 arc sec
Carrier attenuation at maximum tracking error	-0.9 db
Tracking range	$\pm 0.208^{\circ}$
Acquisition-confirm-signal S/N margin	6.1 db

To accomplish the performance objectives, the following operating conditions and system design parameters are specified:

Maximum spacecraft-roll rate	0.001°/sec
Acquisition tracking nutating radius	8 arc sec
Normal tracking-nutation radius	1.5 arc sec
Acquisition-confirm-signal nutating radius	8 arc sec
Tracking-subsystem bandwidth	5.12 Hz
Tracking-subsystem response time	0.112 sec
Acquisition-confirm-signal bandwidth	1.0 Hz

2.2 TRACKING SIGNAL-TO-NOISE RATIO

The tracking-error-signal S/N can be obtained by the modification of Equation (3):

$$\frac{S}{N} = \frac{\left(\frac{C}{N}\right)\left[E(\theta)\right]\left[M(\theta)\right]\left[K(\gamma)\right]}{\left[\frac{2\beta_a}{\beta_I} + \left(\alpha_o \frac{\beta_a}{\Delta f}\right)^2 + \left(\frac{\sigma_b}{N}\right)^2\right]^{1/2}} \tag{82}$$

where

$\frac{C}{N}$ = carrier-to-noise ratio at IF output

$E(\theta)$ = carrier attenuation as a function of target off-axis angle, θ

$M(\theta)$ = percentage of error-signal modulation as a function of θ

$K(\gamma)$ = on-axis carrier attenuation as a function of radius of nutation, γ

β_I = equivalent-noise bandwidth of IF filter

β_a = tracking-subsystem bandwidth

α_o = local-oscillator output-power fluctuations in bandwidths of Δf

$\frac{\sigma_b^2}{N^2}$ = rms fluctuation of background noise from earth

Figure B-9 shows the relative signal amplitude from the detector as a function of target off-axis angle, θ. The curve was obtained by numerical integration of the Gaussian receiver beam on a 32-arc-sec round detector with a uniform LO energy across the detector surface. For a given radius of nutation, γ, the error-signal modulation, $M(\theta)$, at various off-axis angles can be determined from Figure B-9. This is done by finding the maximum signal amplitude (E_{max}), the minimum signal amplitude (E_{min}), and the carrier level $E(\theta)$ at each value of θ. $M(\theta)$ can then be calculated from

$$M(\theta) = \frac{E_{max} - E_{min}}{2} \frac{1}{E(\theta)} \tag{83}$$

During acquisition, the transmitter beam is expanded from 12 arc sec, or .00333°, to 0.177°. If the on-axis power density of the narrow

transmitter beam is assumed to be 23.7 db and acquisition occurs at 5.36 db below the on-axis power density of the expanded transmitter beam as shown in Figure B-3, the carrier-to-noise ratio is

$$\frac{C}{N} = 23.7 - 10 \log \left(\frac{0.177}{0.00333}\right)^2 - 5.36$$
$$= -16.21 \text{ db or } 2.39 \times 10^{-2} \tag{84}$$

A beam expander is used to form the expanded beam, thus bypassing the primary mirror and eliminating beam blockage by the secondary mirror. To account for the difference in the transmission efficiency of the two optical paths, a constant K = 1.2 is introduced into Equation (84):

$$\frac{C}{N} = (2.39 \times 10^{-2})\, K = 2.87 \times 10^{-2} \tag{85}$$

Let

$\beta_a = 5.12$ Hz [value taken from Equation (97)]
$\beta_I = 8.5$ mHz
$\alpha_o = 0.003$
$\Delta f = 45$ Hz
$\frac{\sigma_b}{N} = 2.7 \times 10^{-4}$

Substituting values into Equation (82),

$$\frac{S}{N} = 24.4 \left[E(\theta)\right] \left[M(\theta)\right] \left[K(\gamma)\right] \tag{86}$$

Equation (86) is used to calculate the error-signal S/N as a function of the target off-axis angle at various nutation-radius values. Figure B-10 plots S/N as a function of θ for nutational radii of 6 and 8 arc sec. Acquisition tracking with a nutation radius of 8 arc sec provides a maximum S/N of 6.8 when the target is displaced 14 arc sec from the center of the detector. At a displacement of 1.5 arc sec, S/N = 1.0. This indicates a servo-system inactive zone of $\pm$1.5 arc sec within which no correction is provided.

For operational tracking, the radius of nutation is reduced to 1.5 arc sec. The S/N as a function of θ can be calculated by Equation (82), with C/N representing the narrow transmitter-beam C/N value at the IF output. Figure B-11 plots the normalized S/N as a function of θ for r = 1.5 arc sec.

The nutation frequency is selected as 100 Hz, to ensure that the bimorph-driven nutator is operating at a frequency about twice the resonant frequency of the nutator assembly.

2.3 ACQUISITION-CONFIRM SIGNAL

The acquisition-confirm signal is used during acquisition to verify that the transmitter beam is acquired and the subsystem is tracking the beam. It is generated by driving the nutator with a 200-Hz signal and applies to one axis of the nutator. The acquisition-confirm signal S/N can be calculated from Equation (82):

$$\frac{S}{N} = \frac{\left(\frac{C}{N}\right)\left[E(\theta)\right]\left[M(\theta)\right]\left[K(\gamma)\right]}{\left[\frac{2\beta_a}{\beta_I} + \alpha^2 + \left(\frac{\sigma_b}{N}\right)^2\right]^{1/2}} \tag{87}$$

$K(\gamma)$, $E(\theta)$, and $M(\theta)$ calculated on the basis of data obtained from Figure B-9 have the following values for a radius of nutation of 8 arc sec:

$$K(\gamma) = 0.8$$

$$E(\theta) = 0.8$$

$$M(\theta) = \frac{E_{max} - E_{min}}{2} \frac{1}{E(\theta)}$$

$$= \frac{0.98 - 0.40}{2} \frac{1}{0.8}$$

$$= 0.362$$

Let

$$\frac{C}{N} = 2.87 \times 10^{-2} \text{ [value taken from Equation (85)]}$$

$$\beta_a = 1.0 \text{ Hz}$$

$$\beta_I = 8.5 \text{ MHz}$$

$$\alpha = \alpha_o \frac{\beta_a}{\Delta f}$$

$$= 0.003 \frac{1}{45}$$

$$= 6.67 \times 10^{-5}$$

for LO-output stability of $\alpha_o = 0.3\%$ in the $\Delta f = 45$ Hz frequency range

$$\frac{\sigma_b}{N} = 2.7 \times 10^{-4} \quad \text{[value taken from Equation (59)]}$$

Substituting numerical values into Equation (87),

$$\frac{S}{N} = 11.8 \tag{88}$$

The S/N required to achieve a detection probability of $P_d = 0.98$ and a false-alarm probability of $P_{fa} = 9.1 \times 10^{-4}$, as calculated below, can be obtained using Equation (67) and a curve generated on page 34 of Reference 2:

$$P_{fa} = \frac{1}{T_{fa} \beta_a}$$

where

T_{fa} = false-alarm time
= one for five frames
= 5(220) = 1100 sec

β_a = acquisition-confirm signal bandwidth
= 1 Hz

$P_{fa} = 9.1 \times 10^{-4}$

$$\frac{S}{N} = 5.9 \tag{89}$$

Comparing Equations (88) and (89), the acquisition-confirm signal S/N margin is 6.1 db.

2.4 TRACKING-SERVO SYSTEM

The north-south and east-west axis error signals described in paragraph 2.2 are employed to activate and control the servo system to track the received beam. The ensuing analysis is aimed at determining tracking performance and establishing and selecting numerical values for various servo-system parameters.

2.4.1 Formulation of Mathematical Model

The servo-system configuration is shown in Figure B-12, which represents either the north-south or the east-west axis servo loop. Figure B-13 shows the amplitude of the phase-demodulated signal as a function of the received-beam off-axis angle. Its curve is generated on the basis of data from Figure B-11. The electronic gains of the AM and phase detectors are adjusted to produce the proper signal amplitude. The off-axis angle shown in Figure B-13 is the internal angle or 10 times the external angle, to account for the amplification of the primary telescope. In the analysis, it was considered that tracking is performed over a relatively small error angle around the origin, and a line with a slope equal to K_D as shown in Figure B-13 is used to represent the transfer function of the phase-detected signal, $G_1(S)$. $G_2(S)$ represents the compensation amplifier at the output of the phase detector.

To provide the servo system with a suitable damping factor for stable operation, an inner-loop feedback assembly is incorporated to compensate for the relatively low damping provided by the bimorph assembly. In the inner loop, $G_3(S)$ represents the bimorph driver with a voltage gain of K_A. $G_4(S)$ represents the transfer characteristics of the bimorp assembly, $H_1(S)$ represents a feedback bimorph attached to the driving bimorph, and $H_2(S)$ represents the transfer characteristics of the feedback amplifier with a frequency-compensation filter.

2.4.2 Analysis of Bimorph Assembly with Feedback (Inner Loop)

The open-loop transfer characteristic of the bimorph assembly with feedback, G(S) H(S), is given by

$$G(S)\,H(S) = G_3(S)\text{-}G_4(S)\text{-}H_1(S)\text{-}H_2(S)$$

$$= \frac{K_A K_M K_G K_F W_n^2 S(T_2 S + 1)}{(S + \delta W_n + jW_n\sqrt{1-\delta^2})\,(S + \delta W_n - jW_n\sqrt{1-\delta^2})\,(aT_2S+1)(T_1S+1)} \qquad (90)$$

Analyses and tests of the bimorph assembly indicated that its resonance of frequency is 50 Hz and the damping factor is essentially zero. The bimorph is considered to have an equivalent capacitance of 6000 picofarads.

$W_n = 2\pi f \doteq 314$ rad/sec. for f = 50 Hz

δ = bimorph-assembly damping factor

$\delta = 0$

C = bimorph capacitance $\equiv$ 6000 picofarads

R = input impedance of feedback amplifier = 2.5 megohms

$T_1 = RC = 15 \times 10^{-3}$ sec

$\frac{1}{T_1} = 66.7$

Let

$$\frac{1}{T_2} = 66.7$$

Then

$$\frac{1}{aT_2} = 667$$

$$G(S)\,H(S) = \frac{K_A K_M K_G K_F \left(\frac{W_n^2\, T_2}{aT_1 T_2}\right) S\left(S + \frac{1}{T_2}\right)}{(S+jW_n)(S-jW_n)\left(S+\frac{1}{aT_2}\right)\left(S+\frac{1}{T_1}\right)}$$

$$= \frac{K_A K_M K_G K_F K_M \left[(314)^2\,(667)\right] S\,(S+66.7)}{(S+j\,314)(s-j\,314)(s+667)(S+66.7)} \qquad (91)$$

The inner loop is chosen to have response of 5 Hz by selecting an operating point at S = -32. Substituting S = -32 into Equation (91),

$$G(S)\,H(S) = \frac{K_A K_M K_G K_F \left[(314)^2\,(667)(32)(34.7)\right]}{(315)(315)(635)(34.7)}$$

$$= 33.4\, K_A K_M K_G K_F \qquad (92)$$

The steady-state gain of the inner loop, K_{ss}, can be obtained by making Equation (92) equal to unity:

$$33.4\ K_A K_M K_G K_F = 1$$

$$K_A K_M K_G K_F = \frac{1}{33.4} = 0.03 = K_{ss} \tag{93}$$

The values of K_M and K_G are determined by the characteristics of the bimorph. Applying 140 volts to the bimorph results in 2.0° deflection. The feedback bimorph, when acting as a signal generator, produces 0.14 volt when deflected 2.0°:

$$K_M = \frac{2.0^\circ}{140 \text{ volts}} = 1.43 \times 10^{-2} \text{ degree/volt}$$

$$K_G = \frac{0.14 \text{ volt}}{2.0^\circ} = 0.07 \text{ volt/degree}$$

Substituting the values of K_M and K_G into Equation (93),

$$K_A K_F = \frac{0.03}{K_M K_G} = \frac{0.03}{(1.43 \times 10^{-2})(0.07)}$$

$$K_A K_F = 30$$

Let

$$K_F = 1$$
$$K_A = 30$$

The transfer characteristic of the inner loop, θ_o/θ_e, is

$$\frac{\theta_o}{\theta_e} = \frac{K_I(32)}{(S+32)}$$

$$K_I = \frac{K_A K_M}{1 + K_A K_M K_G K_F}$$

$$= \frac{(30)(1.43 \times 10^{-2})}{1 + 0.03}$$

$$= 0.415$$

2.4.3 Analysis of Servo System (Outer Loop)

The open-loop transfer characteristic of the system, G(S), is

$$G(S) = \frac{K_D K_C\ (0.415)(32)}{S\ (S + 32)} \tag{94}$$

The damping factor of the system can now be selected to provide stable operation, good tracking accuracy, and relatively short response time. Let the damping factor, δ, be 0.5. Figure B-14 plots G(S) on the root-locus plane. For $\delta = 0.5$, the system's operating points are

$$S = 16 \pm j\ 28$$

Substituting the δ value into Equation (94),

$$G(S) = \frac{K_D K_C\ (0.416)(32)}{(16 + j28)\ (16 - j28)}$$

$$= \frac{K_D K_C\ (0.415)(32)}{(32.2)^2} \tag{95}$$

The steady-state gain, K_{ss}, is obtained by setting Equation (95) equal to unity:

$$K_{ss} = K_D K_C\ (0.415) = \frac{(32.2)^2}{32}$$

$$= 32.4$$

Since K_D = 306 volts/degree, as shown on Figure B-13

$$K_C = \frac{32.4}{K_D\ (0.416)}$$

$$= 0.255$$

The closed-loop transfer characteristic of the system, θ_o/θ_i, can now be written as

$$\frac{\theta_o}{\theta_i} = \frac{KW^2}{(S+\delta W+jW\sqrt{1-\delta^2})(S+\delta W-jW\sqrt{1-\delta^2})} \tag{96}$$

$$W = \left| 16 + j28 \right| = 32.2 \text{ rad/sec}$$

$$W\sqrt{1-\delta^2} = 32.2\sqrt{1 - (.5)^2} = 28$$

$$\delta W = 0.5\ (32.2) = 16$$

$$W^2 = (32.2)^2 = 104$$

Let K = 1

Substituting values into Equation (96),

$$\frac{\theta_o}{\theta_i} = \frac{104}{(S + 16 + j28)(S + 16 - j28)}$$

2.5 TRACKING-SUBSYSTEM PERFORMANCE SUMMARY

2.5.1 Tracking Error, θ_e

For a maximum spacecraft-roll rate of 0.001^o/sec

$$\theta_e \approx \frac{\dot{\theta}}{K_{ss}} + \theta_1 + \theta_2$$

θ_1 = tracking error due to noise, offset, and drift of the subsystem electronics

θ_1 = 1.5 arc sec

θ_2 = optical and mechanical misalignment

θ_2 = 1.0 arc sec

$$\theta_e \approx \frac{0.001^o}{32.8} + 1.5 + 1.0$$

$$\theta_e \approx 3 \text{ arc sec}$$

2.5.2 Carrier Signal, $E(\theta)$, at Maximum Tracking Error

Figure B-9 indicates that, with a radius of nutation, γ, of 1.5 arc sec and target displacement of 3 arc sec from the center of the detector, the carrier signal is $E(\theta) = 0.95$, or 0.2 db. The attenuation due to 3-arc-sec misalignment of the receiver and transmitter beams is 0.7 db, according to the optical-link analysis in Section 5.1.3 of Volume I, Part 1. Therefore, the carrier-signal attenuation at maximum tracking error is 0.9 db.

2.5.3 Subsystem Tracking Bandwidth

$$f = \frac{W}{2\pi} = \frac{32.2}{2\pi}$$
$$= 5.12 \text{ Hz} \qquad (97)$$

2.5.4 Response Time

Rise time, t_r, in response to a unit-step input is determined as follows:

$$\theta_o = \left[1 + (1 - \delta^2)^{-1/2} \exp(-\delta W t) \sin \beta t\right]$$
$$= \left[1 + 1.16\, e^{-16t} \sin 28t\right]$$
$$= \left[1 + 1.16\, e^{-16t} \sin 2\pi (4.45)t\right]$$
$$t_r = \frac{1}{2} \text{ cycle of } 4.45 \text{ Hz}$$
$$t_r = \frac{1}{2}\left(\frac{1}{4.45}\right) = 0.112 \text{ sec}$$

REFERENCES

1. E. G. Fubini and D. C. Johnson, "Signal-to-Noise Ratio in AM Receivers," Proc. IRE, Vol. 36, pp. 1461-1466 (1948).

2. M. I. Skolnik, Introduction to Radar Systems, New York, McGraw-Hill, 1962.

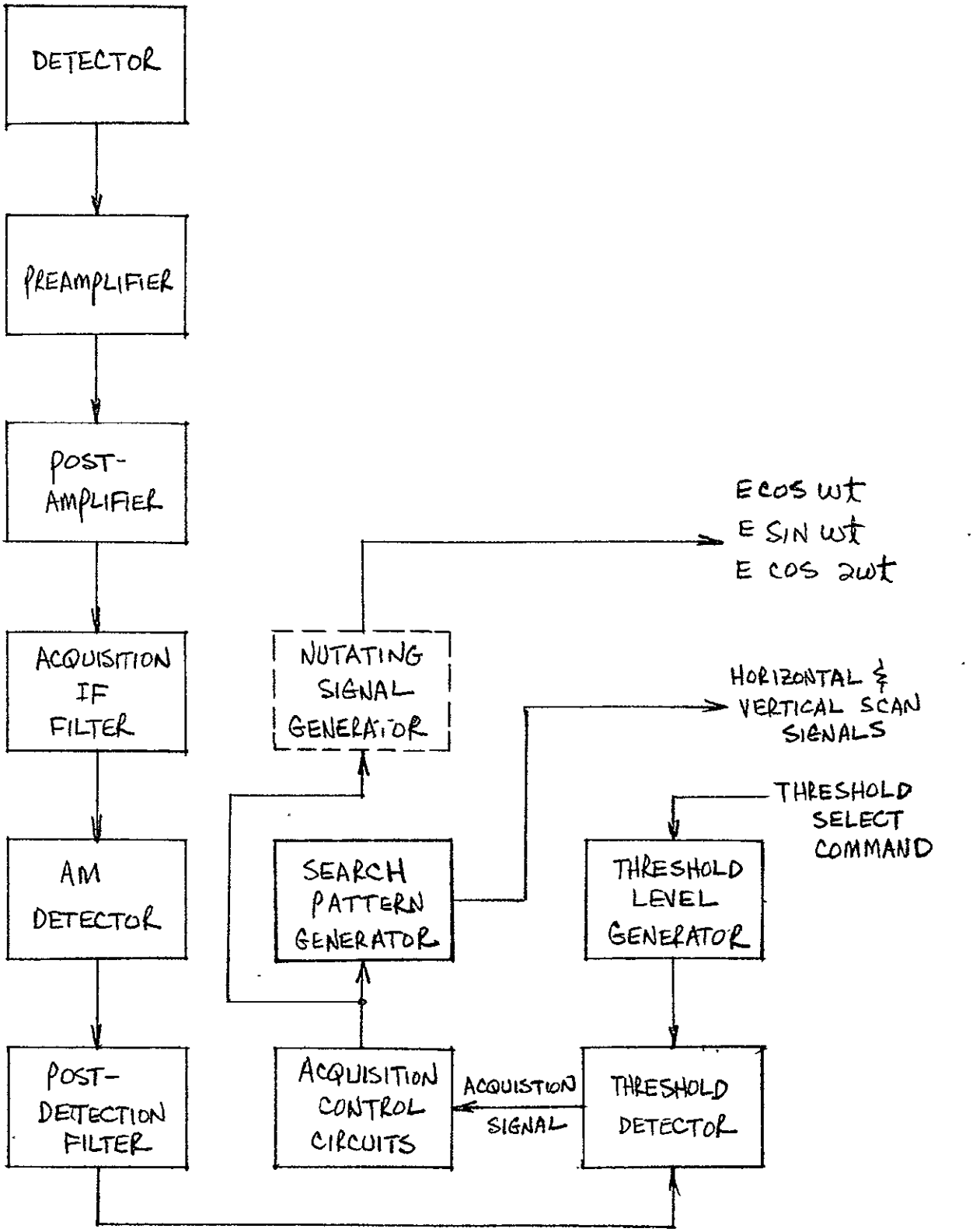

Acquisition Subsystem Functional
Block Diagram

Figure B-1

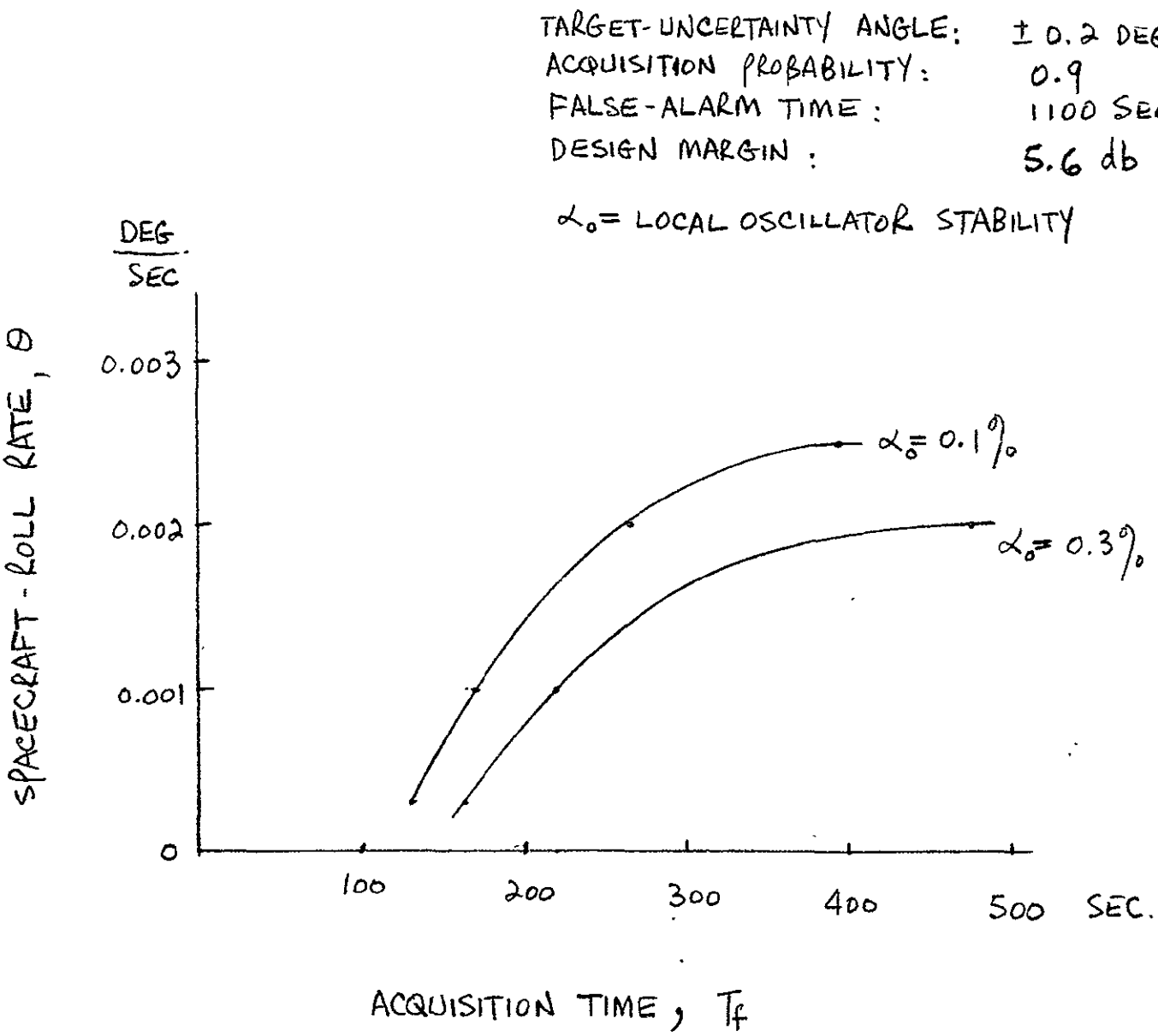

Acquisition-Subsystem Performance

Figure B-2

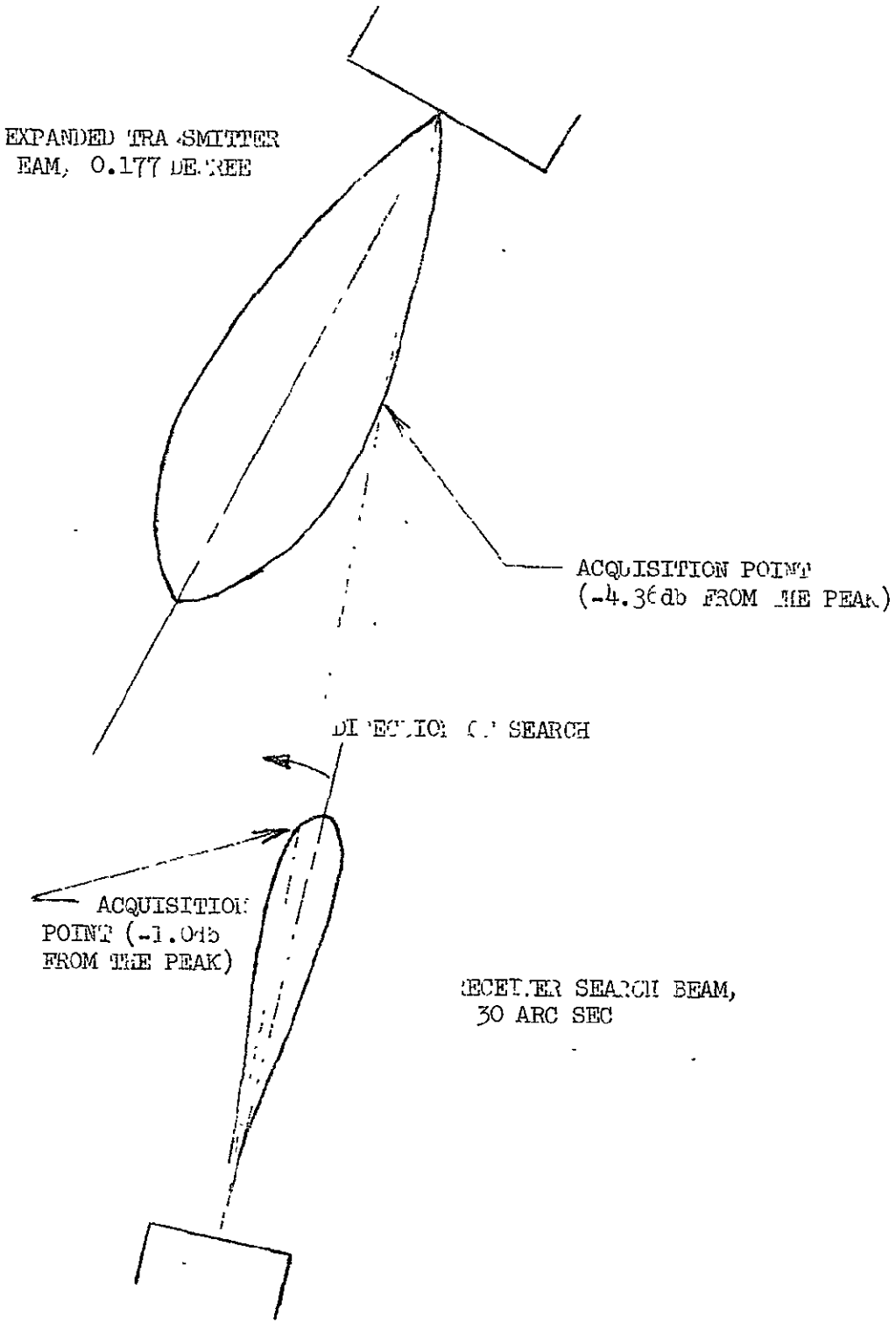

Relative Positions of Transmitter and Receiver
Beams at Time of Acquisition

Figure B-3

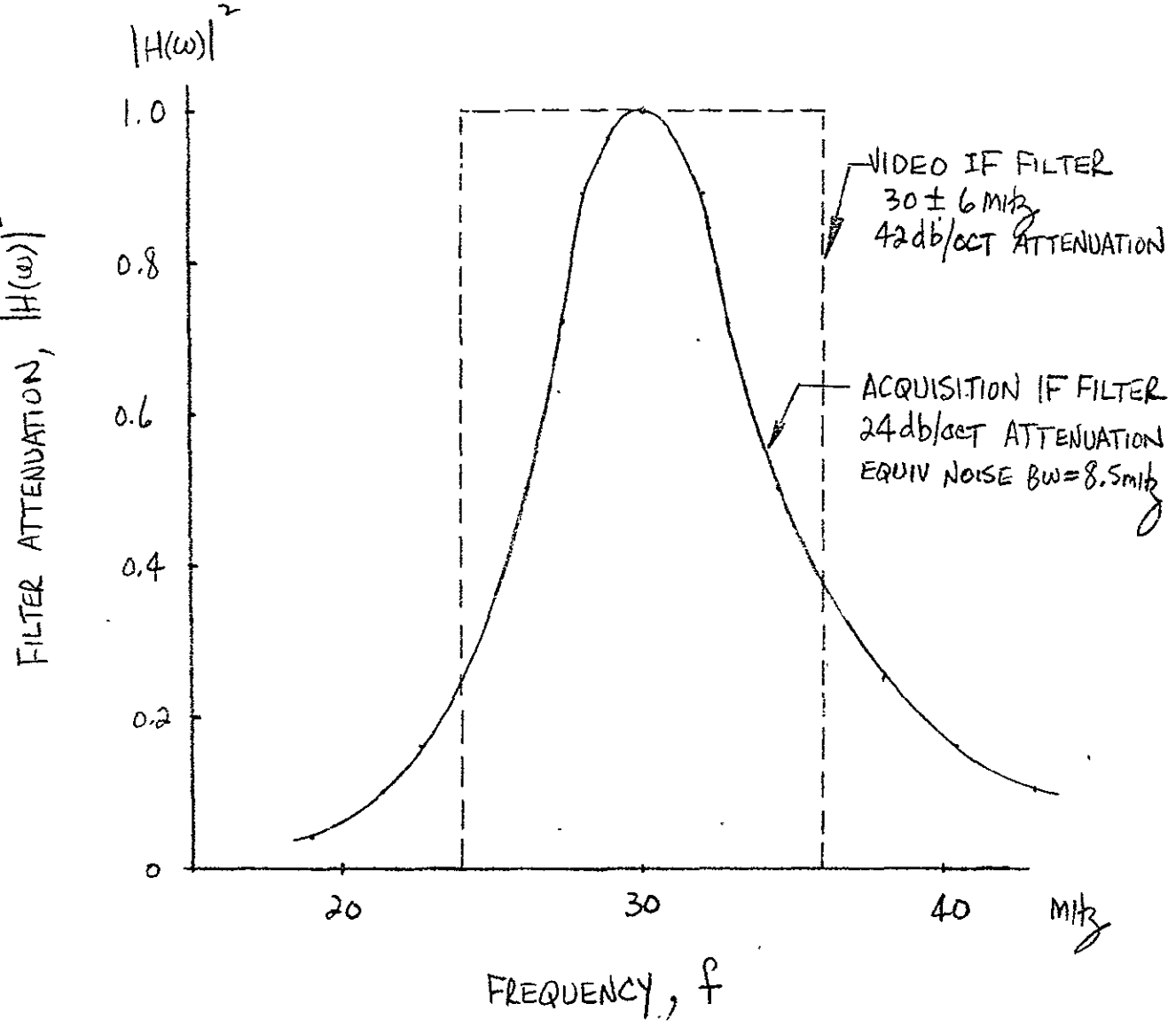

Acquisition IF-Filter Characteristics

Figure B-4

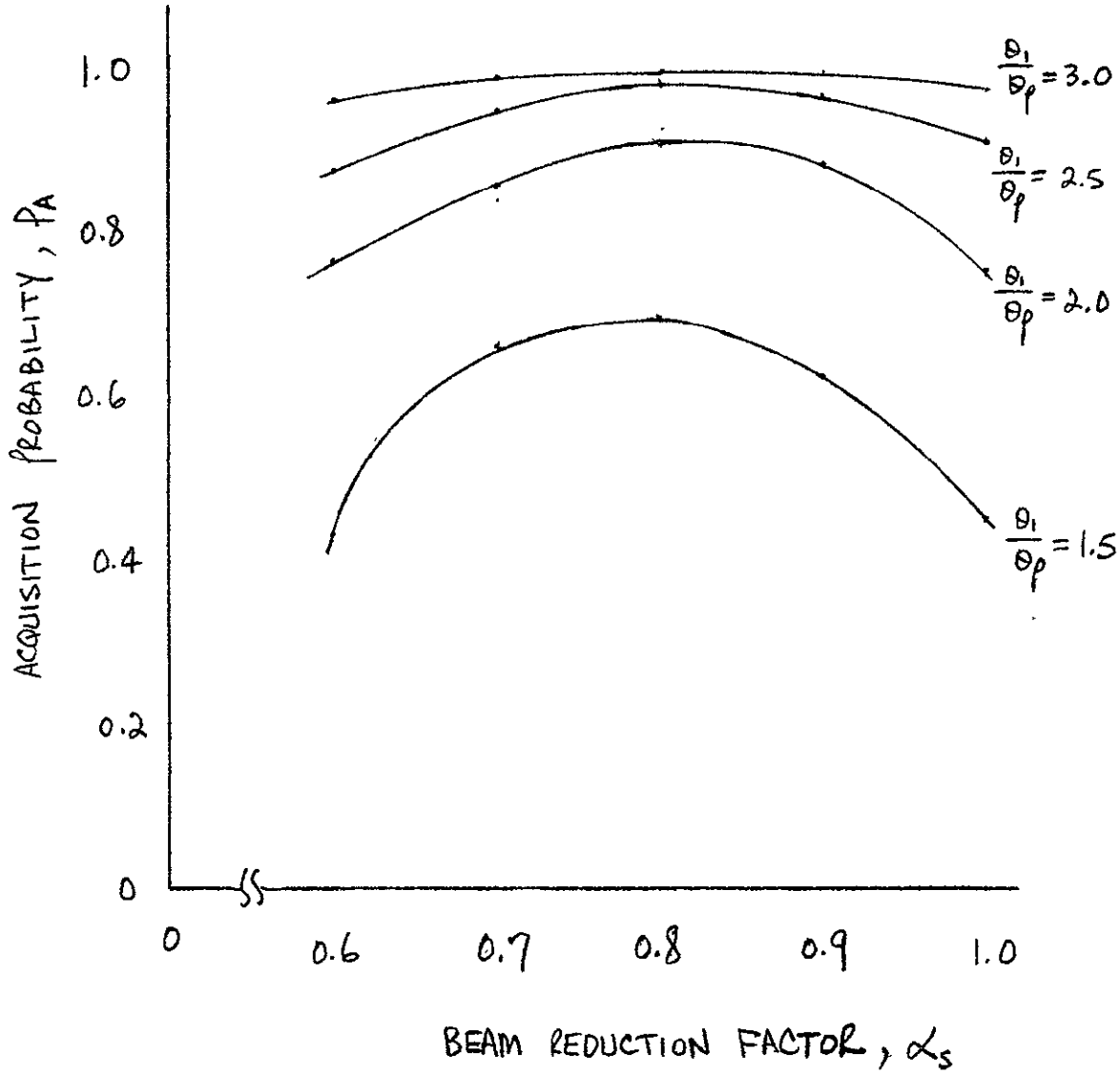

Acquisition Probability as a Function
of Beam-Reduction Factor

Figure B-5

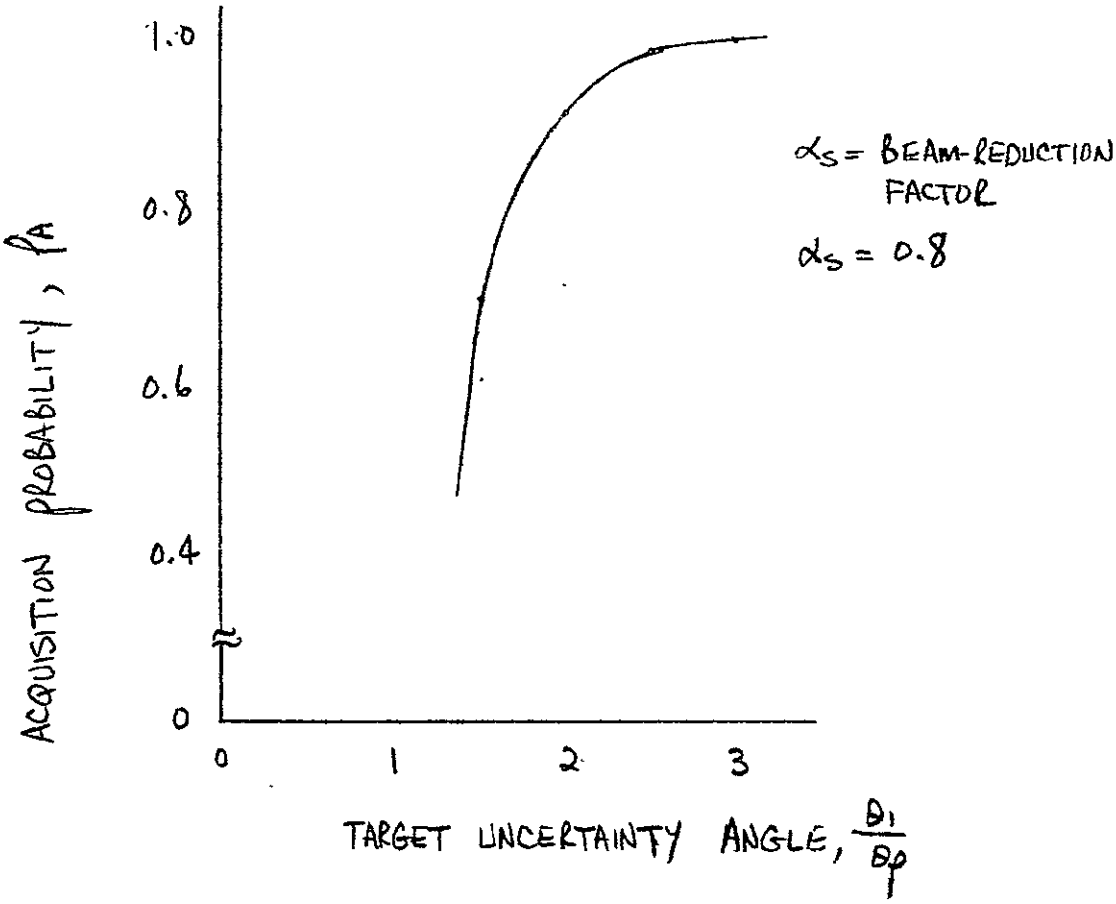

Acquisition Probability as a Function
of Target-Uncertainty Angle

Figure B-6

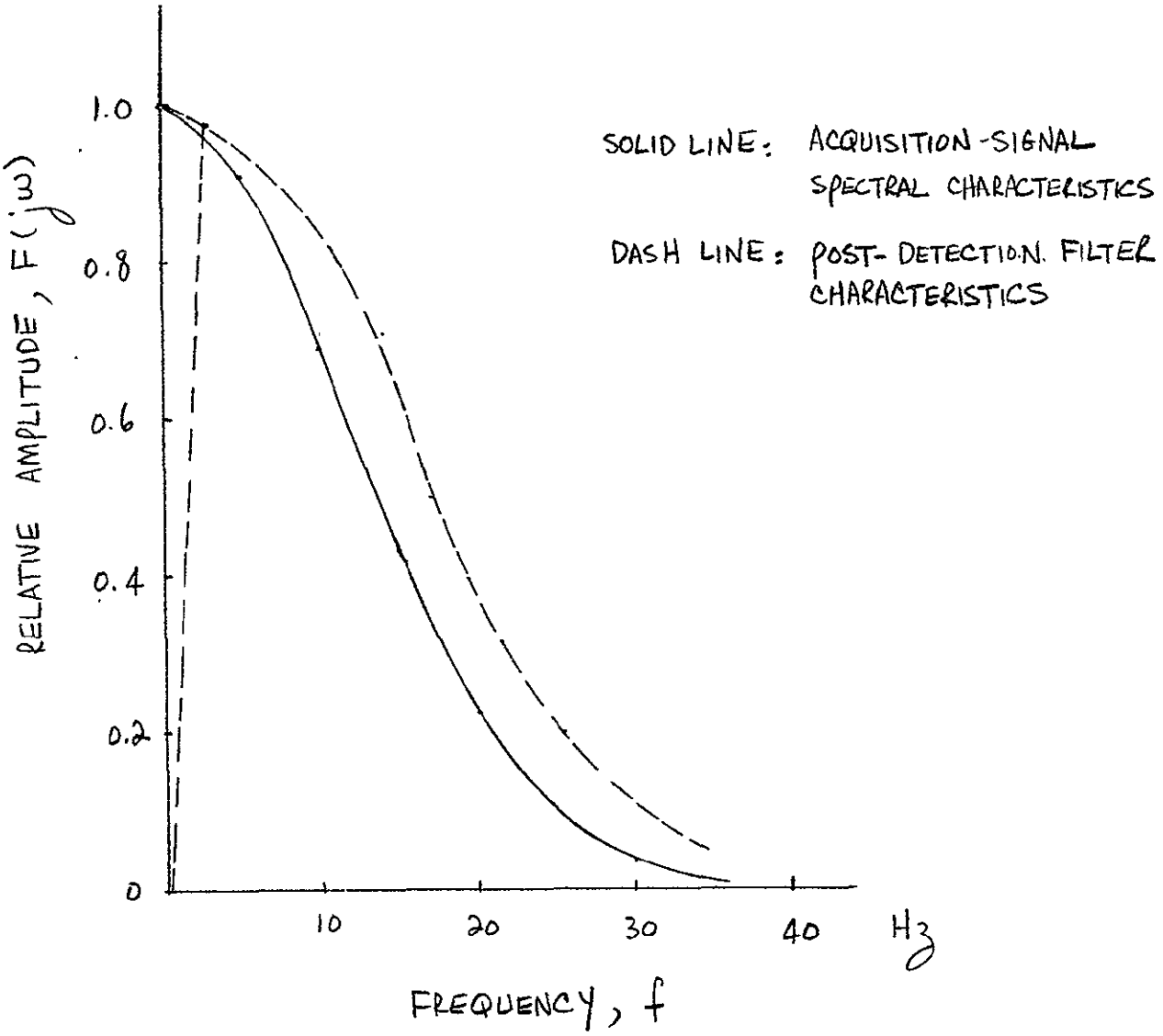

Acquisition Signal and Post-detection Filter Characteristics

Figure B-7

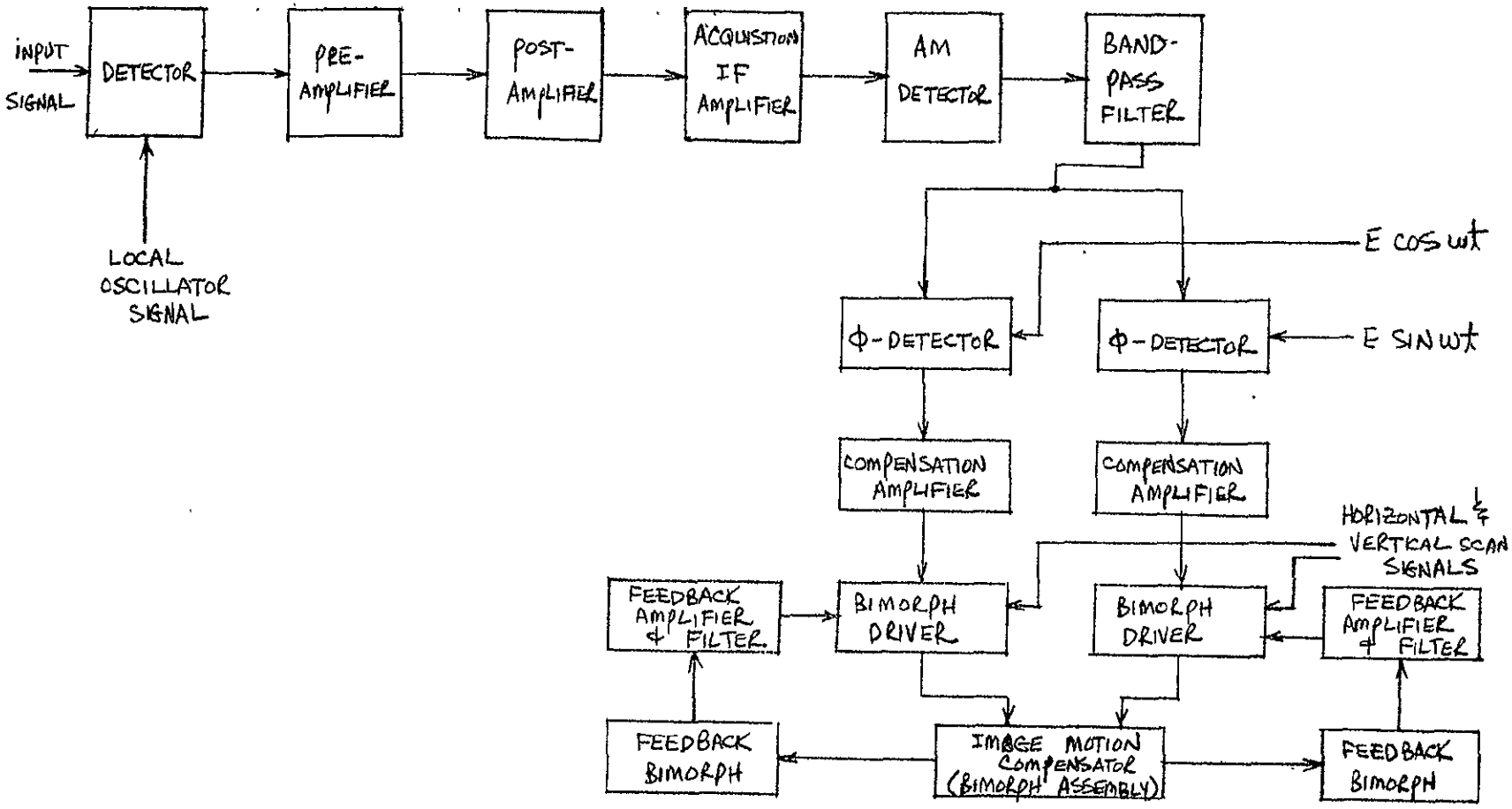

Figure B-8

Tracking Subsystem, Functional Block Diagram

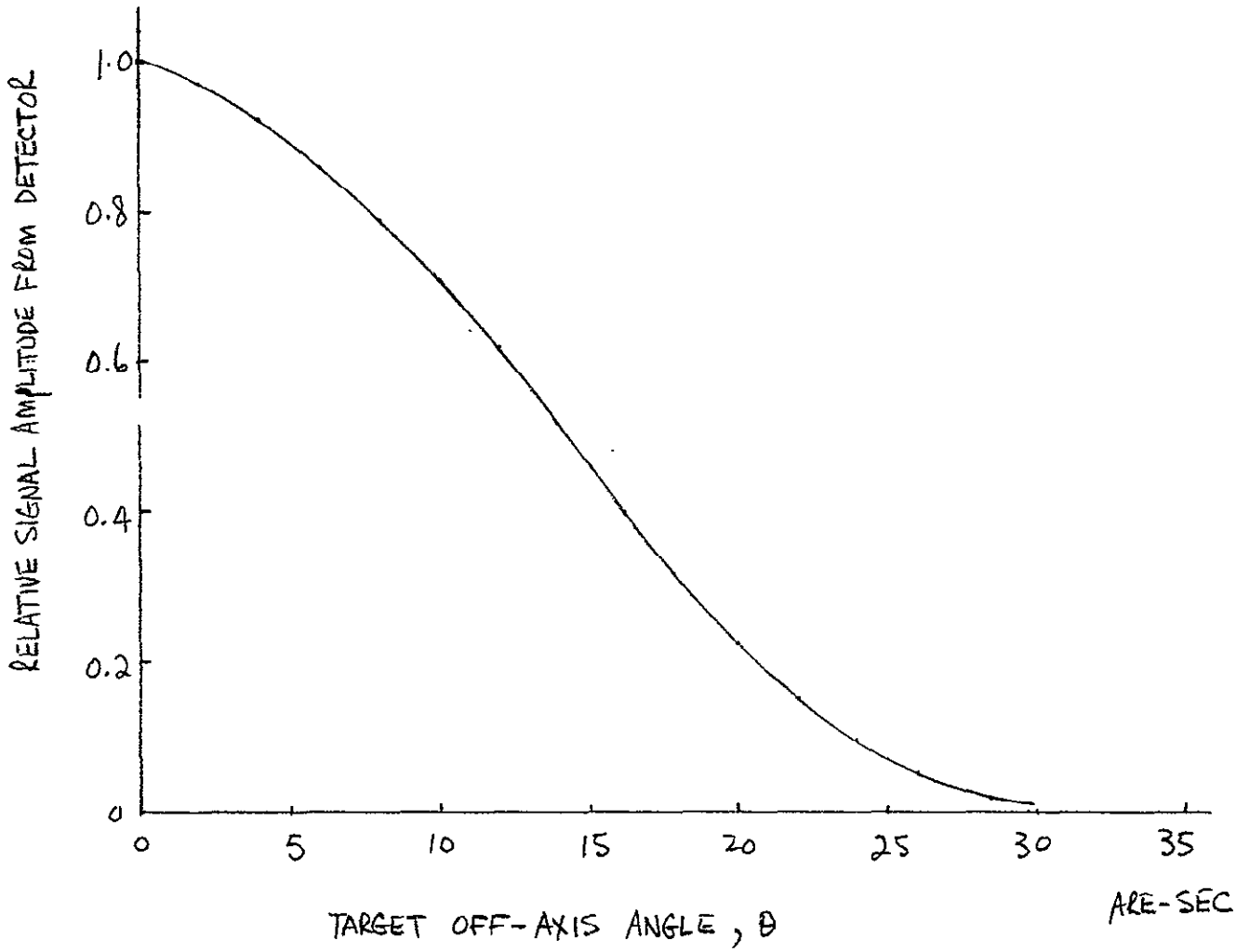

Relative Signal Amplitude from Detector
vs Target Off-Axis Angle

Figure B-9

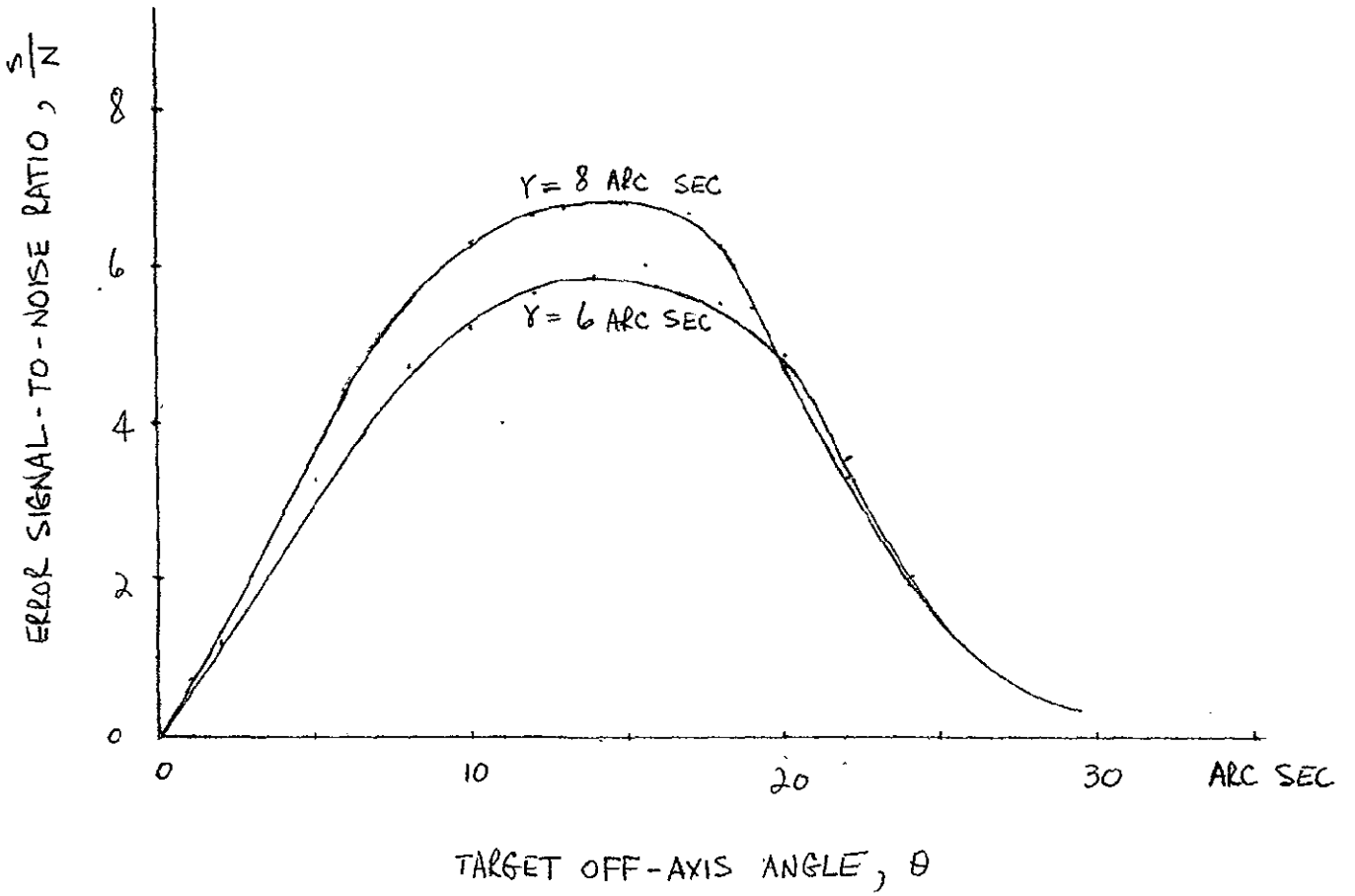

Error-Signal S/N vs Target Off-Axis Angle

Figure B-10

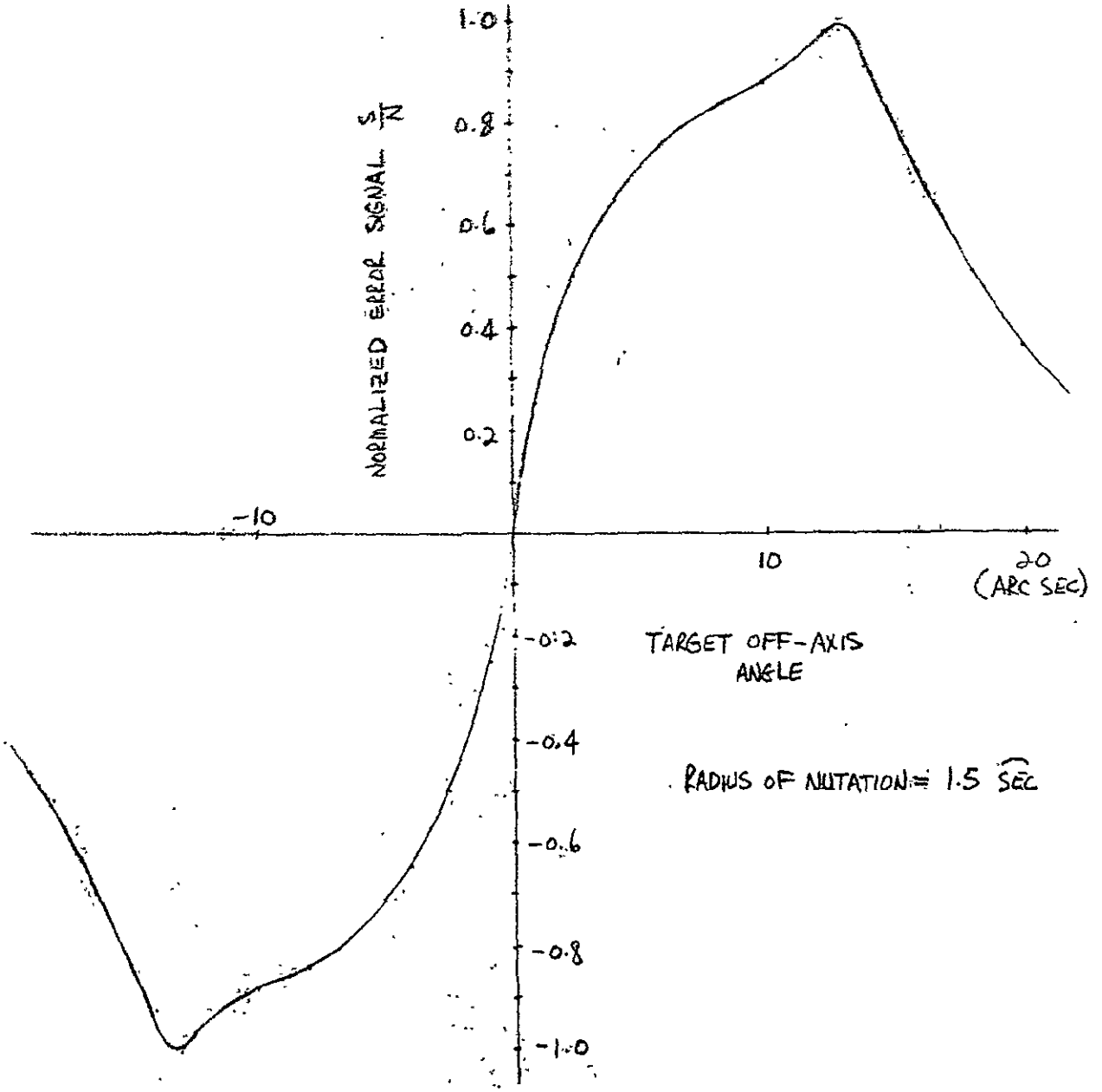

Error-Signal S/N vs Target Off-Axis Angle

Figure B-11

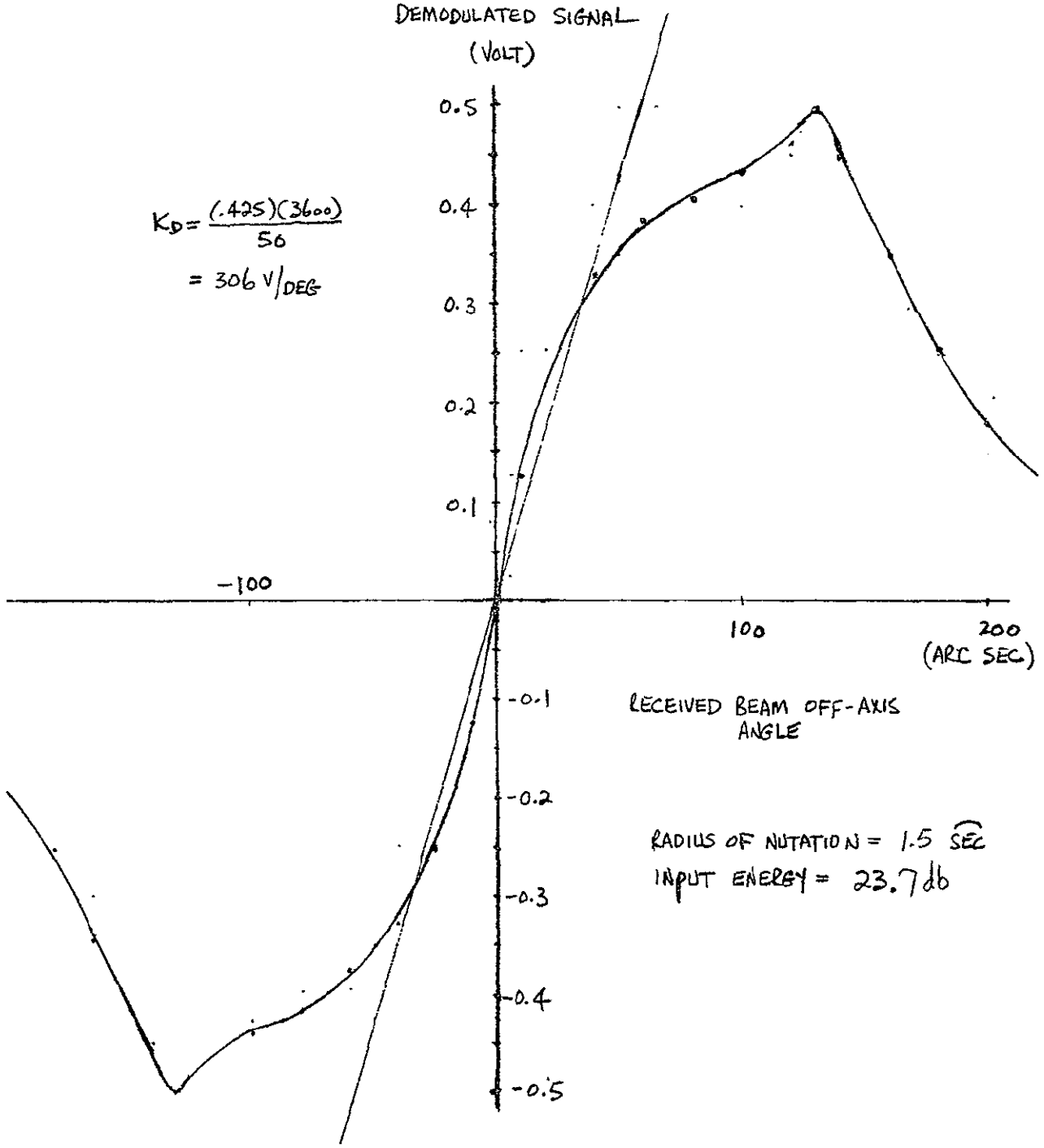

LCE Tracking-Servo System

Figure B-12

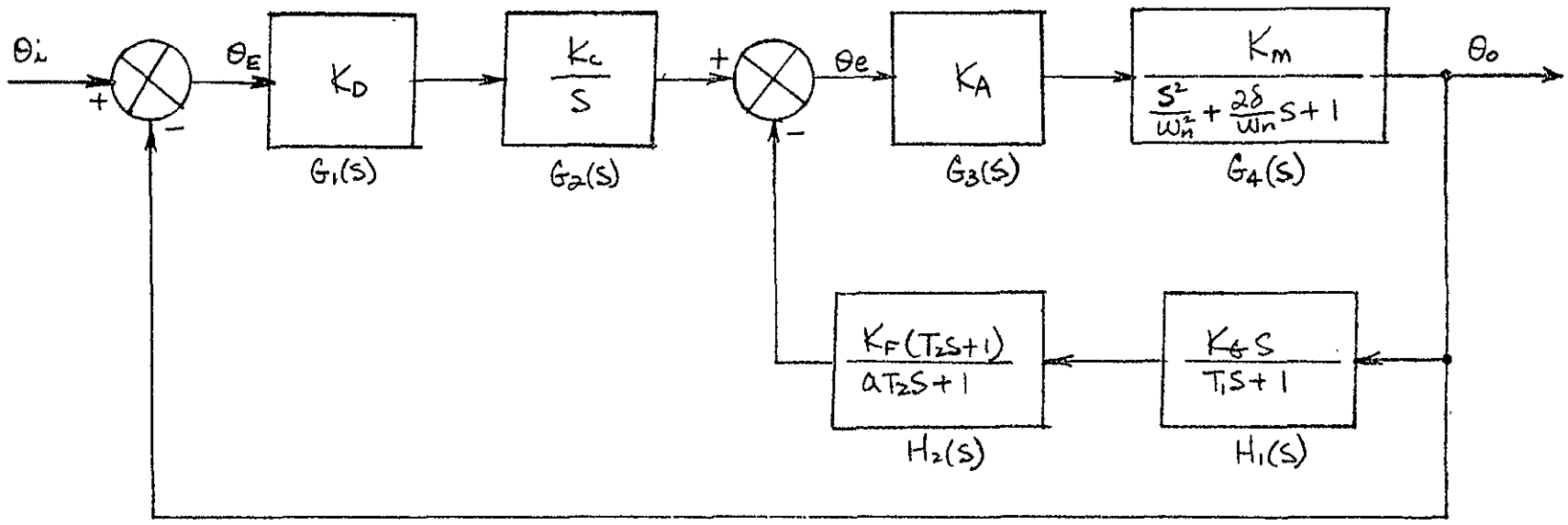

K_D = 306 V/DEG
K_c = .256
K_A = 30

K_m = 1.43×10^{-2} DEG./V
K_G = 0.07 V/DEG
K_F = 1

ω_n = 314 RAD/SEC
$\frac{1}{T_1}$ = 66.7
$\frac{1}{T_2}$ = 66.7
$\frac{1}{\alpha T_2}$ = 667

Figure B-13

Demodulated Signal Amplitude vs Received-
Beam Off-Axis Angle

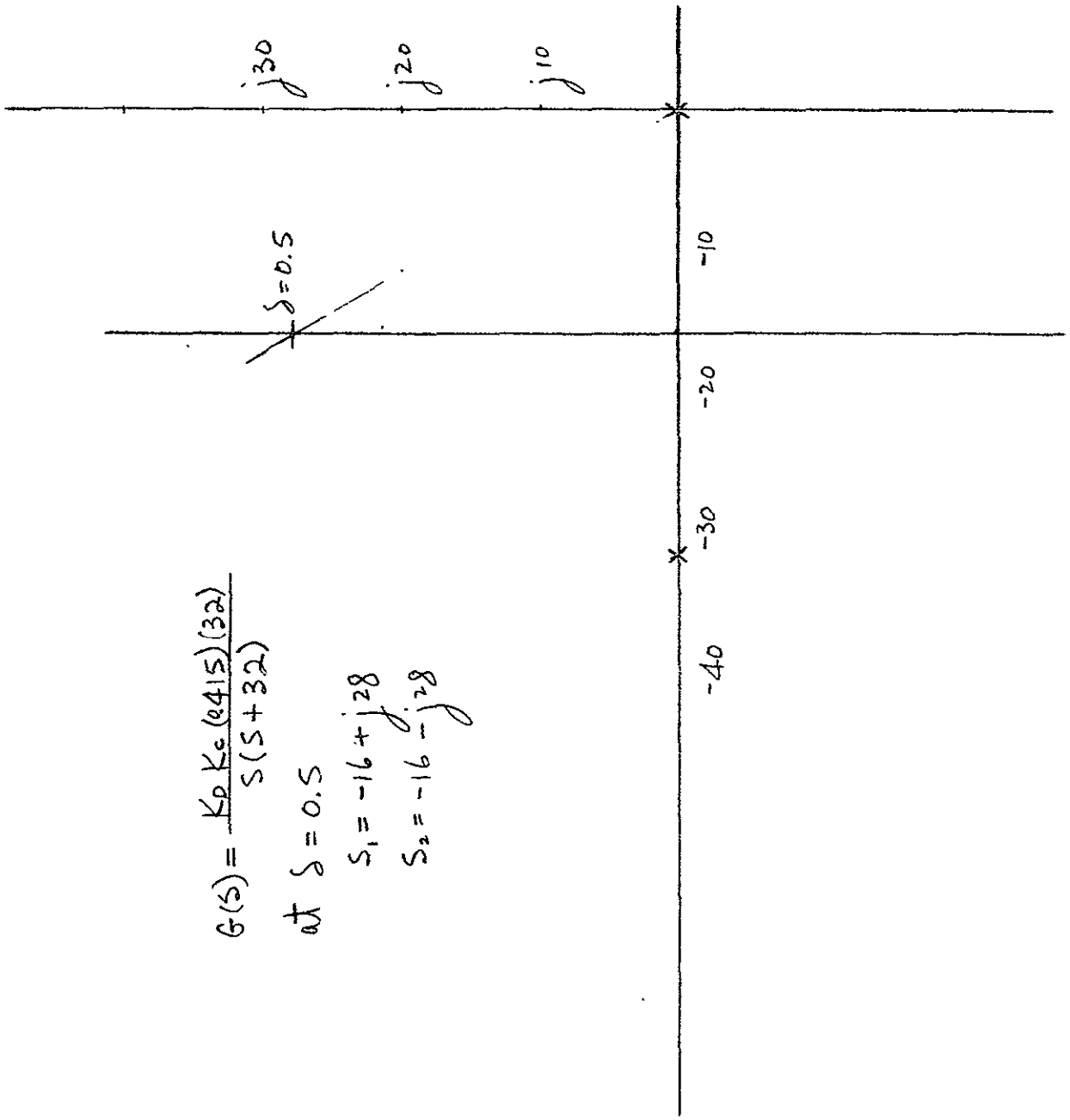

System Open-Loop Characteristics G(S)

Figure B-14

APPENDIX C

LCE TELESCOPE COMPARTMENT/ATS SPACECRAFT INTERFACE HEAT TRANSFER STUDY

This appendix presents the results of a study of the heat transfer between the LCE telescope compartment and the ATS spacecraft. The purpose of the study was to determine what is required in the telescope thermal design in order to reduce the heat transfer across the LCE/ATS mechanical interface throughout the complete orbit. The results of the preliminary transient thermal analysis described by Misselhorn showed a maximum of 9 watts being transferred to the spacecraft when the telescope opening faces the sun.[1] Also, the results showed 51 watts being transferred from the spacecraft when the telescope opening is not in the sun. This difference in heat input needs to be reduced.

The study has shown that the interface heat transfer can be reduced to ± 5 watts ("-" indicating heat transfer from the spacecraft) by insulating the interior of the telescope compartment with 0.2-in.-thick [10 layers - Table IV of Reference (1)] multilayer insulation. All surfaces, with the exception of the mirrored optical surfaces were covered with insulation. Also effective in reducing the interface transfer was the elimination of the earth facing surface [Nodes 63 and 64 of Reference (1)] as a space radiator and insulating it similar to the other internal surfaces. The thermal model used in this analysis was the beryllium-telescope section of the LCE thermal model reported in Reference (1). Figure C-1 shows the orbital interface heat transfer variation for both orbit extremes: solstice ($\phi = 23.5^{\circ}$) and equinox ($\phi = 0^{\circ}$). Figures C-2 and C-3 show the primary and secondary mirror orbital temperature variations for solstice and equinox orbits, respectively. The coarse-pointing mirror temperature varied between 61°F (16.1°C) and 96°F (35.7°C) for both orbits. The maximum temperature gradients in each spider leg was 4.5°F (2.5°C). Removing the insulation from the struts (spider legs) will:

- Increase their temperature gradients
- Increase their temperature oscillations in the orbit
- Increase heat exchange of telescope with spacecraft

All three of these consequences are undesirable for the LCE thermal design. A constant boundary (spacecraft) temperature of 68°F was used in this analysis.

In the analysis, the outer surface of the insulation was coated with white paint similar to that used on the interior surfaces in the Reference (1) analysis: α_s = 0.25 and ϵ = 0.85. The resulting maximum temperature excursion for the insulation was -150°F (-101°C) to +212°F (100°C). Actually it is more desirable to have a lower α_s and ϵ: a low α_s to decrease the absorbed solar energy, and a low ϵ to decrease the emitted energy when there is no solar energy entering the opening. However, there will be a tradeoff, since a low-ϵ surface could possibly give a higher insulation surface temperature. If the outer layer of insulation is not coated at all, then the following possibilities exist:

Kapton film out

- Half-mil Kapton - α_s = 0.33 and ϵ = 0.49*
- Three-mil Kapton - α_s = 0.44 and ϵ = 0.78*

Aluminized surface out

- Half-mil Kapton, with aluminun over nylon tulle - α_s = 0.15 and ϵ = 0.20*
- Half-mil Kapton, without the nylon tulle - α_s = 0.15 and ϵ = 0.04*

In all cases, the surface thermal properties are such as to yield excessively high insulation temperatures. A desirable improvement over the white paint would be second surface mirrors (α_s = 0.08 and ϵ = 0.77 to 0.83). However, these can only be incorporated with a penalty in both weight and cost.

*As given in Reference (2)

Actually, the desirability of the second surface mirrors over white paint would be the stability, and not necessarily the lower α_s and ϵ because of the many reflections (internal), the heat experiences before having been reflected or emitted through the opening.

When the motors and encoders on the coarse-pointing mirror are turned on at some time during the orbit, they will heat up. An analysis should be made during the LCE design on these items to determine just where the internal power dissipation is inside the motor. The analysis should also determine how the power is dissipated within the motor, and whether insulating will cause motor overheating.

Thus, it is believed by Aerojet that the white-painted multilayer insulation on the interior surfaces of the telescope compartment will be best suited for minimizing the LCE/ATS interface heat transfer. Kapton as the film material for the insulation will easily withstand the -150°F to +212°F temperature extremes. The actual insulation system design should be followed closely by Thermal Design to maximize the effectiveness of the insulation in reducing the absorbed solar heat. Another feature of the insulation should be to have only aluminized (low-ϵ) surfaces facing the ATS spacecraft to minimize the radiant interchange. Of the ±5 watts transfer, 10% is from radiation with LCE walls (facing the spacecraft) coated ϵ = 0.05.

REFERENCES

1. J. E. Misselhorn, "Preliminary Transient Thermal Analysis of the 10.6 Micron Laser Communication Experiment Package," Memo. No. TES69-1770, to W. F. Funnell, Dec. 1969.

2. E. E. Leudke and W. D. Miller, "Kapton Base Thermal Control Coatings," Paper presented at ASTM Symposium, Cincinnati, Ohio, Dec. 1969.

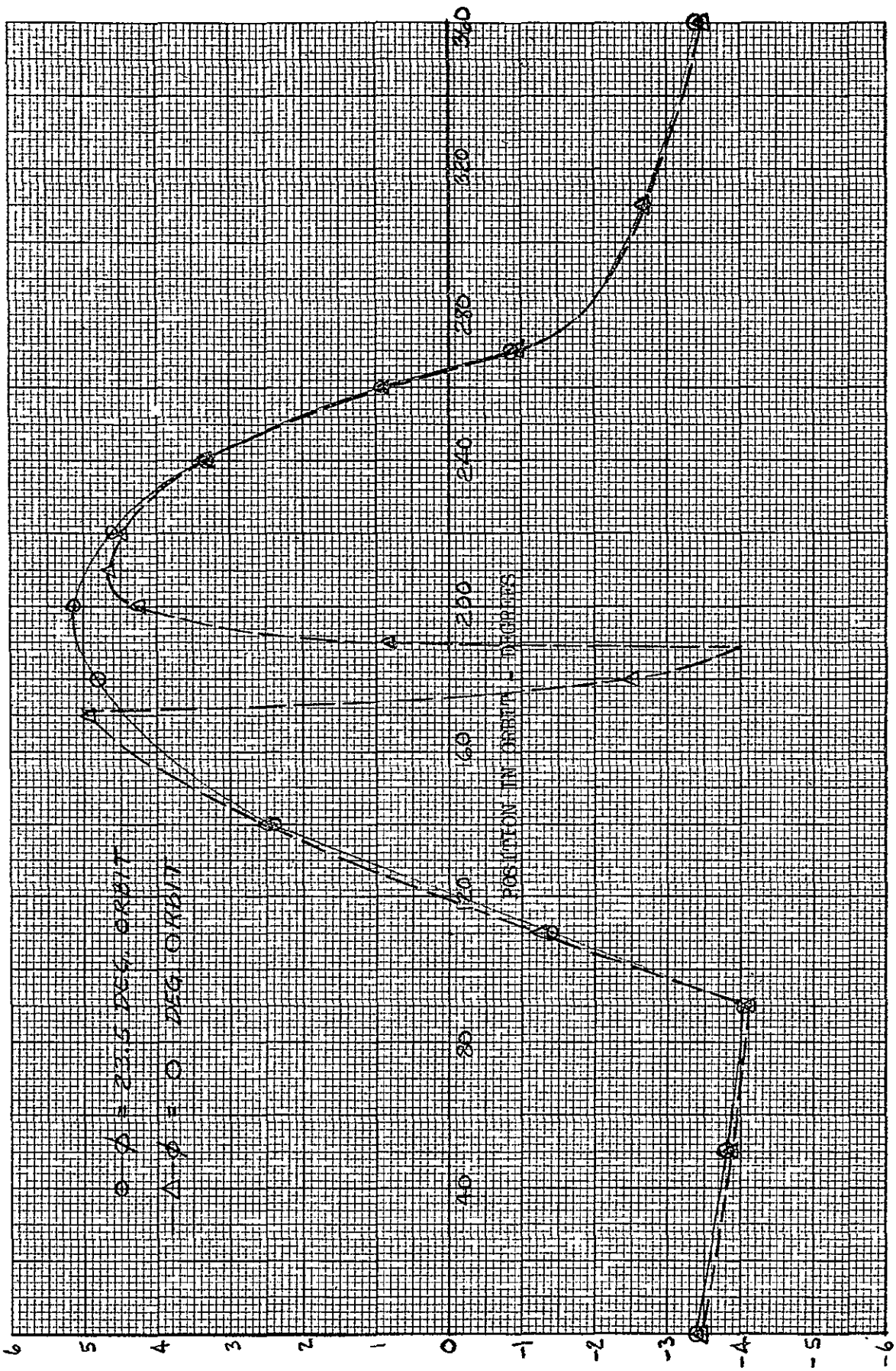
HEAT TRANSFER TO THE SPACECRAFT - WATTS
POSITION IN ORBIT - DEGREES
Orbital Heat Transfer To the Spacecraft from Telescope Compartment

Figure C-1

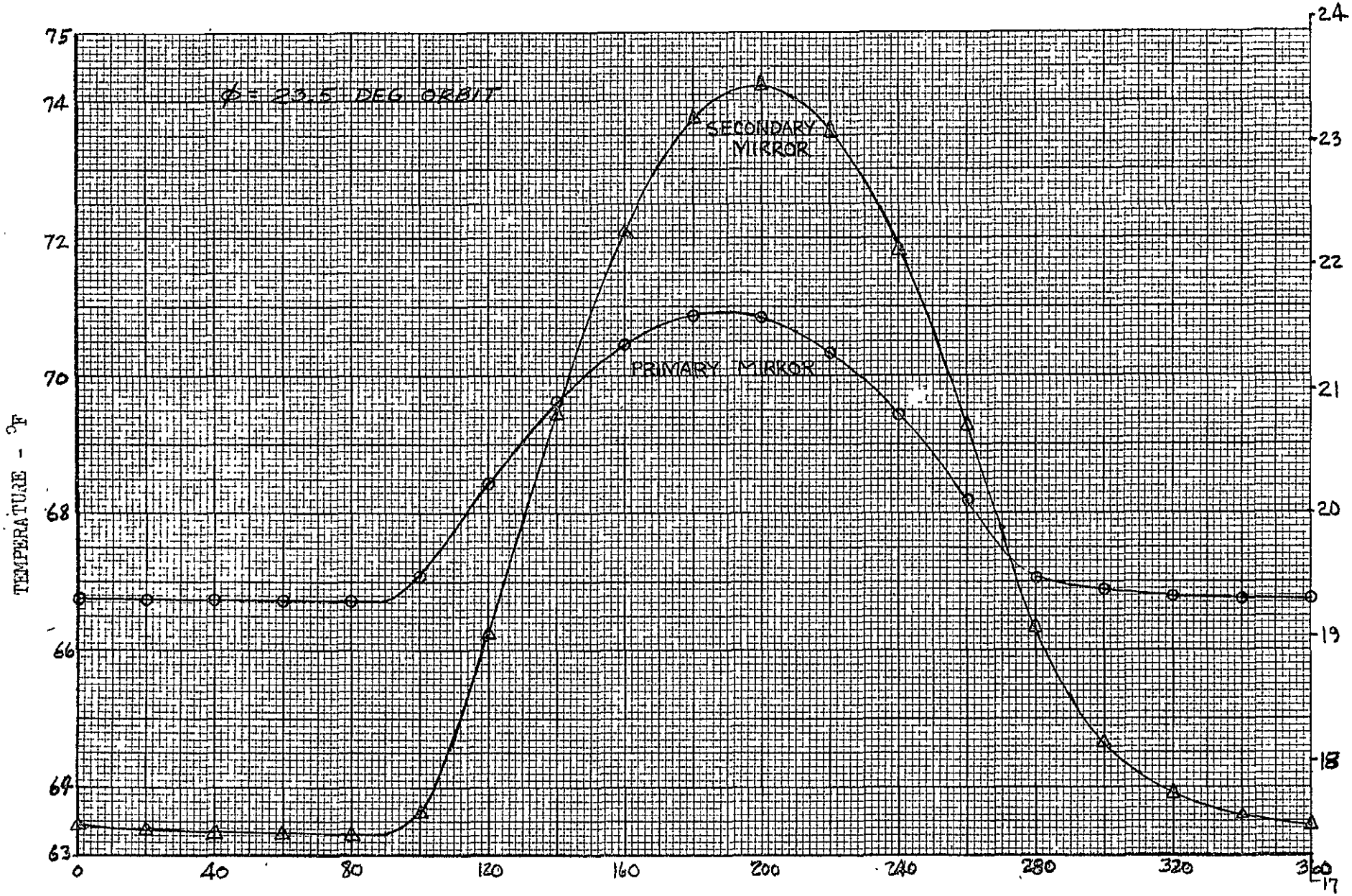

Figure C-2

Primary and Secondary Temperatures - Solstice Orbit

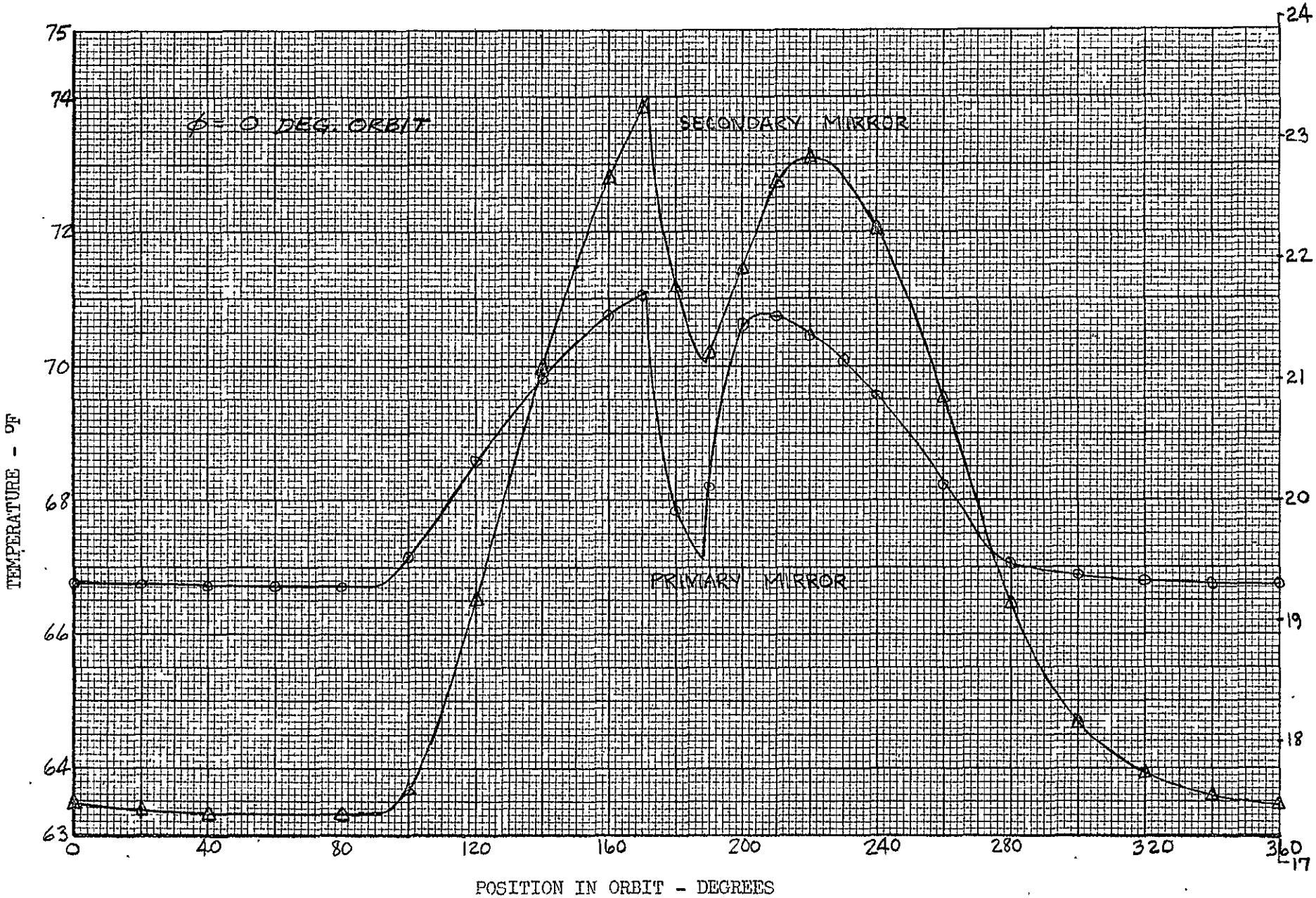

Primary and Secondary Temperatures - Equinox Orbit

APPENDIX D

ANALYSIS OF DISCRIMINATOR LINEARITY

A typical balanced discriminator circuit is shown in Figure D-1. The output voltage of the balanced discriminator is

$$e = \sqrt{2}\left|E_o\right|\left[\frac{1}{\sqrt{1+(x-\alpha)^2}} - \frac{1}{\sqrt{1+(x+\alpha)^2}}\right] \qquad (1)$$

where

$$x \cong \frac{\Delta f}{BW/2}$$

Δf = frequency deviation from the mean tuned-circuit frequency

BW = tuned circuit bandwidth in Hertz

E_o = RMS signal amplitude

$2\alpha BW$ = separation between the two resonant peaks

Normalizing equation 1 yields

$$h = \frac{e}{\sqrt{2}\left|E_o\right|} = \left[\frac{1}{\sqrt{1+(x-\alpha)^2}} - \frac{1}{\sqrt{1+(x+\alpha)^2}}\right] \qquad (2)$$

For small values of α, the discriminator curve in Figure D-2a is obtained. For large values of α the curve in Figure D-2b will result. For small values of α the curve will be linear but only over a narrow bandwidth. For an intermediate value of α the curve will be very nearly a straight line in a region between x_1 and x_2 over a large bandwidth. Figure D-3 shows a discriminator curve with a typical value of α showing such a linear region between x_1 and x_2. To determine the optimum value of α for the required discriminator linearity between points x_1 and x_2, it is helpful to examine the curve h for various values of x and calculate the deviation from linearity. The slope of the curve as it passes through zero is $h'(0)$, and $x*h'(0)$ is the equation of the tangent to the curve at the origin. Thus, the deviation from linearity of the discriminator curve is:

$$\epsilon = h - xh'(0) \qquad (3)$$

A plot of ϵ as a function of x with α as a parameter appears in Figure D-4.

Figure D-4 shows the relation between discriminator linearity and discriminator bandwidth and provides the design value of α when both quantities have been specified and inserted into the figure.

As an example, if one specifies that the discriminator linearity should be no worse than $\pm 2\%$ over as wide a bandwidth as possible, the best value of α for those shown in Figure D-4 is 3/2.

The curves were plotted to display a good range of values for α, but any number of curves could have been drawn in the figure. It is quite possible, that for a given linearity and discriminator bandwidth, there is another value of α not plotted in the figure which will work as well or better. However, since the design is only approximate and the accuracy with which we establish the optimum value of α is not necessarily consistent with circuit tolerances, it is not necessary to include more values of α in the figure.

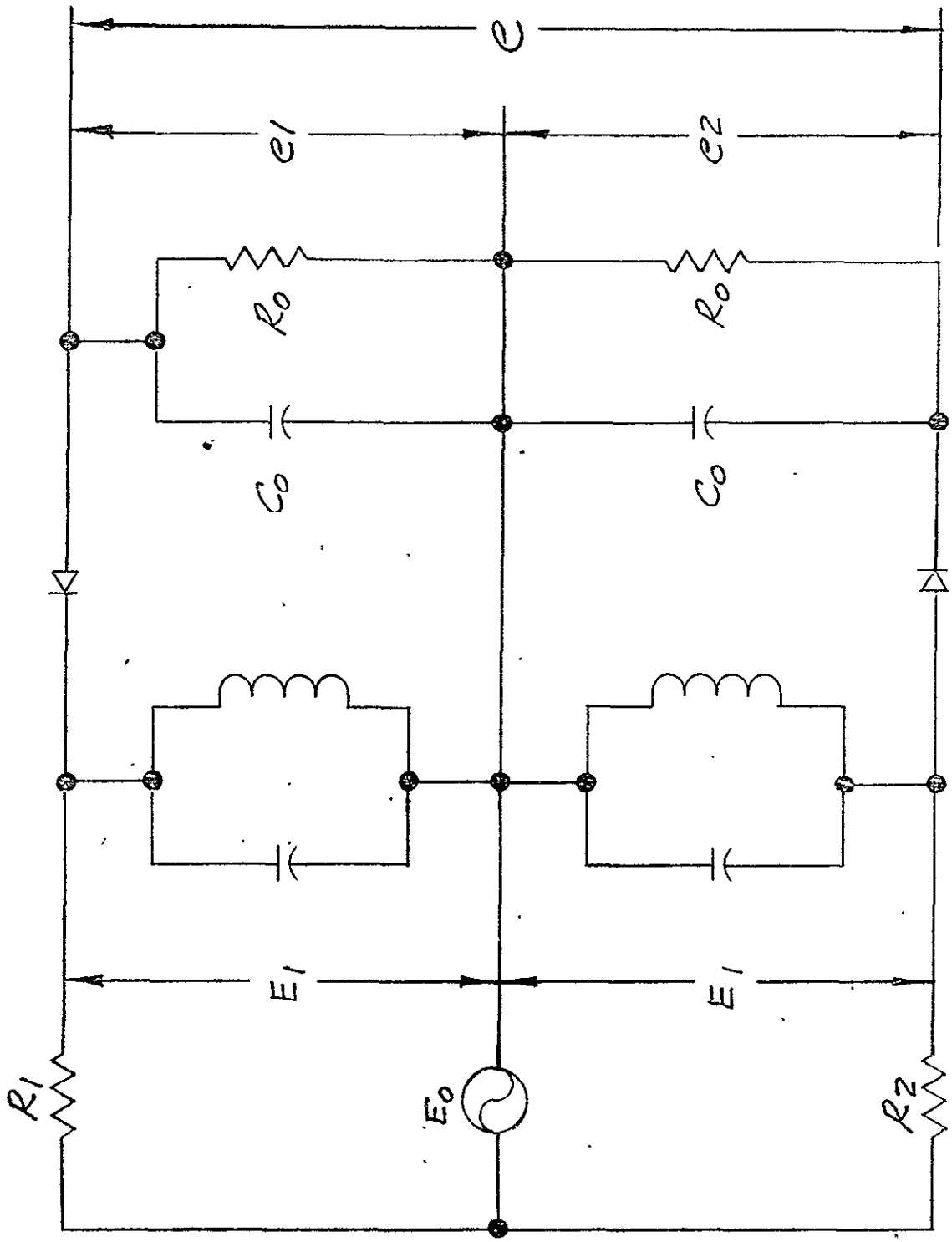

Typical Discriminator Circuit

Figure D-1

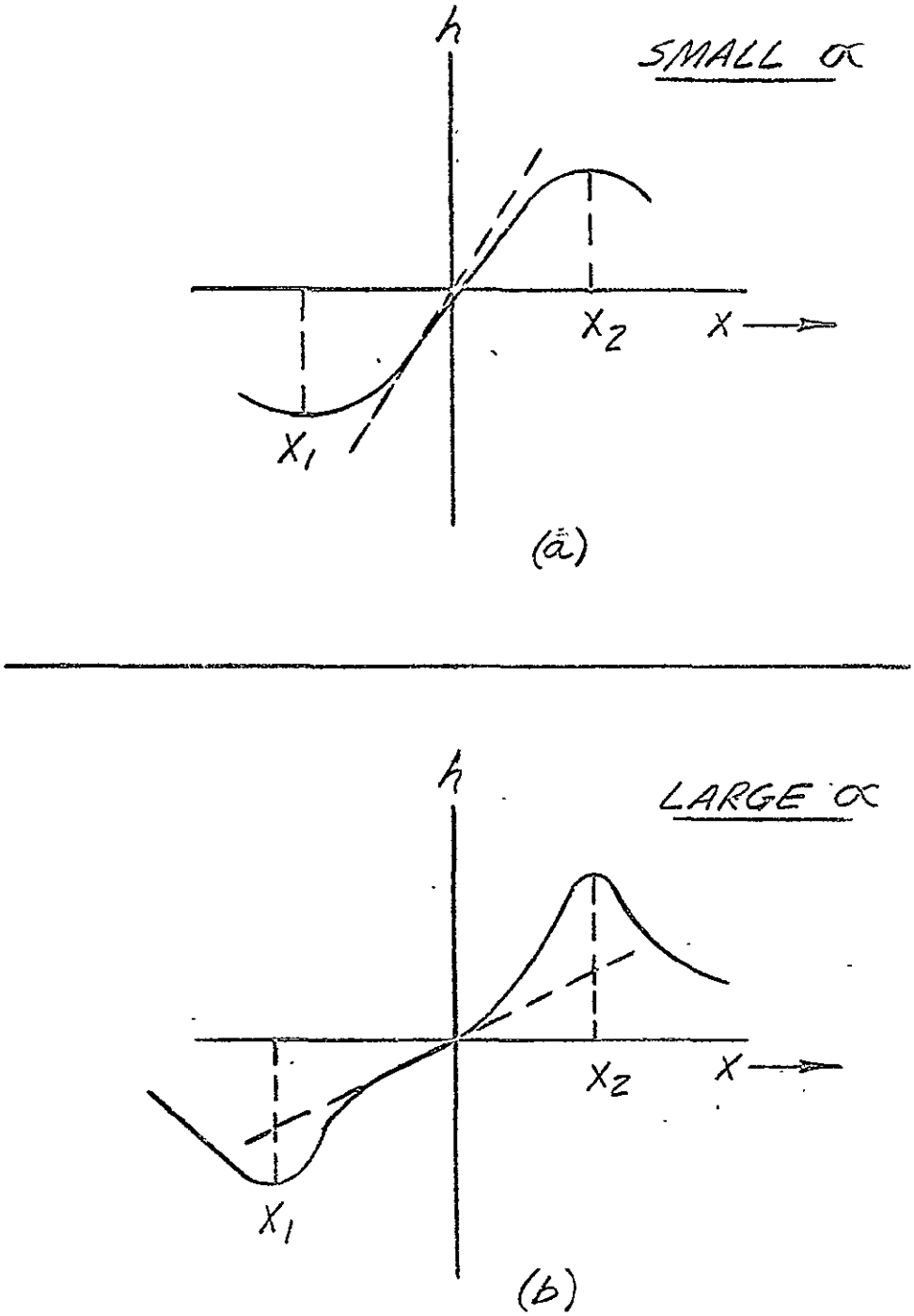

Shape of the Discriminator Curve for
Small and Large Values of α

Figure D-2

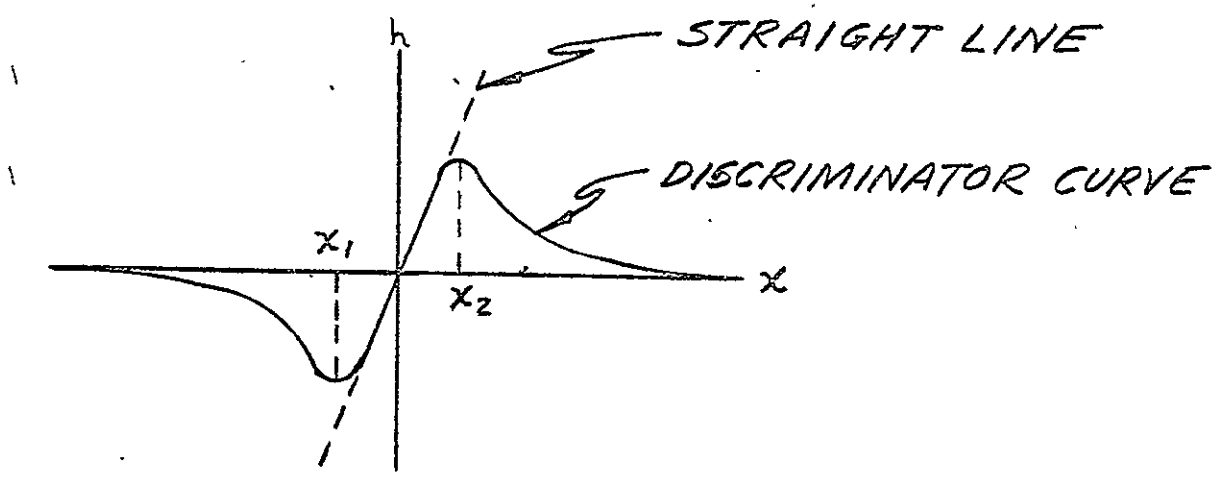

Typical Discriminator Curve
for Properly Selected Value of α

Figure D-3

Discriminator Error Curves

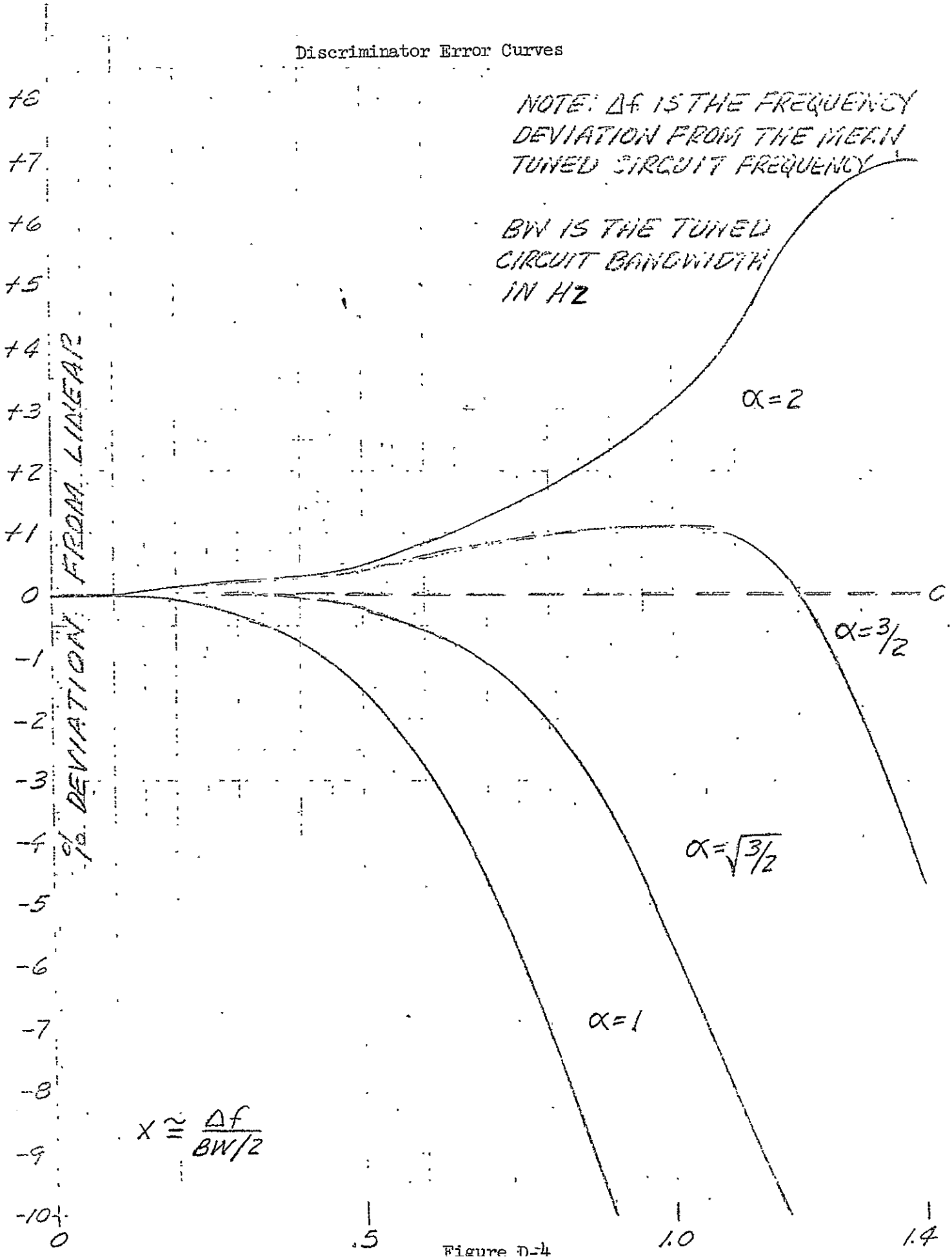

Figure D-4

APPENDIX E

CARBON DIOXIDE LASER ANALYSES

1.0 CO_2 LASER-SIGNATURE PROBLEM*

A carbon dioxide laser may oscillate at any one of many possible lines. As its cavity length is varied over a distance of $\lambda/2$, a large number of such lines oscillate one at a time in succession. The listing of the identities of such sequences of lines constitutes a "signature" of the laser and is a matter of practical importance in operation in remote-controlled applications without the use of mode-selecting elements in the laser cavity. Reported here is a rather remarkable result, namely that the lines P(20) and P(16) of the 10.6-micron transition compete so effectively relative to all the other modes that they can be relied to oscillate over a wide gain curve and for a wide range of operating conditions. These results are consistent with and support the results of concurrent investigations of this same phenomenon carried out by the National Aeronautics and Space Administration at its Goddard Space Flight Center and by RCA, Canada.

1.1 GENERAL DISCUSSION

The use of an appropriate frequency-selecting element (such as a diffraction grating) in the laser cavity can cause any CO_2 laser with reasonable gain to oscillate at any one of a large number of possible rotational transitions in the 9.6 and the 10.6-micron regions. However, such dispersing elements are known to have high insertion losses and in some applications are to be avoided in the interest of increased overall efficiency. For such cases, it is of interest to know whether some lines always compete effectively relative to other lines and whether the relative dominance of such lines persists over large ranges of operating conditions.

A Case Western Reserve University investigation of this matter was conducted in support of parallel investigations at the NASA Goddard Space Flight Center and by the RCA research staff in Montreal.

*Paul C. Claspy and Yoh-Han Pao, Case Western Reserve University.

Somewhat unexpected but very fortunate results were obtained at Case Western. They are consistent with and supported by the NASA and RCA results. The investigation is described below.

1.2 APPARATUS AND EXPERIMENTS

A reasonably stable CO_2 laser was constructed for these experiments. Its cavity consisted of two stainless steel discs connected by three 23-in. Invar rods of 3/4-in. diameter. The mirrors were mounted on the discs and the distance between mirrors was approximately 23 in. The output mirror was a 1/8-in.-thick, flat, germanium disc that was antireflection-coated on the outside and 80% reflecting on the inside. The other mirror was a 4m gold-coated surface attached to a piezoelectric crystal stack.

The laser tube was of 15-in.-long, 5-mm-ID Pyrex with a nickel cathode. It was supported by two clamps attached to one of the Invar spacer rods. Cooling water and vacuum lines were connected by Tygon tubing to minimize the transfer of vibrations to the cavity. The space between the mirrors and Brewster windows on the laser tube was enclosed by Mylar drift tubes, one on each end, to minimize the effect of convection currents. The output power of the laser was in the range from about 0.75 to 1.2 watts.

The oscilloscope traces noted in paragraph 1.3 present laser output as a function of laser-cavity length. Line identification was accomplished with the experimental setup shown schematically in Figure E-1. The cavity length was then swept over a half-wavelength distance for the following sequences of parameter changes:

a. Signature or line sequence vs pressure with discharge current adjusted to optimize laser output at each pressure

b. Signature or line sequence vs current at constant pressure

c. Effect of gross and arbitrary changes in cavity length

d. Effect of insertion of laser-cavity loss in the form of a rock-salt disc and also of an unevenly heated rock-salt disc

e. Effect of gross changes in pressure.

Although individual line sequences may seem to be very complicated and confusing, it is nevertheless remarkable that, except in one or two extreme cases, lines P(20) and P(16) of the (001)-(100) CO_2 band always compete effectively relative to other lines and may be depended upon to appear if the laser is swept over a distance of about $\lambda/2$.

1.3 EXPERIMENTAL RESULTS

Figures E-2 through E-10 represent the changes in line sequence as pressure was changed from 18 torr to 10 torr. In each case the current was adjusted to optimize the output. At 9 torr the laser did not oscillate. In all cases the gas fill was 4.65% H_2, 17.5% N_2, 16.9% CO_2, and 60.95% He by volume.

Figures E-2 through E-5 are not very informative because the voltage of the Lansing sweep drive did not bring about a complete line sequence with adequate repetition. Consequently, it would not be entirely clear from these four traces that P(20) and P(16) are indeed always present with wide gain profiles. The lines are nevertheless present, and subsequent reruns for very similar conditions confirm this conclusion.

Figures E-11 through E-17 illustrate the effect of changes in discharge current, with constant pressure. Lines P(20) and P(16) are always present with satisfyingly well rounded gain curves.*

Figures E-18 through E-21 illustrate the effect of large and arbitrary changes in cavity length. It would seem that such changes drastically change the identity of the weaker lines and also the sequence in which all three lines appear. However, P(20) and P(16) still survive marvelously well.

Figures E-22 and E-23 illustrate the changes in line sequence brought upon by a new gas fill. Although the optimum current is less than before refilling (about 6 ma vs about 10 ma), P(20) and P(16) again show up very clearly.

---

*Strictly speaking, these are not gain curves but are actually the variation of output intensity vs oscillation frequency and are related to the gain curve.

Figures E-24, -25, and -26 show the effects of inserting a 5-mm-thick, polished, rock-salt flat in the cavity to produce some loss. In the cases of Figures E-25 and E-26 the flat was heated unevenly to produce respectively moderate and severe temperature gradients in the rock-salt disc. P(20) and P(16) were essentially always present as long as there was laser oscillation.

Figures E-27 and E-28 illustrate the effects of operation at a much higher pressure range. P(20) is always present, but P(16) does not appear until the pressure is lowered to about 26 torr, at which it appears in a well rounded gain curve.

1.4 SUMMARY OF RESULTS

The results of this investigation indicate that operation should be designed for oscillation at either the P(20) or the P(16) lines in applications requiring the remote switching on and off of CO_2 lasers. Such lasers will operate effectively as long as additional features are provided for recognizing that the laser is indeed oscillating on, say, the P(20) line and if a feedback signal is available for locking on to line center or to a passive absorption line in an independent molecular gas.

2.0 DEPENDENCE OF CO_2 LASER "SIGNATURES" ON HELIUM PARTIAL PRESSURE AND DISCHARGE CURRENT*

The experiment described in this section was designed to determine the dependence of CO_2 laser signatures on helium partial pressure and discharge current.

The tests were performed on highly stable lasers constructed with a low-expansion-material (cervit) mirror separator. While the piezoelectric tuner (PET) used on the laser can move only $\pm$ 1.37 microns for $\pm$ 2000 volts applied, the long-term stability at the laser cavity was sufficient to prevent this from being a problem. In four successive days of operation, despite the laser pumpdown during the night and refilling with a new (and different) gas mixture each morning, it was possible to merely set the PZT

---

*J. H. McElroy and H. E. Walker, NASA Goddard Space Flight Center

voltage to 1650 ± 150 volts and find that the P(20) line was in operation. Furthermore, all significant lines were found to recur in the same positions to either side of P(20).

The first experiments were performed on 25 February 1970 to test the setup and prepare for the actual data runs. Figure E-29 presents four photographs taken on that day. In each case, the gas mixture was at a total pressure of 10 torr and was made up of 66.6% He, 16.7% CO_2. The horizontal scale was 11.1 MHz/cm and the vertical scale was uncalibrated. These photographs are included only to show the stability of the signature in day-to-day operation.

The sloping line across the photographs is 2 to 2000- volt sweep voltage applied to the PZT. The second spectral line from the right side of the photographs (i.e. the smooth, symmetrical curve) is the P(20) line. Its shape should be noted because it will be readily identifiable in subsequent photographs. The peak occurs at a sweep voltage of nominally -1650 volts.

Further calibration measurements were made on 26 February 1970. A totally different gas mixture was used; in these tests, a total pressure of 15 torr was used with 80% He, 15% N_2, and 5% CO_2. The horizontal scale is again 11.1 MHz/cm and the vertical scale is uncalibrated. Figure E-30 presents four photographs taken during the calibration tests. Figures E-29 and E-30 show marked similarities, even though the measurements were made 24 hours apart, with different gas mixtures, different total gas pressure, and different discharge currents. Most important, the principal lines, such as P(20), are least sensitive of all.

On 27 February 1970 the first deliberate data run was made. The results are shown in Figures E-31a through E-31o. The vertical scale is 300 mw/cm and the horizontal is 11.1 MHz/cm. The initial gas mixture was at a total pressure of 14.5 torr with 11.6 torr He, 2.2 torr N_2, and 0.7 torr CO_2. The helium partial pressure was gradually reduced and the effect on the signature was observed. In addition, the dependence on current was measured after each reduction in the helium partial pressure. In Figure E-31, each change in total pressure represents the reduction in the helium partial

pressure. In most photographs, the current was 8, 10, and 15 ma, but in E-31m, n, and o was 8, 10, and 13 ma.

Figure E-32 shows details of the test setup for laser-signature measurements. An essential feature is the very slow sweep employed and the use of dc coupling throughout the measurement channel. The bolometer was calibrated against a Coherent Radiation Laboratories power meter. During calibration, an interesting effect was observed. In the past, most experimenters with CO_2 lasers have noted that the discharge current during lasing action is different than it is if the beam is interrupted in the cavity or the cavity is misaligned and lasing action is not occurring. It was observed in this work that, even though the same voltage was applied to the tube, the current flowing in the tube varied as one line after another was brought into oscillation by tuning the PZT. This appears to be an effect related to, but less than, that previously observed. To avoid this problem all measurements in with specified current were calibrated by adjusting the current to the set value when the laser was operating at the peak of the P(20) line.

The conclusions drawn from these measurements are as follows:

a. The signature is not critically dependent on the helium partial pressure. This is particularly true for the principal spectral lines

b. The signature is not critically dependent on the discharge current. This is also particularly true for the principal spectral lines

c. If a stable laser cavity is employed, the signature can be regarded as essentially a constant in day-to-day operation. Conversely, cavity parameters exert the greatest influence on the laser signature.

3.0 DEPENDENCE OF CO_2 LASER SIGNATURE ON DISCHARGE CURRENT AND COOLING-WATER TEMPERATURE*

The signatures of two sealed-off CO_2 lasers (Sylvania, Honeywell) were investigated as a function of cooling-water temperatures and discharge current. The signature repeats itself every half-wave length (within 5 half-wavelengths) with minor changes, and a change of discharge current (e.g., 10

*G. Schiffner and C. J. Peruso, NASA Goddard Space Flight Center

to 15 ma) has a relatively large effect as compared with a change in cooling-water temperature (e.g., 5°C to 20°C).

3.1 GENERAL DISCUSSION

When the mirror spacing of a CO_2 laser is changed gradually over a range of 5.3 microns (a half-wavelength), a certain sequence of transitions comes into oscillation. The sequence depends critically on the mirror separation and other parameters and is more or less unique for each laser; it is therefore called the signature of the laser.* The output power of the laser as a function of the mirror spacing shows peaks when one of the resonance frequencies of the cavity coincides with the center frequency of one of the CO_2 laser transitions. The power profile as a function of mirror spacing is also called "signature."

Succeeding paragraphs discuss oscilloscope photographs of signatures obtained with two, stable, sealed-off, CO_2 lasers manufactured by Sylvania and Honeywell. The experiments were conducted for two different currents and two different discharge-tube cooling-water temperatures.

One resonator mirror of each laser is mounted on a PZT element so that the cavity length can be changed by an applied voltage. To display the laser signature the PZT element is driven by a triangle generator and a high-voltage d-c amplifier with a frequency of about 0.2 Hz. The attenuated output beam is directed to a Philco-Ford GPC 216 gold-doped germanium detector operating at 77°K. The detector output is connected to the y-amplifier of an oscilloscope; the x-amplifier is connected to the PZT drive over a voltage divider. The laser beam is chopped with about 400 Hz to get a zero power line in the oscilloscope traces.

*H. W. Mocker "Rotational Level Competition in CO_2 Lasers," IEEE J. Quantum Electronics, Vol. QE-4, pp 769-776 (1968).

3.2 SYLVANIA LASER

The Sylvania laser* has a discharge tube with an active length of about 64 cm, the inner diameter of the tube is 7 mm, and the Brewster angle windows are made of gallium arsenide. The resonator consists of two mirrors (within 79 cm) one gold-coated and with a 3.12-m radius of curvature, and the second flat, with a transmission of 6%. The curved mirror is mounted on a ceramic PZT element that allows a travel of about 5 half-wavelengths. The PZT element is designed for a negative applied voltage; the mirror spacing is decreased with increasing voltage.

Because the laser tube has a relatively high gain, the laser sometimes oscillates on two frequencies simultaneously. Another reason for the observed competition effects is the relatively small free spectral range due to the large mirror spacing. The filling pressure of the tube is of the order of 18 torr. The resonator structure is of Invar and aluminum and is temperature-controlled.

Figure E-33 shows the signatures for 10 and 15-ma discharge currents and for 5 and 20°C cooling-water temperatures. Figure E-34 shows magnified portions of these signatures; in one photograph the transitions are labeled. The range of PZT voltages is marked on each picture. Only the P(20) transition (λ = 10.6 microns) has a complete top that is usable for line-center dither stabilization. The ordinate is not calibrated in power, but the scale is the same for Figures E-33 and E-34.

These figures reveal that the signature repeats itself every half-wavelength with minor changes. No significant difference can be seen between 5 and 20°C at 10 ma; at 20°C the signature is a little shifted and a little simplified as compared with 5°C. The latter is probably due to the reduced gain at 20°C.

---

* Final Report on Stabilized CO_2 Gas Laser, prepared by Sylvania Electronics Systems, Western Division, Mountain View, California, for Goddard Space Flight Center under Contract No. NAS5-10309 (1 December 1966 - 30 January 1968)

A change in discharge current from 10 ma to 15 ma remarkably influences the shape of the trace, especially the relationship between the amplitudes of the various transitions. (Probably a change in the rotational temperature of CO_2 molecules occurs.)

With a Coherent Radiation Laboratories (CRL) Model 201 power meter, the output power was measured for the transitions P(20), P(24), and R(18) as a function of the discharge current (see Figure E-35). The power relationships are a little different from those observed in the oscilloscope traces, probably because the gold-doped germanium detector is more sensitive for R lines than for P lines (R lines have shorter wavelengths). Another possible reason is that the curves in Figure E-35 were taken a few days after the photographs in Figures E-33 and E-34; during this time the laser may have changed its signature.

Ten days after the Figure E-33 and E-34 photographs were made, the signature of the Sylvania laser was recorded again for a 20°C cooling-water temperature (see Figure E-36). The shape of the trace has changed significantly (i.e., is more complicated), but the P(20) transition is again the line with the best top. In Figure E-36 the ordinate is calibrated in power; the factor is 215 mw/cm for P920). The two upper photographs were made with 10 and 15-ma discharge currents, respectively; the two pictures on the bottom represent magnified portions of the upper ones.

It is not clear what caused the difference in signature between Figure E-36 and Figures E-33/E-34. The Figures E-33/E-34 photographs were made after the laser had been running for about 6 hours; those of Figure E-36 were made after an operating period of only 1 hour. In both cases the laser was already stable. In former experiments it was observed that the signature of this laser simplifies after several hours of running time.

3.3 HONEYWELL LASER*

The discharge tube of this laser has an active length of 32.5 cm and the ID is 1 cm. One mirror (4-m radius of curvature) is attached directly

*H. W. Mocker "A 10.6 μm Optical Heterodyne Communication System," Applied Optics, Vol. 8, pp 677-684 (1969).

to the tube; the other end of the tube is sealed by means of a salt Brewster angle window. The filling pressure is 18.5 torr and the laser has a modulator compartment. The second resonator mirror is flat and has 15 ± 2% transmission; the mirror spacing is 54 cm. The resonator structure is of quartz and is not temperature-controlled.

Without an element in the modulator compartment, the laser oscillated simultaneously on several transverse modes and on several transitions. The signature was photographed (see Figure E-37, left upper picture) and was irregular in shape. The travel of the PZT element for a zero to -2000 volt sweep signal is less than a half-wavelength. The element increases the resonator length when a negative voltage is applied.

Subsequently, a 6-mm-diameter aperture was mounted in the modulator compartment; it improved the shape of the signature considerably. In Figure E-37, the upper right and the lower picture were taken 3 hours and 30 min. apart; in both the P(20) transition produces a useful top. (Zero voltage on the PZT element corresponds to the left edge of the pictures; the ordinate is not calibrated.)

Figure E-38 shows the signature for 5 and 20°C water temperatures and 14 and 18 ma discharge currents after the 6-mm-diameter aperture was removed and mounted again. The left edges correspond to -2000 volts at the PZT element, and the zero-voltage point is on the right side. The ordinate is calibrated; for the P(20) transition the factor is 400 mw/cm, and for 9.6-micron transitions is 72 mw/cm. This difference is due to the characteristic of the GPC 216 Ge:Au detector.

Figure E-38 shows that an increase in current and a decrease in temperature produce a shift of the trace to the right; the shape of the signature is not changed significantly. Many of the lines have a complete top. Among the P-transitions, P(20) has the highest output power.

Figure E-39 plots output power as a function of discharge current for P(20), P(24), and R(22). For these measurements the laser was tuned to give maximum power at these transitions and the CRL Model 201 power meter was used. These curves look completely different from Figure E-35; the cause is unknown.

3.4 CONCLUSIONS

Experiments with the Sylvania laser show that the signature repeats itself with minor changes over at least 5 half-wavelengths and that only the P(20) transition has a complete top usable for line-center dither stabilization. A change in cooling-water temperature from 5°C to 20°C has a small effect as compared with a change in discharge current from 10 ma to 15 ma. Strong competition effects occur, probably because of the relatively high gain of the tube, due to the low output coupling (6%) and to the large mirror separation (small free spectral range).

Experiments with the Honeywell laser indicate that the signature will be disturbed if transverse modes of higher order occur. A change in discharge current from 14 ma to 18 ma and a change in cooling-water temperature from 5°C to 20°C produce only a shift of the signature, but no significant change in shape. Many transitions show a complete top when an aperture is used to suppress higher-order transverse modes.

4.0 SIGNATURE MEASUREMENTS*

Figure E-40 presents a sequence of pictures of signatures taken so that each picture overlaps a small region of the previous one. The six views represent 3 half-wavelengths of travel. Figure E-41 depicts the various peaks that were identified. The P(18) line is the broadest one and hardly changes from half-wavelength to half-wavelength, while most other peaks change in that interval.

---

* A. Waksbey, RCA Victor Company Research Laboratories, Montreal, Quebec, Canada

5.0 COMPUTER CALCULATIONS OF CO_2 LASER SIGNATURES*

5.1 GENERAL DISCUSSION

For heterodyne communication systems, single-frequency CO_2 lasers should have some capability for tuning over the width of the transition and for line-center dither stabilization. Because of the many laser lines in the active medium, competition effects occur that may restrict the tuning range of a particular line or even may prevent a particular line from oscillating. One solution is the use of an element in the resonator cavity, such as a grating, to select a particular line. This method works well but has the disadvantage of introducing additional losses that reduce laser efficiency.

When the laser resonator is tuned over 5.3 microns (a half-wavelength), a certain sequence of lines appears in the beam. This sequence and the distribution of lines over the tuning range depend critically on gross resonator length and constitute a property, more or less unique for each laser, called signature.**

An attempt is made below to calculate the signature of a laser for a given range of cavity lengths, with the aim of finding a signature that includes a particular line separated clearly from adjacent lines and is uncritical with respect to a gross cavity-length change in this regard.

5.2 THEORY

The resonance condition for a Fabry-Perot resonator with unlimited wide plane mirrors is given by

$$d = q \frac{\lambda}{2} \tag{1}$$

where d is the optical-path length between the mirrors, q is a positive integer, and λ is the wavelength. For an actual laser resonator with

---

* G. Schiffner, NASA Goddard Space Flight Center

**H. W. Mocker, "Rotational Level Competition in CO_2 Lasers," IEEE J. Quantum Electronics, Vol. QE-4, pp. 769-776 (1968)

spherical mirrors,*

$$d = \frac{\lambda}{2}\left[q + 1 + \frac{1}{\pi}(m + n + 1)\arccos\sqrt{\left(1 - \frac{d}{R_1}\right)\left(1 - \frac{d}{R_2}\right)}\right] \qquad (2)$$

where q, m, and n are the longitudinal and transverse mode numbers (positive integers), and R_1 and R_2 are the radii of curvature of the mirrors. The q in Equation (1) is not identical to the q in Equation (2). For the TEM_{∞} mode, which is used in the most cases, m = n = 0.

Equation (1) is used for the computer programs described below because the difference between Equations (1) and (2) in the cavity length d is less than 1 wavelength for a particular transition and comparable values of q. In the most cases it is not possible to measure the cavity length to that accuracy, and one has the advantage that the computation does not require the radii of curvature of the cavity mirrors as an input. Because it is the aim of this investigation to calculate the signature, the difference in cavity lengths for resonance for various laser transitions should be obtained with high accuracy. In this respect Equation (1) is as accurate as Equation (2), because the expression within the brackets in Equation (2) can be assumed as constant for a change in d of the order of a few microns.

Signature calculations require accurate data for the wavelengths of the centers of the laser transitions; if such data are not available, at least the wavelength differences between various lines should be known with high precision. A reasonable value for the accuracy required in cavity-length differences (for resonance) for the lines seems to be 0.1 micron. This is about one-fiftieth of the free spectral range; with this value and with $d \doteq 50$ cm, the accuracy of the wavelength differences must be better than 2.1×10^{-6} micron, or 1.9×10^{-4} cm^{-1} (for $\lambda = 10.6$ microns). The accuracy

*H. Kogelnik and T. Li, "Laser Beams and Resonators," Applied Optics, Vol. 5, pp 1550 - 1567 (Oct. 1966).

of the available values published in the open literature* is assumed to be about 4.5×10^{-4} microns or 0.04 cm^{-1} (i.e., the normalized accuracy is 4.2×10^{-5}). This is about 200 times worse than required.

McCubbin** has published calculated numbers. He claims that the accuracy should be better than 0.005 cm^{-1}. A comparison with more accurate data discussed below shows that this is in general true, but in one case P(32) an error of 0.006 cm^{-1} occurred. With the latter value, the accuracy in terms of wavelengths is 6.8×10^{-5} micron and the normalized accuracy is 6.4×10^{-6}. Table E-1 lists his data in terms of wavenumbers, $\nu = 1/\lambda$.

The data published in two papers (Bridges and Chang***and Evenson, et al****) were used to further improve the accuracy of the laser wavelengths. Bridges and Chang measured beat frequencies between signals obtained from line-center-stabilized CO_2 lasers with an accuracy of better than 1 MHz. By taking, for example, the frequency of the P(20) line from Patel (op. cit.) and by adding and/or subtracting the measured beat frequencies***, values for the laser lines of the 10.6 micron P branch can be obtained that have good accuracy relative to each other. Only for adjacent lines is the accuracy of the frequency difference better than 1 MHz. Between P(16) and P(20) or P(20) and P(24), for example, the accuracy will only be better than

* C.K.N. Patel, "Continuous Wave Laser Action on Vibrational-Rotational Transitions of CO_2," Phys. Rev., Vol. 136, pp A1187-A1193 (1964); N. N. Sobolev and V. V. Sokovikov, "CO_2 Lasers," Soviet Physics, Vol. 10, pp 153-170 (1967).

** T. K. McCubbin, Jr., Research in the Field of High Resolution Infrared Spectroscopy, Report No. AFCRL-67-0437 (AD-659-042, N67-40361), Department of Physics, The Pennsylvania State University, prepared for Air Force Cambridge Research Laboratories, 31 January 1967.

*** T. J. Bridges and T. Y. Chang, "Accurate Rotational Constants of CO_2 from measurements of CW Beats in Bulk GaAs Between Vibrational-Rotational Laser Lines," Phys. Rev. Letters, Vol. 22, pp 811-814 (1969).

**** K. M. Evenson, J. S. Wells, and L. M. Matarrese, "Absolute Frequency Measurements of the CO_2 CW Laser," Applied Phys. Letters, Vol. 16, pp 251-253 (1970).

2 MHz and between P(14) and P(26) it will only be better than 6 MHz. In terms of wavelengths, 1 MHz corresponds to an accuracy of 3.7×10^{-7} micron. This is about 5 times better than required and 6 MHz is only a little worse than required. Because lines P(16) to P(24) have the highest gain, they are of most interest for signature calculation; fortunately, their wavelengths can be obtained with sufficient accuracy. The accuracy of the P(20) line wavelength that was used to start the calculation is not so important for determination of wavelength differences, and the value given by Patel is sufficiently accurate.

Unfortunately, no beat-frequency measurements were performed for P and R transitions or for 10.6-micron and 9.4-micron bands. Meaningful signature calculations are only possible for sets connected by accurate beat-frequency measurements.

Evenson, et al.* recently accomplished absolute frequency measurements of the P(18) and P(20) lines in the 10.6-micron band with an accuracy of 25 MHz. These data were combined with those given by Bridges and Chang. The results are shown in Table E2 and represent values that are probably the most accurate known at present. For the conversion of frequencies to wavenumbers and wavelengths, $c = 2{:}997926\ 10^{10}$ cm/s was used for the speed of light.

5.3 COMPUTER PROGRAMS

Several versions of computer programs were tried. In each case a starting resonator length was assumed, and for this length the initial q-values were calculated** by Equation (1) for all given transitions. The resulting q-values are not integers, but are changed to integers by the program and are then used to calculate the cavity lengths.

The program organizes the data in such a way that the smallest cavity length is selected at first and is printed out together with some other data. The q-value belonging to this transition is then increased by unity

* Op. Cit.

**B. G. Walker, private communication

and the corresponding cavity length is calculated. The program again searches among the various cavity lengths for the smallest one, etc.

Table E-3 presents values obtained with the foregoing program. For a starting length of about 500 mm, it includes cavity lengths, q-values, and transitions. The wavenumbers of the transitions P(16) to P(24), as given in Table E-2 were used as input.

Another version of the program was tried. Its printout was divided in portions between P(20) resonances, because the P(20) transitions are best visible in actual oscilloscope traces of signatures. In addition, the relative positions of resonances of various lines between two resonances of the P(20) transition were calculated and displayed. The relative position of the resonance of a particular line is characterized by the variable D, which is defined as follows:

$$D = \frac{2}{\lambda_1}(d_2 - d_1) \qquad (3)$$

where d_1 is a cavity length for which the resonance condition for P(20) is fulfilled, λ_1 is the wavelength of the P(20) transition, and d_2 is the cavity length associated with the resonance of the transition. In the program, it holds that $0 \leq (d_2-d_1) \leq \lambda_1/2$, and d therefore varies between 0 and 1.

Table E-4 presents a program listing, and FORTRAN IV program. Table E-5 provides explanations and additional information. Table E-6 presents a sample printout, containing (from left to right) the cavity lengths for resonance, the values of q, the wavenumbers and the names of the transitions, the variable D, and a display of the signature. The display starts always with P(20), for which D = 0, and shows the positions of the resonance within one half-wavelength interval according to the values of D. The display field contains 51 elements; a letter printed in the first element corresponds to D = 0, and a letter printed in the 51st element corresponds to D = 1.

The program in Table E-4 prints all signatures between a given starting cavity length and a terminating cavity length if the variable

LC = 0. For LC ≠ 0 (e.g., LC = 1), the signatures listed are those that contain a sequence of transitions (counted with increasing cavity length) corresponding to the sequence of transitions of the input cards. Therefore, with LC = 1, the program searches a certain range of cavity lengths for a certain sequence of transitions in the signature.

Table E-7 presents another version of a computer program. That program searches through a given range of cavity length; if the sequence of transitions in the signature changes, the cavity length and the new sequence are printed out. Table E-8 presents a sample of the printout. This program provides for the printing of a list for the whole range of cavity lengths normally used to build stable lasers. Such a list is helpful, for example, in determining the cavity length of a laser (to about 0.1 mm) when only the sequence of transitions in the signature and a coarse value for the cavity length are known. In addition, if a laser is to be designed for operation at a certain line, the list can be used to determine which lines are next to this line in the signature at various cavity lengths.

Figure E-42 presents a sample display of a result for this program. The width of the cavity-length regions in which the P(20), P(26), P(24), P(18), and P(22) sequence is present is plotted against the cavity length for the region from d = 700 mm to d = 800 mm.

It is planned to use an improved computer program to search in the signature for resonator spacings in which a certain transition is free on both sides by more than a certain frequency (e.g., 50 MHz). Because the free spectral range of the laser resonator decreases with increasing cavity length, good separation between resonance is likelier at short resonator lengths than at long ones.

5.4 . COMPARISON OF COMPUTED WITH EXPERIMENTALLY DETERMINED SIGNATURES

Difficulties occur when an attempt is made to compare a calculated with an experimentally determined signature. It is sometimes not easy to determine cavity length to an accuracy of a few tenths of a millimeter. The optical path length of the Brewster windows has to be considered, and the mirror spacing must be measured accurately. In addition, the direction of movement of some PZT elements is not known.

Figure E-43 presents a drawing of the signature of a CO_2 laser that has 41-cm mirror spacing (courtesy of RCA Victor Company, Research Laboratories, Montreal); the distance between the mirrors increases to the right. The discharge tube is sealed with two salt Brewster windows, each 3 mm thick; their index of refraction is n = 1.49. The optical path length of the cavity is therefore 420.77 mm. The calculated signature shown in Figure E-43 coincides well with the observed signature for a cavity length of 421.42 mm. An error of 0.65 mm is likely to occur in the course of cavity-length determination.

A second comparison was performed with the signature of a Honeywell laser having a 350-mm-long cavity. If its PZT element is assumed to increase the cavity length with increasing negative voltage, good coincidence can be found (as in Figure E-43) for a length of 350.2 mm. Other experiments seem to indicate that the PZT element is moving in the opposite direction with negative voltage. No coincidence was found for this reversed sequence. Further work is necessary to determine in which direction the PZT element is moving.

5.5 CONCLUSIONS

It has been shown that, for the dominant CO_2 laser transitions (10.6-micron lines), data are available that should be accurate enough to permit signature prediction. Accurate data are lacking for 10.6-micron R lines and 9.4-micron lines, and these lines cannot yet be included in the calculation. Computer calculations show that the signature repeats itself with minor changes over many half-wavelength intervals. Comparison between an observed and a calculated signature shows good coincidence, but more comparisons are required. With the computer programs described above, a given range of cavity lengths can be searched to find a length for which a certain transition is clearly separated from adjacent ones. Such cavity lengths exist, but improved programs might make the search more systematic and reduce the printout. Further experimental effort will be necessary to determine if a CO_2 laser designed according to the results of one of these computer programs works as expected.

TABLE E-1

VACUUM WAVENUMBERS OF CO_2 TRANSITIONS

	$00^0 1 - 10^0 0$ Band		$00^0 1 - 02^0 0$ Band	
j	P(j)	R(j)	P(j)	R(j)
8	954.545	967.707	1057.294	1070.456
10	52.878	69.138	55.608	71.877
12	51.191	70.545	53.917	73.271
14	49.477	71.927	52.188	74.639
16	47.738	73.284	50.434	75.980
18	45.976	74.617	48.653	77.294
20	44.191	75.926	46.846	78.581
22	42.381	77.210	45.013	79.842
24	40.546	78.469	43.154	81.077
26	38.687	79.703	41.269	82.285
28	36.804	80.912	39.359	83.467
30	34.898	82.097	37.423	84.622
32	32.967	83.268	35.462	85.752

As calculated and reported by T. K. McCubbin , Jr. in Research in the Field of High Resolution Infrared Spectroscopy, Report No. AFCRL-67-0437 (AD-659-042, N67-40361), Department of Physics, The Pennsylvania State University, prepared for Air Force Cambridge Research Laboratories, 31 January 1967.

TABLE E-2

FREQUENCIES, WAVENUMBERS, AND WAVELENGTHS
FOR
10.6 MICRON P-TRANSITIONS CALCULATED
FROM
FREQUENCY AND BEAT-FREQUENCY MEASUREMENTS *

$C^{12}O^{16}_2$ LASER TRANSITIONS

	f(mHz)	$\nu(cm^{-1})$	λ(microns)
P(12)	28. 516 052	951. 192 67	10. 513 117
P(14)	28. 464 700	949. 479 73	10. 532 084
P(16)	28. 412 616	947. 742 40	10. 551 390
P(18)	28. 359 800	945. 980 64	10. 571 041
P(20)	28. 306 251	944. 194 47	10. 591 039
P(22)	28. 251 967	942. 383 74	10. 611 389
P(24)	28. 196 948	940. 548 50	10. 632 094
P(26)	28. 141 191	938. 688 66	10. 653 160
P(28)	28. 084 695	936. 804 15	10. 674 590
P(30)	28. 027 457	934. 894 90	10. 696 389
P(32)	27. 969 475	932. 960 83	10. 718 564

Accuracy absolute: $\pm$25 mHz, 8.8×10^{-7}, $\Delta\nu = 8.34 \times 10^{-4}$ cm^{-1}; $\Delta\lambda = 9.3 \times 10^{-6}$ micron

Accuracy relative: $\pm$1 mHz, 3.5×10^{-8}, $\Delta\nu = 3.3 \times 10^{-5}$ cm^{-1}; $\Delta\lambda = 3.7 \times 10^{-7}$ micron
(between adjacent lines)

*Sources:

K. M. Evenson, J. S. Wells, and L. M. Matarrese, "Absolute Frequency Measurements of the CO_2 CW Laser," Appl. Phys. Letters, Vol. 16, pp. 251-253, (1970).

T. J. Bridges and T. Y. Chang, "Accurate Rotational Constants of $C^{12}O^{16}_2$ from Measurements of CW Beats in Bulk GaAs Between Vibrational-Rotational Laser Lines," Phys. Rev. Letters, Vol. 22, p. 811-814 (1969).

TABLE E-3

SAMPLE PRINTOUT OF A SIGNATURE COMPUTER PROGRAM*

Cavity Length, mm	q	Transition
500.000 796	94055	P(24)
:002 930	94420	P(20)
.003 322	94239	P(22)
.004 011	94775	P(16)
.004 947	94599	P(18)
.006 113	94056	P(24)
.008 226	94421	P(20)
.008 628	94240	P(22)
.009 287	94776	P(16)
.010 232	94600	P(18)
.011 429	94057	P(24)
.013 521	94422	P(20)

* Wavenumbers of transitions taken from Table E-2.

TABLE E-4

FORTRAN IV COMPUTER PROGRAM LISTING FOR CALCULATION AND DISPLAY OF SIGNATURE

```
C
C
C       SIGNATURE PROGRAM -- PRINTOUT OF SIGNATURE
C
C       IF LC = 1  A PRINTOUT IS OBTAINED ONLY FOR A SEQUENCE EQUAL TO
C       THE SEQUENCE OF THE INPUT CARDS
C
        DIMENSION LQ(15),NN(16),NAME(16),IE(52)
        DOUBLE PRECISION ANU(16),PL(15),R,RM,Q
        DATA IE/52*1H /
        NE=IE(1)
4       READ(5,12)AL,BL,LC
12      FORMAT(F7.3,F8.3,4X,I1)
        IF(BL.EQ.0.0.0) GO TO 100
        WRITE(6,71)AL,BL,LC
71      FORMAT(1H1,17HSTARTING LENGTH =,F9.3,5X,20HTERMINATING LENGTH =,
       1F9.3,5X,3HLC=,I2//26X,2HNU,7X,4HNAME,10X,1HC,15X,2HLQ,10X,
       210HRES.LENGTH)
        BL=10.**BL
        RM=AL
        K=1
        LL=2
        LA=0
        LB=0
        DO 5 I=1,16
        READ(5,10) ANU(I),NAME(I),NN(I)
10      FORMAT(F12.6,2X,A1,I2)
        IF(ANU(I))6,6,99
99      ML=I
        Q=2.*AL*ANU(I)
        LQ(I)=0
        PL(I)=FLOAT(LC(I))/(2.00*ANU(I))
        WRITE(6,11)ANU(I),NAME(I),NN(I),Q,LQ(I),PL(I)
11      FORMAT(20X,F12.6,6X,A1,I2,5X,F12.3,5X,I10,5X,F12.6)
5       CONTINUE
6       WRITE(6,70)
70      FORMAT(//7X,10HRES.LENGTH,13X,1HQ,17X,2HNU,13X,12HREL.POSITION,
       -13X,1H0,8X,3H0.2,7X,3H0.4,7X,3H0.6,7X,3H0.8,7X,3H1.0//)
33      N=1
        M=2
40      IF(RL(N)-PL(M))20,20,21
20      I=(M-ML)30,31,31
30      M=M+1
        GO TO 40
21      IF(M-ML)42,41,41
42      N=M
        M=N+1
        GO TO 40
31      L=N
        GO TO 50
41      L=M
50      R=1.01*RL(L)
        LQ=0
        AB=DABS(ANU(L)-944.19400)
        IF(AB-0.1)83,84,84
83      LQ=1
```

continued

Table E-4 (Sheet 1 of 2)

TABLE E-4 (cont.)

FORTRAN IV COMPUTER PROGRAM LISTING FOR CALCULATION AND DISPLAY OF SIGNATURE

```
      RM=PL(L)
      K=L
      LB=LA
      IF(LC.EQ.0) LB=VL
      LL=0
      LA=0
84    D=PL(L)-RM
      LL=LL+1
      IF(L.EQ.LL) LA=LA+1
      D=2.*D**ANJ(K)
      PD=D*50.+1.5
      PD=ABS(PD)
      IF(PD.GE.52.) PD=52.
      ID=PD
      IF(LB.NE.ML)GO TO 56
      IS(ID)=NAME(L)
      IF(PL(L).LT.A1)GO TO 55
      IF(LD.EQ.1) WRITE(6,75)
75    FORMAT('H ')
      WRITE(6,55) J,LO(L),ANU(L),NAME(L),AA(L),J,(IF(J),J=1,51)
55.   FORMAT(5X,F14.8, 3X,I5,10X,F12.6,3X,A1,I2,5X,F9.5,3X,51A1,1H+)
56    LO(L)=LO(L)+1
      IS(ID)=NE
      PL(L)=FLOAT(LO(L))/(2.00*ANJ(L))
      IF(P-BL)33,60,60
60    CONTINUE
      GO TO 4
100   CONTINUE
      STOP
      END
```

TABLE E-5

EXPLANATIONS FOR TABLE E-4

ANU (I)	Wavenumbers of CO_2 transitions
ML	Number of wavenumbers
NAME (I)	Equal to P or R
NN (I)	Number of the transition (for example, 20 in P(20)
LQ (I), Q	Number of half-wavelengths between resonator mirrors
RL (I)	Resonator length, cm
R	Resonator length, mm
AL	Starting resonator length
BL	Terminating resonator length
IE(j)	Field of literals for displaying signature
Formula for determination of resonator length:	$RL(I) = \frac{LQ(I)}{2.0 * ANU(I)}$
Initial Q values	Q = 2.* AL * ANU(I)

TABLE E-6

SAMPLE OF PRINTOUT OBTAINED WITH COMPUTER PROGRAM LISTED IN TABLE E-4

Cavity Length mm	q	Wavenumbers
421.48271948	79581	944.194467
421.42430675	79274	940.548501
421.42511459	79732	945.980641
421.42599027	79429	942.383738
421.42780763	79891	947.742397
421.42901500	79582	944.194467
421.42962280	79275	940.548501
421.43040008	79733	945.980641
421.43129506	79430	942.383738
421.43309273	79892	947.742397
421.43331052	79583	944.194467
421.43493885	79276	940.548501
421.43568560	79734	945.980641
421.43660165	79431	942.383738
421.43835042	79893	947.742397

Names	D	DISPLAY
P20	0.0	P
P24	0.29974	P
P18	0.45228	P
P22	0.61765	P
P16	0.96073	P
P20	0.0	P
P24	0.30352	P
P18	0.45040	P
P22	0.61957	P
P16	0.95698	P
P20	0.0	P
P24	0.30749	P
P18	0.44851	P
P22	0.62150	P
P16	0.95324	P

Table E-6

TABLE E-7

FORTRAN IV COMPUTER PROGRAM LISTING FOR DETERMINATION OF SEQUENCE OF TRANSITIONS IN SIGNATURE

```
C       SIGNATURE PROGRAM - SEQUENCE AS A FUNCTION OF RESONATOR LENGTH
C
        DIMENSION LQ(15),NN(16),NAME(16),KD(15),KNAME(15),KNN(15)
        DOUBLE PRECISION ANU(16),RL(15),R
        DATA KB,NN,KNN,NAME,KNAME/15*0,16*0,15*0,16*1H ,15*1H /
        READ(5,12)AL,BL,LC
12      FORMAT(F7.3,F8.3,4X,I1)
        IF(BL.LE.0.0) GO TO 100
        WRITE(6,71)AL,BL,LC
71      FORMAT(1H1,17HSTARTING LENGTH =,F9.3,5X,20HTERMINATING LENGTH =,
       1F9.3,5X,3HLC=,I2//26X,2HNU,10X,4HNAME)
        BL=10.*BL
        LL=0
        LA=0
        LB=0
        KA=0
        LE=0
        J=1
        DO 5 I=1,16
        READ(5,10) ANU(I),NAME(I),NN(I)
10      FORMAT(F11.6,1X,A1,I2)
        IF(ANU(I))6,6,99
99      ML=I
        Q=2.*AL*ANU(I)
        LQ(I)=Q
        RL(I)=FLOAT(LQ(I))/(2.D0*ANU(I))
        WRITE(6,11)ANU(I),NAME(I),NN(I)
11      FORMAT(20X,F12.6,6X,A1,I2)
5       CONTINUE
6       WRITE(6,70)
70      FORMAT(//3X,10HRES.LENGTH,8X,8HSEQUENCE/)
33      N=1
        M=2
40      IF(RL(N)-RL(M))20,20,21
20      IF(M-ML)30,31,31
30      M=M+1
        GO TO 40
21      IF(M-ML)43,41,41
43      N=M
        M=N+1
        GO TO 40
31      L=N
        GO TO 50
41      L=M
50      R=1.D1*RL(L)
        AB=DABS(ANU(L)-944.194D0)
        IF(AB-0.1)83,84,84
83      LL=0
        KA=0
        LB=LA
        LA=0
84      CONTINUE
        IF(LB-ML)22,23,22
22      KA=KA+1
```

continued

Table E-7

TABLE E-7, (cont.)

FORTRAN IV COMPUTER PROGRAM LISTING FOR DETERMINATION OF SEQUENCE OF TRANSITIONS IN SIGNATURE

```
      KB(L)=KA
      LP=1
 23   L=LL+1
      IF(KB(L).EQ.LL)LA=LA+1
      IF(LB-ML)56,25,56
 25   IF(LE.NE.1)GO TO 56
      DO 9 LZ=1,ML
      J=KB(LZ)
      KNAME(J)=NAME(LZ)
  9   KNN(J)=NN(LZ)
      R=R-0.005295519276
      WRITE(6,54)R,(KNAME(JK),KNN(JK),JK=1,15)
 54   FORMAT(3X,F10.3,3X,15(A1,I2,1X))
      LE=0
 56   LQ(L)=LQ(L)+1
      RL(L)=FLOAT(LQ(L))/(2.D0*ANU(L))
      IF(R-RL)33,60,60
 60   CONTINUE
      GO TO 4
100   CONTINUE
      STOP
      END
```

TABLE E-8

SAMPLE OF PRINTOUT OBTAINED WITH PROGRAM LISTED IN TABLE E-7

Cavity Length mm	SEQUENCE						
420.470	P20	P26	P22	P14	P24	P16	P18
420.501	P20	P26	P22	P14	P16	P24	P18
420.650	P20	P26	P22	P14	P16	P18	P24
420.665	P20	P26	P14	P22	P16	P18	P24
420.724	P20	P14	P26	P22	P16	P18	P24
420.819	P20	P14	P16	P26	P22	P18	P24
420.835	P20	P14	P16	P22	P26	P18	P24
420.988	P20	P16	P22	P26	P18	P24	P14
420.999	P20	P16	P22	P26	P18	P14	P24
421.015	P20	P24	P16	P22	P18	P26	P14
421.184	P20	P24	P16	P22	P18	P14	P26
421.200	P20	P16	P24	P18	P22	P14	P26
421.370	P20	P16	P24	P18	P14	P22	P16
421.380	P20	P26	P24	P18	P14	P22	P16
421.545	P20	P26	P24	P14	P18	P22	P16
421.560	P20	P26	P14	P24	P18	P22	P16
421.571	P20	P26	P14	P18	P24	P22	P16
421.650	P20	P14	P26	P18	P24	P22	P16
421.703	P20	P14	P18	P26	P24	P22	P16
421.751	P20	P14	P18	P26	P24	P16	P22
421.889	P20	P14	P18	P26	P16	P24	P22
421.931	P20	P18	P16	P26	P24	P22	P14
422.074	P20	P18	P16	P26	P24	P14	P22
422.085	P20	P18	P14	P24	P26	P14	P22
422.111	P20	P18	P16	P14	P24	P26	P22
422.185	P20	P18	P16	P14	P24	P22	P26
422.286	P20	P26	P18	P16	P14	P22	P24
422.387	P20	P24	P18	P26	P16	P14	P22
422.482	P20	P22	P24	P18	P16	P26	P14
422.492	P20	P22	P18	P24	P16	P26	P14
422.577	P20	P22	P18	P24	P16	P14	P26
422.588	P20	P18	P22	P16	P24	P14	P26
422.683	P20	P18	P16	P22	P14	P24	P26
422.699	P20	P16	P22	P14	P24	P26	P18
422.784	P20	P14	P22	P24	P26	P18	P16
422.879	P20	P22	P24	P26	P16	P18	P14
422.969	P20	P22	P24	P26	P16	P14	P18
423.033	P20	P22	P24	P16	P14	P26	P18
423.064	P20	P22	P24	P14	P16	P18	P26
423.191	P20	P26	P22	P24	P14	P16	P18
423.239	P20	P26	P22	P14	P24	P16	P18
423.281	P20	P26	P22	P14	P16	P24	P18
423.409	P20	P26	P22	P14	P16	P18	P24
423.483	P20	P26	P14	P22	P16	P18	P24

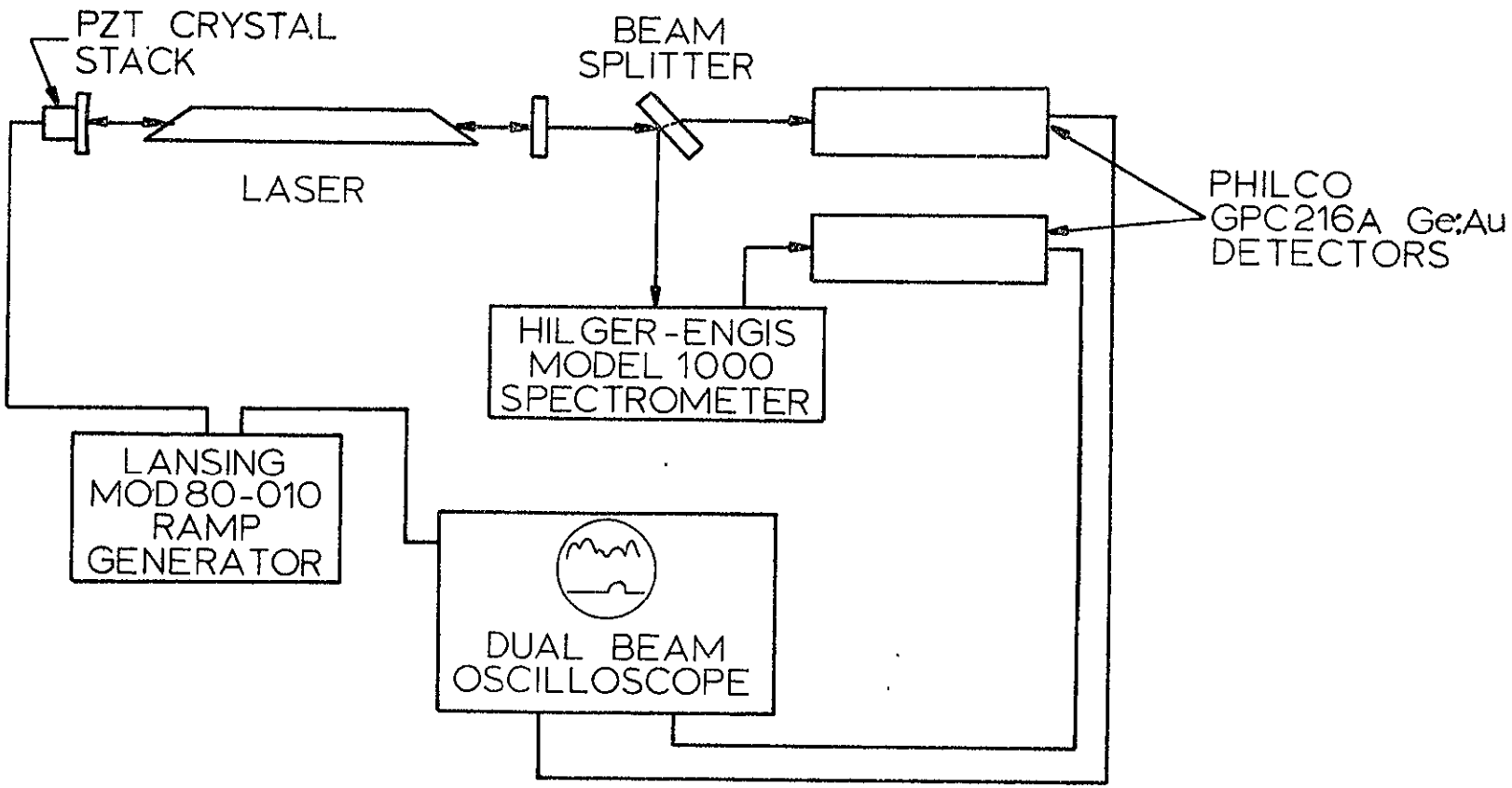

Figure E-1

Experimental Setup

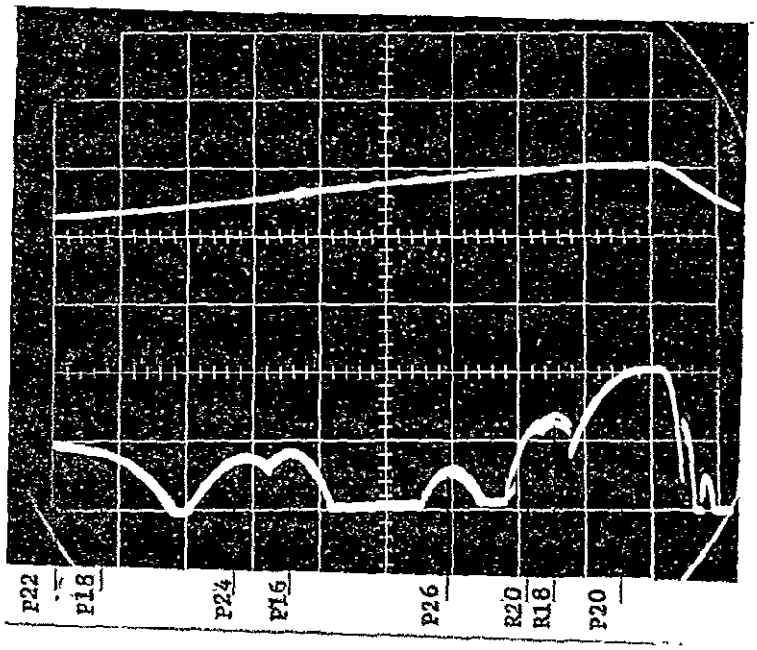

Fig. E-2. Sequence of Lines with 18-torr Pressure and 11-ma Discharge Current

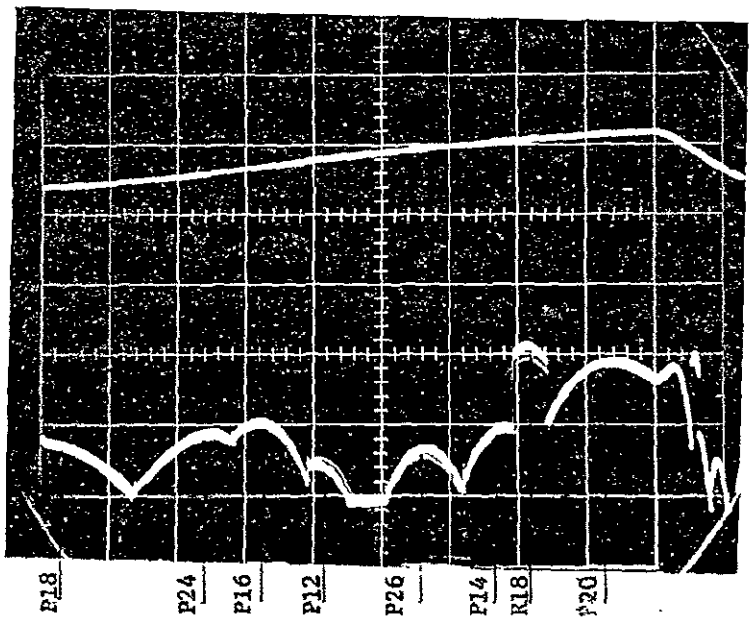

Fig. E-3. Sequence of Lines with 17-torr Pressure and 10-ma Discharge Current

Figures E-2 and E-3

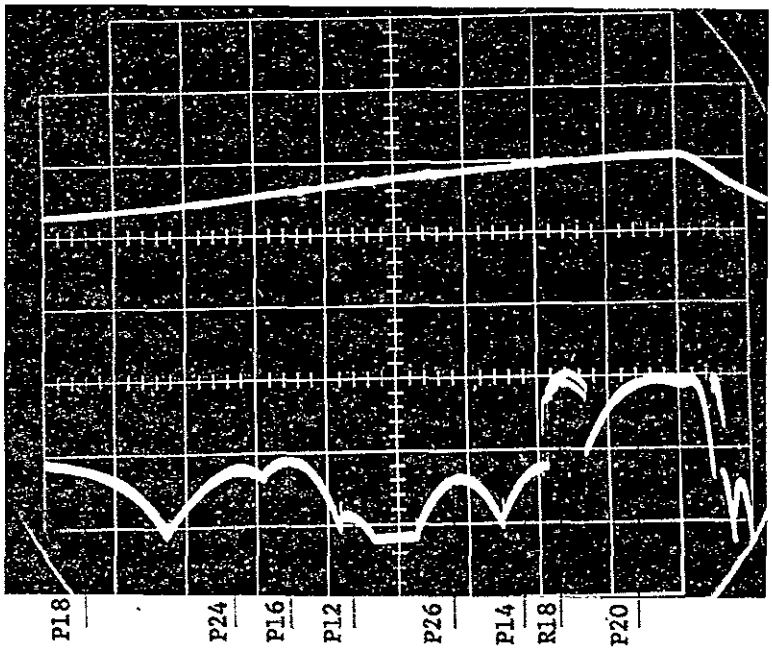

Fig. E-4. Sequence of Lines with 16-torr Pressure and 10-ma Discharge Current

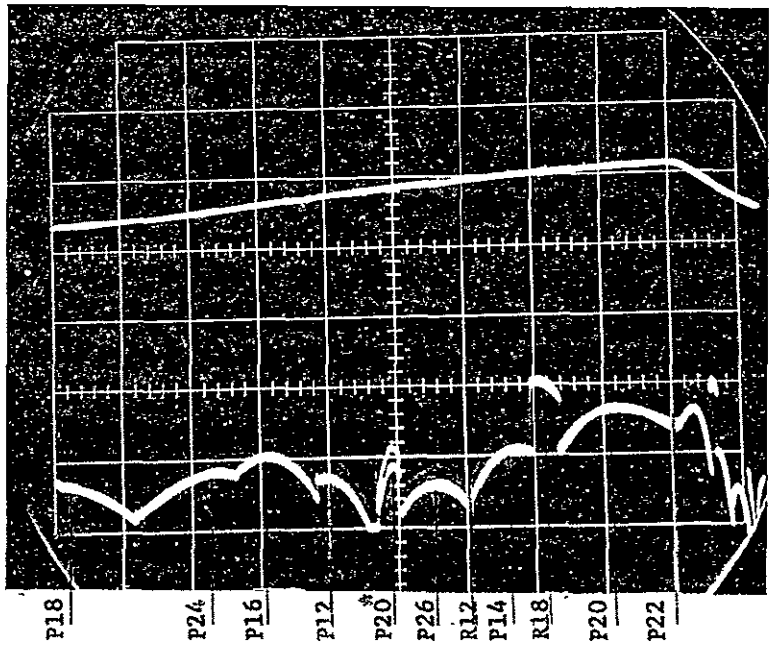

Fig. E-5. Sequence of Lines with 15-torr Pressure and 8-ma Discharge Current
* Indicates lines of the 9.4-micron band.

Figures E-4 and E-5

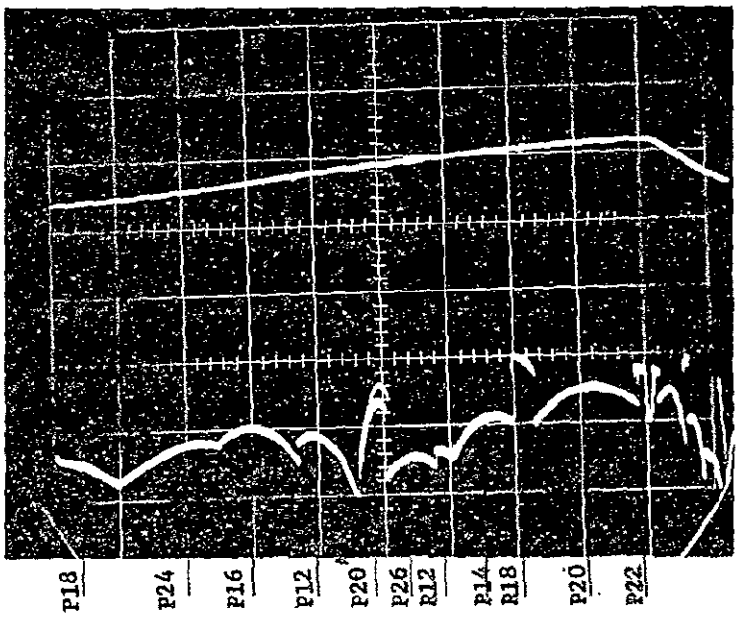

Fig. E-6. Sequence of Lines with 14-torr Pressure and 7.8-ma Discharge Current

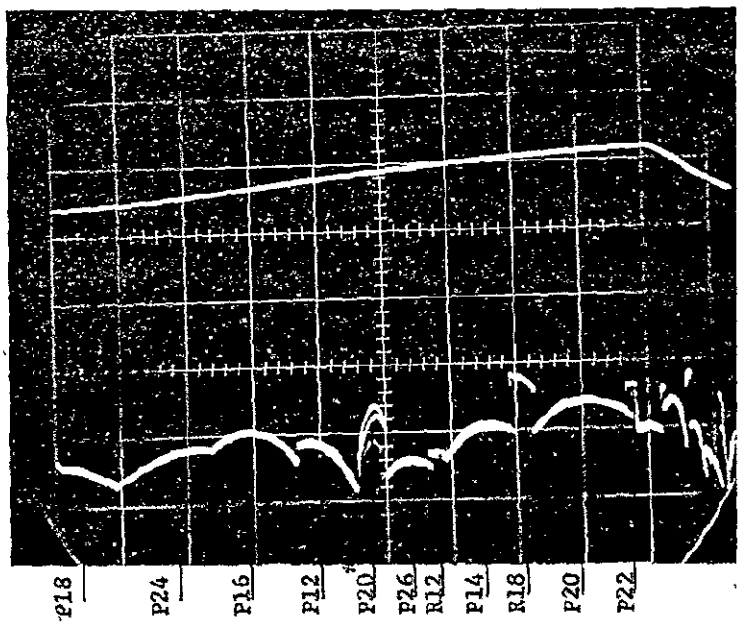

Fig. E-7. Sequence of Lines with 13-torr Pressure and 6.8-ma Discharge Current
* Indicates lines of the 9.4-micron band.

Figures E-6 and E-7

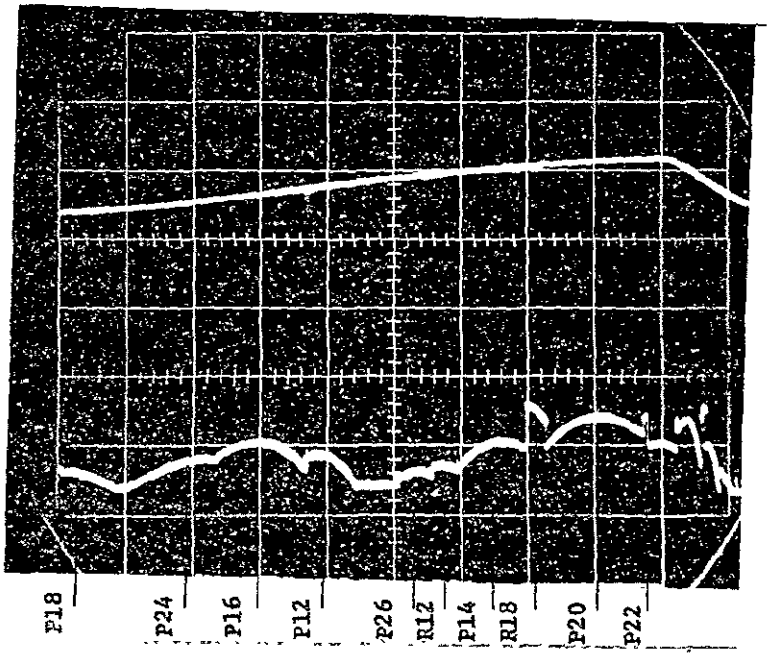

Fig. E-8. Sequence of Lines with 12-torr Pressure and 6-ma Discharge Current

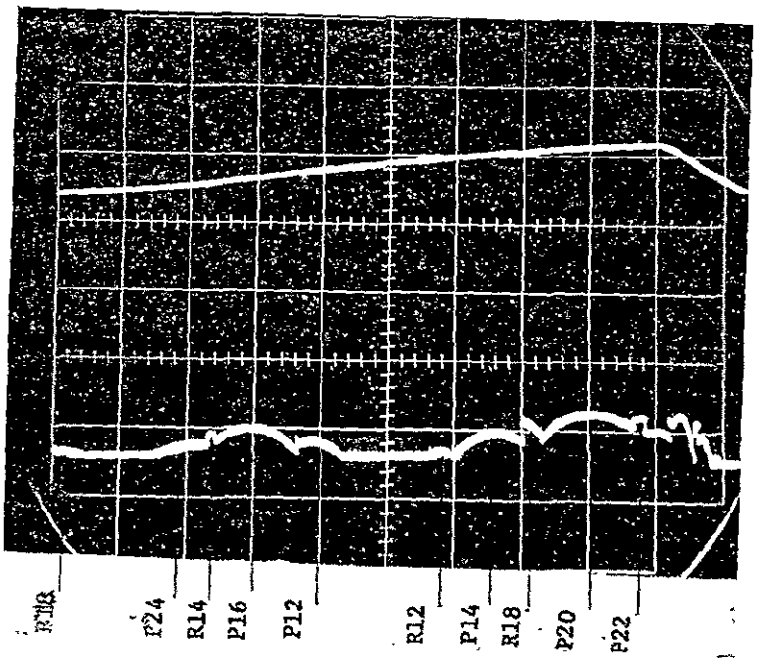

Fig. E-9. Sequence of Lines with 11-torr Pressure and 5-ma Discharge Current

Figures E-8 and E-9

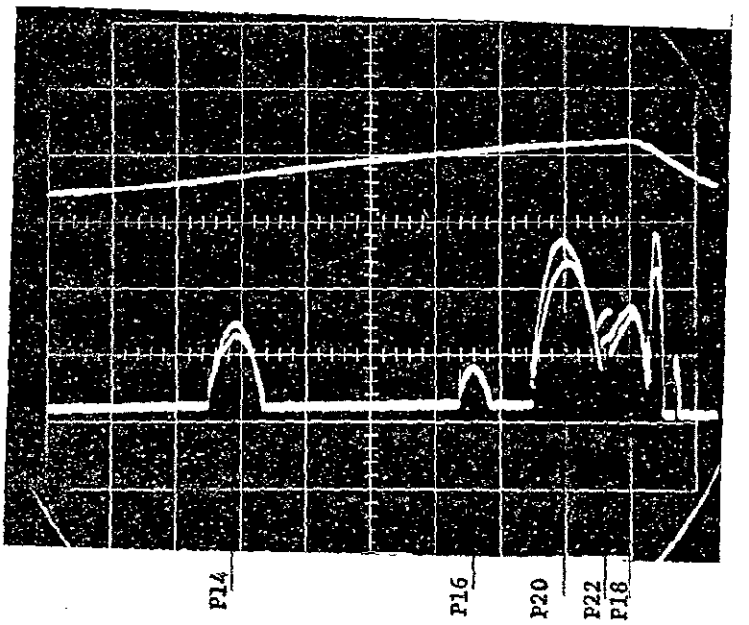

Fig. E-10. Sequence of Lines with 10-torr Pressure and 4.4-ma Discharge Current

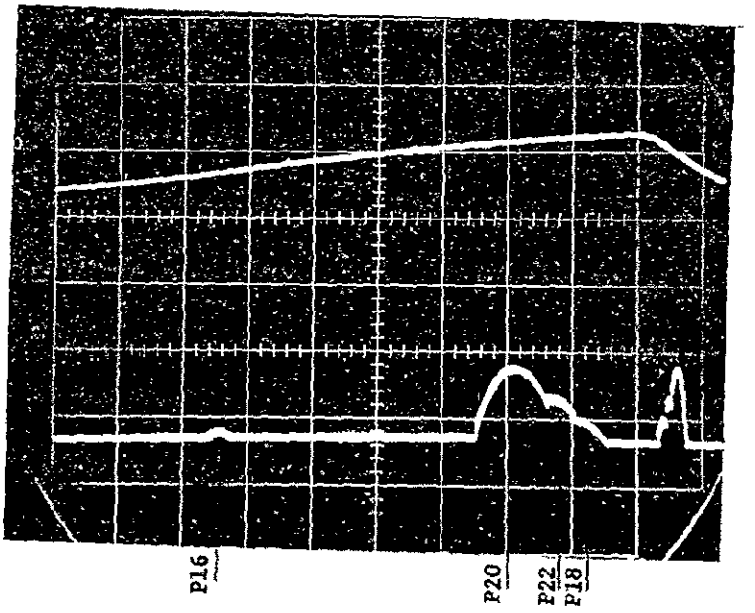

Fig. E-11. Sequence of Lines with 15-torr Pressure and 11-ma Discharge Current

Figures E-10 and E-11

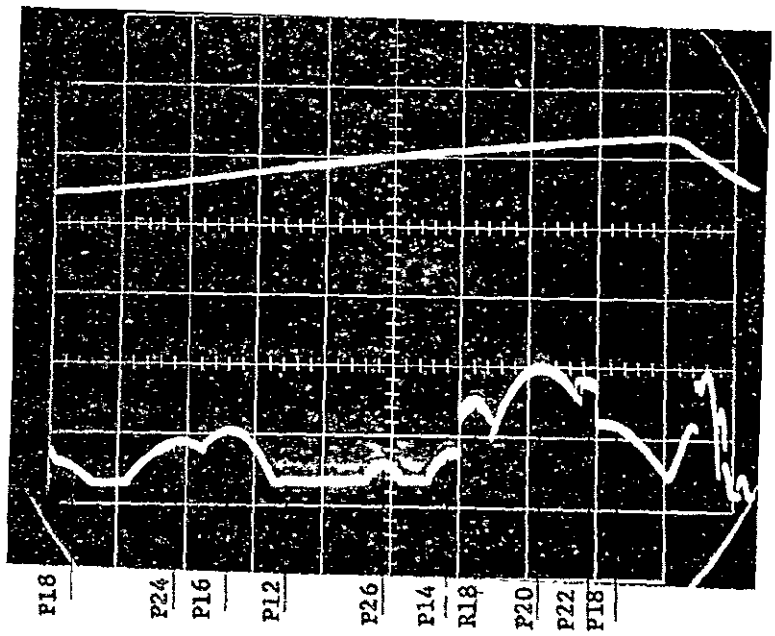

Fig. E-12. Sequence of Lines with 15-torr Pressure and 10-ma Discharge Current

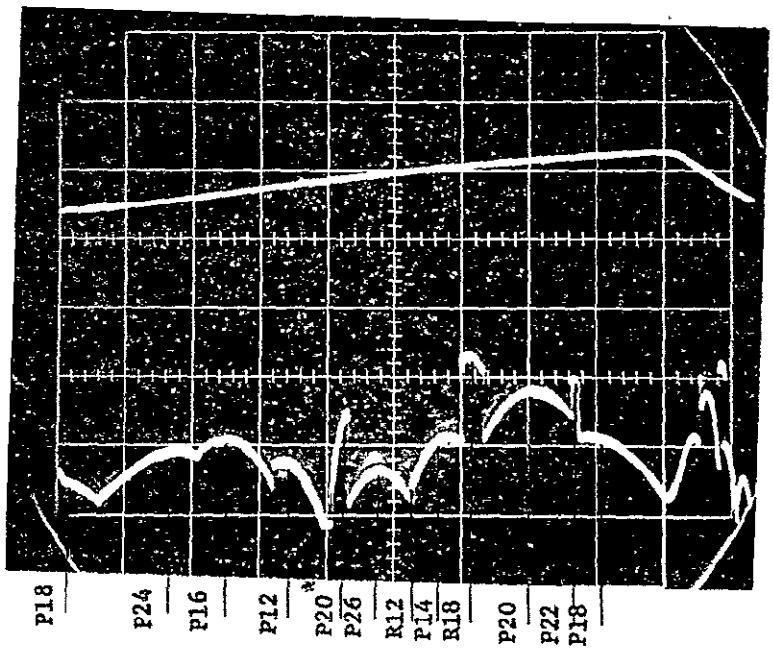

Fig. E-13. Sequence of Lines with 15-torr Pressure and 9-ma Discharge Current

* Indicates lines of the 9.4-micron band.

Figures E-12 and E-13

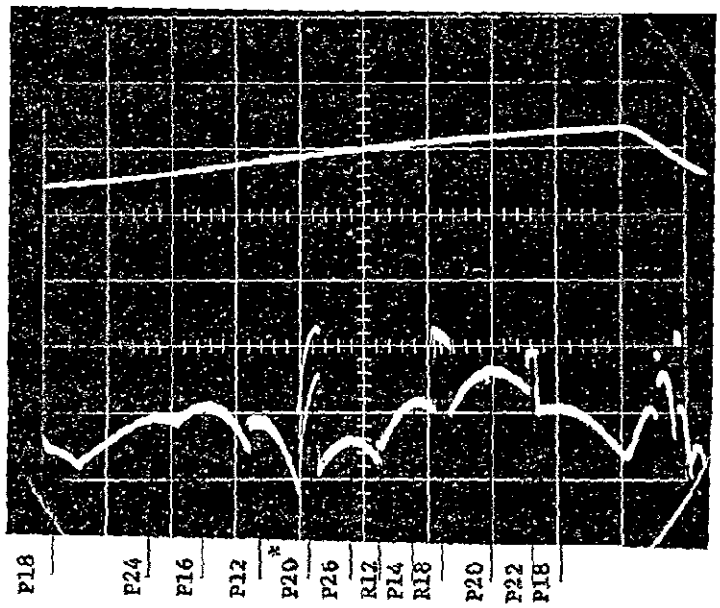

Fig. E-14. Sequence of Lines with 15-torr Pressure and 8-ma Discharge Current

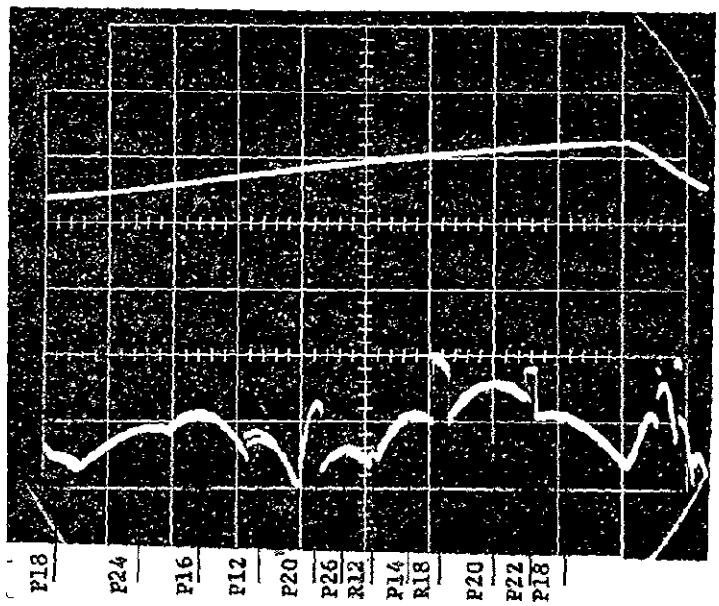

Fig. E-15. Sequence of Lines with 15-torr Pressure and 7-ma Discharge Current
* Indicates lines of the 9.4-micron band.

Figures E-14 and E-15

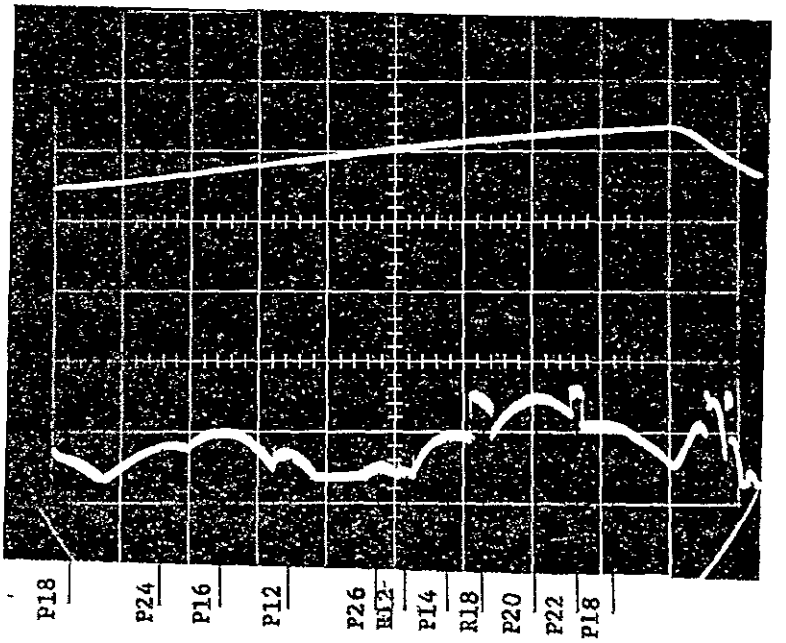

Fig. E-16. Sequence of Lines with 15-torr Pressure and 6-ma Discharge Current

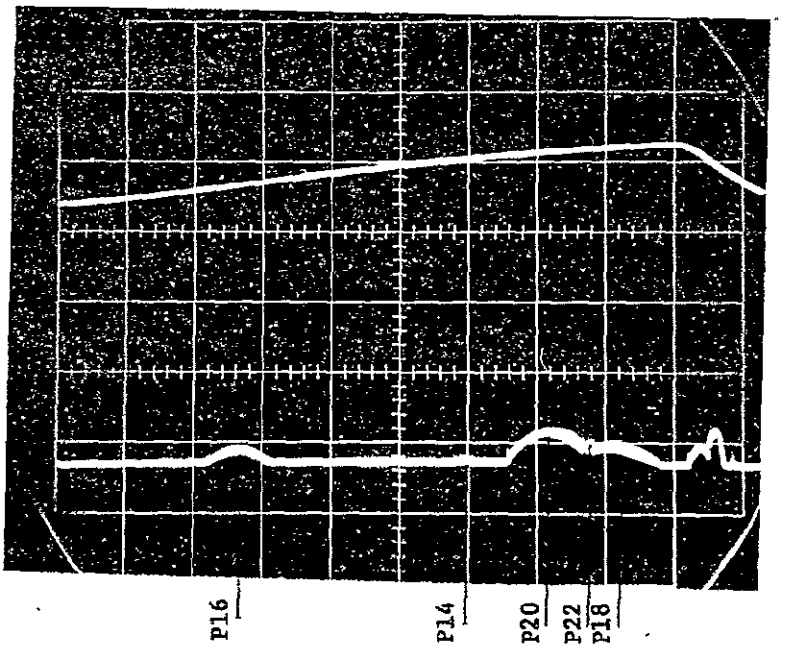

Fig. E-17. Sequence of Lines with 15-torr Pressure and 5-ma Discharge Current

Figures E-16 and E-17

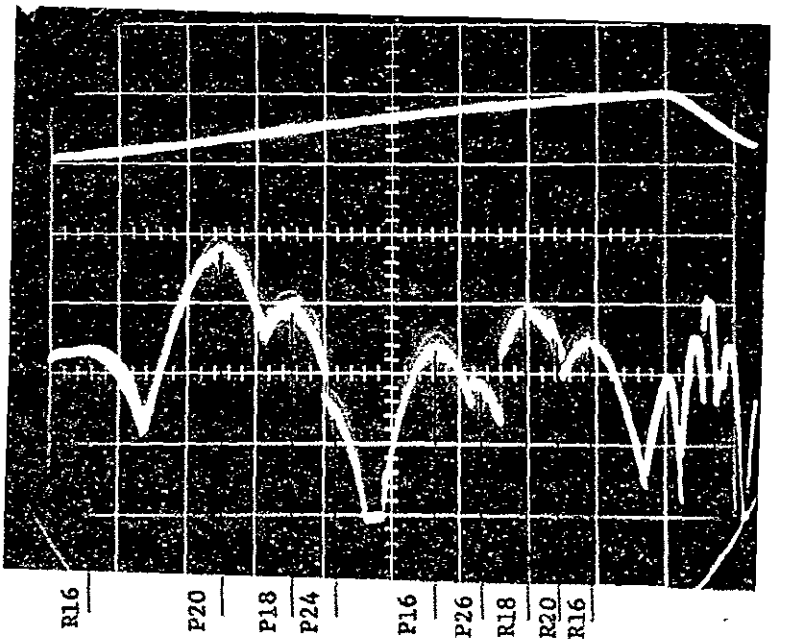

Fig. E-18. Sequence of Lines with 15-torr Pressure and 10-ma Current, Cavity Length L

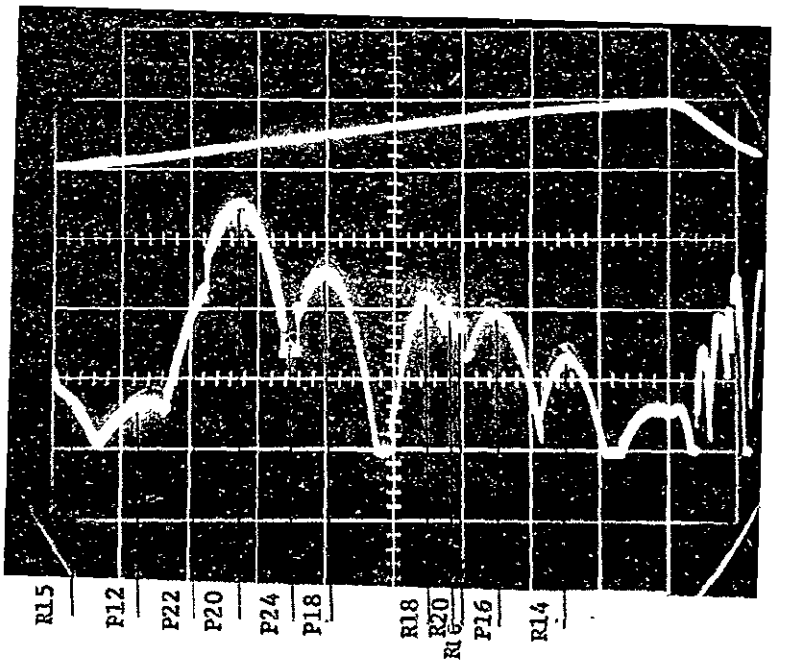

Fig. E-19. Sequence of Lines with 15-torr Pressure and 10-ma Current, Cavity Length Increased to L + 100 Microns

Figures E-18 and E-19

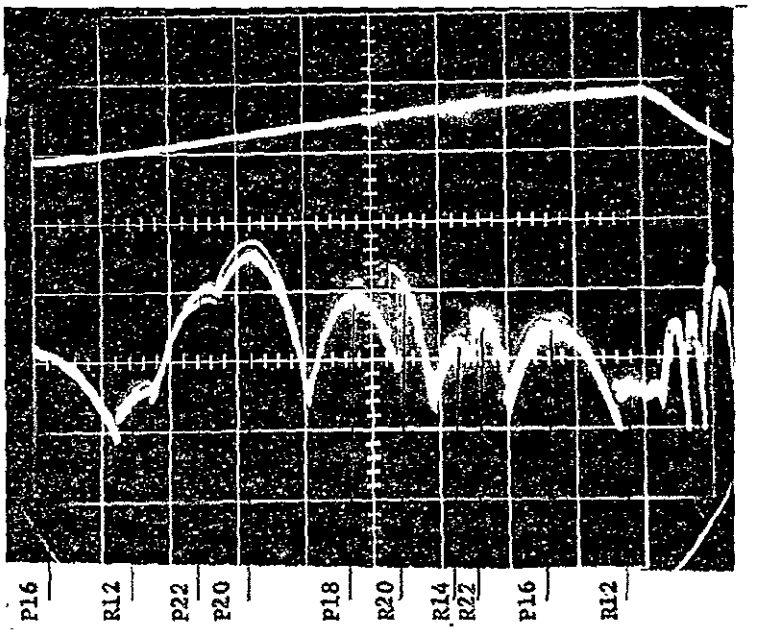

Fig. E-20. Sequence of Lines with 15-torr Pressure and 10-ma Current, Cavity Length Increased to L + 200 Microns

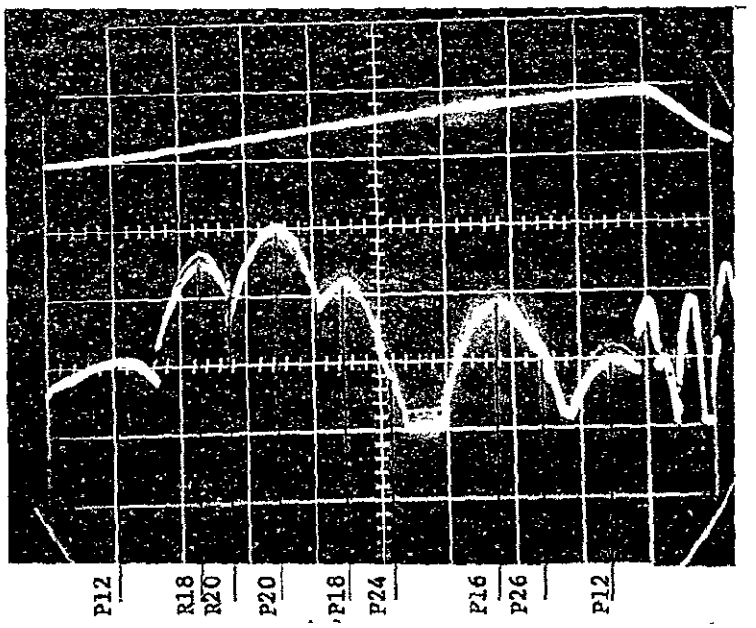

Fig. E-21. Sequence of Lines with 15-torr Pressure and 10-ma Current, Cavity Length Decreased to L

Figures E-20 and E-21

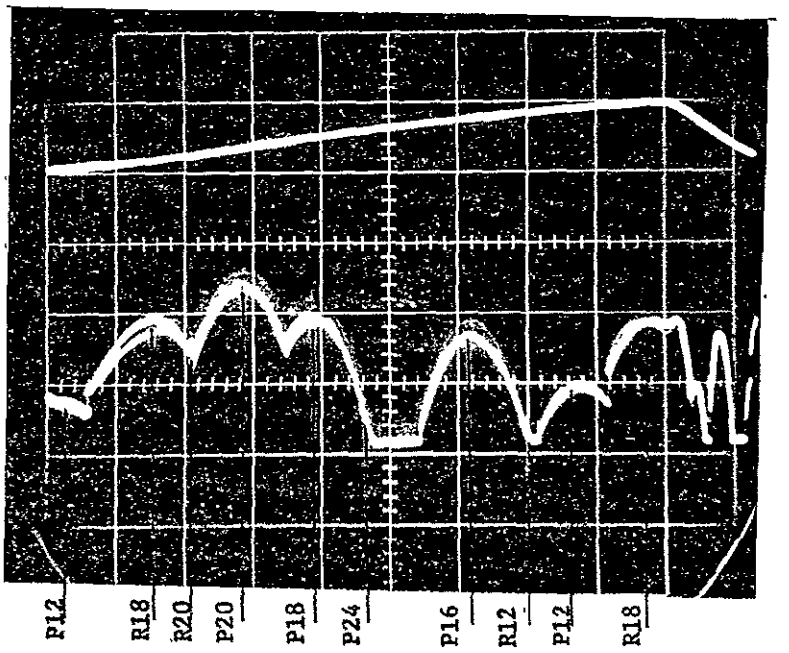

Fig. E-22. Sequence of Lines with 15-torr Pressure and 7-ma Current

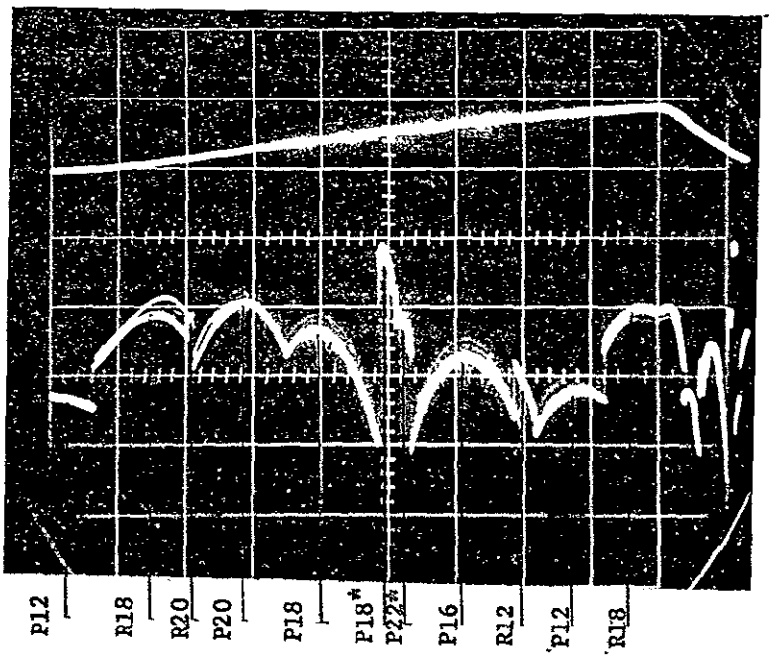

Fig. E-23. Sequence of Lines with 15-torr Pressure and 6-ma, Fresh Gas Fill
* Indicates lines of the 9.4-micron band.

Figures E-22 and E-23

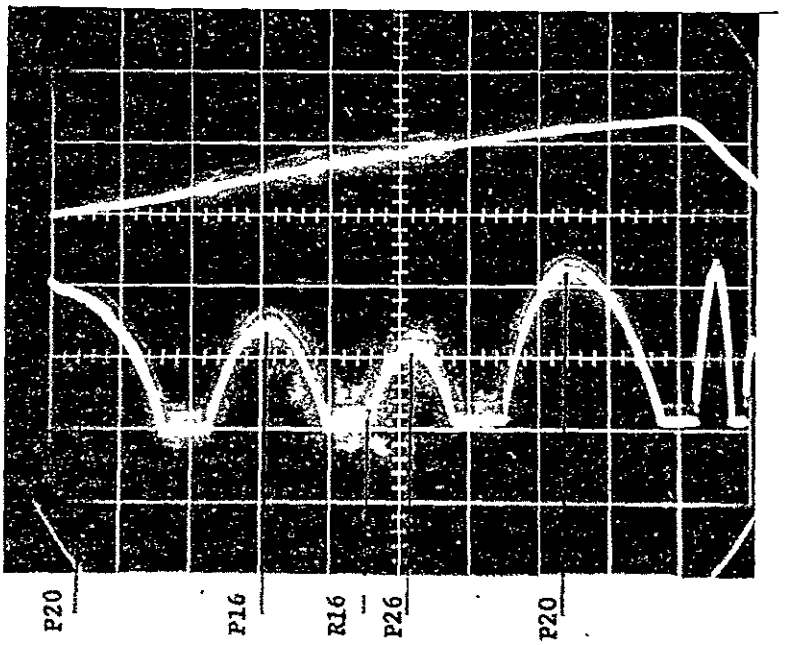

Fig. E-24. Sequence of Lines with 15-torr Pressure and 6-ma, Polished NaCl Flat in Cavity

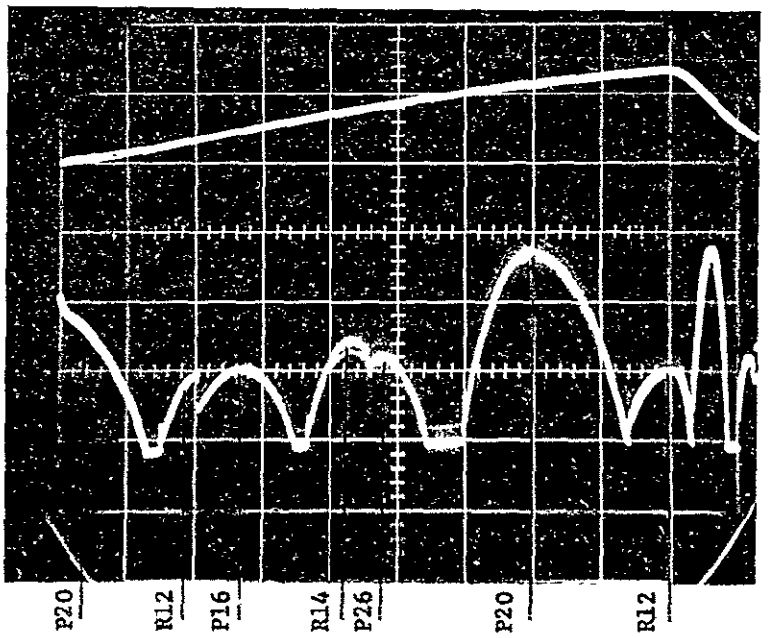

Fig. E-25. Sequence of Lines with 15-torr Pressure and 6-ma, Polished NaCl Flat in Cavity, Small Temperature Gradient in NaCl

Figures E-24 and E-25

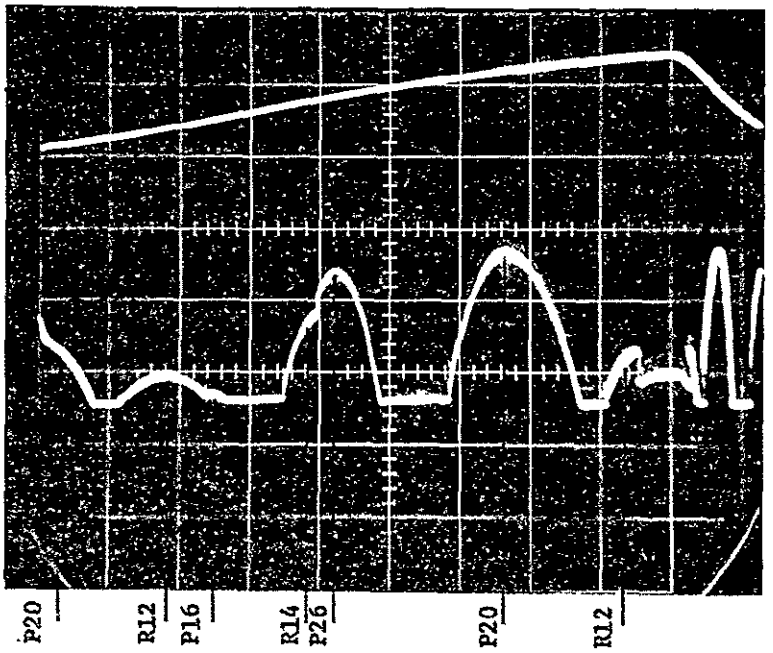

Fig. E-26. Sequence of Lines with 15-torr Pressure and 6-ma, Polished NaCl Flat in Cavity, Large Temperature Gradient in NaCl

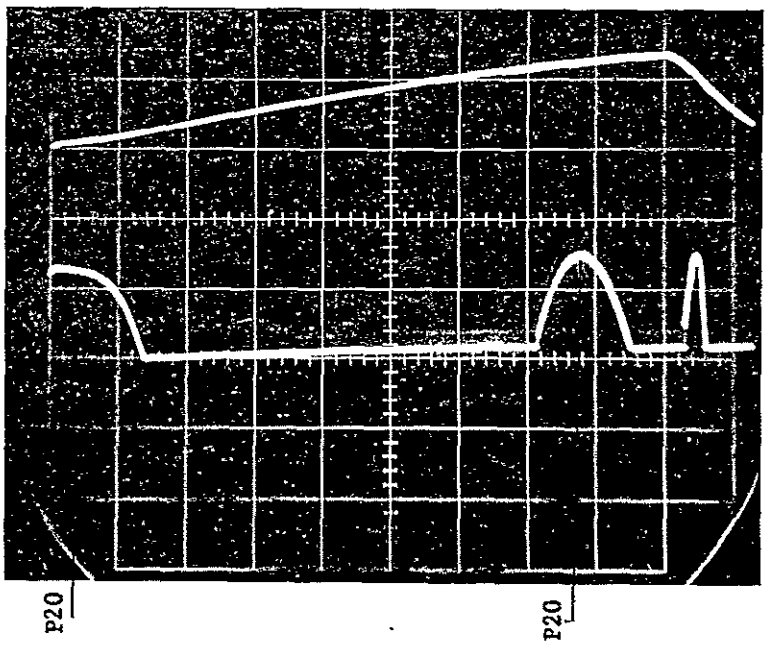

Fig. E-27. Sequence of Lines with 30-torr Pressure and 10-ma Current

Figures E-26 and E-27

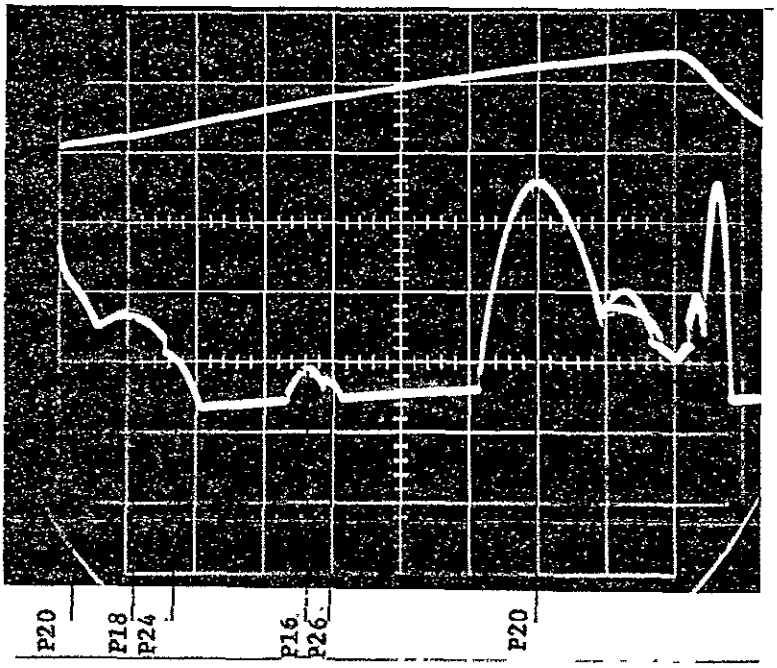

Sequence of Lines with 25-torr Pressure and 10-ma Current

Figure E-28

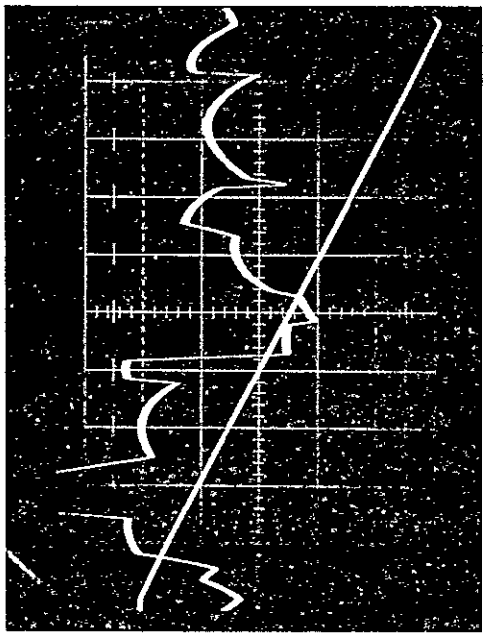

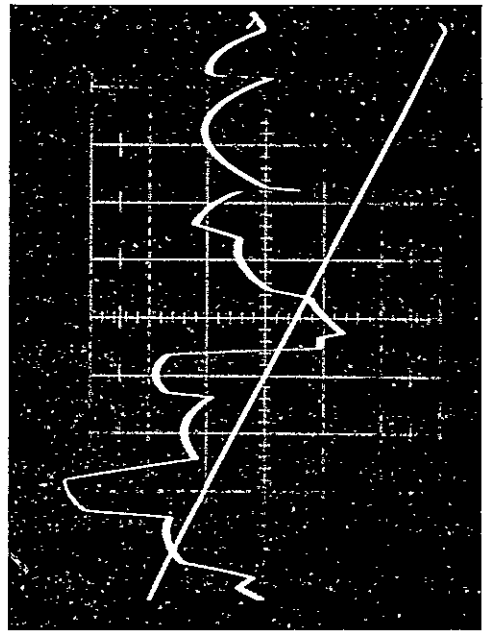

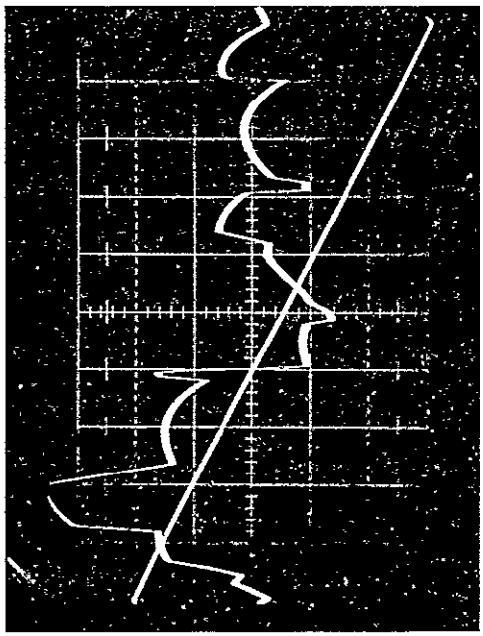

A' I=8 ma

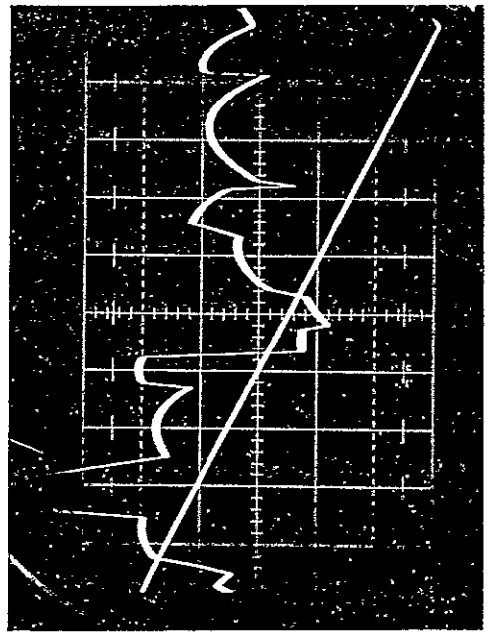

C I=10.9 ma

CO_2 Laser Signatures During Testing of Setup

Figure E-29

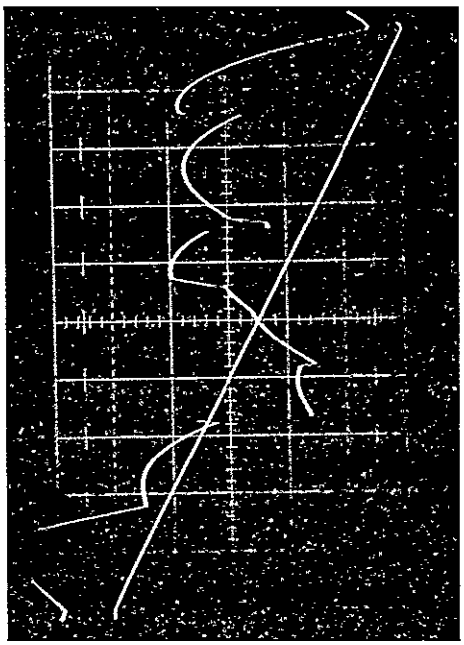

B I=7 ma

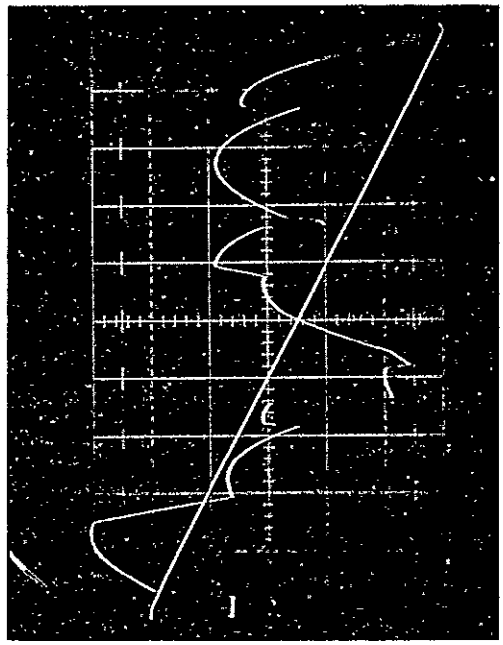

D I=9 ma

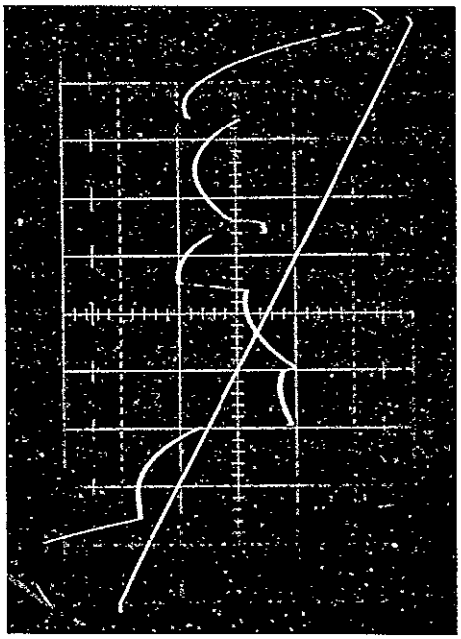

A I=6 ma

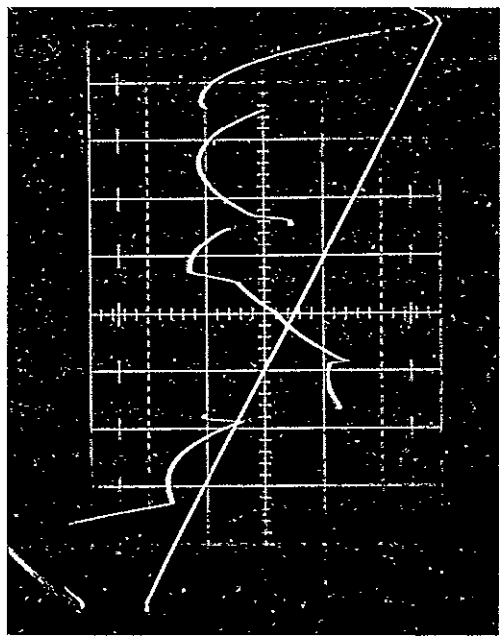

C I=8 ma

CO_2 Laser Signatures During Calibration Tests

Figure E-30

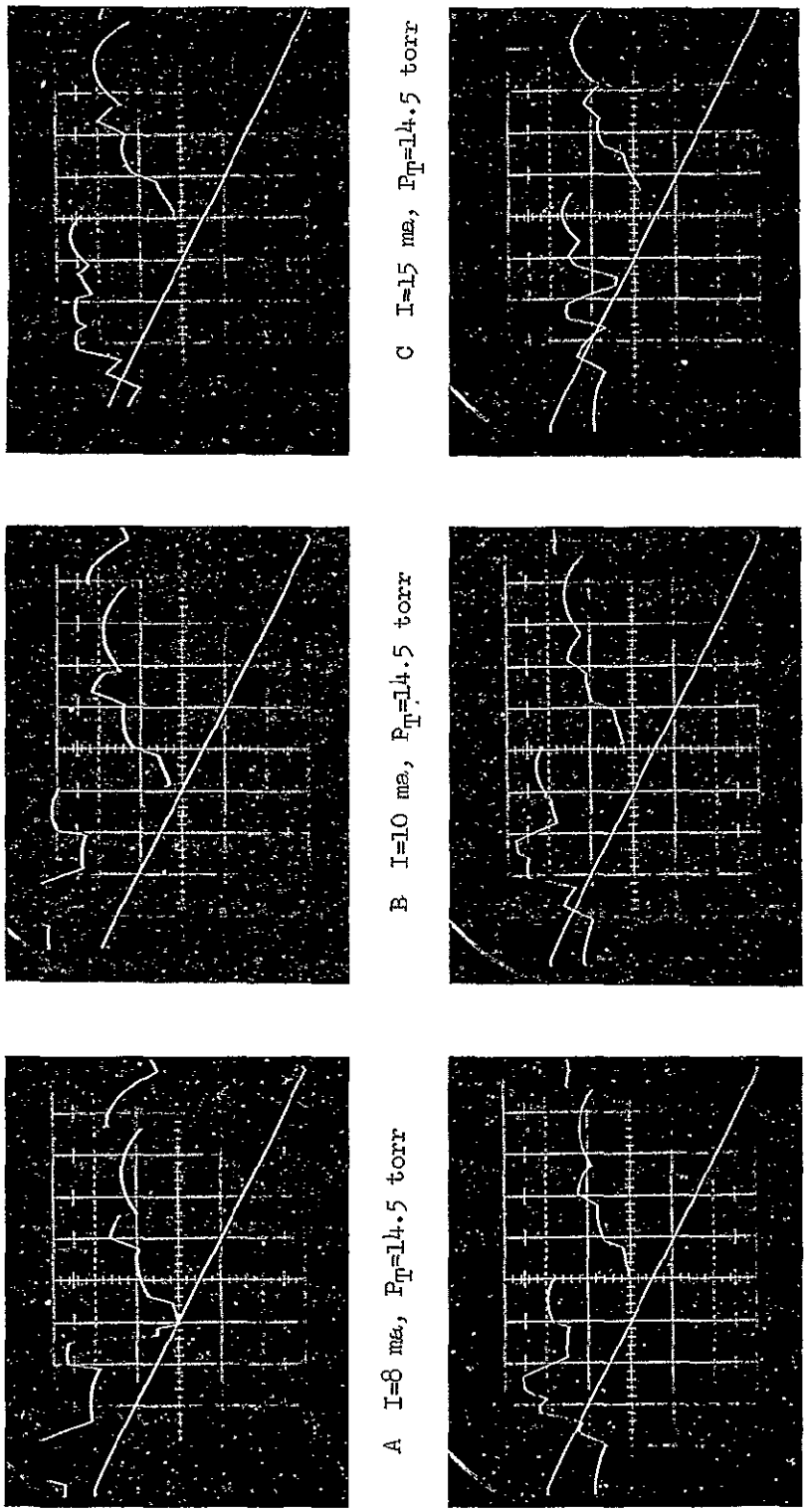

A I=8 ma, P_T=14.5 torr

B I=10 ma, P_T=14.5 torr

C I=15 ma, P_T=14.5 torr

D I=8 ma, P_T=12.3 torr

E I=10 ma, P_T=12.3 torr

F I=15 ma, P_T=12.3 torr

CO_2 Laser Signatures with Variations in Heluim Partial Pressure and Discharge Current

Figure E-31 (Sheet 1 of 3)

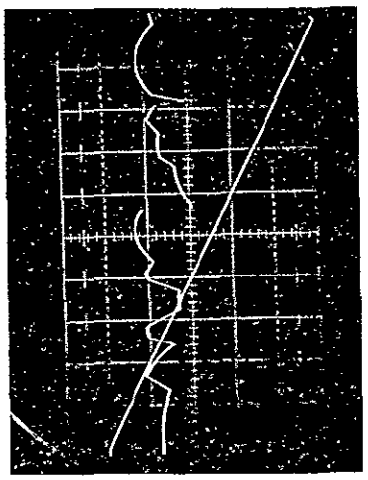

I. I = 15 ma, P_T = 11.4 Torr

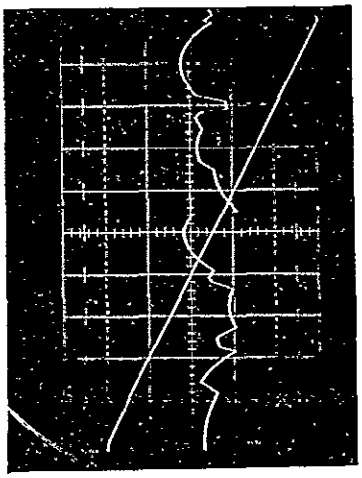

L. I = 15 ma, P_T = 10.3 Torr

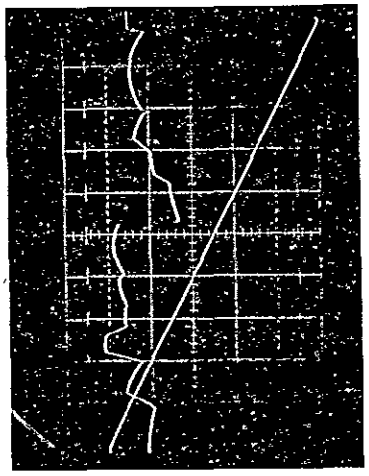

H. I = 10 ma, P_T = 11.4 Torr

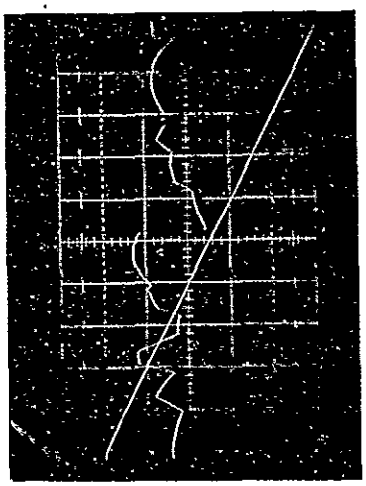

K. I = 10 ma, P_T = 10.3 Torr

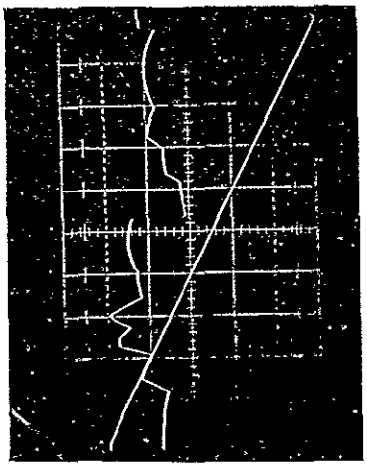

G. I = 8 ma, P_T = 11.4 Torr

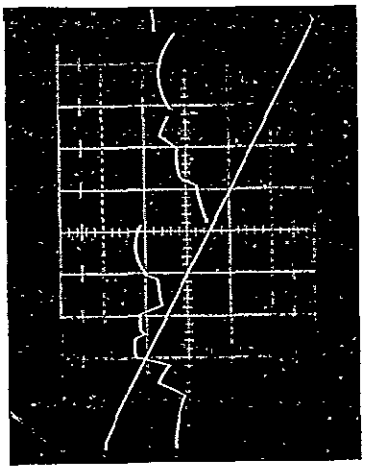

J. I = 8 ma, P_T = 10.3 Torr

FIGURE 3

Figure E-31 (Sheet 2 of 3)

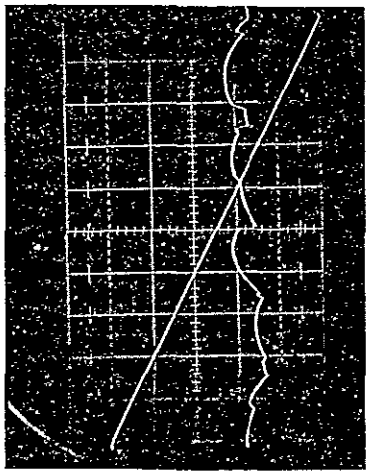

O I=13 ma, P_T=9.3 torr

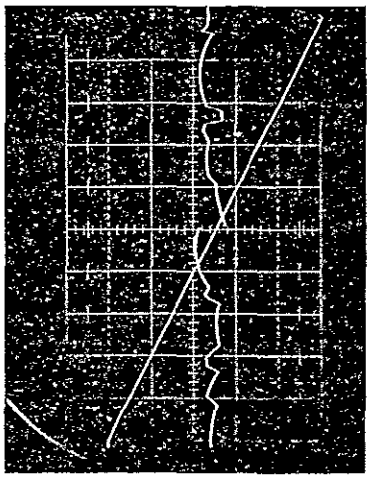

N I=10 ma, P_T=9.3 torr

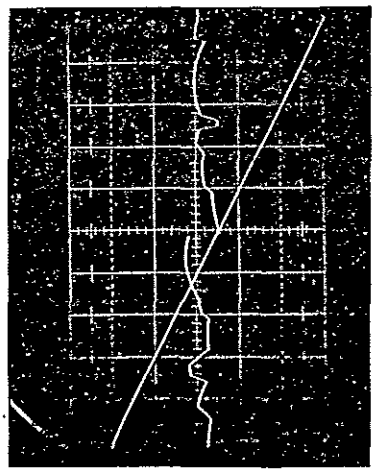

M I=8 ma, P_T=9.3 torr

Figure E-31 (Sheet 3 of 3)

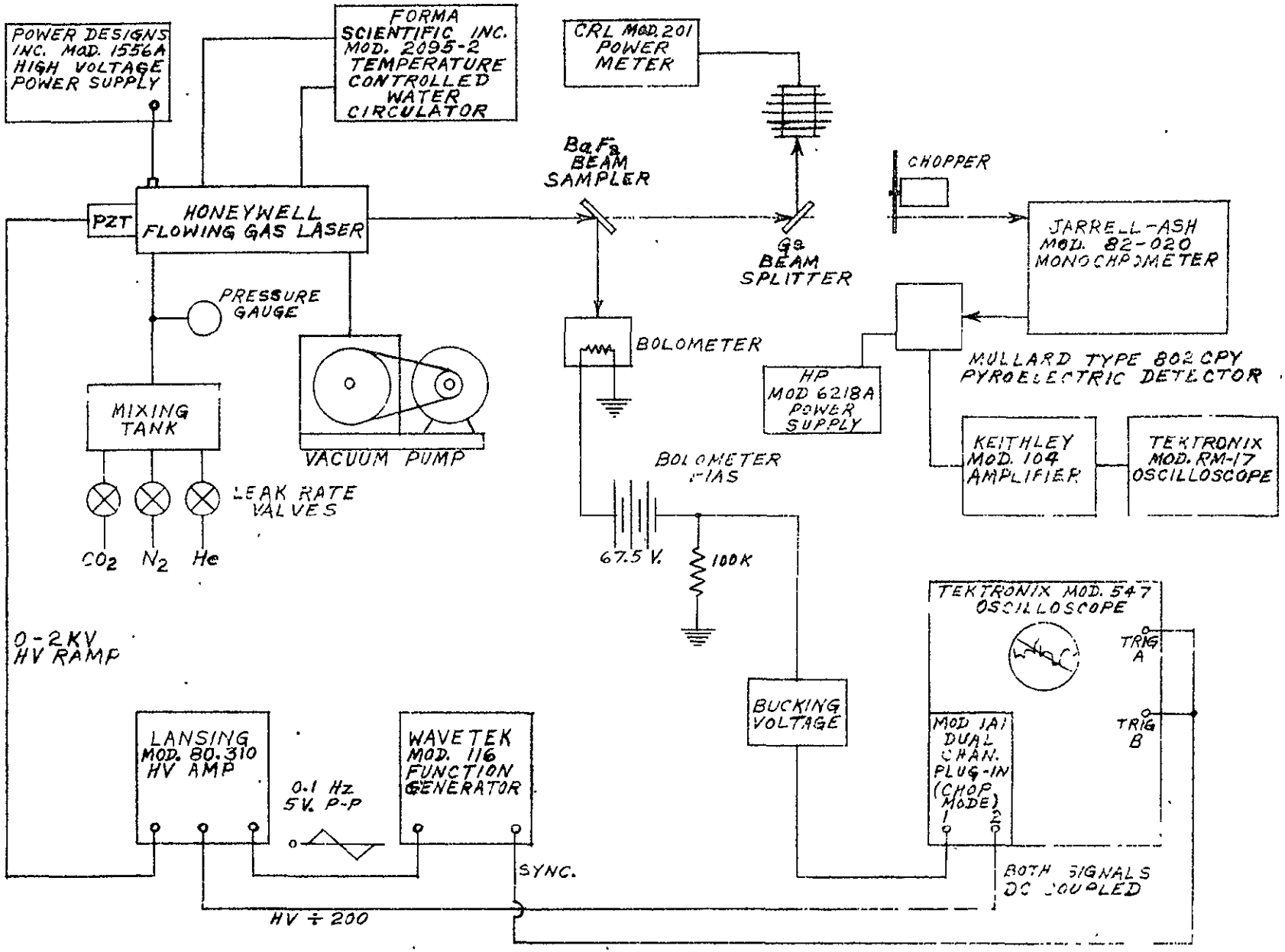

Figure E-32

Laser Signature Measurements Test Setup

SYLVANIA LASER

RESONATOR: R_1 = 3.12 m, R_2 = ∞ (6% TRANSMISSION), d = 79 cm
TUBE: ID = 7 mm, active length about 64 cm, Ga As Brewster angle windows.

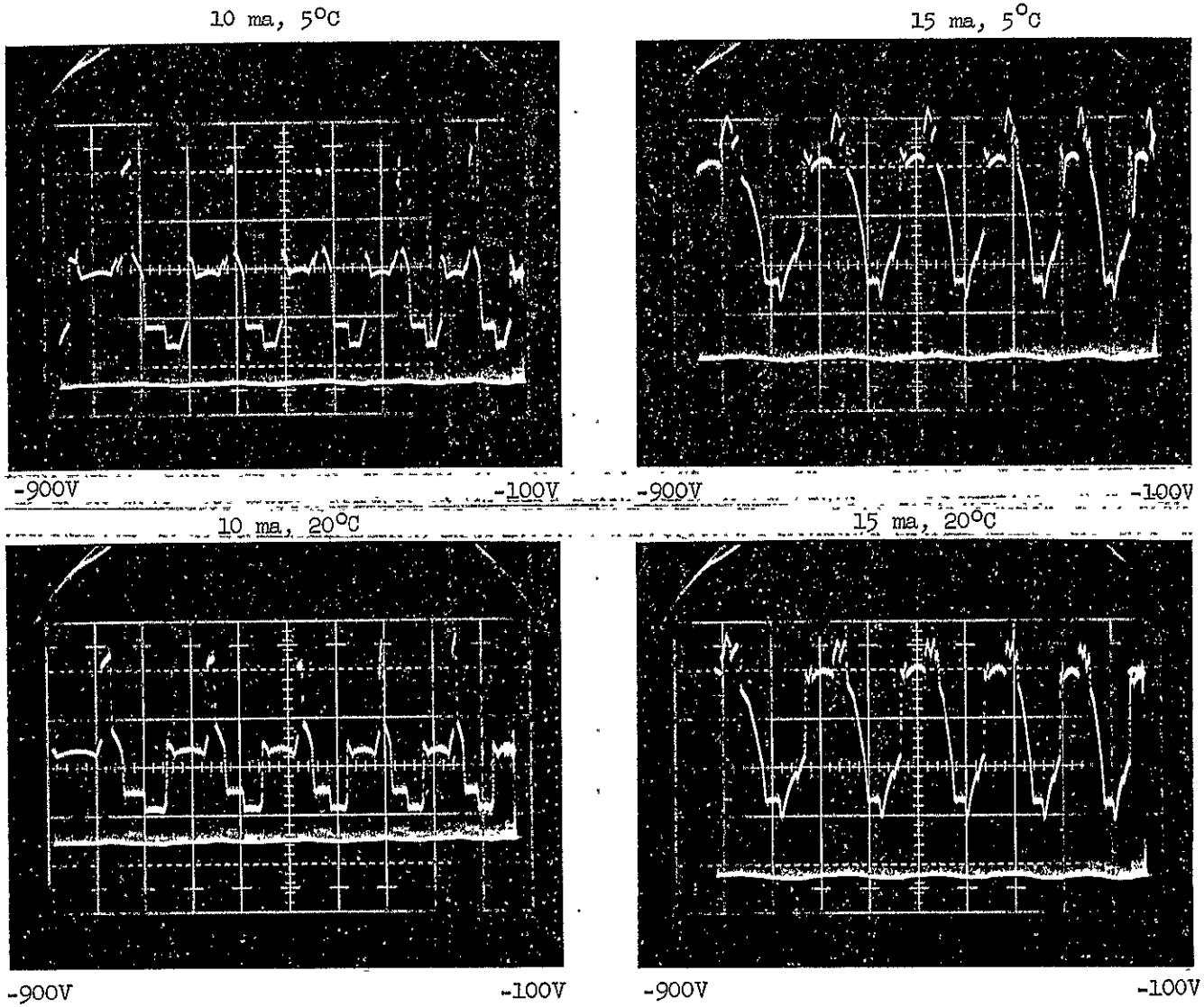

Figure E-33

Output of Sylvania Laser vs PZT Voltage (Signature) Measured with a Philco-Ford GPC 216 Ge:Au from -100V to -900V for 10 ma and 15 ma Discharge Current and for 5°C and 20°C Temperature

SYLVANIA LASER - SIGNATURE

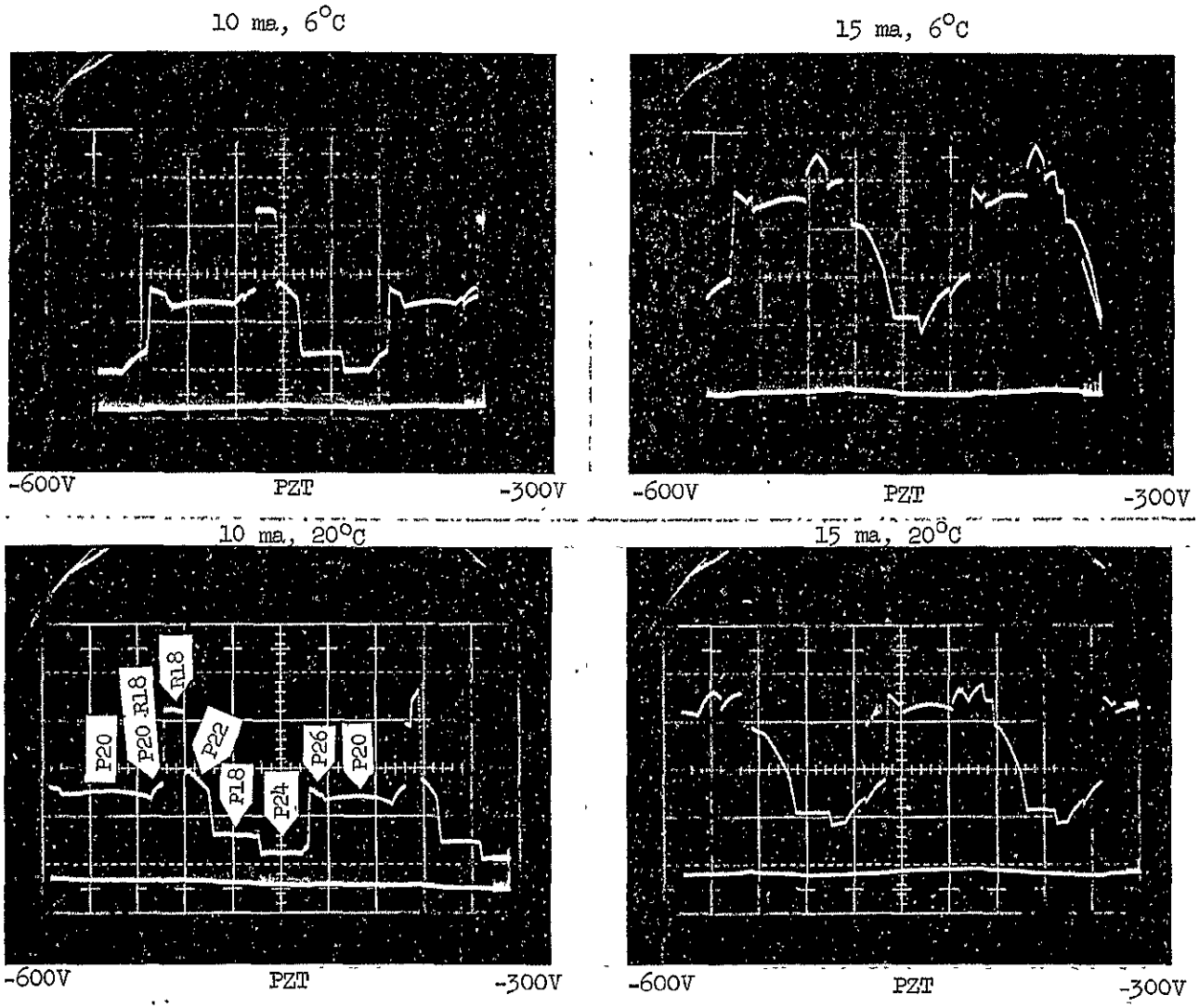

Figure E-34

Conditions as in Figure E-33, but Range of PZT Voltages Reduced to -300V to -600V
Note: Power (Ordinate) Scale Same as in Figure E-33

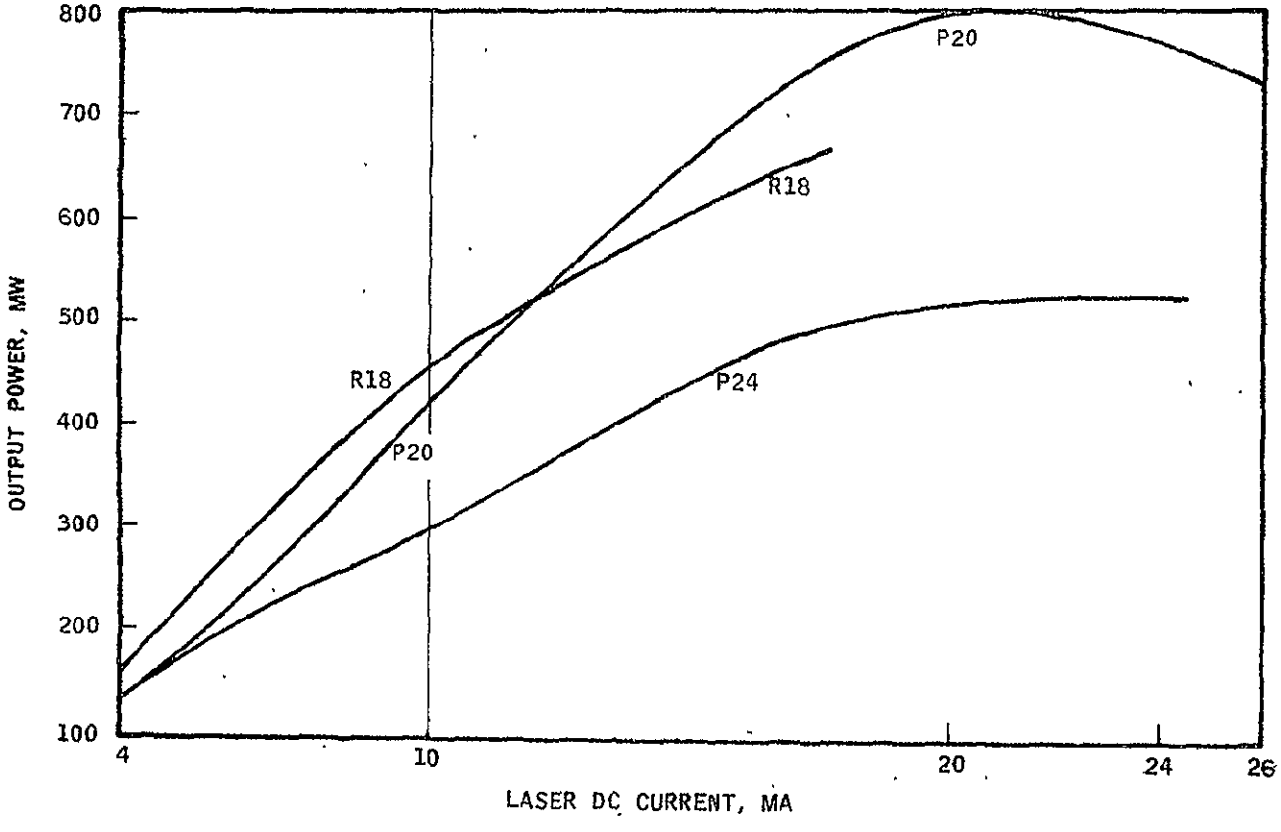

OUTPUT OF SYLVANIA LASER VS DISCHARGE CURRENT
AS MEASURED WITH POWER METER FOR TRANSITIONS P20, P24, AND R18

SYLVANIA LASER SIGNATURE

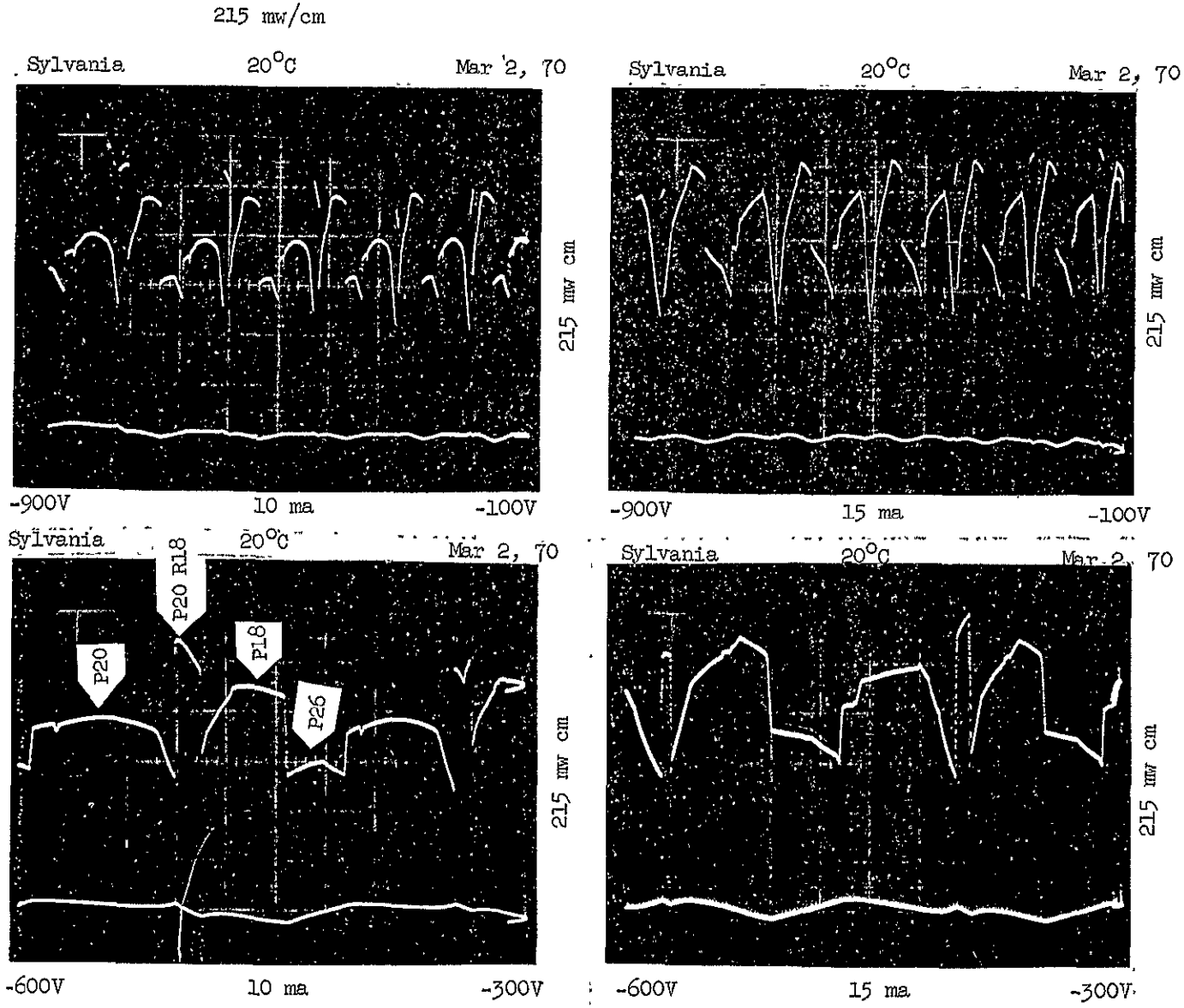

Sylvania Laser (GPC 216) Signatures for 10 ma and 15 ma Discharge Current, 20°C Cooling Water Temperature, and PZT Voltages of -100V to -900V (See Top) and -300 to -600V (See Bottom)
Note: Ordinate Scale: 215 mw/cm (P20)

HONEYWELL LASER
Resonator Length = 54 cm, Long Radius Mirrors
Tube: ID = 8mm, Active Length = 32.5 cm, One Salt Brewster Angle Window

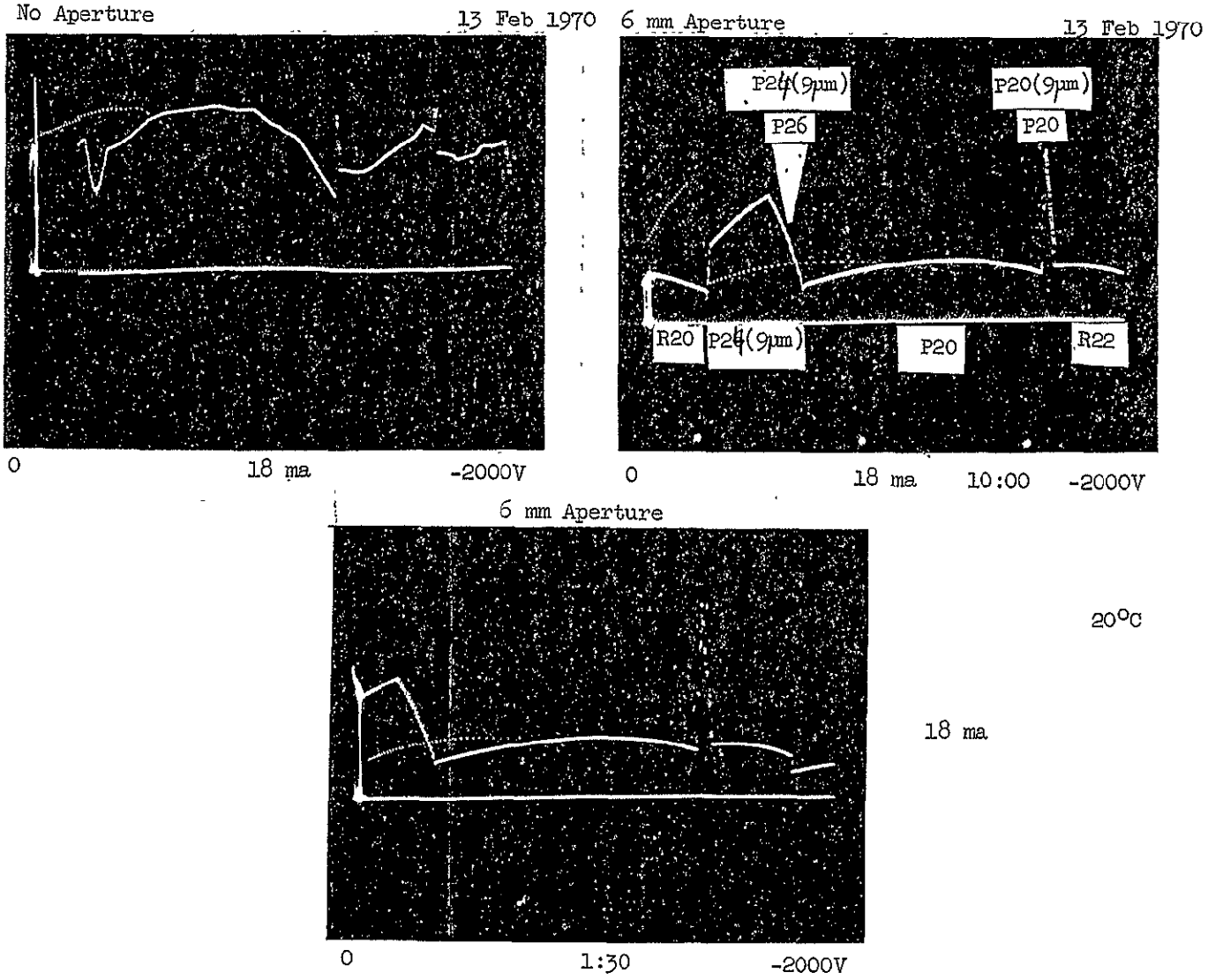

Honeywell Laser (GPC 216) Signatures
Note: Upper Left Picture Taken Without Aperture Within the Resonator;
The Remaining Two were Taken
with a 6-mm dia Aperture, 3-hr, 30 min Apart

Figure E-37

HONEYWELL LASER (6 MM APERTURE)
Ordinate scale: 400 mW/cm (10.6 μm) and 72 mW/cm (9.6μm)

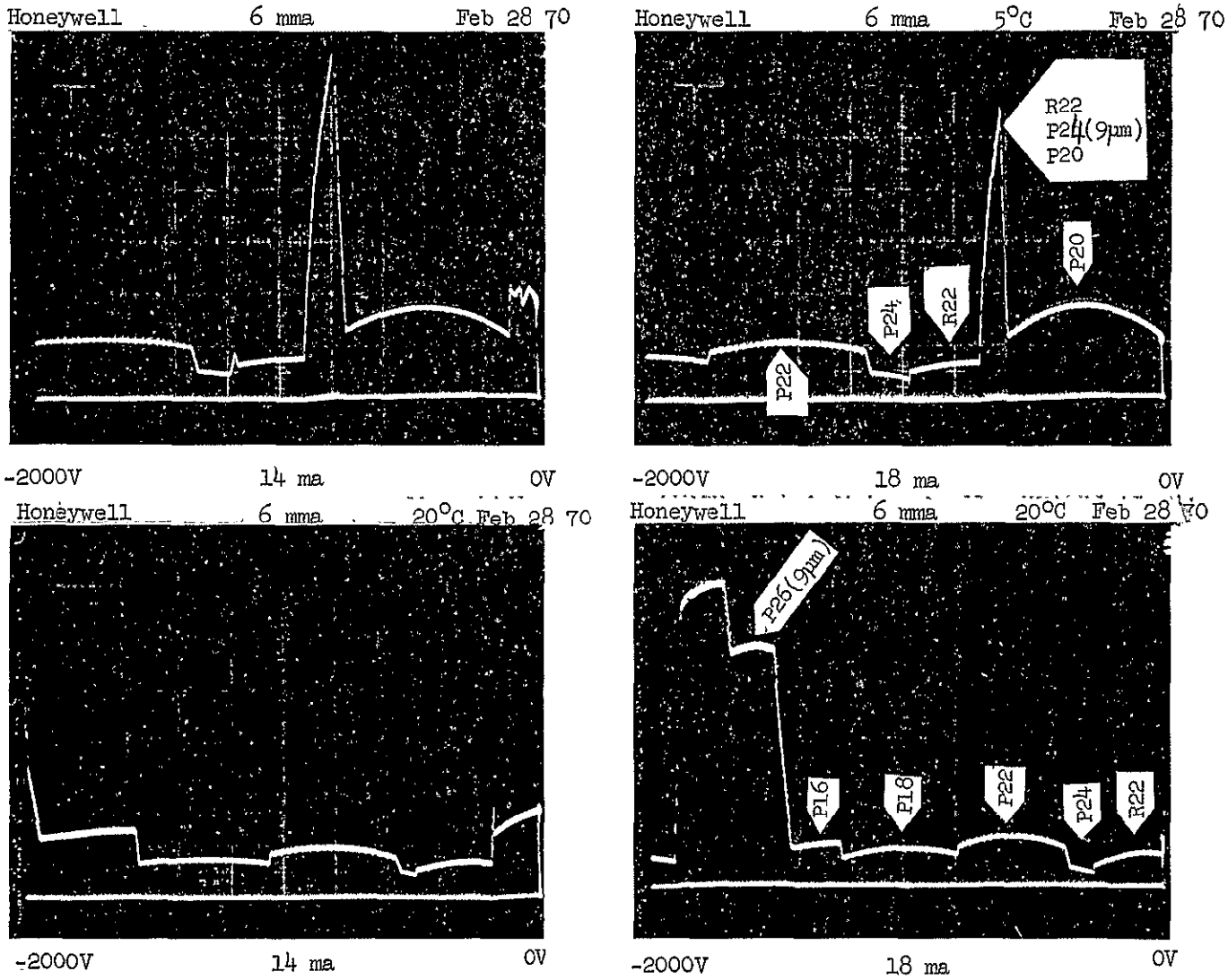

Honeywell Laser (GPC 216) From Aero to -2000V for 14 ma and 18 ma Discharge Current and 5°C and 20°C Cooling Water Temperature

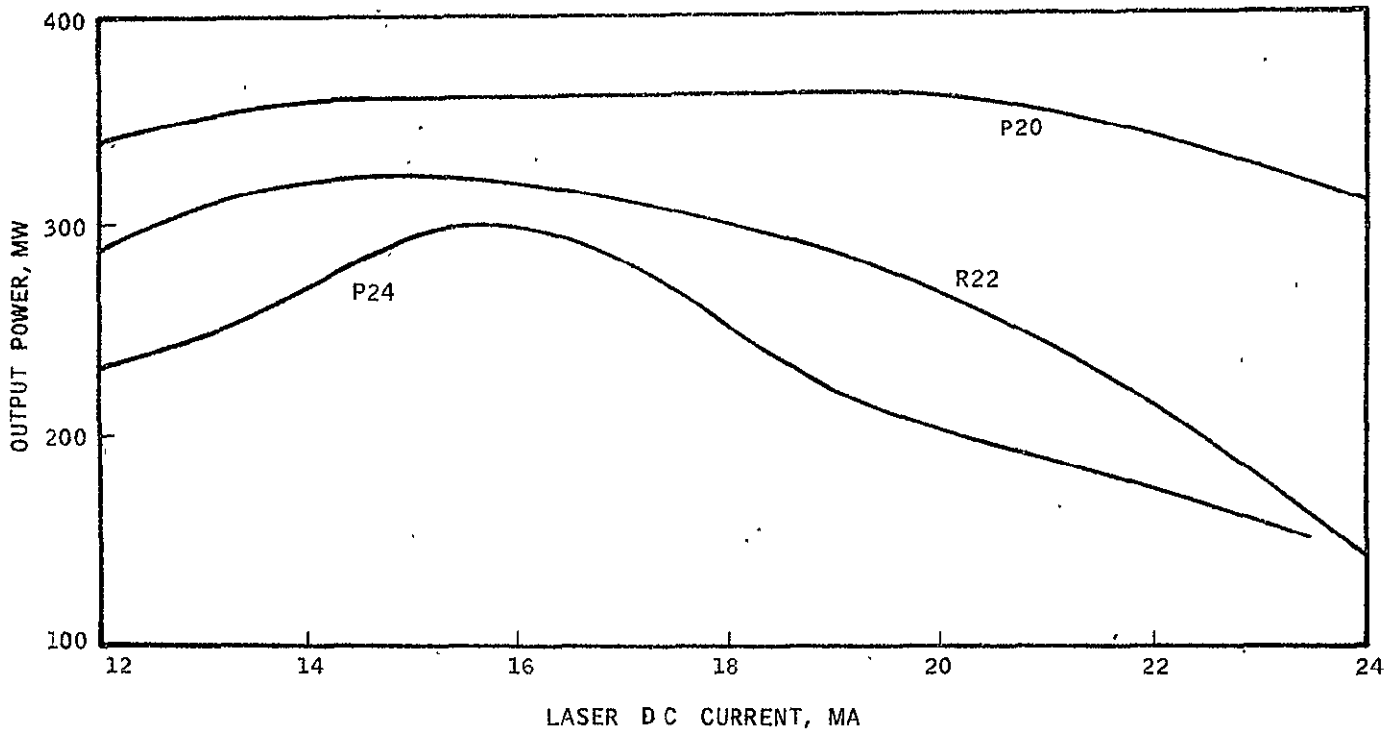

Output of Honeywell Laser (Power Meter) vs Discharge Current
for Transitions P(20), P(24), and P(22)

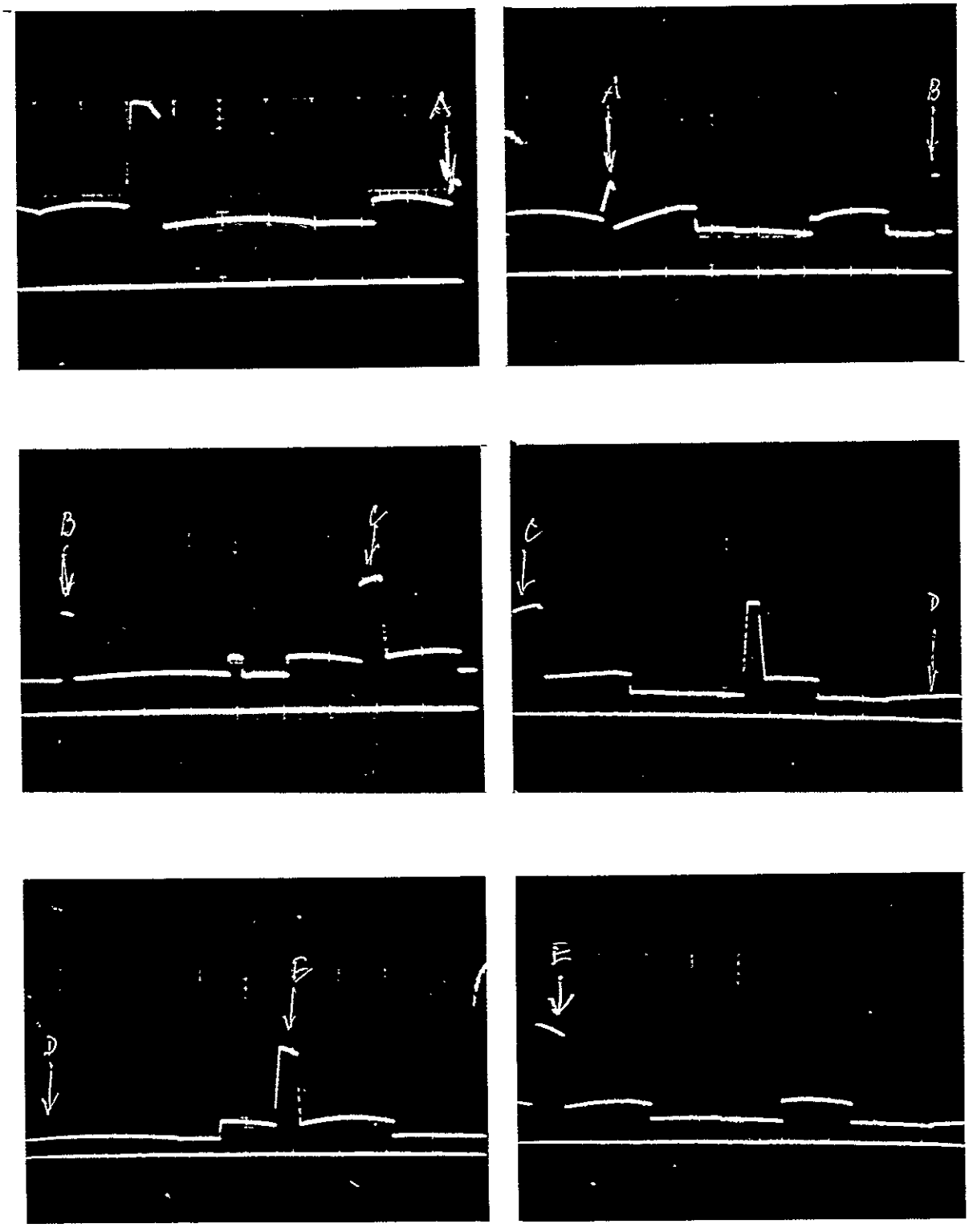

RCA Laser Signatures Representing 3 Half-Wavelengths of Travel

Figure E-40

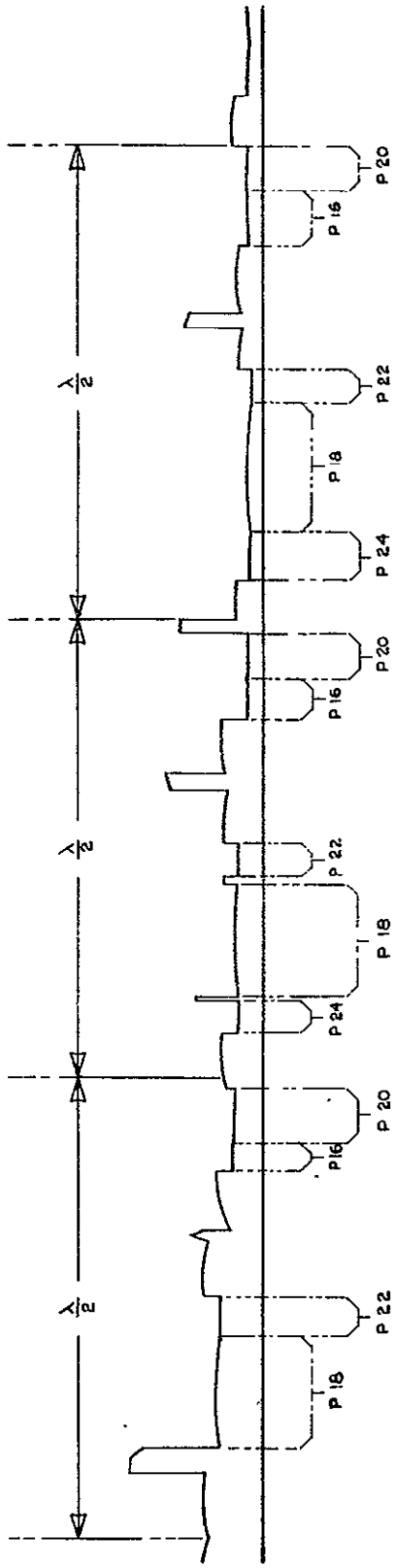

Figure E-41

RCA Laser Signature Peaks

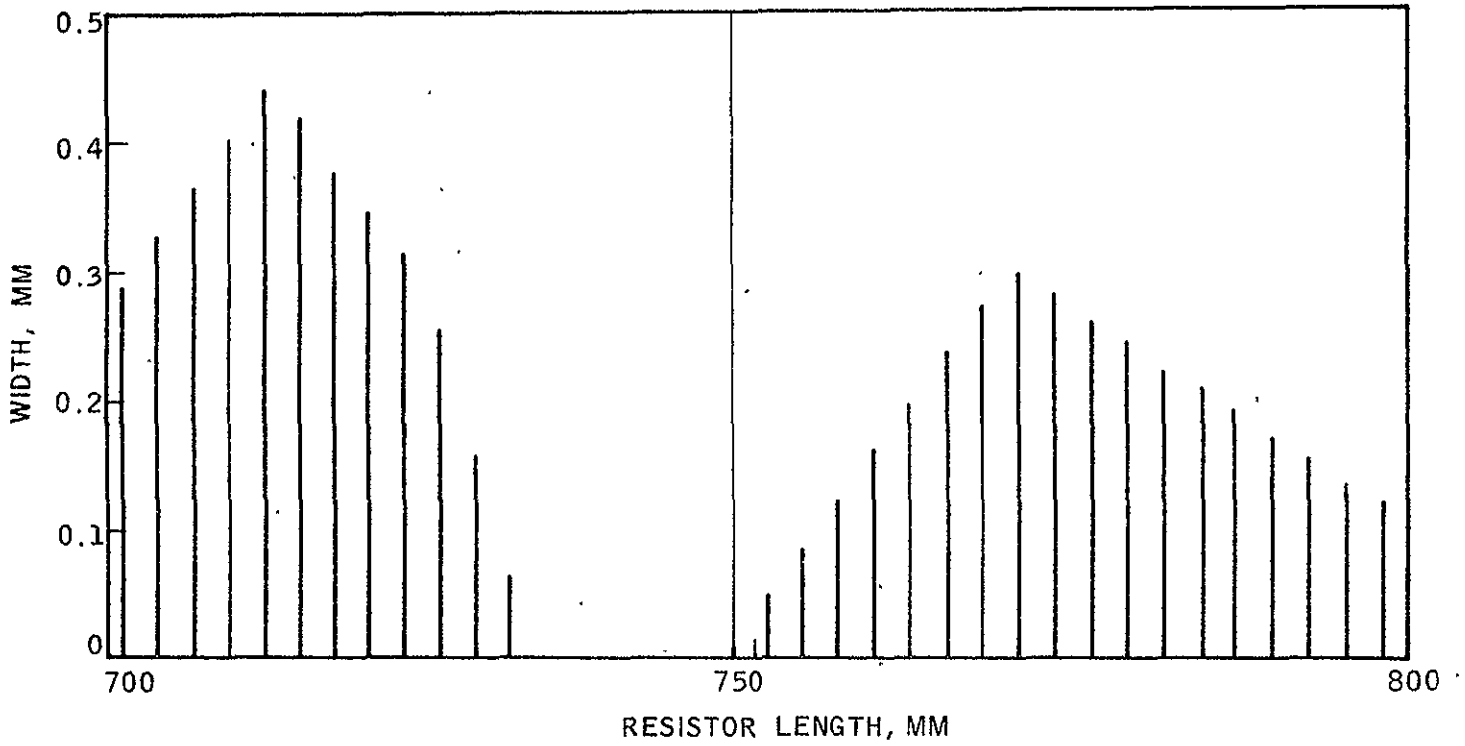

WIDTH OF CAVITY LENGTH REGIONS WHERE SIGNATURE OF SEQUENCE P20, P26, P24, P18, AND P22 OCCURS VS CAVITY LENGTH FOR D = 700 MM TO D = 800 MM

Figure E-42

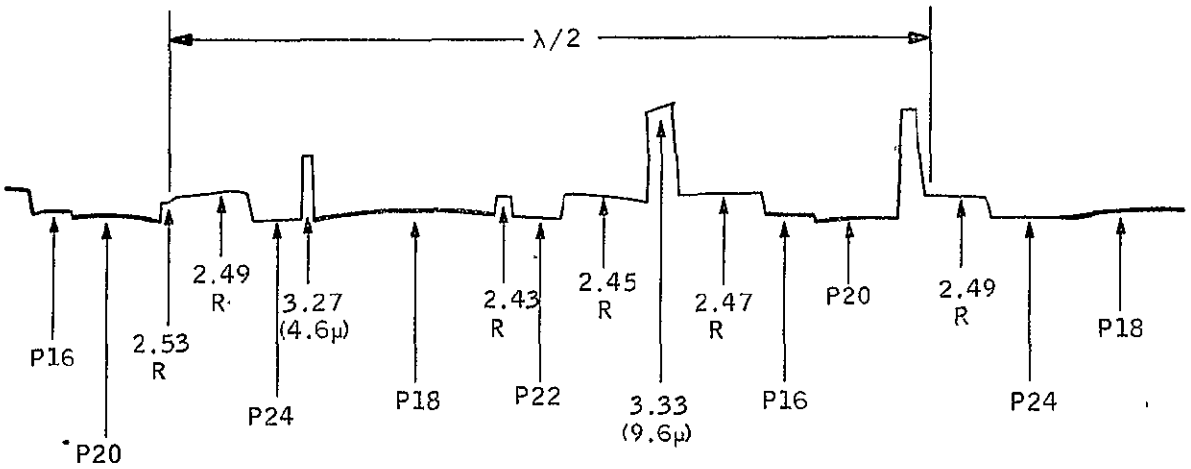

CAVITY LENGTH MM		LINE
421	422	P20
421	424	P24
421	425	P18
421	425	P22
421	427	P16

NOTE: THE TUNING RANGE OF THE P20 LINE IS DECREASED DUE TO THE NEARBY RESONANCE OF P16. THE COMPUTER PRINTOUT INDICATES THAT AT ABOUT 421.75 MM CAVITY LENGTH MUCH BETTER CONDITIONS EXIST FOR P20. THE PRINTOUT SHOWN ABOVE IS INDENTICAL WITH THAT IN TABLE E-6. THE CAVITY LENGTH INCREASES TO THE RIGHT.

COMPARISON OF AN OBSERVED AND A CALCULATED SIGNATURE

Figure E-43

APPENDIX F

LASER FREQUENCY STABILIZATION

1.0 LASER FREQUENCY CALIBRATION

In conjunction with two government-sponsored research programs and several independent development programs, Sylvania has been studying for several years techniques for obtaining a high degree of frequency calibration accuracy of CO_2 laser sources. In the course of this work, a method of electronically locking the CO_2 laser to the center of its gain profile has been successfully demonstrated[1]. In addition, a study of schemes that will allow stabilization of a CO_2 laser oscillator to the center of the gain or absorption profile of an external amplifier cell is currently under way. Both of these techniques make use of a more or less ideal universal frequency standard: the center frequency of a quantum mechanical energy transition.

The results of these programs indicate that this standard can be used to full advantage in the present design. The technique, which will allow the required accuracy with minimum complexity in peripheral equipment, is implemented by sinusoidally tuning the laser cavity frequency over a small range at a low audio rate and observing the FM-to-AM conversion produced by the dependence of laser power output on frequency. The error signal used for the stabilization is derived from the gain profile of the oscillating transition by measuring the amplitude-modulated signal produced on the laser output when a small amount of frequency modulation, which has an amplitude of f_d and a frequency of ω, is introduced on the laser signal. The component of AM at the modulation frequency is given by

$$P_1 = \frac{8\, G\, P_m\, f_d}{(\Delta f_{osc})^2} (f_a - f_c) \cos \omega t \qquad (1)$$

where P_m is the maximum laser power output, Δf_{osc} is the frequency spread over which laser oscillation at a single transition can occur, and G is a factor

which depends on such parameters as modulation frequency, laser pumping rate, cavity and upper lasing level decay rates. This factor becomes unity at low modulation frequencies (as will be used in the proposed application), but can become important at modulation frequencies in the 100-kHz range.

The quantity $(f_a - f_c)$ in Equation (1) is just the detuning of the laser oscillation frequency f_c from the center frequency of the transition f_a. The proportionality between P_1 and $(f_a - f_c)$ results in the usefulness of P_1 as an indicator of laser frequency offset from line center. The technique by which P_1 is generated is shown diagramatically in Figure F-1. Phase-sensitive detection of the electrical signal produced by P_1 then yields a typical discriminator characteristics as a function of detuning. This discriminant is directly usable in a feed-back control loop for frequency stabilization. Figure F-2 is a block diagram, showing the components used in such a system

The limitation on frequency stability obtainable with this technique is determined by the minimum signal detectable above the noise level of the control loop. From Equation (1), the expression is obtained for the amplitude of the voltage signal at the output of the detector terminals or the input to the first amplifier:

$$V_s = \frac{8\, V_m\, f_d}{(\Delta f_{osc})^2}\ (f_a - f_c) \qquad (2)$$

where V_m is the peak dc voltage produced at the detector by the laser output. This equation assumes that the dc responsivity of the detector is equal to the responsivity at the audio modulation frequency. The minimum detectable detuning $(f_a - f_c = f_{min})$ will be determined by the condition when the signal is approximately equal to the input referred noise of the system (i.e., $V_s = V_{noise}$). From this is obtained

$$f_{min} = \frac{(\Delta f_{osc})^2}{8\, v_m\, f_d}\ V_{noise} \qquad (3)$$

The noise produced by the detector within a bandwidth, B, is given by

$$V_n = (R)\ (NEP)\ (\sqrt{B}) \tag{4}$$

Results of experiments show that frequency instabilities can be kept well within the required values. Figure F-3 shows the results obtained from a heterodyne experiment in which two independently stabilized lasers maintained a stable heterodyne beat frequency to better than ± 75 kHz over a period of about 1 hour. Of course, the long-term accuracy, over weeks or months, of this calibration technique requires that the center frequency of the gain profile either does not change in time, or that any changes be known and predictable. Early analysis indicates that a shift in center frequency will not be a problem. Measurements verifying this have been made by Mocker[2], who observed no change in the center frequency of the CO_2 laser gain curve as a function of pressure.

2.0 THERMAL EFFECTS ON LASER FREQUENCY

The operating frequency, f, of a single-mode laser is given by:

$$f = \frac{qC}{2\ (\ell_c)} \tag{5}$$

where q is the number of half-wavelengths between the laser mirrors and ℓ_c is the optical distance between mirrors. The change in laser frequency due to change in cavity length is given by the expression:

$$\Delta f = -f\ \frac{\Delta\ \ell_c}{\ell_c} = \frac{-f}{\ell_c} \sum_{n=1}^{n} \Delta \ell_n \tag{6}$$

where ℓ_n is the optical length change due to the various components which contribute to cavity length changes. Figure F-1 shows the elements that must be considered. The mirrors are separated optically by the modulator, Brewster angle windows, and gas discharge; they are also separated mechanically by the frame, piezoelectric transducer, and mirror substrate. Table F-1 lists the thermal parameters of the materials in the laser cavity.

TABLE F-1

THERMAL EFFECTS ON LENGTH AND OPTICAL THICKNESS FOR SOME MATERIALS

Material	α ($^{o}C^{-1}$)	$\frac{dn}{dT}$ ($^{o}C^{-1}$)	n
Aluminum	24.0×10^{-6}		
Invar	1.0×10^{-6}		
Super Invar	1.8×10^{-7}		
Germanium		$+4.6 \times 10^{-4}$*	4.0
Gallium arsenide	6.86×10^{-6}	$+2.05 \times 10^{-4}$*	3.30
PZT	$\approx 5 \times 10^{-6}$		
Mirror substrate	$\approx 5 \times 10^{-6}$		

*As measured at Sylvania by interference techniques using a stabilized CO_2 laser.

As is apparent from this table, the effect of physical length changes with temperature in GaAs is small compared to optical length changes. The major contributors to the laser thermal drifts are:

$$f = \frac{-f}{l_c} \Delta\ell_{windows} + \Delta\ell_{Invar} - \Delta\ell_{PZT} - \Delta\ell_{al} - \Delta\ell_{mirror}$$

The expected physical lengths of each of the components are:

Length in Centimeters					
t_w	l_{IN}	l_{PZT}	l_{al}	ℓ_{mirror}	l_c
0.3	30	0.15	Variable	0.5	25
Total					

Then:

$$\Delta f = \left[\frac{f}{\ell_c} t_w \left(\frac{dn}{dT}\right)_w + (\ell\alpha)_{Invar} - (\ell\alpha)_{PZT} - (\ell\alpha)_{al} - (\ell\alpha)_{mirror}\right] \qquad (7)$$

and

$$\Delta f = -72\ \text{MHz}/^\circ\text{C}\Big|_{win.} - 34\ \text{MHz}/^\circ\text{C}\Big|_{Inv.}$$

$$+ .85\ \text{MHz}/^\circ\text{C}\Big|_{PZT} + \frac{f(\ell\alpha)_{al}}{\ell_c} + 5.7\ \text{MHz}/^\circ\text{C}\Big|_{mirror} \qquad (8)$$

The aluminum thickness can be accurately chosen to work in conjunction with the PZT stack and grating to compensate for the Invar expansion. If Super Invar or Cervit were chosen as the cavity spacer material, the aluminum would have to be added in the other direction to compensate for the PZT and grating expansions. Since thermal compensation is desirable as a general practice, standard Invar can be just as effective as any other low-expansion cavity material. Sylvania has demonstrated this compensation effect on several CO_2 lasers, in which thermal control alone was used to achieve good frequency stability. At least one order of magnitude reduction in the effective expansion coefficient of the Invar can be achieved; with care, two orders of magnitude can be reached, using aluminum compensating material.

Grouping the mechanical components of the cavity (assuming a factor of 10 compensation by the aluminum), the expected frequency instabilities are:

$$f = -\frac{72\ \text{MHz}/^\circ\text{C}}{\text{Windows}} - \frac{3\ \text{MHz}/^\circ\text{C}}{\text{Max. for cavity}} \qquad (9)$$

To meet the stability requirements for the system, temperature variations of the laser components (including the laser windows) must be kept to $1.4 \times 10^{-3}\ ^\circ\text{C/min}$.

3.0 HETERODYNE DETECTION OF OPTICAL-FREQUENCY FM COMMUNICATIONS SIGNALS IN THE PRESENCE OF FM NOISE

In an optical-frequency heterodyne receiver system using a square-law (power) detector, the detector is illuminated by a signal from a local (power) detector, the detector is illuminated by a signal from a local oscillator given by

$$a_1(t) = A_1 \sin (\omega_1 t + \phi_1) \tag{10}$$

and by some presumably narrow-band, received signal, expressed as

$$a_2(t) = A_2 \sin (\omega_2 t + \phi_2) \tag{11}$$

The following sketch shows the essentials of such a receiver from FM communications.

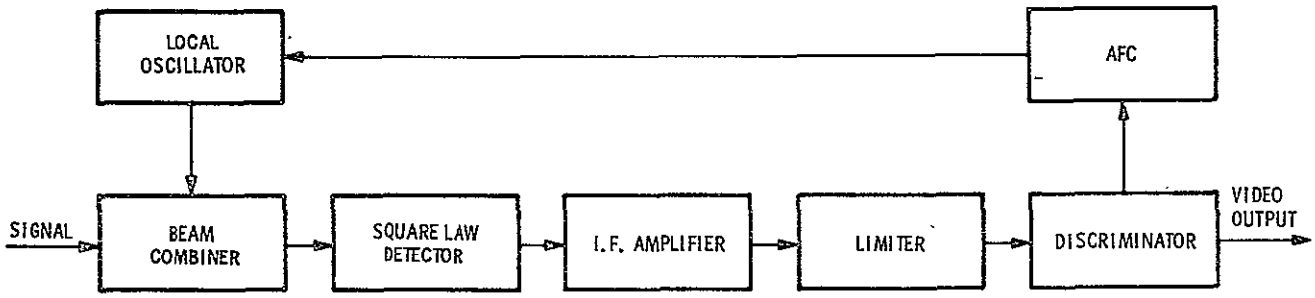

The voltage signal at the output terminals of the detector will be given by

$$V_d(t) = R \left[P_1 + P_2 + 2\sqrt{P_1 P_2} \cos (\omega_1 - \omega_2) t + \phi_1 - \phi_2\right] \tag{12}$$

where R is the responsivity of the detector (volts per watt) and P_1 and P_2 are the powers of the two beams at the detector. In writing Equation (12), it is assumed that the detector has constant responsivity out to at least a frequency $(\omega_1 - \omega_2)$, but that there is no response at optical frequencies.

However, P_1 and P_2 can themselves vary in time if a relatively narrow-band amplifier and limiter are used following the detector; the resulting output from the limiter will have a fundamental component given by

$$V_1(t) = A \cos \left(\omega_1 - \omega_2\right) t + \phi_1 - \phi_2 \tag{13}$$

Other components occurring at odd harmonics of $(\omega_1 - \omega_2)$ produced by the limiter can be filtered out and, therefore, are neglected.

The instantaneous frequency of $V_1(t)$ may be written directly as the time derivative of the phase of $V_1(t)$:

$$\omega_1 = (\omega_1 - \omega_2) + \dot{\phi}_1 - \dot{\phi}_2 \tag{14}$$

The discriminator into which $V_1(t)$ is fed will in general produce an output voltage of the form

$$V_o(t) = k_1 (\omega_i - \omega_c) + k_2 (\omega_i - \omega_c)^2 + k_3 (\omega_i - \omega_c)^3 + - - - - \tag{15}$$

where ω_c is the center frequency of the discriminator. To the extent that k_2, k_2, and higher-order terms are small, the discriminator is linear.

Assuming that the $(\omega_1 - \omega_2)$ term in Equation (14) is maintained constant, then the information and noise will be contained in the $\dot{\phi}_1$ and $\dot{\phi}_2$ terms. To treat the effect of the FM-stabilization technique on the proposed system, it is assumed that $\dot{\phi} = 0$ and that ϕ_2 equals the sum of some information term ϕ_a plus a term resulting from the FM stabilization modulation, ϕ_b. Thus,

$$\dot{\phi}_1 = 0 \tag{16}$$

$$\dot{\phi}_2 = \dot{\phi}_a + \dot{\phi}_b$$

The discriminator output (neglecting dc terms) is then

$$V_0(t) = k_1 (\dot{\phi}_a + \dot{\phi}_b) + k_2 (\dot{\phi}_a + \dot{\phi}_b)^2 + k_3 (\dot{\phi}_a + \dot{\phi}_b)^3 + - - - \tag{17}$$

$$= k_1 (\dot{\phi}_a + \dot{\phi}_b) + k_2 (\dot{\phi}_a^2 + 2\dot{\phi}_a\dot{\phi}_b + \dot{\phi}_b^2)$$

$$+ k_3 (\dot{\phi}_a^3 + 3\dot{\phi}_a^2\dot{\phi}_b + 3\dot{\phi}_a\dot{\phi}_b^2 + \dot{\phi}_b^3) + - - - \tag{18}$$

The first term in Equation (18), $k_1 (\dot{\phi}_a + \dot{\phi}_b)$ shows that the first-order linear effect of the discriminator does not mix the information signal with the stabilization modulation and, therefore, because of the wide separation in frequency (greater than 1 MHz compared to 75 Hz), the two signals are easily separated by proper filtering. The second term with coefficient k_2 is made up of three additional terms. The first of these, $k_2 \dot{\phi}_2^2$, is the second harmonic distortion due to discriminator non-linearity and occurs at twice the information signal frequency. The second term is the mixing term between the stabilization FM and the information. Both of these signals can fall within the information and, thus, reduce the fidelity of the channel. The ratio of the amplitudes of these two signals may be shown to be

$$\frac{\text{Mixing term}}{2^{\text{nd}}\ \text{Harmonic term}} = \frac{\Delta f_b}{\Delta f_a}$$

where f_b and f_a are the peak frequency deviations of the stabilization and information signals respectively. Since the stabilization FM uses a peak-frequency deviation which is nearly an order of magnitude less than that used for the information, the mixing signal will always be smaller than the 2nd harmonic signal. Thus discriminator linearity must be determined by the maximum allowable harmonic distortion in the channel, and the use of FM stabilization will not impose a more stringent requirement.

As a consequence of the use of baseband conversion and a discriminator which is sufficiently linear to provide low harmonic distortion, it is possible to use FM stabilization of the transmitter continuously while the channel is open and thereby eliminate the reference cavity and associated electronics which were thought to be required earlier. Low-frequency FM noise on either of the laser oscillators similarly becomes unimportant as a noise source in the information band. Finally, the problems of modulator resonances occurring in the 100-kHz range are also eliminated.

REFERENCES

1. M. W. Sasnett, R. S. Reynolds, and A. G. Siegman, "10.6 Micron Single Mode Frequency Control," Technical Report AFL-TR-69-337, 31 October 1969.

2. M. W. Mocker, "Pressure and Current Dependent Shifts in the Frequency of Oscillation of the CO_2 Laser," App. Phys. Lett. 12, pp. 20-23 (1 January 1968).

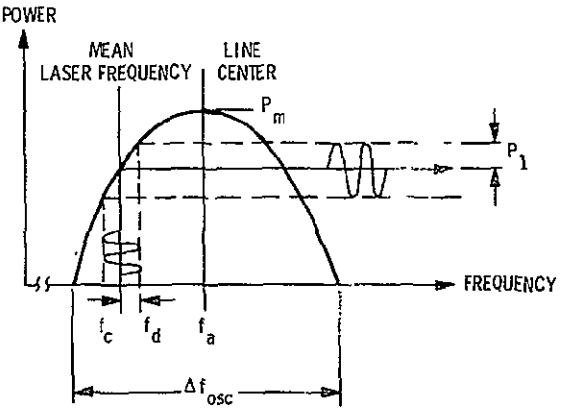

Fig. F-1 Generation of Stabilization Discriminant

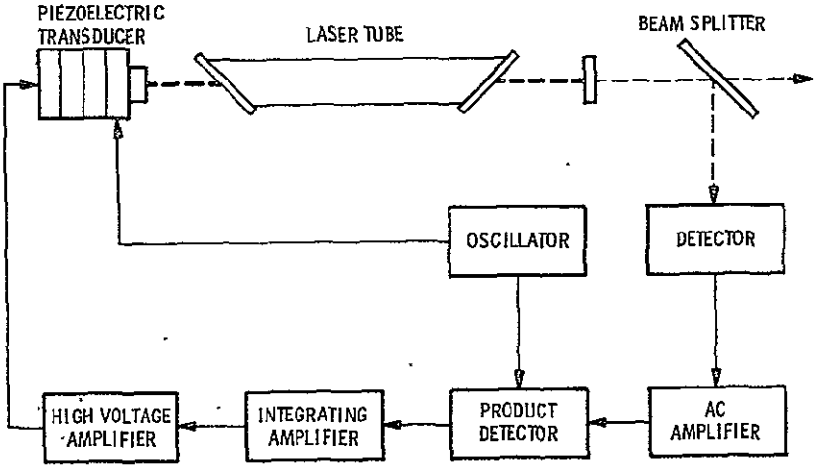

Fig. F-2 FM Stabilization System Block Diagram

Figures F-1 and F-2

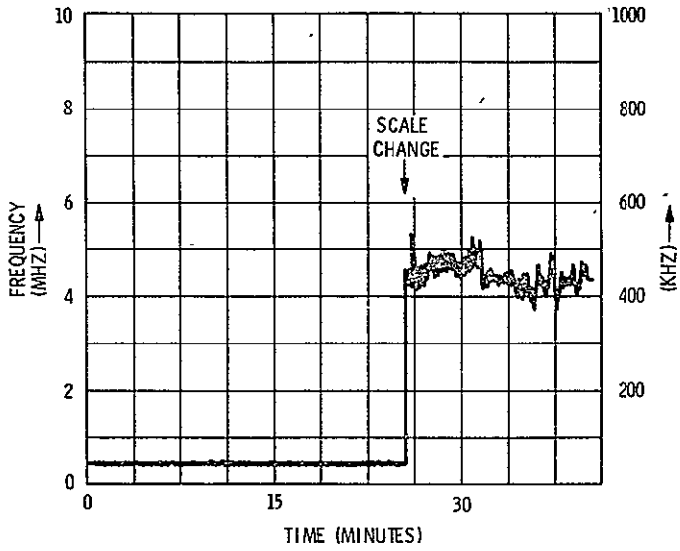

Fig. F-3 Heterodyne Beat-Frequency for Stabilized 1-Watt CO_2 Lasers

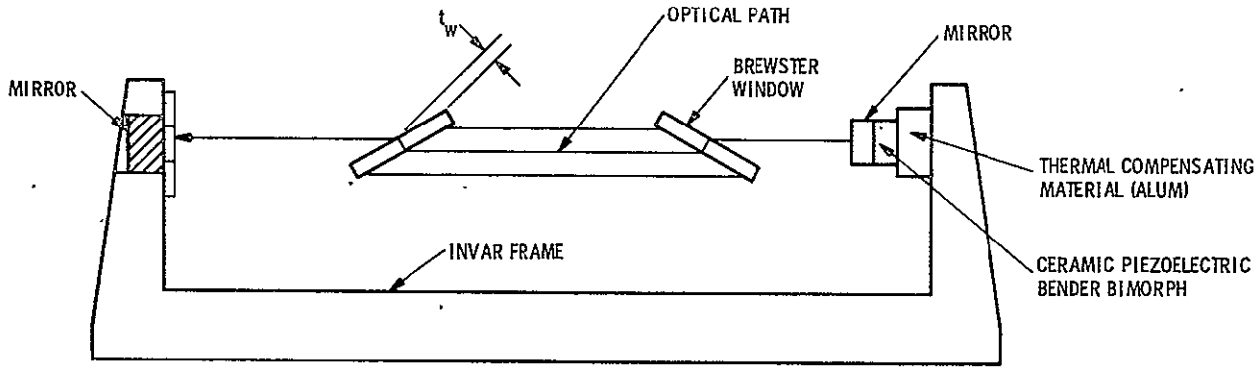

Fig. F-4 Schematic Diagram of Laser Showing Elements Affecting Frequency Stability Due to Temperature Drifts

Figures F-3 and F-4

APPENDIX G

THEORETICAL MODEL FOR LASER POWER OUTPUT COMPUTATION

It is important in the design of compact and efficient lasers that a mathematical model be available which can be used to accurately predict laser output power given the available design parameters such as mirror transmittance, losses, active length, etc. In addition, for cases where active intra-cavity elements are used in a laser, such a model forms an essential part of any tradeoff analysis performed to optimize the overall system. For example, in the present LCE system, the transmitter laser uses an electro-optic phase modulator within the optical cavity to produce an FM signal on the laser output. The particular choice of modulator length and active tube length must be made so as to minimize the power required by the entire transmitter system. The choice of these lengths is, of course, subject to the constraint that laser power must exceed some value. It is therefore necessary to be able to express this output power analytically.

In developing an expression for laser power output we have essentially followed a derivation given by Rigrod[1] except that the case where output occurs at one mirror only has been specifically analyzed and provision has been made for including intra-cavity losses, in addition to those associated with the mirrors. It is assumed that the laser transition line is homogeneously broadened so that the gain coefficient at any point z along the active region of the laser is given by

$$g(z) = \frac{g_o}{1 + B_+ + B_-} \qquad (1)$$

Here B_+ is the intensity of the forward traveling wave normalized to the saturation intensity, $B_+ = \frac{I_+}{I_s}$, and likewise $B_- = \frac{I_-}{I_s}$. Also, g_o is the unsaturated gain coefficient. Radial variations in gain are not considered and Equation (1)

[1] W. W. Rigrod, "Saturation Effects in High-Gain Lasers," Jour. Appl. Phys., 36, pp. 2487-2490, August 1965.

is, therefore, some average value over the diameter of the region. This is not particularly serious since this is the quantity which is most easily measured in a basic experiment and it can, therefore, be used directly here. Since the gain is independent of direction,

$$g(z) = \frac{1}{B_+}\frac{dB_+}{dz} = -\frac{1}{B_-}\frac{dB_-}{dz} \tag{2}$$

This yields

$$B_+ B_- = \text{constant} = C \tag{3}$$

Figure G-1 shows the laser schematically including mirrors with reflectances given by: $r_1 = 1 - a_1$, $r_2 = 1 - a_2 - t$ where a_1 and a_2 are the dissipative losses and t is the output transmittance. In addition, an element with single pass loss A, is included in the region near mirror 1 so that the laser medium sees an effective reflectivity $r'_1 = 1 - a_1 - 2A$. The oscillation will stabilize at a level such that

$$\frac{B_2}{B_3} r_2 = \frac{B_4}{B_1} r'_1 \tag{4}$$

From Equation (3),

$$B_1 B_4 = B_2 B_3 = C \tag{5}$$

and therefore,

$$\frac{B_2}{B_4} = \sqrt{\frac{r'_1}{r_2}} \tag{6}$$

From Equations (1), (2), and (3), the following identity for the power flow in the positive direction can be written:

$$\frac{1}{B_+}\frac{dB_+}{dz} = \frac{g_o}{1 + B_+ + \frac{C}{B_+}} \tag{7}$$

After integrating, the following is obtained

$$g_o L = \ell n \frac{B_2}{B_1} + B_2 - B_1 - C\left(\frac{1}{B_2} - \frac{1}{B_1}\right) \tag{8}$$

The same procedure for the negative direction gives

$$g_o L = \ell n \frac{B_4}{B_3} + B_4 - B_3 - C\left(\frac{1}{B_4} - \frac{1}{B_3}\right) \tag{9}$$

Adding Equations (8) and (9) gives

$$B_2 = \frac{\sqrt{r'_1}}{\left[\sqrt{r'_1} + \sqrt{r_2}\right]\left[1 - \sqrt{r'_1 r_2}\right]}\left[g_o L + \ell n \sqrt{r'_1 r_2}\right] \tag{10}$$

The normalized output intensity from the laser is then,

$$\frac{I_o}{I_s} = B_2 t \tag{11}$$

To simplify this expression, it is assumed that the mirror losses a_1, a_2 are equal and define mirror efficiency K as $K = 1 - a$. Substituting Equation (10) into (11) and making use of the expressions for r'_1 and r_2 given prior to Equation (4) gives

$$\frac{I_o}{I_s} = \frac{\sqrt{K - 2A}\; t\left[g_o L + \ell n \sqrt{(K - 2A)(K - T)}\right]}{\left[\sqrt{K - 2A} + \sqrt{K - T}\right]\left[1 - \sqrt{(K - 2A)(K - T)}\right]} \tag{12}$$

This expression then allows direct computation of laser output power once data is available on gain and saturation for the active medium and the mirror properties are known. Plots of $\frac{I_o}{I_s}$ as a function of mirror transmittance for several values of gain and loss are shown in Figures G-2 through G-6.

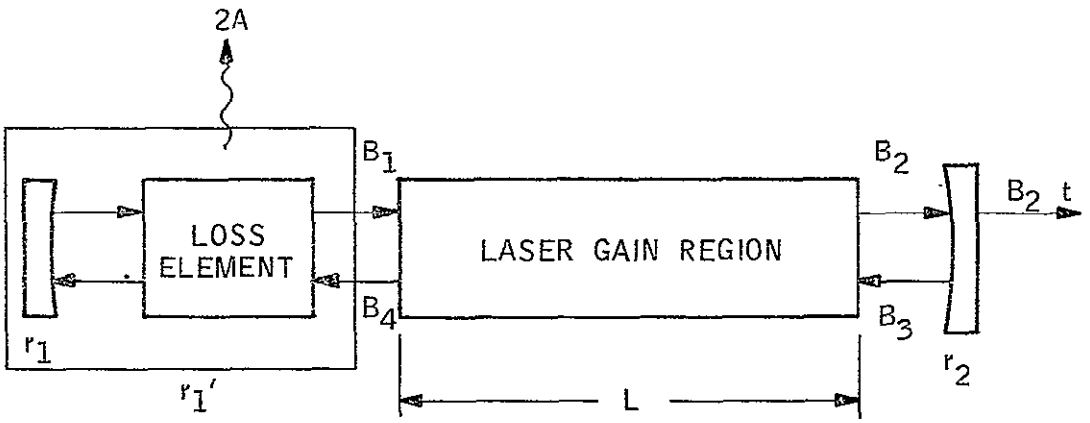

POWER FLOW IN A GENERALIZED LASER CAVITY

Figure G-1

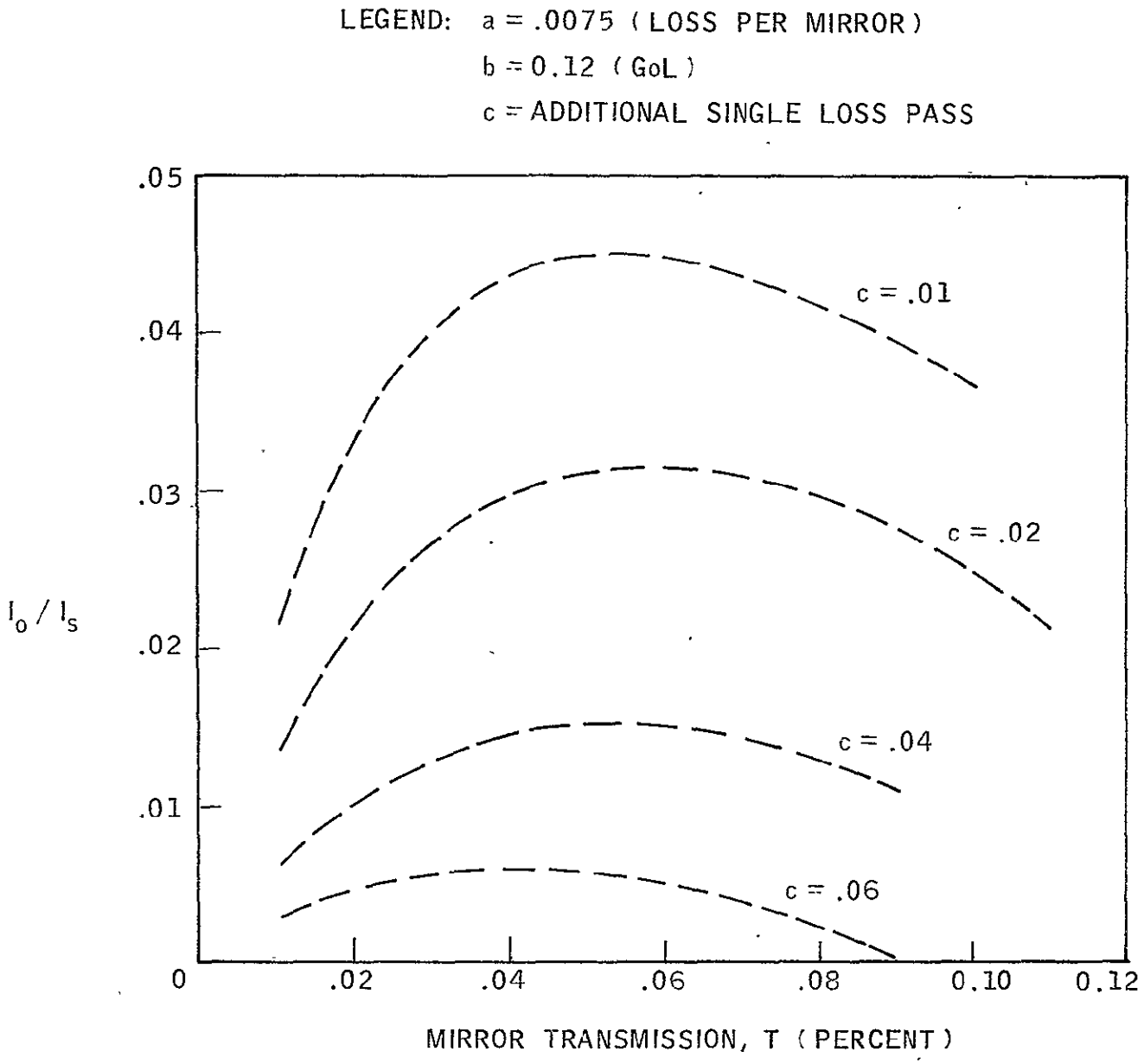

I_o / I_o VS MIRROR TRANSMISSION FOR A LASER GAIN OF 12 PERCENT

Figure G-2

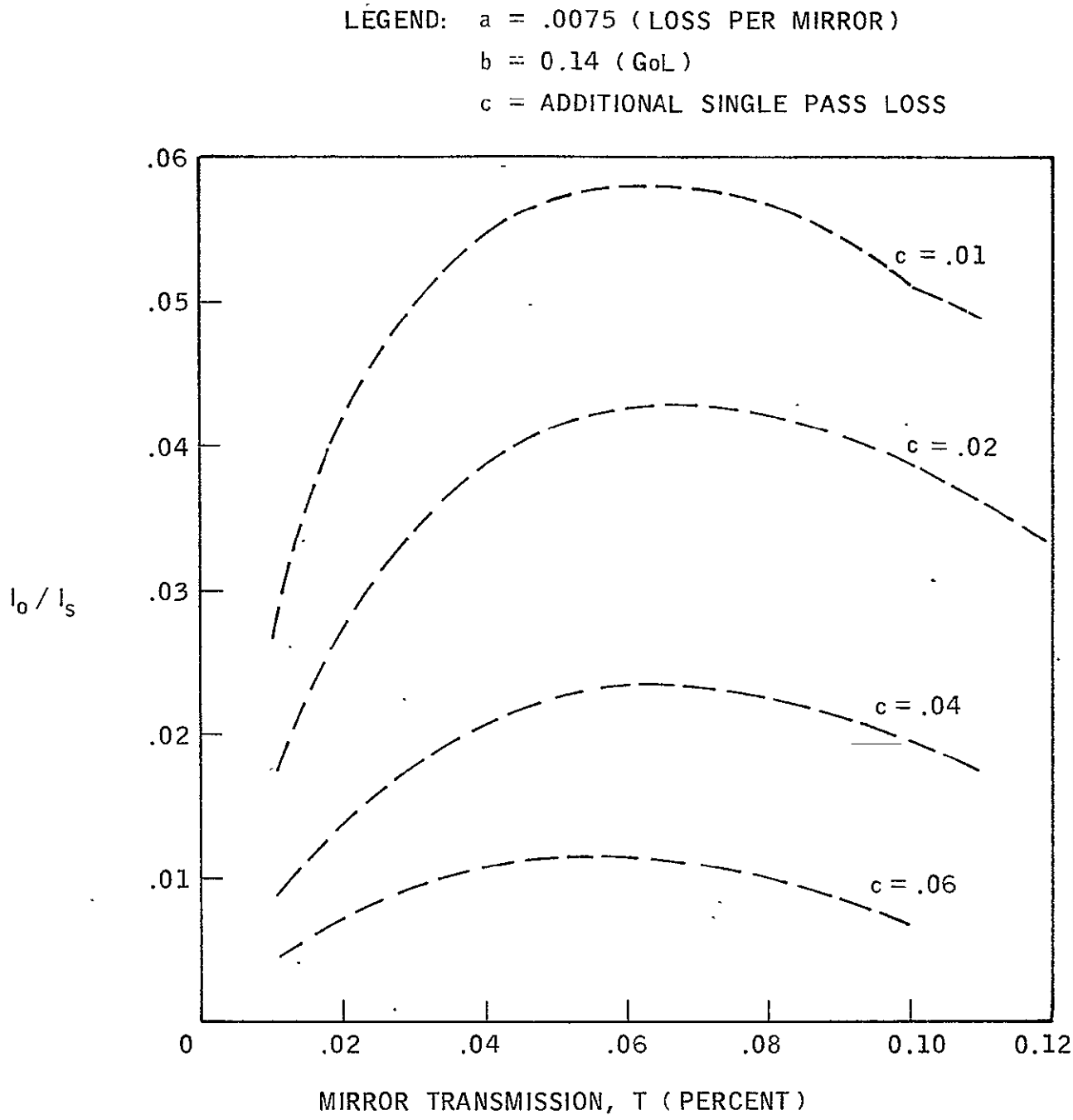

I_o / I_s VS MIRROR TRANSMISSION FOR A LASER GAIN OF 14 PERCENT

Figure G-3

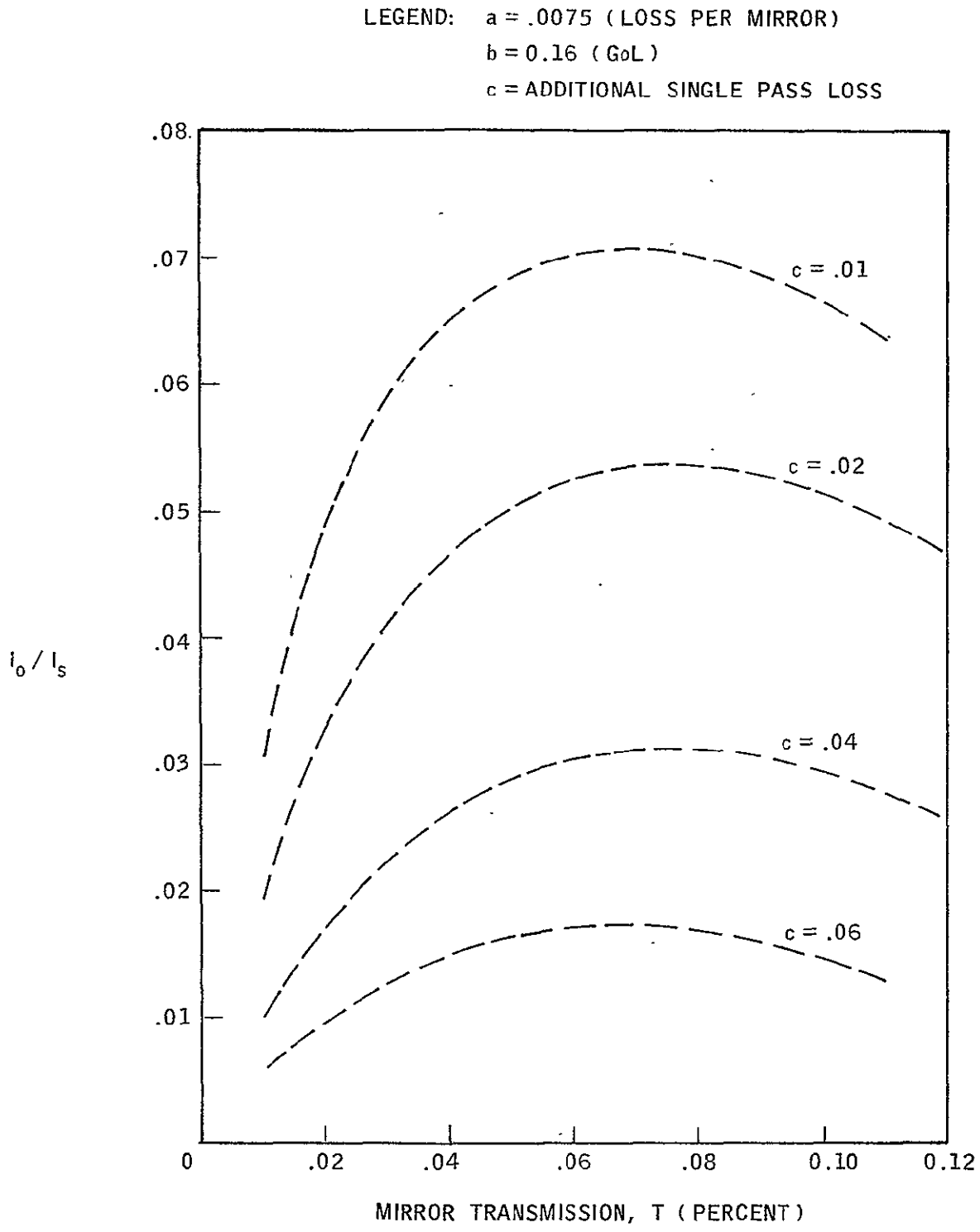

I_0 / I_s VS MIRROR TRANSMISSION FOR A LASER GAIN OF 16 PERCENT

Figure G-4

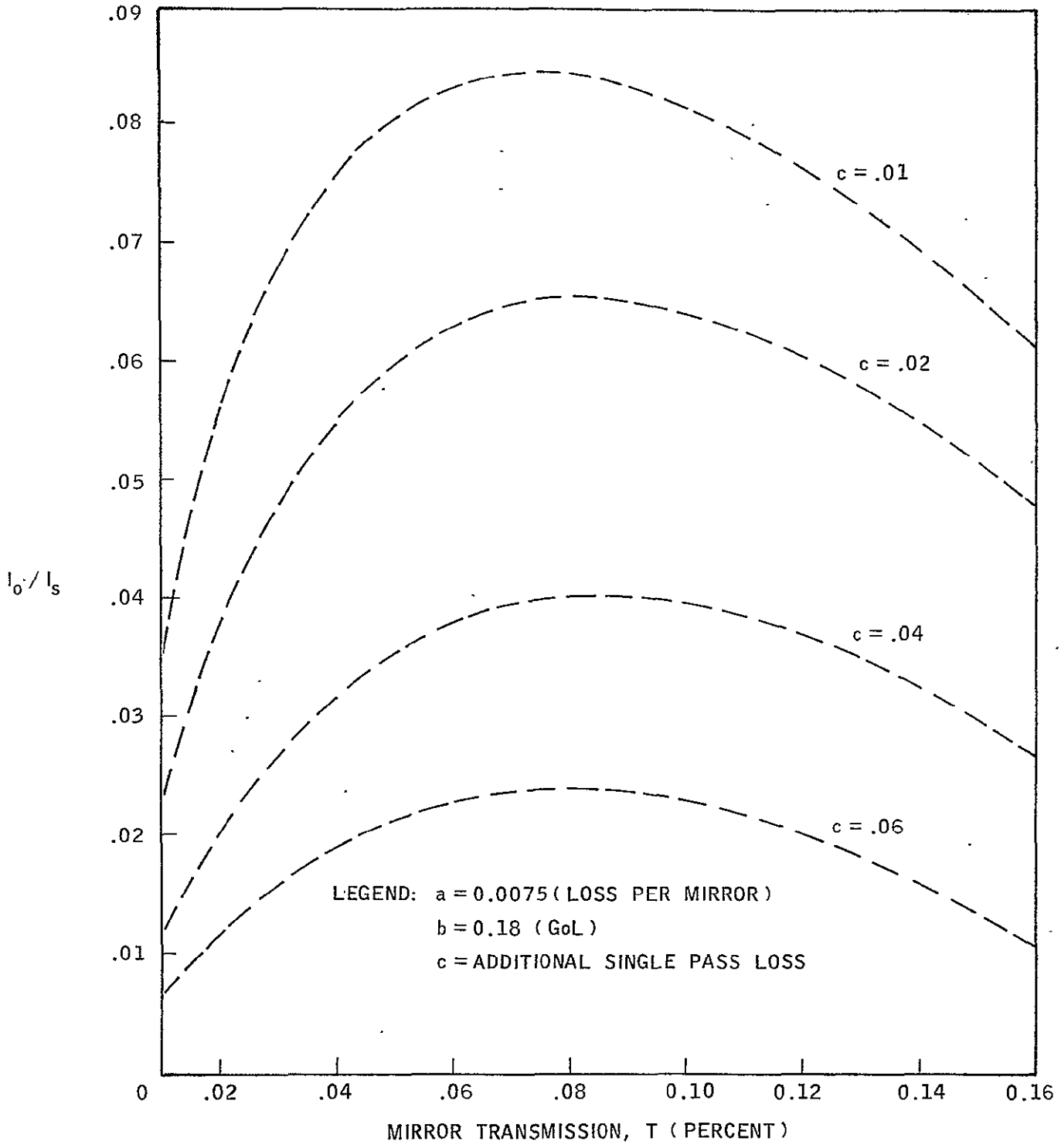

I_o / I_s VS MIRROR TRANSMISSION FOR A LASER GAIN OF 18 PERCENT

Figure G-5

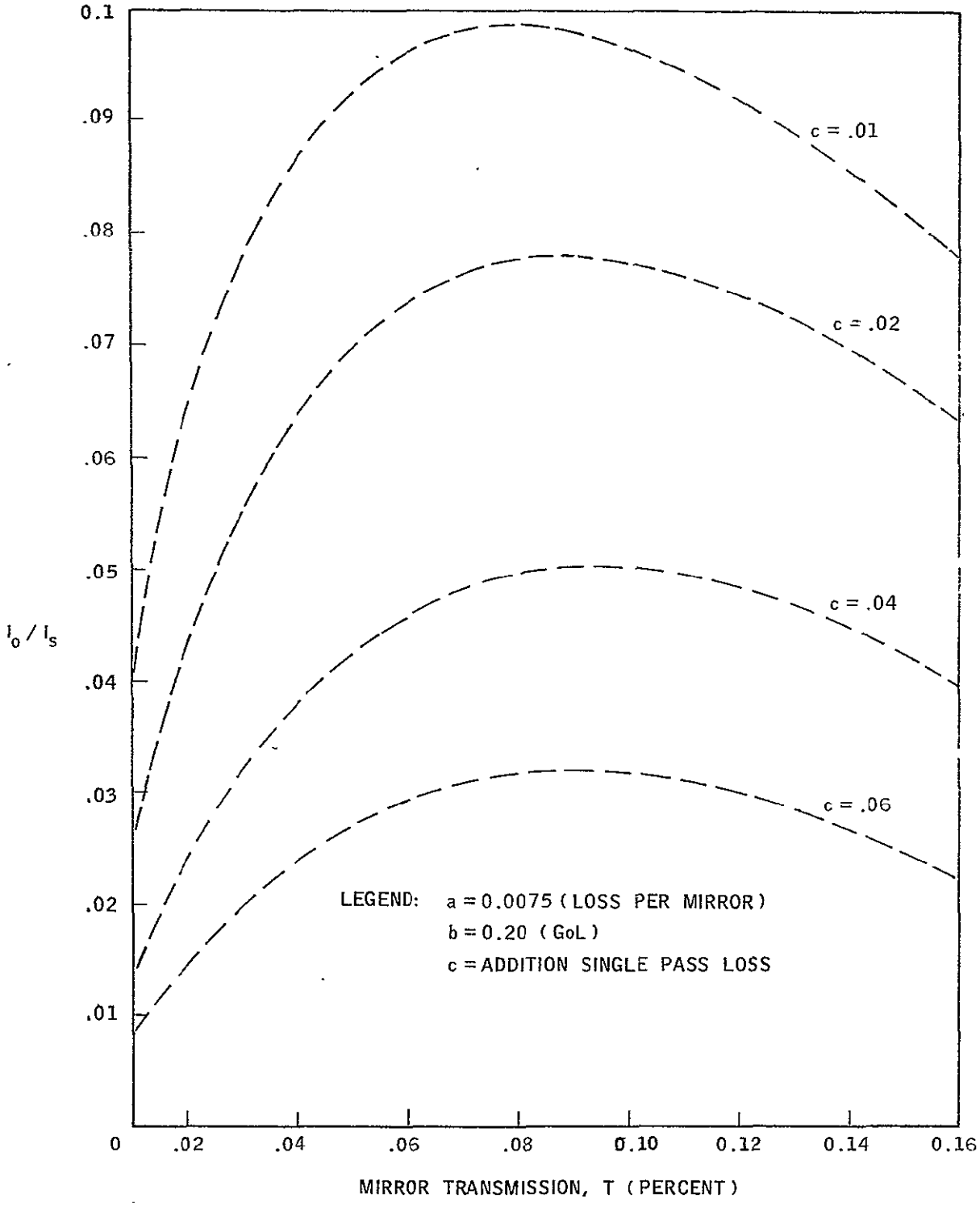

I_o / I_s VS MIRROR TRANSMISSION FOR A LASER GAIN OF 20 PERCENT

Figure G-6

APPENDIX H
PRELIMINARY STRUCTURAL ANALYSIS OF RADIATOR/SUNSHADE AND SUPPORT

The differential coefficient of thermal expansion, $\Delta\alpha$, between the beryllium support structure and the magnesium radiator is

$$\Delta\alpha = \alpha_{mg} - \alpha_{Be} \tag{1}$$

$$\Delta\alpha = (14 - 6.7) \times 10^{-6}$$

$$\Delta\alpha = 7.3 \times 10^{-6} \text{ in./in./°F}$$

The maximum temperature differential, ΔT, the spacecraft/or experiment will experience is

$$\Delta T = (95 - 41) \qquad (20°C \pm 15°C) \tag{2}$$

$$\Delta T = 54°F$$

Therefore, the maximum strain imposed on the radiator will be

$$\epsilon = \Delta\alpha\,(\Delta T) \tag{3}$$

$$\epsilon = 7.3 \times 10^{-6}\,(54)$$

$$\epsilon = 394 \times 10^{-6} \text{ in./in.}$$

and the compressive stress is

$$f_c = E\,\epsilon \tag{4}$$

$$f_c = 6.5 \times 10^{6}\,(394 \times 10^{-6})$$

$$f_c = 2560 \text{ psi}$$

The allowable buckling stress, based on a factor of safety of 1.5 is then

$$F_{buckling} = f\,(F.S.) \tag{5}$$

$$F_{buckling} = 2560\,(1.5)$$

$$F_{buckling} = 3840 \text{ psi}$$

The thickness of the magnesium radiator,[1] based on this allowable buckling stress is then

1. Roark - Formulas for Stress and Strain

$$t_{req} = \sqrt{\frac{F_{buckling}\ (1 - \mu^2)\ r^2}{K\ E}} \qquad (6)$$

and where K = 0.35

$$t_{req} = \sqrt{\frac{3840\ (1 - .3^2)\ 3.9^2}{0.35\ (6.5 \times 10^6)}}$$

$$t_{req} = 0.153 \text{ inch}$$

The approximate weight of the radiator and the detector/mixer is

Radiator	0.5 lb
Detector/mixer	0.15 lb

The lg static deflection normal to the surface of the radiator is then:

$$S_{st} = \frac{3\ W_R\ (m - 1)(5m + 1)\ r^2}{16\ \pi\ E\ m^2\ t^3} + \frac{3\ W_{D/M}\ (m - 1)(3m + 1)\ r^2}{4\ \pi\ E\ m^2\ t^3} \qquad (7)$$

and substituting

$$S_{st} = \frac{3\ (.5)(\frac{1}{.3} - 1)(\frac{5}{.3} + 1)\ 3.9^2}{16\ \pi\ (6.5 \times 10^6)(\frac{1}{.3})^2(.153)^3} +$$

$$\frac{3\ (.15)(\frac{1}{.3} - 1)(\frac{3}{.3} + 1)\ 3.9^2}{4\ \pi\ (6.5 \times 10^6)(\frac{1}{.3})^2(.153)^3}$$

$$S_{st} = (72 + 54)\ 10^{-6}$$

$$S_{st} = 126 \times 10^{-6}$$

The first mode natural frequency, assuming single degree of freedom in the transverse direction of the radiator is then

$$f_n = \frac{1}{2\ \pi} \sqrt{\frac{g}{S_{st}}} \qquad (8)$$

$$f_n = \frac{1}{2\ \pi} \sqrt{\frac{386}{126 \times 10^{-6}}}$$

$$f_n = 278 \text{ Hz}$$

The differential coefficient of thermal expansion, $\Delta\alpha$, of the beryllium support structure and the aluminum sunshade is

$$\Delta\alpha = \alpha_{Al} - \alpha_{Be} \tag{9}$$

$$\Delta\alpha = (13 - 6.7) \times 10^{-6}$$

$$\Delta\alpha = 6.3 \times 10^{-6} \text{ in./in./°F}$$

As in the analysis of the radiator, the compressive strain from expansion of the aluminum with respect to the beryllium, over the 54°F temperature differential, will be

$$\epsilon = 6.3 \times 10^{-6} (54)$$

$$\epsilon = 340 \times 10^{-6} \text{ in./in.}$$

And the compressive stress in the mounting ring is conservatively

$$f_c = 10 \times 10^6 \times 340 \times 10^{-6}$$

$$f_c = 3400 \text{ psi}$$

The allowable buckling stress, with a factor of safety of 1.5 is then

$$F_{buckling} = 3400 (1.5)$$

$$F_{buckling} = 5100 \text{ psi}$$

The minimum flange thickness of the sunshade support ring would then be[1]

$$t = \sqrt{\frac{F_{buckling} (1 - \mu^2) r^2}{K E}}$$

where

$$K = 0.17$$

then

$$t = \sqrt{\frac{5100 (1 - .3^2) 3.9^2}{0.17 (10 \times 10^2)}}$$

$$t = 0.203 \text{ in.}$$

This thickness is an approximate first-mode, single-degree of freedom, natural sunshade frequency in the transverse direction, assuming a cylinder 7.8 inches in diameter, 7.4 inches long, 0.10 inches thick, and fixed at the flange or support.

The approximate static deflection of the shade would then be

$$S_{st} = \frac{1}{3} \frac{W_1 \ell^3}{E I} + \frac{1}{8} \frac{W_2 \ell^3}{E I} \qquad (10)$$

where

$$W_1 = \pi (7.8)(.10)(7.4)(.10)$$

$$W_1 = 1.8 \text{ lb}$$

$$W_2 = (15.56^2 - 9.56^2) .7854 \times .10 \times .10$$

$$W_2 = 1.2 \text{ lb}$$

$$I = \pi (3.9^3)(.1)$$

$$I = 18.6 \text{ in.}^4$$

then

$$S_{st} = \frac{1.8 (7.4)}{3 (10 \times 10^6)(18.6)} + \frac{1.2 (7.4)}{8 (10 \times 10^6)(18.6)}$$

$$S_{st} = .03 \times 10^{-6}$$

and the natural frequency is

$$f_n = \frac{1}{2\pi} \sqrt{\frac{386}{.03 \times 10^{-6}}}$$

$$f_n = 18{,}000 \text{ Hz}$$

APPENDIX I

PRELIMINARY THERMAL ANALYSIS OF THE LCE PASSIVE RADIATOR

1.0 SUMMARY

A thermal analysis was made on the passive radiator portion of the Laser Communication Experiment package described in Reference 1. The location of the radiator is as shown in Figure I-1. It is necessary for the passive radiator to maintain the surface on which the detector is mounted at a temperature of approximately 100°K in order that the detector operate with adequate sensitivity. To obtain a surface at such a low temperature using passive means it is necessary to isolate the surface, to the maximum extent possible, from all external heat sources while still allowing the surface to view space. Therefore, the passive radiator design presented herein, was an attempt to maximize the heat loss from the cold surface by providing a good view to space while at the same time minimizing the heat gain from its surroundings by the use of insulation and radiation barriers.

The purpose of this analysis was to determine if the passive radiator design concept for the 10.6-micron Laser Connunications Experiment package suggested in Reference 1 could provide a cold surface temperature of 100°K for the detector, assuming its most severe thermal environment. A schematic of this design is presented in Figure I-2 and consists of an 8-stage radiator surrounded by a truncated conical shield.

This analysis showed that the cold surface would reach a peak temperature of 130°K and have a temperature fluctuation of 43°K during the 23° orbit using the radiator configuration suggested and a surface specularity of 0.95 for the inside of the shield. If the specularity of the inside surface of the shield could be increased to 0.99, then the maximum cold surface temperature could be reduced to approximately 105°K and the temperature fluctuation of that surface could be reduced to about 17°K.

This report recommends that a comprehensive investigation be initiated to determine the highest specularity which can be practically obtained for the surfaces on the inside of the shield. It also suggests that it would be possible to reduce the cold stage temperature fluctuation during an orbit by removing a portion of the shield on the antenna side. Another approach to improving performance would be to paint the radiator white or install second surface mirrors to reduce absorption of incident energy.

The previous analysis described in Reference 1 suggested that the shield be enlarged on the side facing the antenna so that there would be no direct view from the antenna to the inside of the shield and the radiator. It was also recommended that the shield be divided into a number of nodes to account for circumferential and axial variations in shield temperature. These suggestions were incorporated into this analysis.

The analysis just completed shows that, in order to make a realistic evaluation of the capabilities of the passive radiator for this application, it is essential that the magnitude of the solar heat load on the cold stage of the radiator be predicted with a high degree of confidence. This requires an accurate prediction of the final destination of solar rays both specularly and diffusely reflected from the inside surface of the shield.

2.0 METHOD OF ANALYSIS

The Monte Carlo computer program was used to provide infrared radiation heat transfer information and to determine the solar heat load on the various surfaces. The CINDA computer program was used for the general heat transfer solution.

The passive radiator model used in this thermal analysis consisted of an eight-step radiator surrounded by a shield which acted as a radiation barrier to the solar rays, and the infrared radiation from the antenna. The thermal model used in the CINDA analysis is shown in Figure I-2. In order to prevent the antenna (whose temperature was assumed to be 150°F) from seeing the inside surfaces of the shield and the radiator, the shield height was increased on the side facing the antenna. In this configuration the shield was

the second largest heat source for the radiator cold surface and, therefore, the temperature gradient through the shield had to be determined if the magnitude of this heat source was to be accurately represented in the thermal model. For this reason, the shield was axially divided into two nodes and circumferentially divided into 8 nodes for the analysis. Axial and circumferential conduction in the shield were taken into account in the analysis. In addition, conduction between the radiator stages, as well as radiation between the stages, was accounted for.

In determining the B_{ij}'s for this analysis, it was assumed that a symmetry plane could be established which passed through the highest and lowest points on the shield and lay perpendicular to the vehicle surface. Solar B_{ij}'s were determined for five orbit positions, 0°, 180°, 225°, 270°, and 315°, and the remainder (i.e., 45°, 90°, and 135°) were derived by reversing the shield nodes about the above mentioned symmetry plane. The size of the fictitious sun was changed for the various orbit positions, in order to minimize the number of rays which went directly to space. It was assumed in the analysis that the sun rotated clockwise around the radiator shield. The line joining the highest point on the shield with the shield center line was defined as the zero degree orbit angle, see Figure I-2. The summer solstice condition (with a sun angle of 23.5°) was used.

Albedo and earthshine effects were assumed to be negligible. The solar constant, S, was assumed to be 442 Btu/hr-ft^2. The solar heat loads on the various surfaces were determined as follows (i.e., for surface j):

$$Q_j = B_{sj} A_s \cdot S$$

Where: B_{sj} is the graybody view from the sun to surface j

A_s is the area of the fictitious sun

S is the solar constant

The construction of the simulated sun at an orbit angle of 180° is shown in Figure I-3. It was assumed that the antenna did not obscure or partially block the view from the radiator assembly to the sun for any orbit angle.

It was also assumed that 75% of the rays generated in the radiator assembly passed through the antenna to space (i.e., three quarters of the antenna cross-section perpendicular to the rays was occupied by space rather than the antenna). The radiation properties of the surfaces used in this analysis are presented in Table I-1.

The vehicle skin temperature was assumed to be a constant 70°F. The heat load on the cold stage from the detector wire losses was assumed to be 19 mw.

All radiant heat flow paths were taken into account in the analysis regardless of how small the magnitude of the heat flow to the cold surface appeared to be. In the initial CINDA run the specularity of the inside shield surface was assumed to be 0.95. Since the results of the initial run indicated that this value must be 0.99 or greater to approach a cold surface temperature of 100°K, the specularity was increased to 0.99 for the remaining CINDA run.

The units used in the analysis were as follows:

Parameter	Unit
Time	Orbit angle (hours times 15)
Length	Feet
Heat	Btu
Temperature	°F

In the CINDA output, some of the data was converted to other units. When this was done it was so specified in the output label at the head of the converted data. A periodic temperature convergence criteria was established in the CINDA computer program which terminated the solution when all of the node temperatures at the end of an orbit were within 1°F of their values at the end of the previous orbit. Convergence was obtained after the second orbit.

3.0 RESULTS AND DISCUSSION

The results of this analysis are presented graphically in Figures I-4, -5, and -6 and are summarized in Tables I-2, -3, and -4.

It is clear from the results that the specularity of the surface on the inside of the shield must be 0.99, or greater, if a cold-surface temperature of approximately 100°K is to be maintained. If the truncated cone configuration for the shield is used, a cold-stage temperature fluctuation of 17°K or greater can be expected during an orbit, depending upon the specularity of the inside surface of the shield. If a surface with a specularity of less than 0.99 were used for the inside of the shield the values of these parameters would increase. For instance, a specularity of 0.95 would result in an increase in the peak cold surface temperature to 130°K and an increase in the temperature fluctuation of that surface to 43°K.

By far the greatest heat load on the cold surface came from solar energy which was diffusely reflected from the shield onto the cold surface. The raised portion of the shield, unfortunately, provided a larger target area from which these rays could be diffusely reflected onto the cold surface during a portion of the orbit. The conclusion from this analysis is that raising the shield height on the side facting the antenna did result in eliminating the antenna as a heat source for the cold surface but at the expense of increasing the sun load through a portion of the orbit and this resulted in a higher cold surface maximum temperature and also greatly increased the cold surface temperature fluctuations during an orbit. Shield temperatures and circumferential and axial temperature differences are shown in Table I-4. The differences between 95% and 99% specularity are negligible. The highest shield temperatures are on the side toward the sun. No further analysis of gradients was performed.

4.0 RECOMMENDATIONS AND CONCLUSIONS

It appears that one way to obtain a cold-surface temperature of approximately 100°K is to find a surface coating or material for the inside of the shield which has a specularity of 0.99 or greater. A specularity of 0.99

on the inside surface of the shield would reduce the maximum cold surface temperature to about 105°K and the temperature fluctuations of that surface to about 17°K. The cold surface temperature fluctuation could be further decreased by reducing the shield cone truncation (by reducing the truncation angle) thus equalizing the heat load on the cold surface during the orbit.

The temperature fluctuation in the cold stage during an orbit is caused by the variation in the sun load around the orbit resulting from the non-symmetrical shape of the shield. It can be reduced by:

- Increasing the surface specularity of the inside of the shield (since it appears that only surfaces using the highest possible specularity can be used to keep the cold surface temperature within the allowed limits, a reduction below 17°K does not seem possible by this method)
- Remove or reduce the degree to which the shield cone is truncated, as suggested above, and thus decrease the sun load variation during the orbit
- Significantly increase the capacitance of the cold stage and thus dampen the cold stage temperature fluctuation during an orbit

The second alternative is the most practical especially if surface specularities of 0.99 or greater on the inside of the shield cannot be obtained. It will result in a heat load from the antenna but that heat load will be nearly constant throughout the orbit. The peak solar heat load will be reduced while the minimum solar heat load will be increased thus more evenly distributing the total heat load during the orbit. It is not suggested that the raised portion of the shield be eliminated since that might result in too high a cold-surface peak temperature. Instead, what is suggested is a tradeoff be made between the increase in antenna heat load which would result from taking away part of the raised portion of the shield and the more even distributions of the solar heat load during an orbit which would also result. The following parameters would have to be taken into account in such a tradeoff:

- Maximum allowed cold surface temperature
- Maximum allowed cold surface temperature fluctuation during an orbit
- The maximum specularity of the inside surface of the shield which could be practically obtained and maintained
- The antenna temperature, infrared emissivity and effective surface area

The most influential factor in determining cold-stage temperature, found from this analysis, is the degree of surface specularity (i.e., a practically achievable value). The sun load is the largest load on the cold stage and is directly related to surface specularity.

At the present time, shield gradients are a secondary factor in determining cold-stage temperature. Consequently, further analysis of gradients is not suggested at this time.

Additional studies of passive radiator design should consider other approaches to improving performance besides surface specularity. One approach might be to reduce the absorption of incident energy on the cold stage by replacing the black surface with a white paint or second surface mirrors. Another area not to be forgotten pertains to ease of fabrication (e.g., problems associated with mounting second surface mirrors on the outside surface of the shield and on the stacked radiator surfaces, detector alignment and support, and fabrication of the shield and radiator).

TABLE I-1

RADIATION PROPERTIES OF THE SURFACES

Surface Description	Properties* α_s	ϵ	S	T
Radiator Step (3M black paint)	0.95	0.95	0.	0.
Radiator Side (Gold plate)	0.15	0.03	0.95	0.
Shield Inside Case I**	0.15	0.03	0.95	0.
Shield Inside Case II (Gold plate)	0.15	0.03	0.99	0.
Shield Outside** (Second surface mirrors)	0.06	0.77	0.95	0.
Vehicle Skin (Second surface mirrors)	0.06	0.77	0.95	0.
Antenna		0.9	0.	0.75

* Notes:

α_s ~ Solar absorptivity

ϵ ~ Infrared emissivity

S ~ Specularity

T ~ Transmissivity

** Shield material is 0.010 in. thick aluminum

TABLE I-2

COLD STAGE TEMPERATURE SUMMARY*

Case No.	Inside Shield Surface Specularity	Maximum Cold-Stage Temperature °K	Minimum Cold-Stage Temperature °K	Cold-Stage Temperature Fluctuation °K diff.
I	0.95	130.4	87.7	42.7
II	0.99	104.5	87.7	16.8

*See Figure I-4

TABLE I-3

COLD STAGE HEAT GAIN AND LOSS SUMMARY*

Case No.	Inside Shield Surface Specularity	Heat Gain, milliwatts: Sun Max	Sun Min	Shield Max	Shield Min	Bias and Cond. Loads	Radiator Conduction Max	Radiator Conduction Min	Radiation From Rest of Radiator Max	Radiation From Rest of Radiator Min	Antenna	Space Heat Loss, mw Max	Space Heat Loss, mw Min
I	0.95	423.5	0	76.6	62.4	19	3.7	-30.1	0.49	0.21	0	451.4	92.5
II	0.99	84.7	0	82.5	62.4	19	10.5	0.49	0.49	0.45	0	186.4	92.5

*See Figures I-5 and I-6.

TABLE I-4

SHIELD TEMPERATURES*

	Orbit Position: 180° Max	180° Min	180° ΔT	270° Max	270° Min	270° ΔT	360° Max	360° Min	360° ΔT
Circumferential-Lower Portion	-11.6°F	-78.3°F	66.7	-34.9°F	-75.3°F	40.4	-47°F	-96.3°F	49.3
Circumferential-Upper Portion	-40.2	-100.5	60.3	-68.6	-106.5	37.9	-89.	-123.2	34.2
Axial-Upper to Lower	-33.6	-62.6	29.0	-50.	-106.	56.	-47.	-121.	74.

*Results for 95% and 99% specularity are the same for engineering purposes.

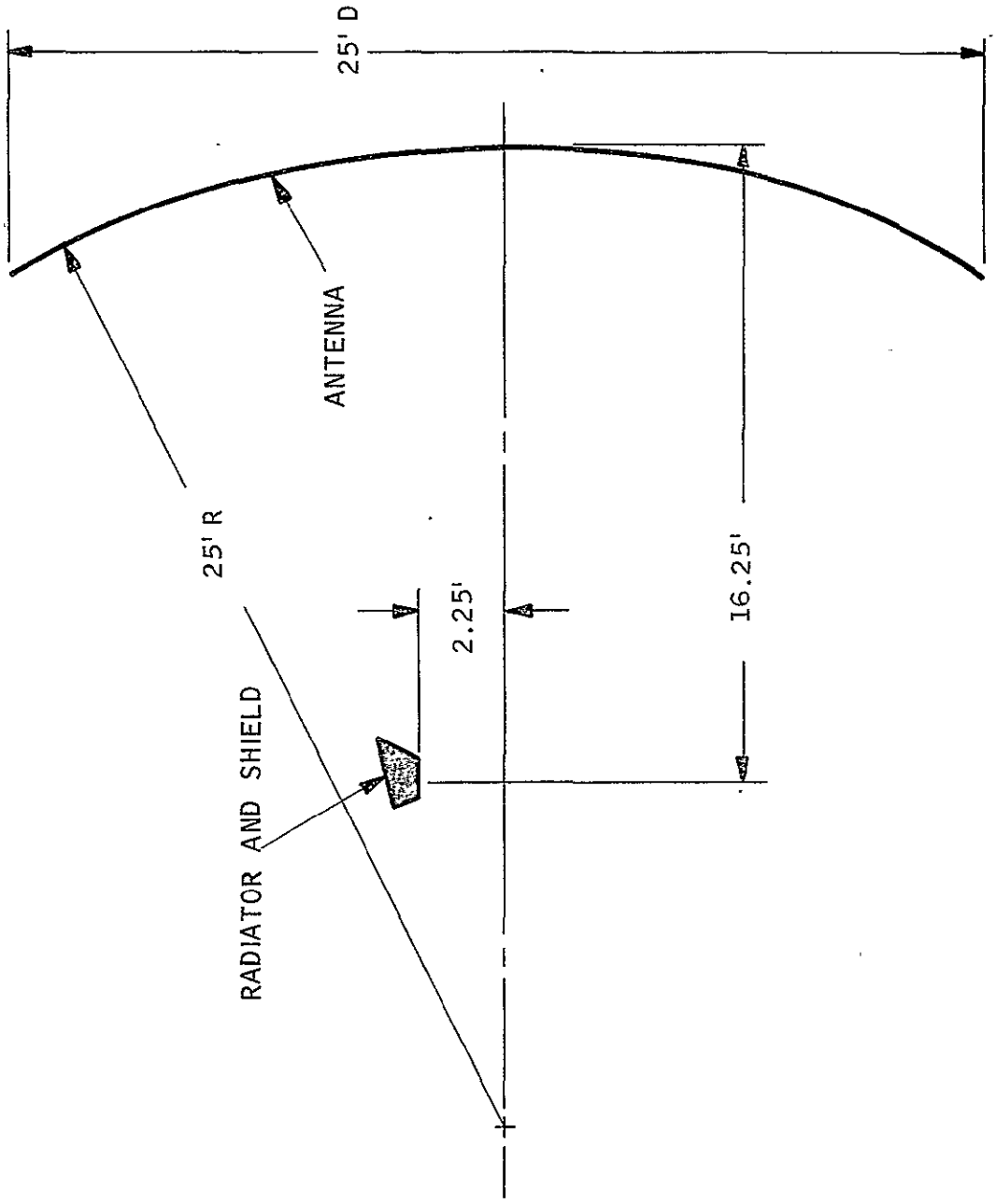

SPATIAL LOCATION OF PASSIVE RADIATOR

Figure I-1

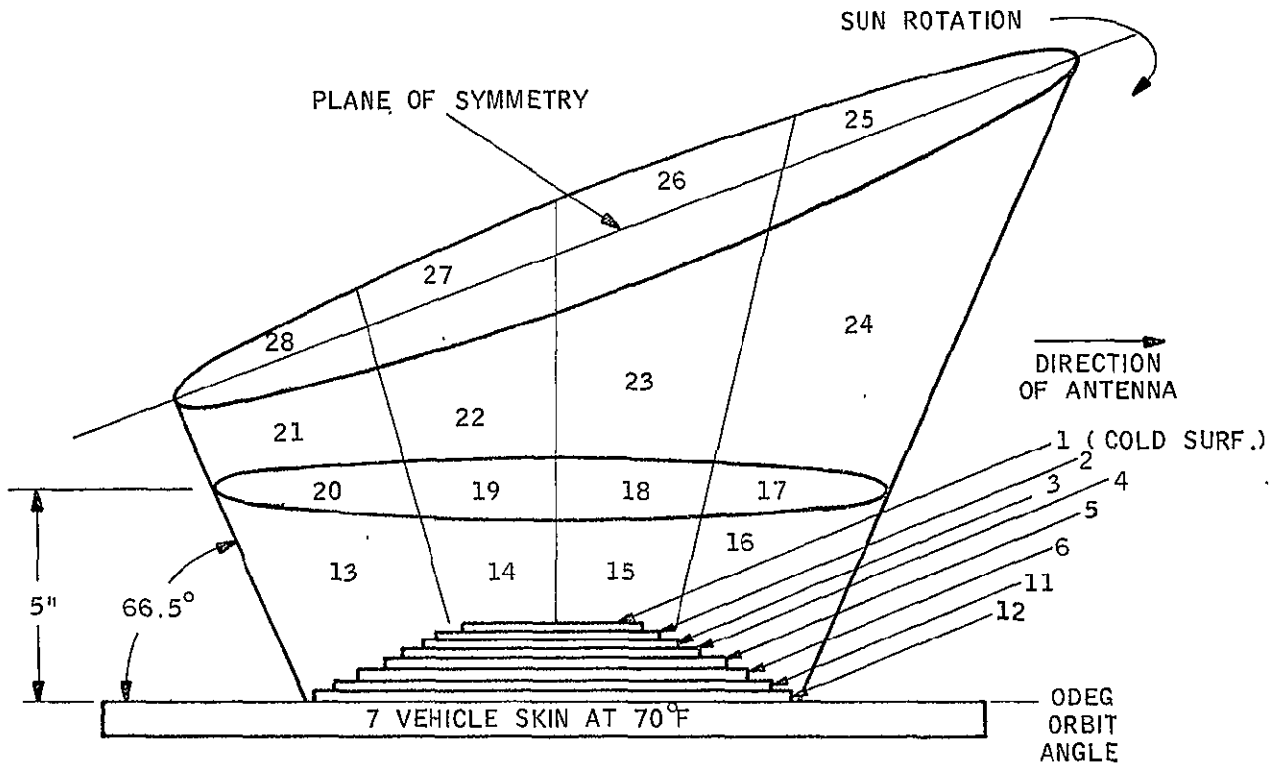

Figure I-2

RADIATOR NODAL SCHEMATIC FOR THE SINDA PROGRAM

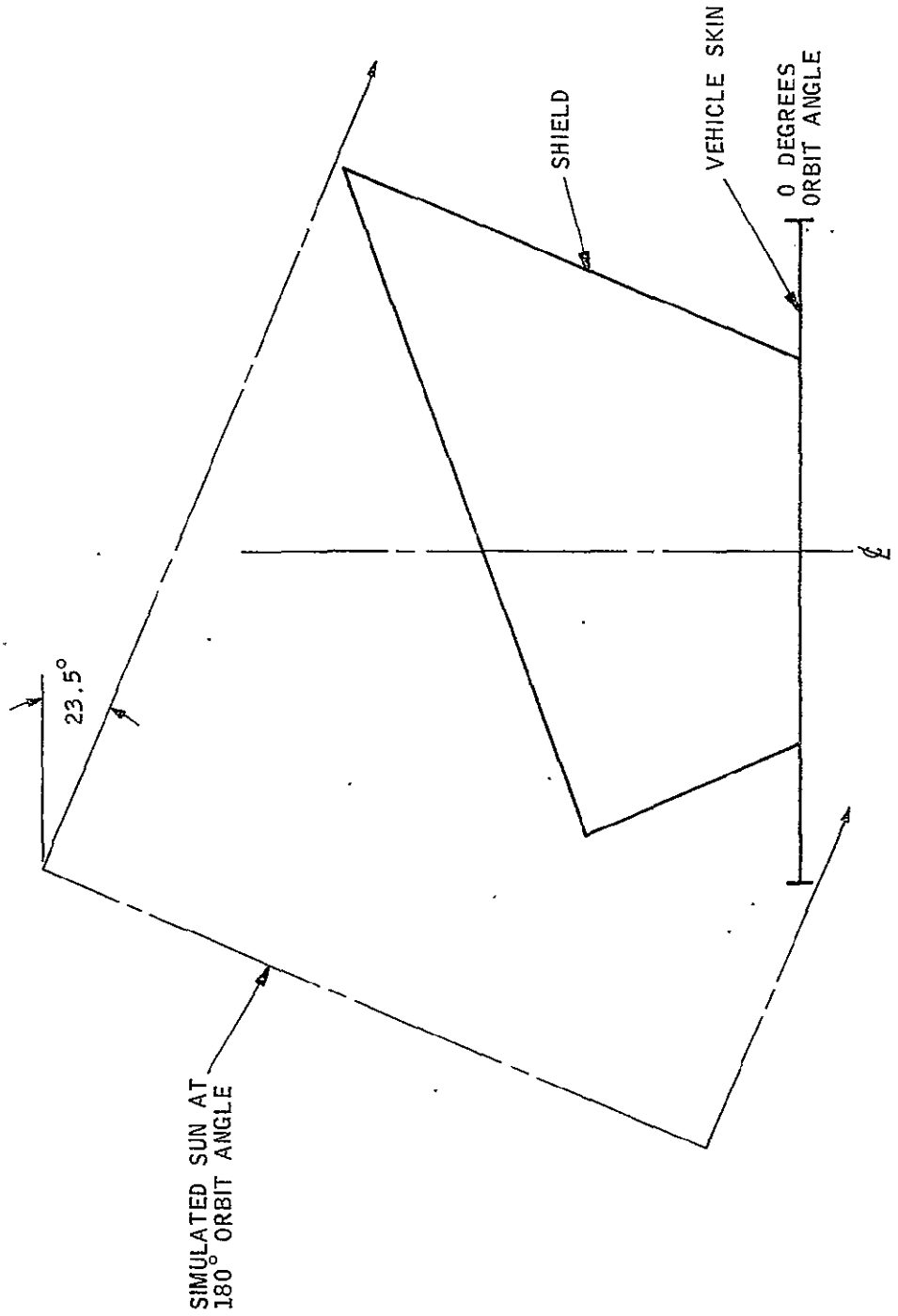
SHIELD
VEHICLE SKIN
0 DEGREES
ORBIT ANGLE
23.5°
SIMULATED SUN AT
180° ORBIT ANGLE
SUN SIMULATION

Figure I-3

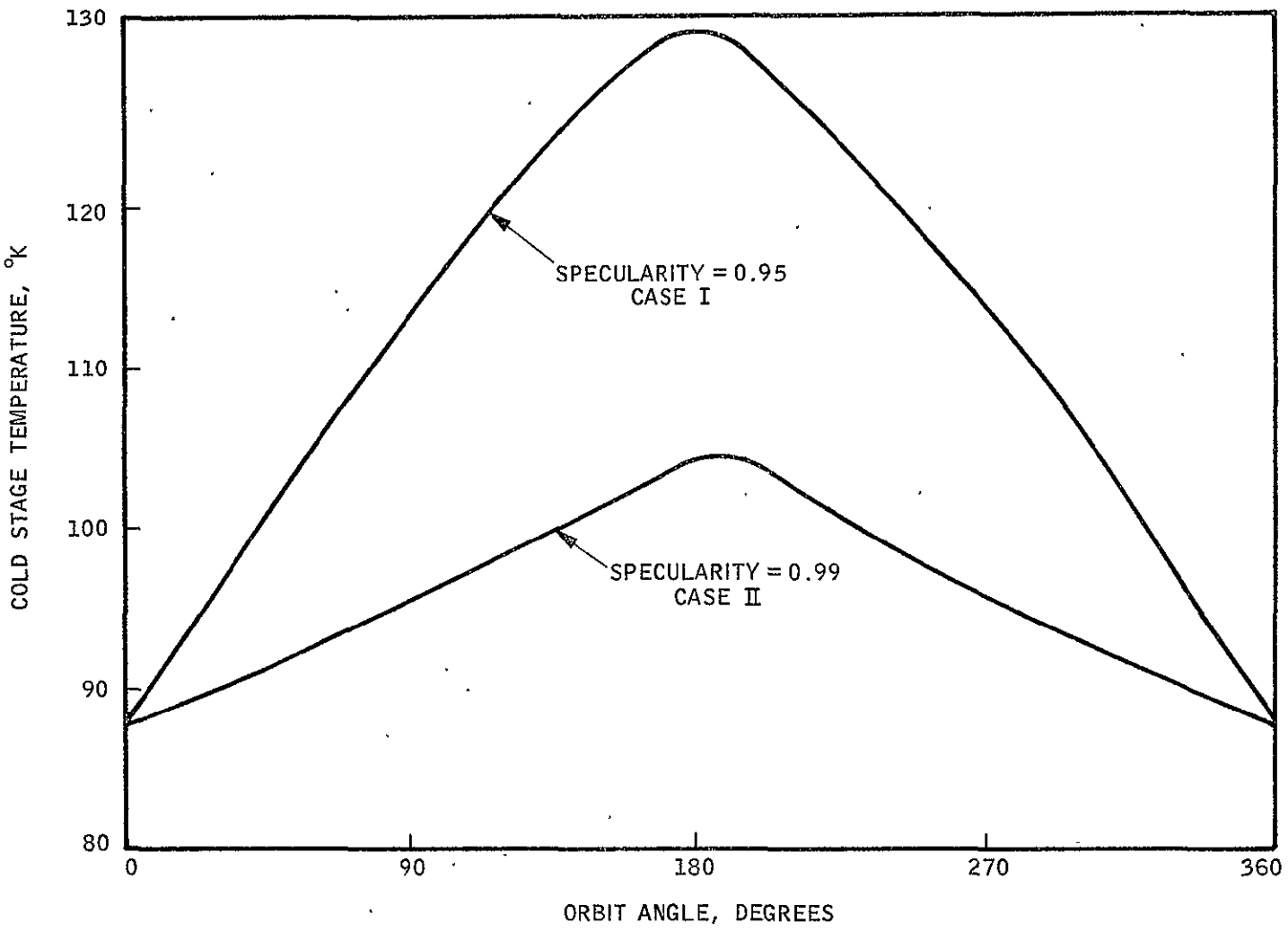

Figure I-4

RADIATOR COLD STAGE TEMPERATURE FOR TWO INSIDE SHIELD SURFACE SPECULARITIES

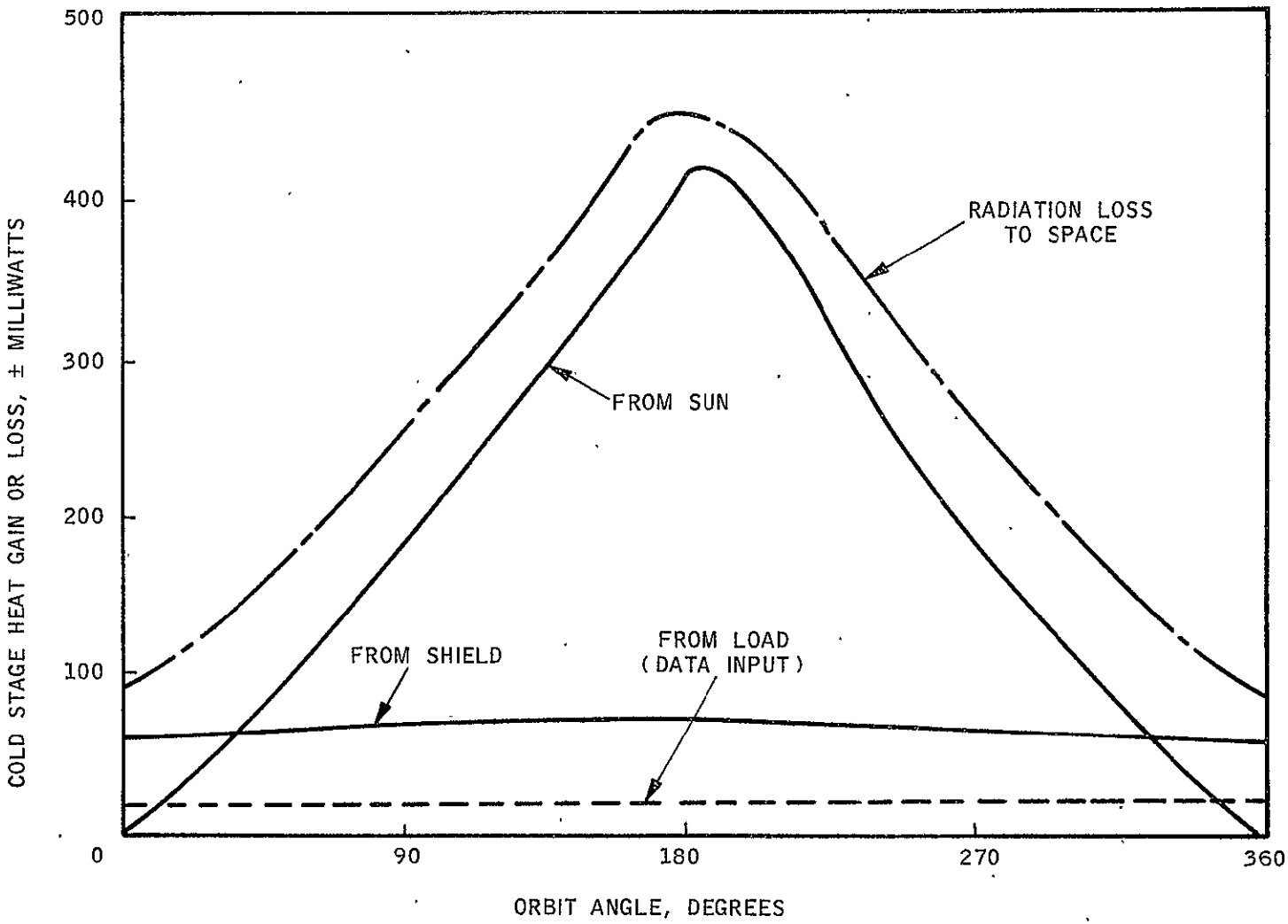

RADIATOR COLD STAGE HEAT GAIN AND LOSS INSIDE SHIELD SPECULARITY = 0.95

CASE I

Figure I-5

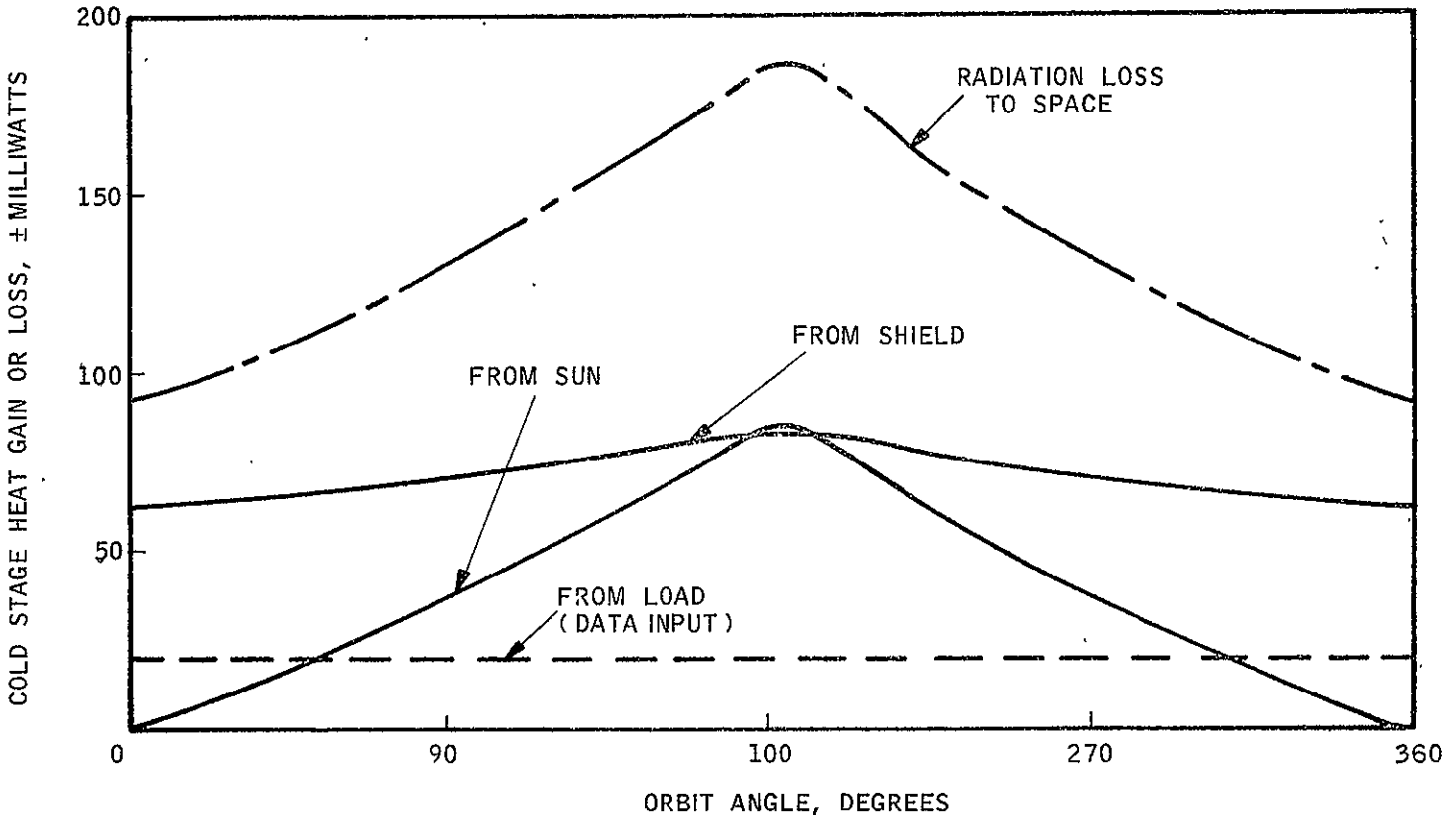

RADIATOR COLD STAGE HEAT GAIN AND LOSS

INSIDE SHIELD SPECULARITY = 0.99

CASE II

Figure I-6

APPENDIX J

TECHNICAL MEETING WITH PHILCO-FORD, PALO ALTO, ON 22 JANUARY 1970

On 22 January 1970, the writer made a trip to Philco-Ford in Palo Alto, California. The purpose of this trip was to learn more about the work Philco-Ford was doing on their 77°K passive radiator design study and to exchange information that we had learned from our past experience with low temperature passive radiator systems.

Philco-Ford personnel were very open about what they had learned from their studies and willing to exchange information. Contact was made with Richard H. Hullett (analyst for the design study) and Carl Zierman (Supervisor, Thermal Technology Group).

In Philco-Ford's design study, detail analyses were performed for one particular orbital altitude; i.e., the lowest earth altitude. The other altitudes were given a much more cursory look. The altitudes and vehicle orientation of concern were:

1. A 200-nautical mile altitude, earth oriented satellite with the longitudinal axis of the satellite always parallel to the sun throughout the year.

2. A 600-nautical mile altitude, spin stabilized satellite, inclined 45° to the equatorial plane. Satellite is always 45° to the sun rays throughout the year.

3. A synchronous altitude, spin-stabilized satellite.

In all of the analyses no concern had to be given to spacecraft appendages.

The general design configuration they finally arrived at for the 200-nautical mile altitude is shown in Figure J-1. They used a low conductance shield (made out of fiberglass honeycomb) mounted with low conductance mounts (fiberglass brackets). They were dissipating a 10-milliwatt heat load, excluding IR and other heat loads from the shields on the radiator, they predicted a radiator temperature of 121°F (67.39°K) for the ideal case (i.e.,

adiabatic walls and 100% specularity for the shields). Focus of each parabolic shield was outside the spacecraft boundary.

A parametric summary of their results for the 200-nautical mile altitude radiator design is presented below:

10-mw Heat Load on Radiator

Parameter	Temperature, ^{o}R
1. α_s shields (0.12)(1) 0.06 - 0.16	145-152
2. ϵ shields (0.04) 0.02 - 0.06	148-153
3. Specularity (100%) solar IR	0.3^{o}R/%) over the range 1.0^{o}R/%) of 90-100%
4. ϵ radiator (0.9) 0.9 - 1.0	150-148
5. Insulation thickness (1.5") 0.5 - 3.0 in.	165-145
6. Unit conductance(2) (.003 Btu/hr-ft^2-^{o}R) 0 - 0.05	150-105

(1) The numbers in brackets are nominal values.
(2) Unit conductance is defined as area for conduction/area of shield.

The Philco representatives expect no seasonal variations, only orbital changes. Radiator temperature would vary $\pm 2^{o}K$ and the first shield would vary $\pm 12^{o}K$. They were obtaining $460^{o}R$ ($273^{o}K$) on the first shield and $280^{o}R$ ($156^{o}K$) on the second shield. They didn't have any details on detector mounting. Detector wire under consideration is constantan or stainless steel. (No other details as to length or size.) They are using a stacked radiator design as shown in Figure J-1. For this radiator design, conduction became the primary mode of heat transfer.

They didn't have much detail on the other two orbits, because they felt the 200-nautical mile orbital altitude would be the most difficult. They certainly agreed upon the double shield configuration as the most promising approach to obtaining low temperatures passively.

They said they were willing to talk about bidding for the work on the radiator, i.e., shield design and building.

We did talk to some extent on the Laser Communications Experiment proposal work they had done. Their design was very similar to ours except that their stacked radiator acted as a multiple radiative shield (as shown in Figure J-1) where our design isolated each radiator stage with TG1500 insulation. They had a single shield design which was allowed to look at the antenna and solar panel. They were not able to achieve 100°K during summer solstice, they did obtain 125°K on the cold stage during this time of the year.

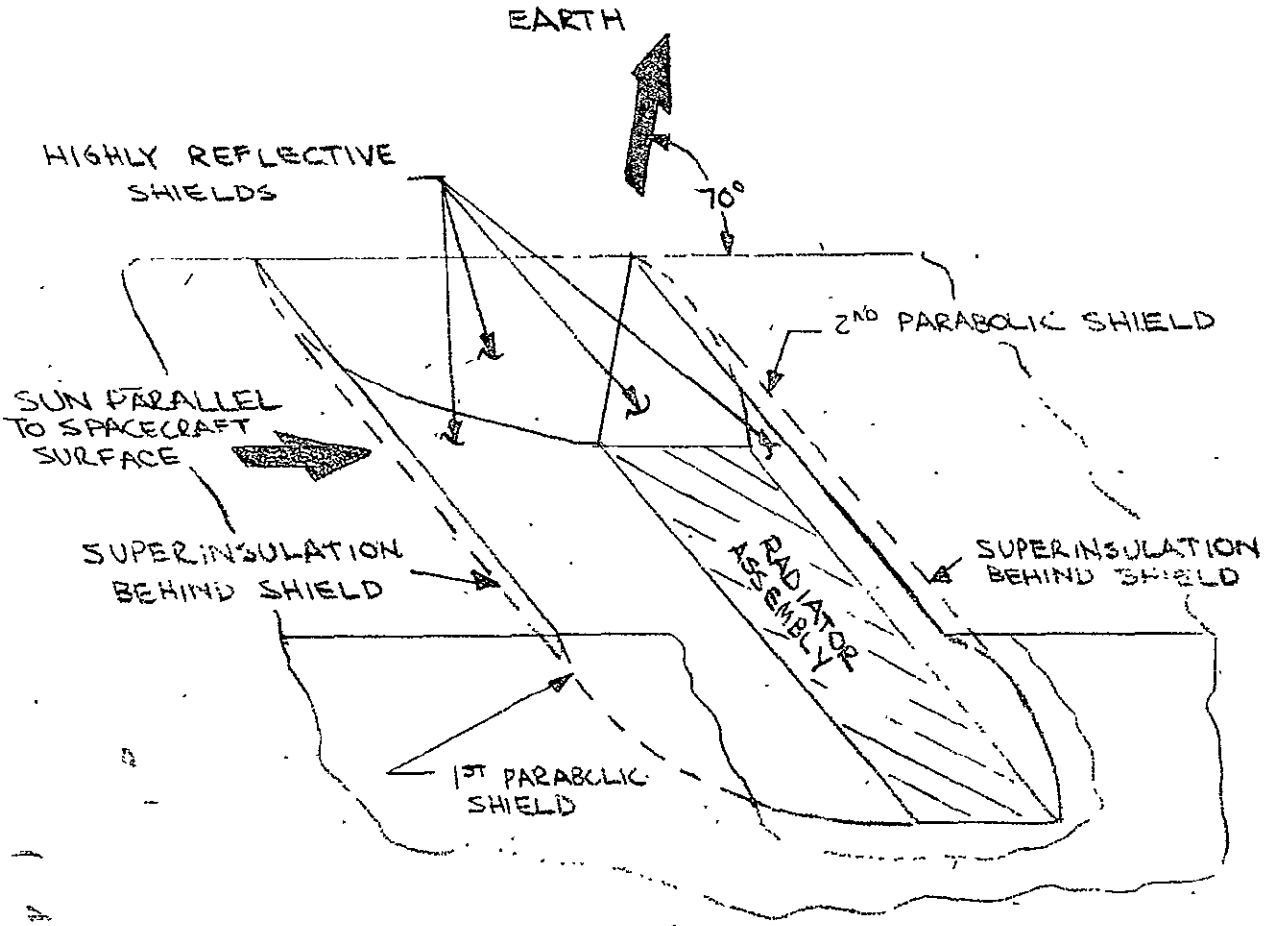

RADIATOR ASSEMBLY

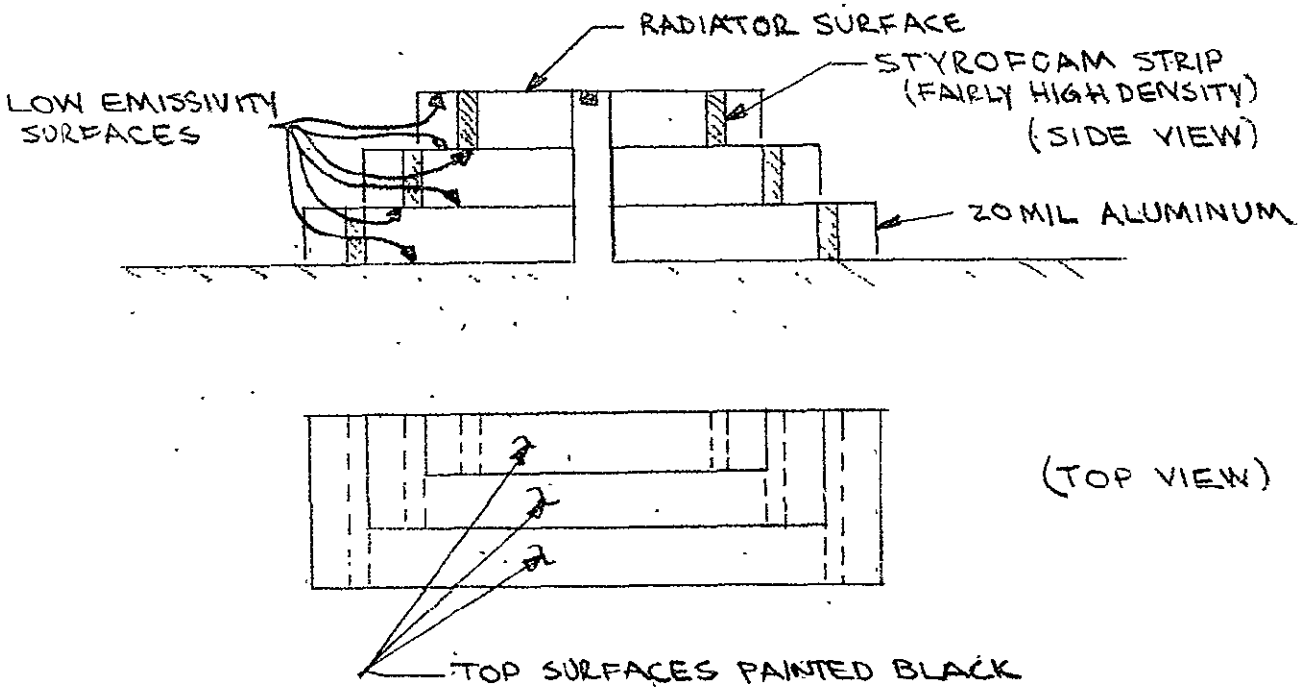

General Configuration of Philco-Ford's
Double Shielded Passive 77°K Radiator

Figure J-1

APPENDIX K

ANALYSIS OF WIRE-GRATING-POLARIZER DUPLEXER

Grating performance can readily be analyzed following the method of Auton (Ref. 1). If the grids are assumed to form an infinitely extended plane grating of metallic strips of zero thickness and infinite conductivity at the boundary between air and a transparent dielectric medium (Figure K-1), the equivalent impedance can be determined from equations given by Marcuvitz (Ref. 2). For a grating of period d and strip width a, the equivalent impedance (reactive for a high-conductivity grid) for incident radiation with an E-field vector parallel to the grooves is given by

$$\left(\frac{X_g}{Z_o}\right)_{\parallel} = \frac{d \cos\theta}{\lambda}\left\{\ell n\left(\csc\frac{\pi a}{2d}\right) + \frac{1}{2}\frac{(1-\beta^2)^2\left[\left(1-\frac{\beta^2}{4}\right)(A_+ + A_-) + 4\beta^2 A_+ A_-\right]}{\left(1-\frac{\beta^2}{4}\right) + \beta^2\left(1+\frac{\beta^2}{2}-\frac{\beta^4}{8}\right)(A_+ + A_-) + 2\beta^6 A_+ A_-}\right\} \qquad (1)$$

$$\beta = \sin\frac{\pi a}{2d}$$

$$A_{\pm} = \left[1 \pm \frac{2d \sin\theta}{\lambda} - \left(\frac{d\cos\theta}{\lambda}\right)^2\right]^{-1/2} - 1$$

If the E-field vector is perpendicular to the strips,

$$\left(\frac{Z_o}{X_g}\right)_{\perp} = \frac{4d\cos\theta}{\lambda}\left\{\ell n\left(\csc\frac{\pi(d-a)}{2d}\right) + \frac{1}{2}\frac{(1-\gamma^2)^2\left[\left(1-\frac{\gamma^2}{4}\right)(A_+ + A_-) + 4\gamma^2 A_+ A_-\right]}{\left(1-\frac{\gamma^2}{4}\right) + \gamma^2\left(1+\frac{\gamma^2}{2}-\frac{\gamma^4}{8}\right)(A_+ + A_-) + 2\gamma^6 A_+ A_-}\right\} \qquad (2)$$

$$\gamma = \frac{\sin \pi (d-a)}{2d}$$

$A_{\pm}$ = same expression as above

The grating geometry and transmission-line equivalent circuit are shown in Figure K-2. For a nonconducting substrate, the characteristic impedance of the circuit is

$$Z_s = \frac{1}{n} Z_o$$

where Z_o is the impedance of free space and n is the refractive index.

The transmittances of the grid on an interface can be shown to be

$$t_{\perp} = \frac{4 n (X_g/Z_o)_{\perp}^2}{(1 + n)^2 (X_g/Z_o)_{\perp}^2 + 1} \tag{3}$$

and

$$t_{||} = \frac{4 n (X_g/Z_o)_{||}^2}{(1 + n)^2 (X_g/Z_o)_{||}^2 + 1} \tag{4}$$

When $\lambda/d \gg 1$, $(X_g/Z_o)_{\perp} \longrightarrow \infty$ while $(X_g/Z_o)_{||} \longrightarrow 0$, which results in

$$t_{\perp}(n)/t_{\perp}(1) = 4 n/(1 + n)^2 \tag{5}$$

and, by successive application of L'Hospital's rule,

$$t_{||}(n)/t_{||}(1) = n \tag{6}$$

The substrate has the doubly adverse effect of reducing the perpendicular transmittance and increasing the parallel transmittance. This effect can be removed by the use of a quarter-wavelength impedance matching layer (which also functions as an antireflection coating), as shown in Figure K-3. The transmittances in this case reduce to those of an unsupported grid. It is not satisfactory to place the coating on top of the grid, because there is still an impedance mismatch that can be shown to cause losses proportional to n^2.

Equations (1) through (4) were evaluated as a function of λ/d and a/d for $\theta = 0$ and 45°, with n = 1, 2.5, and 4. The results are presented in Figures K-4 to K-8. The degree of polarization, P, is defined as $(t_\perp - t_{||})/(t_\perp + t_{||})$, which from the requirements (paragraph 5.2.1.6 of Volume I, Part 1), must be 0.7 or greater. Before discussing application of the theory to LCE polarizer design, it is pertinent to point out some restrictions on the use of the equivalent-circuit equations. The wavelength and angle of incidence must satisfy the following relationship:

$$d(1 + \sin\theta)\lambda < 1$$

or at $\theta = 45^\circ$, $\lambda/d > 1.71$. This requirement is equivalent to the statement that the first-order diffraction peak does not leave the grating at a grazing angle $(\pi/2)$ - i.e., there are no diffraction losses. The accuracy claimed for the equations is 5% or better for $\lambda/d \geq 1$ and 1% or better for $\lambda/d \geq 2$. This claim is essentially substantiated experimentally (Ref. 1).

Figures K-4 and K-5 show results for $\theta = 0$ and $\theta = 45^\circ$ for λ/d between 2 and 16. The polarization efficiency is slightly higher for a 45° angle of incidence, which helps the present experiment somewhat. The small effect of angle of incidence has been verified by the detailed studies of Pursley (Ref. 3) (provided, of course, that the requirement for no diffraction is fulfilled). It appears that a λ/d value as small as 2 would meet the present requirements. However, the slope of the $t_{||}$ curve is very large here and, as an added safety margin, a value of λ/d of 4 to 5 will be specified.

Figures K-4 and K-5 apply to a value of $a/d = 0.5$ - i.e., equal wires and spaces. Figures K-6 and K-7 show how the performance varies with a/d for λ/d fixed at 4 and 10. The objective is to attain large $t_\perp$ and P. While the performance is fairly insensitive to a/d for large λ/d, there is still wide latitude over which satisfactory performance results at $\lambda/d = 4$. An a/d of 0.5 is selected for a nominal value. Figure K-8 shows the effect of using uncoated substrates of index 2.5 (Irtran-type materials) and 4 (germanium). It is obviously necessary to coat Ge, and is desirable to coat lower-index materials for added safety margin. Ge is the best choice optically and mechanically.

For coherent light, the substrate can act like a Fabry-Perot interferometer. For low reflectance, however, the finesse is small and the transmission peak of the interferometer is broad. Furthermore, the properties of the polarizer are such that the multiply reflected light that would result in interference in the transmitted beam is efficiently coupled back through the grating. It is not expected that interference effects will be harmful. Auton (Ref. 1) observed no effects due to film thickness, presumably because the thinnest film (0.2 micron) was almost an order of magnitude thicker than the skin depth at the longest wavelength (100 microns). At 10 microns, there should likewise be no problem with film thickness. Casey and Lewis (Ref. 4) have shown that absorption in the wires is negligible in far-infrared one- and two-dimensional grids.

REFERENCES

1. J. P. Auton, "Infrared Transmission Polarizers by Photolithography," Appl. Opt., 6, 1023 (1967).

2. N. Marcuvitz, MIT Waveguide Handbook, New York, McGraw-Hill, 1951, p. 284.

3. W. K. Pursley, PhD Thesis, University of Michigan, 1956.

4. J. P. Casey and E. A. Lewis, J. Opt. Soc. Am., 42, 971 (1952).

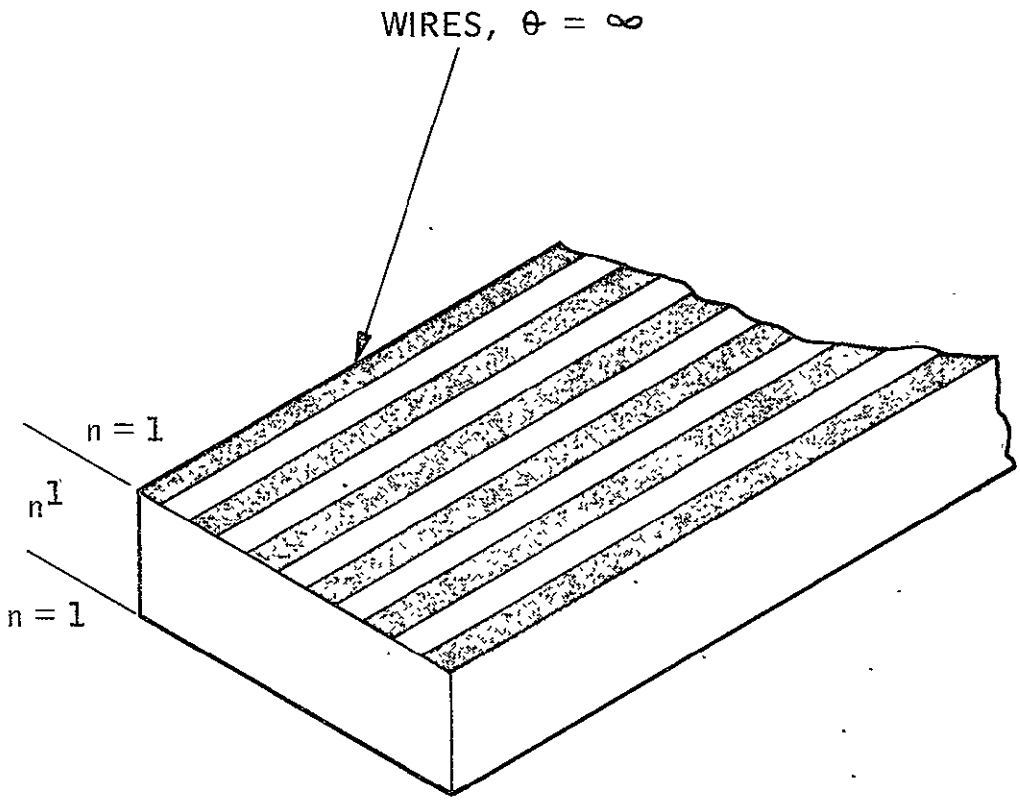

WIRE GRATING ON DIELECTRIC SUBSTRATE

Figure K-1

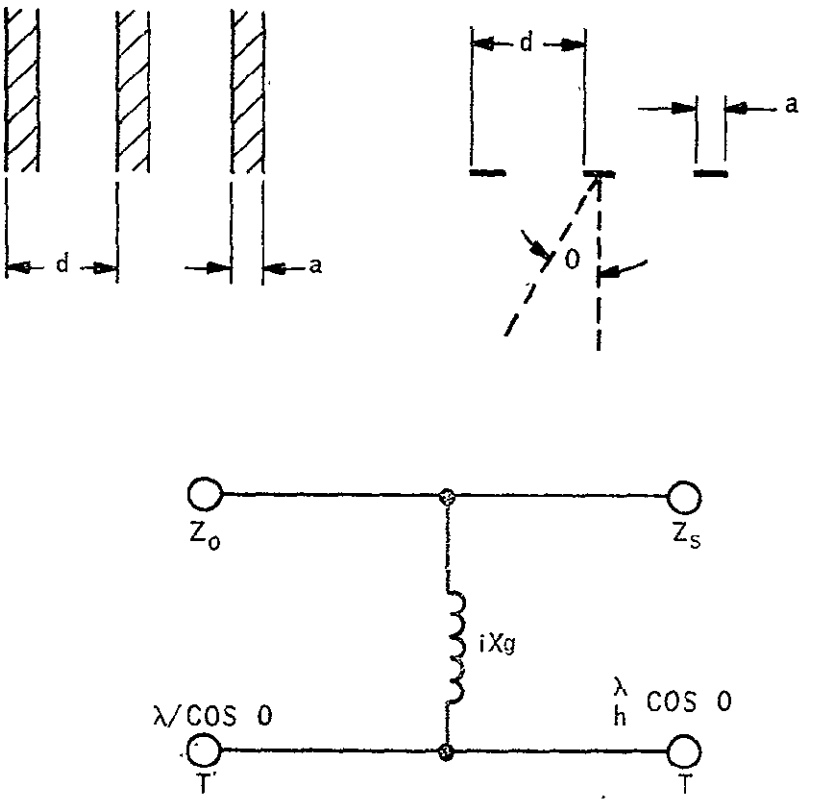

WIRE GRATING GEOMETRY AND
EQUIVALENT CIRCUIT

Figure K-2

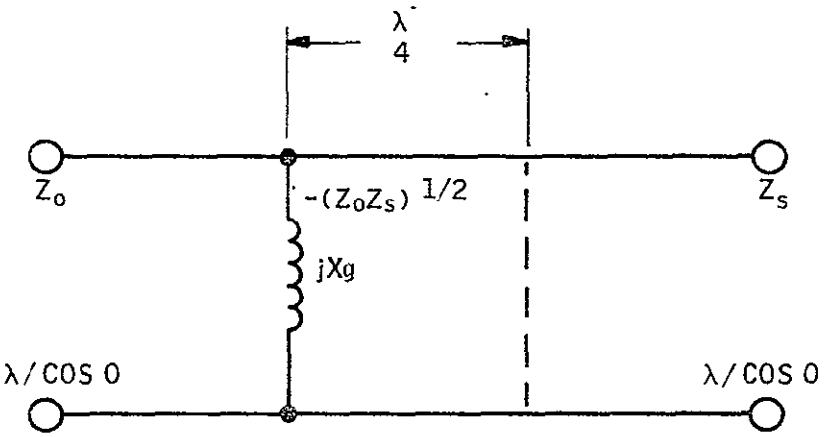

EQUIVALENT CIRCUIT OF WIRE GRID ON SUBSTRATE WITH IMPEDANCE MATCHING

Figure K-3

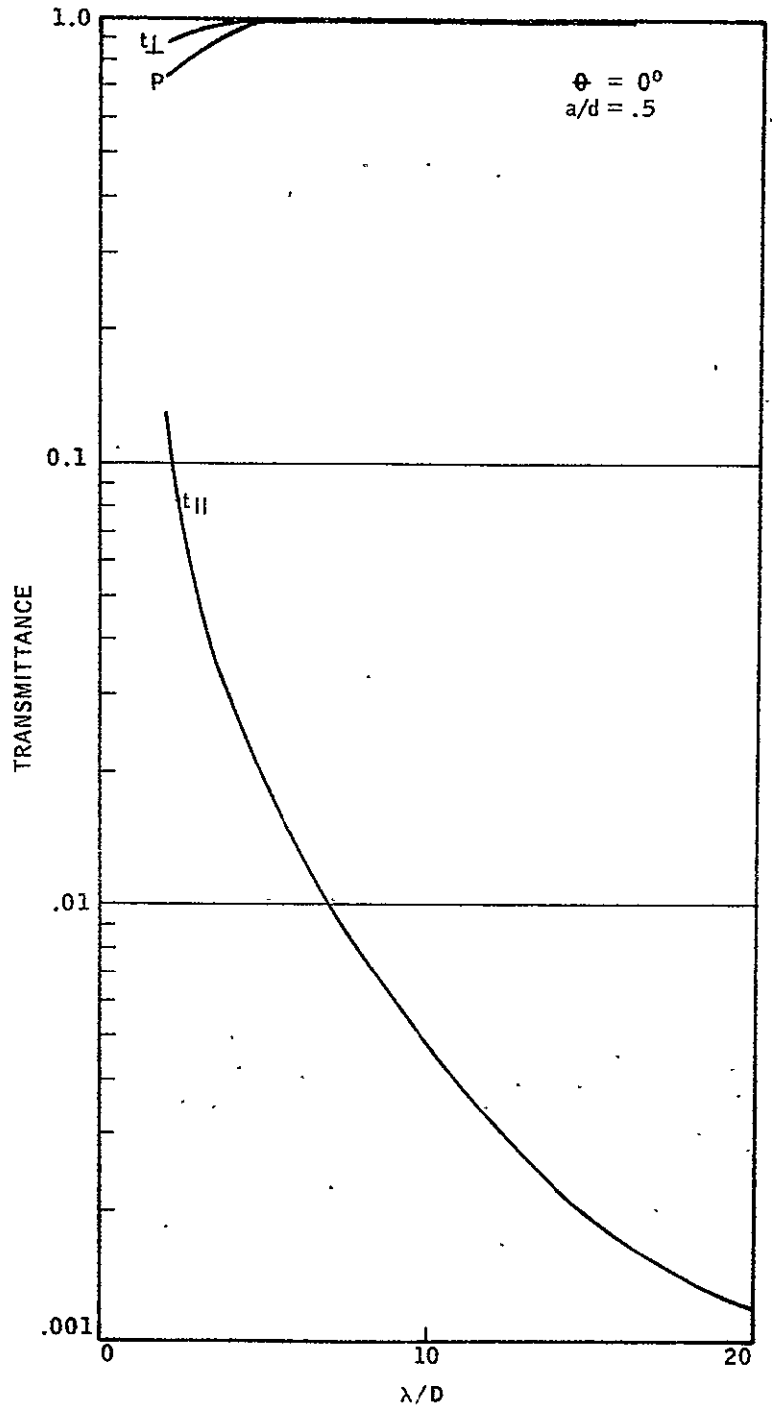

WIRE GRATING PERFORMANCE NORMAL INCIDENCE

Figure K-4

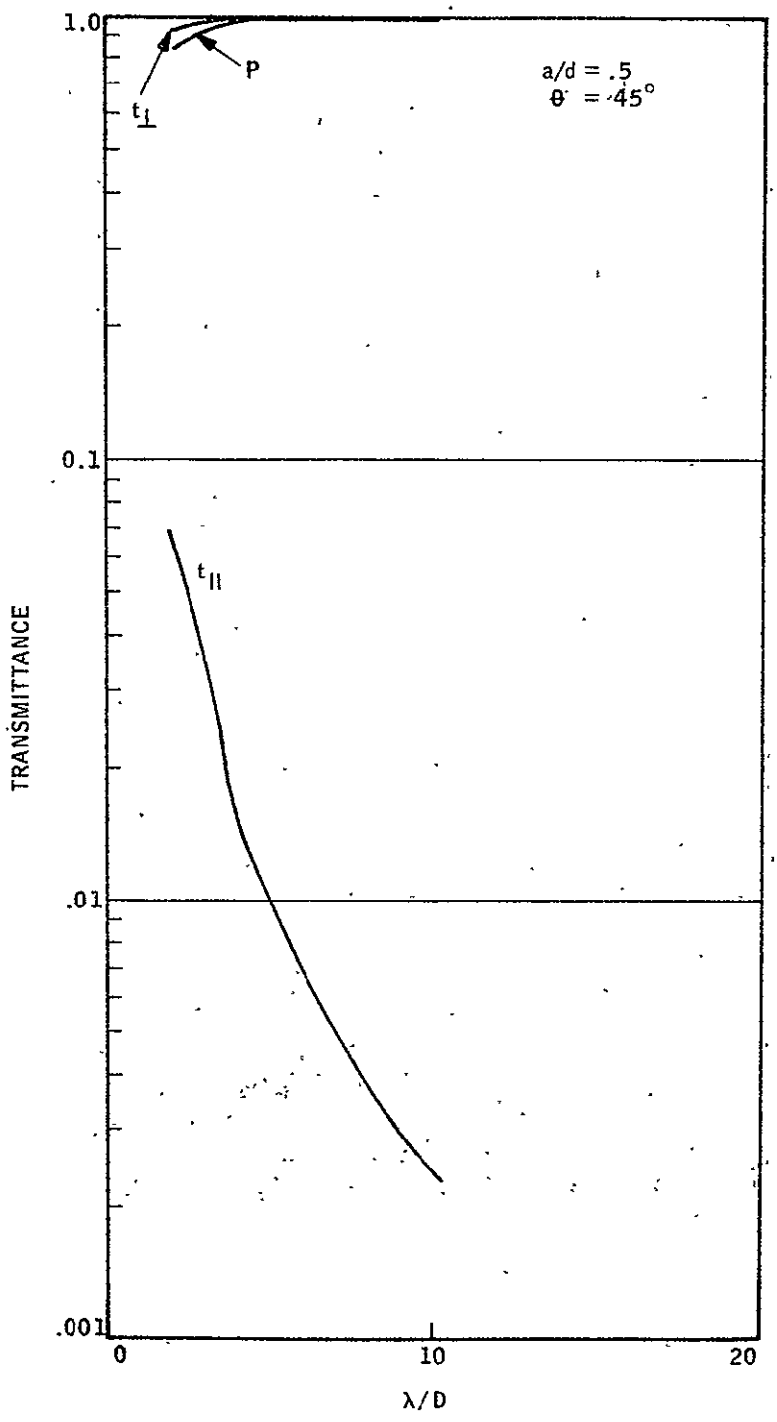

WIRE GRATING PERFORMANCE 45° INCIDENCE

Figure K-5

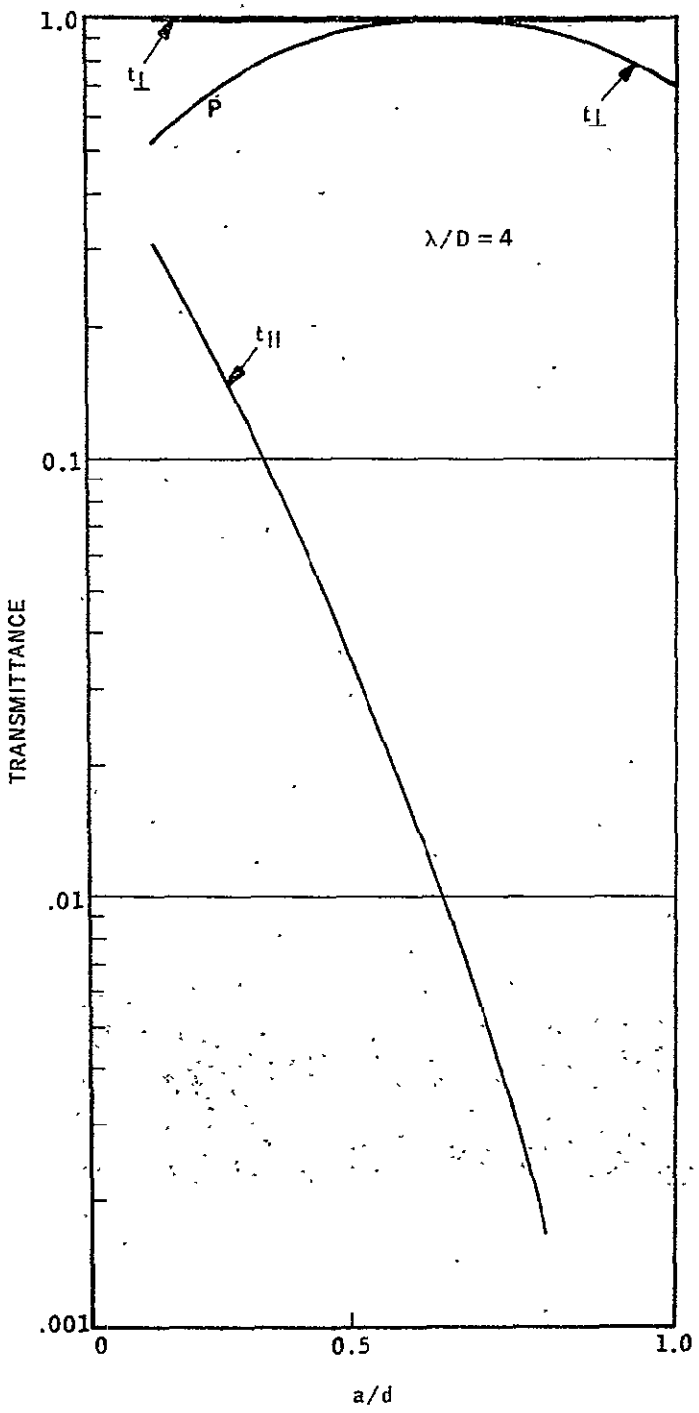

WIRE GRATING PERFORMANCE AT λ/D = 4

Figure K-6

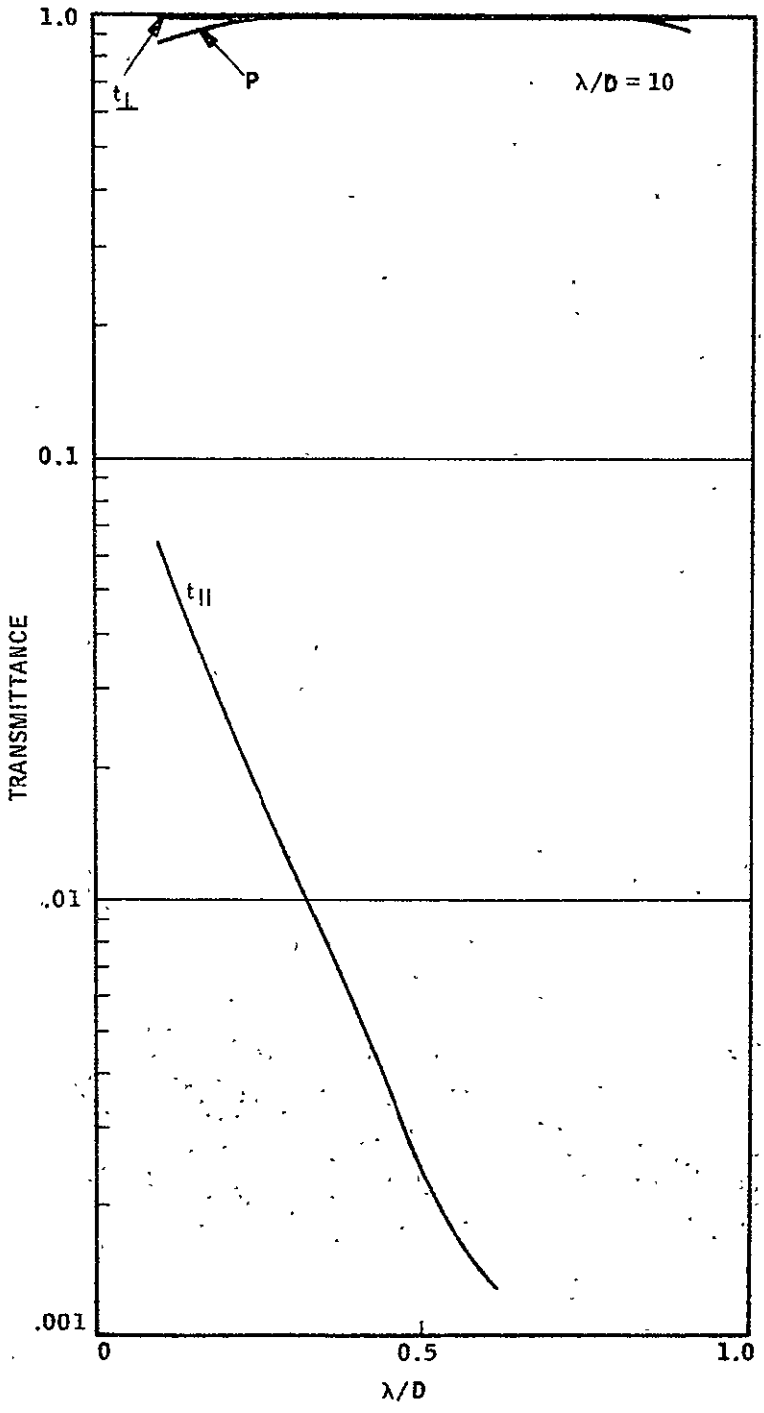

WIRE GRATING PERFORMANCE AT Λ/D = 10

Figure K-7

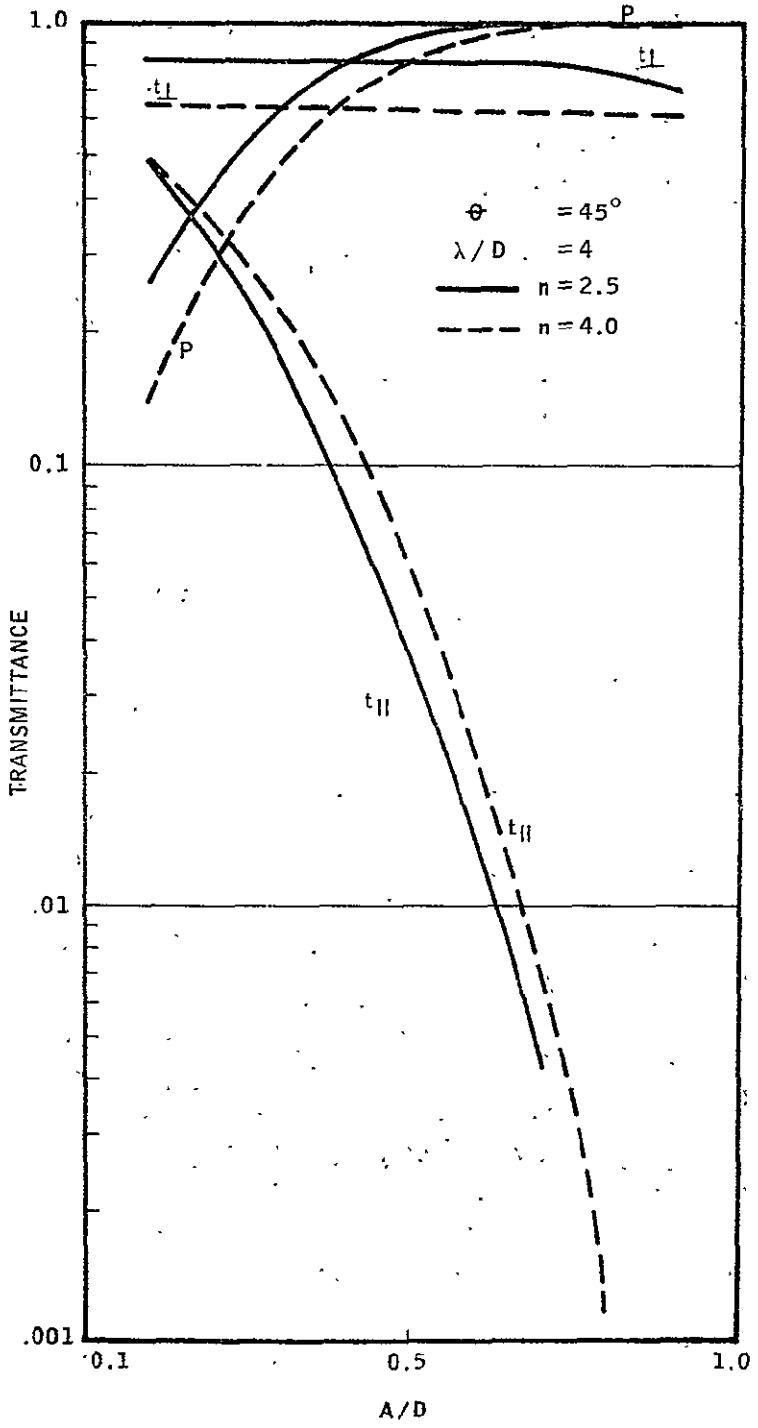

PERFORMANCE OF WIRE GRATING POLARIZER WITHOUT λ/4 COATING

Figure K-8

APPENDIX L

LCE OPTICAL TRAIN ANALYSIS

1.0 OPTICS DESIGN

1.1 CRITICAL OPTICS

The LCE optical-path schematic is shown in Figure 5.2.1-1 and the function and requirements of the overall system are described in Section 5.2.1 (Part I). In this section, the critical optical components requiring detailed design to optimize experiment efficiency are discussed. These are the image-forming components which operate on collimated beams in the transmit and receive optical paths:

- Telescope-relay lens system
- Beam expander
- Mixer focusing element

All other mirrors and beam splitters redirect a parallel beam and are only required to be fabricated to a flatness and surface finish which do not introduce excessive distortion of the nominally plane wavefront. Geometrical aberrations should be reduced to a point at which the image energy and phase distributions closely approach those of a nearly perfect system.

1.2 OPTIMIZATION PHILOSOPHY

In the optical design field, the terms "optimization" and "automatic design" are frequently encountered in reference to certain types of computer programs. More appropriate terminology would be "lens design improvement," for the problem involves so many variable parameters (radii, thickness, spacings, index of refraction) that one would be hard pressed to unequivocally stated that the final output is "the optimal solution." The result of the multidimensional nature is that the mathematical surface invariably contains local minima which can rapidly trap the computer, and prevent it from finding the lowest minimum. Far less subtle "traps" are created by such a program left to its own devices. For example, it is not uncommon under such conditions for a program to design a

system with negative thicknesses, or with surfaces which cannot be fabricated. Because of capacity limitations, it is not possible to include all possible error sources, and even the most sophisticated optimization programs only begin to pay lip service to practical items such as thermal and alignment tolerances. Consequently, an optimization program might design a fantastic system which is stable with respect to parameters in the program, but highly unstable with respect to an infinitesimally small misalignment.

The point here is that it is practically impossible to unequivocally call any system influenced by as many parameters as is the LCE optical system an "optimal" system. What is possible is to apply engineering experience and judgment, backed up by analysis, to establish a basic configuration which meets the experiment objectives within the physical constraints imposed by the spacecraft environment. This basic system can then be investigated in some detail, again within practical limits of variation of experiment parameters.

This approach has been followed in designing the LCE optics. The basic system (i.e., image forming optics, as stated in 1.1) is described and analyzed below, including the tradeoff reasoning applied in its selection. Subsequent sections discuss in great detail optimization of this basic system.

1.3 TRADEOFF CONSIDERATIONS

The image forming optics are shown in Figure L-1. The telescope is a standard Cassegrain system. (Lens systems of the required size and operating at 10 microns can be summarily dismissed from tradeoff considerations.) At first glance, a potential two-way gain of 2.5 to 3 db appears possible by removing the central obscuration and using an off-axis telescope. A number of arguments can be raised against an off-axis telescope:

A. Practical experience has shown that fabrication of an off-axis system of parameters similar to those on Figure L-1 to the required accuracy of $\lambda/2$ (green light - see the optical system specification) is a formidable task not easily accomplished. The telescope parameters are imposed by the space allotted to the LCE.

B. The present placement of the telescope is convenient from the point of view of heat dissipation when the sun is in the field of view of the telescope. The off-axis angle required for the secondary to clear the coarse pointing mirror is quite large, creating a severe requirement on fabrication of the primary. 90° rotation of the telescope to reduce the off-axis angle aggravates the thermal problem and requires another large 45° mirror.

C. Although ray traces have not been performed, it is suspected that the system image quality deteriorates rapidly as the beam goes 0.2° off-axis.

Thus, the high probability of image deterioration, low probability of satisfactory fabrication, and increased thermal, weight, and space problems of the off-axis telescope suggest that the 3-db gain might not be realized, and new problems are created which affect other aspects of the experiment.

Having selected the on-axis system, it is necessary to establish the beam reduction ratio (power or magnification) between the primary and the collimated output of the relay lens. Higher powers mean smaller secondary and reduced obscuration loss. However, higher powers also mean increased fabrication difficulty (particularly with a hyperbolic secondary) and decreased stability with respect to thermal variations. Ray traces on the 10-power telescope have shown that a 0.001-in. spacing change between primary and secondary introduces a wavefront distortion of about $\lambda/4$ of 10.6 microns. Based on elementary diffraction theory of aberrations, this distortion results in a loss of about 25% of the signal energy, and possibly results in phase distortion at the mixer, further reducing the heterodyne IF output. (Phase loss estimates are discussed later in this section.) Thus, the 10-power telescope is marginally stable with respect to alignment perturbations, and apparent gains by reducing the central obscuration are either not practically achievable or can be had only at the expense of incurring other serious problems. Also, the angular excursion at the IMC increases, complicating the mechanical design and operation of that element. Examination of the thermal stability of the telescope structure indictaes that 0.001-inch spacing tolerance is barely attainable. Therefore, an upper limit of 10 has been established for the beam reduction ratio.

The relay lens configuration does not involve a tradeoff, since the IMC must be placed in a position at which the angular excursions of the beam are compensated without introduction of lateral shift, which creates IF signal loss at the mixer. The relay lens forms a reduced image of the primary mirror which is fixed in space irrespective of the angle of incident. The IMC is placed in this image plane. The intermediate image of the object is formed in space, off the Newtonian mirror, to prevent overheating of components.

A two-element beam expander is selected so that a single component can accommodate both the transmitter and backup lasers. A single lens could achieve the beam expansion if the laser output is not recollimated at the end cavity mirror. However, it was not mechanically feasible to keep the same path lengths between the two lasers which must share the beam expander. Therefore, additional complexity in the mechanical design (flip lenses for the beam expander) would result, with only 3 to 5% gain from removing a coated Ge lens.

The two-element mixer imaging lens shortens the lens-mixer physical separation while maintaining the required focal length. Because of the packaging constraints, a single-element imaging lens would be placed in a position at which separate lenses would be required to focus the signal and local oscillator beams. The doublet configuration allows mixing of the two signals in the parallel beams at a single component, enhancing alignment stability at the mixer.

1.4 DESIGN RESULTS: GEOMETRICAL RAY TRACES

The three image forming subsystems have been ray-traced independently using the parameters given on Figure L-1. Since wavefront distortion has been selected as the performance criterion for this coherent, heterodyne system, the ray trace program has been set up to compute angular deviations between marginal rays and the chief ray in the parallel beam. Such differences can be related to the wavefront distortion by a simple integration process. For a set of tangential and sagittal rays (upper and lower marginal, upper and lower .7 x full aperture, and chief ray), the telescope/relay lens system wavefront distortion has been evaluated in the parallel beam after the relay lens. The results are shown in Table L-1 for the on-axis and 0.2° off-axis beams. Aberrations in the off-axis beam of a single lens system seem somewhat marginal,

but can be reduced by use of the doublet. (Diffraction calculations, currently being evaluated, may ultimately show that the single lens is adequate. See Section 1.5.)

The beam expander is a conventional 6.5 power telescope which, with the 10 power telescope/relay lens, produces the optimized truncation of the Gaussian shaped laser beam. Its performance has been evaluated by examining the image produced by a focusing element (parabola) inserted after the output beam. The geometrical aberrations in that image are essentially unmeasurable. The doublet mixer imaging lens has been ray traced, and it, too, produces an essentially perfect geometric image of a collimated beam.

1.5 DESIGN RESULTS: POINT SPREAD FUNCTION AND PHASE

The performance of the telescope/relay system, which is the most critical element, has been investigated with a ray trace program which calculates the system point spread function. This gives a direct evaluation of the image energy distribution of the realistic system, including the total combination of all the abeirrations in the system. The problem is handled in the following manner. The complex amplitude in the diffracted image is

$$a(x,y) = \iint A\ (\xi,\eta)\ \exp\left[i\ \frac{k}{f}\ (\xi x + \eta y)\right]\ d\xi d\eta$$

where

ξ,η are coordinates in the exit pupil plane

x,y are coordinates in image plane

and the integration is over the exit pupil aperture. The quantity $A(\xi,\eta)$ is called the pupil function and is

$$A\ (\xi,\eta) = \frac{\text{amplitude distribution of wave over exit pupil}}{\text{amplitude distribution of wave over entrance pupil}}$$

and

$$A\ (\xi,\eta) = A_o(\xi,\eta)\ e^{i2\pi\ W\ (\xi,\eta)}$$

with

$A_o(\xi,\eta)$ = real amplitude distribution over exit pupil

and

$W(\xi,\eta)$ = wavefront aberration in wavelength units

$W(\xi,\eta)$ is calculated from the geometrical optical paths through the system to a reference spherical wave in the exit pupil. A numerical two-dimensional Fourier transform gives a (x,y) of which the absolute value squared is the point-spread function.

The system has been simulated as shown in Figure L-2, which is a computer output trace. Note that a single relay lens has been used here. A parabolic focusing surface is placed in the collimated beam to investigate the image quality of the telescope. Also note the intersection of rays from on- and off-axis incident beams, showing that the IMC can indeed be rotated at this position without lateral beam displacement. Since the system is centered, the off-axis image spread function can be determined without introducing a dummy surface at the IMC position.

The point spread function numerical outputs are shown in Figures L-3 and L-4 for 0° and $.2^\circ$ angle of incidence. For the off-axis beam, the spread function is evaluated at the on-axis nominal focal point where the mixer is placed. The on-axis spread function can be seen to correspond with the theoretical diffraction pattern in terms of size of the rings and energy distribution. More happily, the off-axis pattern is not greatly disturbed, showing the effects of slight astigmatism and coma. From the accuracy of the computer calculation, it appears that a loss of 5% or less is sustained. When the total system spread function is evaluated, it may be possible to specify the single rather than double relay lens.

In the heterodyne system, the phase of both beams should be constant at the mixer, which is at the mixer lens image in the LCE. Therefore, an attempt has been made to evaluate the phase of the signal beam in the image plane of the real-life system with its combined aberrations. It can be shown (Born and Wolf, Principles of Optics, 1st Edition, Chapters 8 and 9) that some

first-order aberrations cause phase changes in the diffraction image, while others do not. What happens in a complex case of combined aberrations is a problem not amenable to analytical solution. However, the phase information should be contained in the complex amplitude calculated to determine the point spread function.

The theoretical phase behavior for a perfect diffraction image is:

- Constant across each ring (purely imaginary amplitude)
- Indeterminate at ring boundaries (amplitude = 0)
- 180° phase change between rings (amplitude changes sign)

The numerical results from the spread function calculations are:

- Constant phase across the diffraction rings, but 360° rather than 180° change from ring to ring, for the on-axis image
- Essentially constant phase over the central ring in the off-axis image, with peculiar behavior at the boundary and into the first ring

In order to attach some physical significance to the mathematical manipulations, some test cases are being devised:

Case 1 A parabola forming a perfect image

Case 2 An off-axis image of a parabola with the stop at the front focal plane (zero astigmatism, coma only)

Case 3 An off-axis image of a parabola with the stop at the mirror (coma + astigmatism)

Case 1 has been run and shows the 360° phase flip between rings; Cases 2 and 3 have not been completed.

At this time, it is not poasible to assess the phase condition at the mixer quantitatively. However, it appears qualitatively that there are no drastic phases shifts in the signal beam image on and off-axis. This conclusion is drawn from the quantitative behavior of the spread function, and qualitative (not yet fully understood), but constant behavior of the phase. No significant IF signal loss should be experienced.

1.6 SUMMARY

The critical image forming components of the LCE optical system transceiver are diffraction limited. This has been demonstrated by geometrical and numerical diffraction ray traces. The phase behavior is qualitatively acceptable, but not completely understood due to mathematical peculiarities. The component specifications are shown in Figure L-1. A single relay lens might be acceptable, and this decision will be based on the image quality of the overall system.

2.0 TRANSMITTER SIGNAL PATH OPTIMIZATION

There are two parts to the optimization of the transmitter signal path - the optimization of the far field on-axis intensity as determined by the diffraction of the Gaussian distributed laser beam through the telescope, and the optimization of coupling the transmitter laser output to the telescope. The following sections analyze both of these areas for the presently derived telescope design, and compare it by parameter variations with similar designs. The graphs showing variation of telescope and laser beam parameters are also interpreted as the tolerance requirements for design specifications of the optical components. Other factors such as thermal and mechanical design contribute to determining the overall telescope dimensions and design, so this analysis is not self-contained in optimizing the complete telescope design.

2.1 FAR FIELD INTENSITY OF THE TRANSMITTED BEAM

If the receiving telescope is not at the center of the incoming beam, the signal will be less than maximum. It is, therefore, important to determine the decrease in signal power received as a function of the angle, Θ, between the beam axis and a line joining the receiver (RCVR) and transmitter (XMTR) telescopes.

The far field amplitude, E_R, of a truncated, centrally blocked, Gaussian, uniform-phase, diffraction-limited beam is given by

$$E_R(\theta) = \frac{k}{R}\sqrt{\frac{P}{2\pi\sigma_I^2}}\int_{R_B}^{R_p} \exp\left(-r_T^2/4\sigma_I^2\right) J_o\left(\theta r_T k\right) r_T dr_T$$

where

P = power of beam if $R_B = 0$, $R_p = \infty$

R_p = outer radius of beam at transmitter primary

R_B = inner radius of beam at transmitter primary

σ_I = standard deviation of beam intensity at transmitter primary

R = range between transmitter and receiver

$k = 2\pi/\lambda$

r_T = radial coordinate in plane of transmitter primary

The far field intensity, $I(\theta)$, at angle θ is given by

$$I(\theta) = E_R^2(\theta),$$

Therefore,

$$I(0) = \frac{2\sigma_I^2 k^2}{\pi R^2}\left(e^{-\frac{R_B^2}{4\sigma_I^2}} - e^{-\frac{R_p^2}{4\sigma_I^2}}\right)^2$$

The ratio of the off axis intensity to that at the center is given by

$$\frac{I(\theta)}{I(0)} = \left[2\sigma_I\left(e^{-\frac{R_B^2}{4\sigma_2^2}} - e^{-\frac{R_p^2}{4\sigma_2^2}}\right)\right]^{-2}\left[\int_{R_B}^{R_p} e^{-\frac{r_I^2}{4\sigma_2^2}} J_o\left(k\theta r_1\right) r_1 dr_1\right]^2$$

Figure L-5 shows how this ratio varies with θ, when $R_p = 98.42$ mm, $R_B = 21.45$ mm, and $\sigma_I = R_p/2.10 = 46.1$ mm which are the optimized design parameters. Each of these values has been derived from other analyses such as thermal/mechanical analysis, link analysis and optical design analysis, and the

interplay among the parameters considered here in the optical train analysis. The central blockage radius, for instance, arises from the physical limitations of supporting the secondary mirror along with alignment adjustments, and the optical limitations of telescope magnification and its constraints. From the viewpoint of link analysis, the central blockage should be as small as possible in order to minimize the telescope blockage loss and have a 10-power telescope. Hence, there is an interplay between the analyses for R_B. For σ_I however, the optimization is based solely on the analysis given in the next sections. For the given values of R_p and R_B, σ_I is optimized.

2.1.1 Off-Axis Transmitter Blockage

An additional consideration of the far-field intensity is required for this optical system, since it includes an image motion compensator (IMC) for tracking received signals up to 0.2 degrees off of the telescope's optical axis. The transmitted beam is also directed by the IMC, resulting in a radial movement of the Gaussian distribution at the relay imaging lens, which redirects the beam to the center of the primary mirror and offsets the transmitted beam in the direction of the received beam. Since the center ray of the transmitted beam is always directed at the center of the primary mirror, the Gaussian distribution of transmitted power is always symmetric at the primary which determines the diffraction limited far field dispersion.

The stationary secondary mirror, however, does cause a slight perturbation of the central blockage as shown in Figure L-6. The displacement, d, for a maximum offset angle of 0.2 degrees is

$$d = 176 \times \tan .2^{\circ} = .6 \text{ mm}$$

The transmitted power remains the same, since the displacement of the blockage also exposes an equal area of the telescope primary.

For the small perturbation of central blockage, the resultant effect of asymmetrical power along the axis of displacement has been calculated to be less than 1% change of the total distribution of energy. Accordingly,

the far-field pattern and on-axis gain will not have any noticeable variation caused by off-axis IMC tracking.

2.1.2 Effect of Varying Transmitter Beam Width

The effect of varying the beam width from the transmitter laser must be considered. There is a variation of the far-field axial intensity, and the far-field axial intensity can be maximized by the proper choice of the width of the Gaussian transmitter beam at the telescope primary. Varying the beam width from its optimum value reduces the power collected at the receiving telescope.

The far-field axial intensity, I, normalized to the total laser output power, P, is given by

$$\frac{I}{P} = \frac{2\sigma_p^2 k^2}{\pi R^2} \left(e^{-\frac{R_B^2}{4\sigma_p^2}} - e^{-\frac{R_p^2}{4\sigma_p^2}} \right)^2$$

Hence,

σ_p = standard deviation of transmitter beam intensity at telescope primary

$k = 2\pi/\lambda$

R = range between XMTR and RCVR

R_B = radius of central blockage of the beam at the telescope primary

R_p = radius of telescope primary

The standard deviation at the primary mirror, σ_p, can be related to the radius, $R_{1/e}$, at the $1/e$ intensity point at the exit of the transmitter laser (neglecting angular divergence) through the expression

$$\sigma_p = R_{1/e} M_T / \sqrt{2}$$

where M_T is the product of the telescope power and beam expander power. Since there esists an optimum value of σ_p which maximizes I/P for any given values of R_B and R_p, there also exists an optimum value of M_T if $R_{1/e}$ is fixed.

The procedure, then, is as follows: The optimum value of σ_p is found for given values of R_B and R_p. This is done by using Newton's method to maximize the quantity

$$\frac{\pi R^2 I}{2 k^2 P} = \sigma_p^2 \left(e^{-\frac{R_p^2}{4\sigma_p^2}} - e^{-\frac{R_p^2}{4\sigma_p^2}} \right)^2$$

With this value of σ_p, the total telescope power, M_T, is found for a given beam radius $R_{1/e}$. Using this value of M_T, the far-field axial intensity for any arbitrary value of $R_{1/e}$ is compared to the maximum intensity obtained with σ optimized.

The resulting intensity decrease as $R_{1/e}$ is varied from its optimized value is shown in Figure L-7. Here, the blockage radius is 21.4 mm because of the secondary mirror within the telescope. With the radius of the telescope primary being 98.425 mm, the optimum value of σ_p is 46.1 mm or $R_p/\sigma_p = 2.1$. This leads to a value of M_T of 65.0 if the telescope is to be matched to a transmitter beam radius, $\sqrt{2}\, R_\sigma = R_{1/e}$ for $R_v = 0.71$ mm. Note that R_σ can be varied by 10% without degrading the axial intensity by more than 0.3 db.

2.1.3 Effect of Central Blockage of Transmitter

Much of the transmitter laser power is lost as a result of the blockage of the central part of the transmitted beam. This central blockage - whether caused by the secondary mirror, the hole in the coarse pointing mirror, or by the 45° coupling mirror - affects four parameters used in calculating the signal to noise ratio:

- The total power in the Gaussian beam exiting the transmitter telescope is less than that entering the telescope due not only to the central blockage but also to the truncation of the beam by the telescope primary.
- The transmitter telescope gain (far-field intensity) depends on the amount of central blockage and truncation of the Gaussian transmitted beam.

- The total power exiting the receiving telescope (on its way to the mixer) is less than that contained in the uniform beam collected by the receiver telescope because of the central blockage within it.
- The central blockage within the received beam also affects the amount of energy intercepted by the mixer in the focal plane of the mixer lens.

The first two effects will be analyzed here and the second two will be discussed in the receiver path optimization, section 6.0.

2.1.3.1 Transmitter Blockage

The power contained in the transmitted beam is less than that at the input to the telescope because of the truncation of the incident Gaussian beam by the telescope primary and because of the central blockage. The optical field at the telescope primary, E, is represented by

$$E = E_o \exp\left(-r^2/4\sigma_I^2\right)$$

$$E_o^2 = P_o/\sigma 2\pi\ \sigma_I^2)$$

where

P_o = power in incident (unblocked, untruncated) beam

r = radial coordinate in plane of primary mirror

σ_I = standard deviation of intensity at primary

The power transmitted, P_T, is given by

$$P_T = 2\pi \int_{R_B}^{R_p} E^2\, r\, dr$$

where

R_p = radius of primary

R_B = radius of blockage in beam of radius R_p

Therefore,

$$\frac{P_T}{P_o} = e^{-\frac{R_B^2}{2\sigma_I^2}} \cdot e^{-\frac{R_p^2}{2\sigma_I^2}}$$

As discussed in the previous section, σ_I can be chosen to maximize the far field axial intensity for each value of R_B and R_p by maximizing the quantity

$$\sigma_I \left(e^{-\frac{R_B^2}{4\sigma_I^2}} - e^{-\frac{R_p^2}{4\sigma_I^2}} \right)$$

2.1.3.2 Transmitter Gain

The transmitter gain, G_T, is defined by the expression

$$G_T = \frac{I(\theta)\, 4\pi\, R^2}{P_T}$$

where

$I(\theta)$ = far-field intensity at an angle, θ, with respect to the telescope optical axis

R = range

As discussed in the first section, the far field axial intensity, $I(0)$, is given by

$$I(0) = \frac{2\, \sigma_I^2\, k^2\, P_o}{\pi R^2} \left(e^{-\frac{R_B^2}{4\sigma_I^2}} - e^{-\frac{R_p^2}{4\sigma_I^2}} \right)^2$$

where

$k = 2\pi/\lambda$

Since $P_T = (P_T/P_o)\, P_o$, we have

$$G_T = \frac{(4)(2)\,\sigma_I^2\, k^2}{(P_T/P_o)} \left(e^{-\frac{R_B^2}{4\sigma_I^2}} - e^{-\frac{R_p^2}{4\sigma_I^2}} \right)^2$$

Here, (P_T/P_o) and σ_I are determined as per the previous paragraph.

Figure L-8 is a graph relating transmitter gain to central blockage radius. For each radius of central blockage, the optimum σ_I of the transmitter beamwidth is calculated. The total gain is indicated by the curve showing the difference of transmitter gain and power loss resulting from central blockage.

2.2 TELESCOPE COMPARATIVE ANALYSIS

In this section, a comparison of the present telescope design parameters of aperture radius, centered blockage radius, and beam width is made with similar designs by varying these parameters and analyzing the effects on transmitter gain and central blockage losses.

To begin with, in the previous section, the transmitter gain was defined as

$$G_T = \frac{I(\theta)\, 4\pi\, R^2}{P_T}$$

where $I(\theta)$ is the far-field intensity, which varied according to the primary and secondary mirror radii. To show the relative contribution of central blockage to the far-field pattern, Figure L-9 was calculated, plotting transmitter gain versus primary clear diameter. For the designed diameter of 7.75 in., the clear diameter gain is 94.9 db; while with central blockage of 21.4 mm, the gain derived from Figure L-8 is 94.7 db. Thus, the central blockage has only slight effect on the far field pattern on axis intensity and principally affects the transmitted power by blocking the central portion of the beam, which amounts to 0.9 db loss (Figure L-8).

The central blockage, as it affects the optimum beamwidth σ_I at the primary mirror, was discussed in Paragraph 2.1.2 from the standpoint of transmitter laser beamwidth tolerance. In Figure L-10, the same equations are used to plot the optimum beamwidth σ_I at the primary (enlarged from the laser by a beam expander and the telescope) versus central blockage radius. Given a primary mirror radius of 98.42 mm (7.75 inches) the second graph of the optimum ratio of primary radius to beamwidth at the primary (R_p/σ_I) versus central blockage radius can also be presented in graphic form (Figure L-10).

3.0 BEAM EXPANDER

The transmitter beamwidth has to be increased to the optimum size to maximize the far-field on-axis intensity as described in the previous sections. The output beamwidth accordingly must be expanded by both the telescope, by a power of 10, and by a beam expander of the appropriate power. If the transmitter and backup laser output beamwidths of radius 1.42 mm amounts to the $1/e^2$ of power, then the beam-expander power is a function of telescope central blockage radius. This relationship is plotted in Figure L-11.

The beam expander also provides for recollimation of the output laser beam. The output laser beam is specified to have a collimated output from the transmitted laser within 1 milliradian. By varying the distance between the two beam-expander lenses, the laser output beam can be collimated with only a negligible change in beamwidth. Then, both collimation and beam expansion can be designed into the transmitter signal path in the single beam-expander unit.

The possibility of using an uncollimated laser output in conjunction with a single recollimating lens beam expander was considered, since the optical coupling losses of the transmitter signal path would be reduced. The backup laser path length to the single lens could not be made equal to the transmitter path length because of the baseplate space constraints. The effect of the difference in path lengths is that the backup basic output beam either would not be completely collimated, since the spread angle from the backup laser would be different from the transmitter laser output spread angle (in order to

achieve the same beam size); or the beam size of the backup laser would be suboptimal, since the beam spreader lens would be designed and located to optimize the transmitter laser beam size. The tradeoff between on-axis intensity of the backup laser and the 2 to 5 percent loss from the two surfaces of the additional beam expander lens favored the latter. Thus, the two-lens beam expander is used.

4.0 DUPLEXER CONSIDERATION

The duplexer separates the transmitted and received beams by distinguishing the polarity difference between the beams. Section 5.2.1.6 discusses the design of the duplexer with respect to optimization of losses and physical characteristics.

5.0 IMAGE MOTION COMPENSATOR CONSIDERATIONS

When tracking the received signal, the image-motion compensation (IMC) can deflect the transmit beam off the telescope optical axis, up to 0.2 degree. The effect on the transmitted beam was discussed with respect to the far-field, on-axis intensity in Section 2.1 and shown to have a negligible effect, since the telescope/IMC configuration minimized the perturbation of symmetry of the transmitted beam. The only effect was shown to be a 0.2-degree shift of the secondary mirror in the transmitted beam, with no loss in power, since the shifted central blockage exposed an equal area of the primary mirror beam. Further discussion of the IMC is given in the receiver path optimization in section 6.0.

6.0 RECEIVER SIGNAL PATH OPTIMIZATION

The analysis of the receiver optical path optimizes the transmissivity, phase coherence, and alignment requirements for the optical components that comprise the heterodyne receiver system up to the mixer element. This includes an analysis of the local-oscillator-to-mixer path, since the methods of combining the two optical beams at the mixer, in view of the stringent spatial mixing requirements, must also be considered. Most important in this case is the requirement that the two beams be collinear to within 1 milliradian at the mixer.

Along with this problem is the problem of beam or mixer lateral displacement, which can be caused by signal tracking in some telescope designs and by the mixer and mixer heat radiator cone lateral displacement tolerance. With this problem there are multiple losses involved with the carrier to noise ratio from the mixer.

6.1 EFFECT OF CENTRAL BLOCKAGE ON THE RECEIVED SIGNAL

As mentioned in the transmitter path optimization, the central blockage of the telescope by the secondary mirror has two effects on the received beam. First, it decreases the amount of energy received by the blocking of the central portion of the telescope. Second, it affects the ratio of energy in the focused Airy-disk image on the mixer to the energy in the diffracted rings in the focal plane. This first section of the receiver path optimization discusses these effects, showing that the central blockage should be minimized as much as possible.

6.1.1 Receiver Blockage

Since the beam is essentially uniform in intensity across the receiving aperture, the ratio of the power out of the telescope, P_R, to that received, P_{RO}, is given by

$$\frac{P_R}{P_{RO}} = 1 - \left(\frac{R_B}{R_p}\right)^2$$

6.1.2 Mixer Outer Ring Power Loss

The received beam at the mixer lens is considered to be a plane wave of uniform, annular amplitude. The outer radius of the annulus is R_{SM}, while the inner radius is R_I. With the proper choice of focal length, the radius of the Airy disk at the focus of the lens can be made equal to the radius of the mixer. When this is done, the power intercepted by the mixer (the power in the central Airy disk) depends on R_I.

The field, E_{sd}, at the focus of the lens which results from a uniform annular incident beam is given by

$$E_{sd}(r) = \frac{E_{so}}{r}\left[R_{SM} J_1 (k R_{SM} r/F) - R_I J_1 (k R_I r/F)\right]$$

with

$$E_{so} = \frac{1}{R_{SM}}\sqrt{\frac{P_{so}}{\pi}}$$

where

$k = 2\pi/\lambda$

r = radial coordinate in the focal plane

F = focal length of lens

P_{so} = incident power at lens if $R_I = 0$

The power, P_s, intercepted by the mixer of radius R_d is given by

$$P_s = 2\pi \int_o^{R_d} E_{sd}^2 \, r \, dr$$

or

$$\frac{P_s}{P_{so}} = \frac{2}{R_{SM}^2} \int_o^{R_d} \left[R_{SM} J_1 (k R_{SM} r/F) - R_I J_1 (k R_I r/F)\right]^2 \frac{dr}{r}$$

If P_{OL} = power at the lens, then

$$P_{OL} = \left[1 - \left(\frac{R_I}{R_{SM}}\right)^2\right] P_{so}$$

to account for the hole. Therefore, the ratio of power intercepted by the mixer P_S, to that incident on the lens P_{OL}, is given by

$$\frac{P_s}{P_{OL}} = \frac{(P_s/P_{so})}{1 - \left(\frac{R_I}{R_{SM}}\right)^2}$$

It is assumed that $R_{SM} = R_P/10$ and $R_I = R_B/10$; i.e., that the radii of the beam at the lens are equal to those at the telescope reduced by the telescope power.

The proper value of the ratio of mixer radius, R_d, to the focal length of the lens, F, is that value which equates the radius of the Airy disk to the radius of the mixer. This value is determined by finding the smallest value of R_d/F which causes the quantity $\left[R_{SM} J_1 (kP_{SM} RL/F) - R_I J_1 (kR_I R_d/F\right]$ to equal zero.

There are, then, two receiver-path quantities dependent on the amount of central blockage:

A. Receiver blockage: P_R/P_{RO}

B. Mixer overlap: P_S/P_{OL} with the ratio R_d/F chosen to match the Airy disk to the mixer size.

These quantities are evaluated with a computer program and the results are shown in Figures L-12 and L-13. Figure L-12 shows how the optimum ratio of mixer radius to focal length depends on the radius of the central blockage. Figure L-13 shows how the receiver blockage and the mixer power lost to outer rings depend on the radius of the central blockage.

6.2 SIGNAL LOSS AS THE SIGNAL BEAM TILTS AT THE MIXER

One of the primary requirements imposed by superheterodyne detection of the signal is maintaining parallel-plane phase fronts of the received signal beam, and the local oscillator beam at the mixer. Any angular tilt between them results in a reduction of detected signal output from the mixer. Initially, these two beams are aligned to be parallel, so the only loss is the power lost to the outer rings around the Airy disk, which is centered on the mixer as calculated in the previous section. In this analysis, the loss caused by relative phase tilts between these two beams is calculated and combined with the outer ring power loss.

The origin of the tilt is in the angular misalignment tolerances of optical components in the receiver signal path and in the lateral position tolerance of the mixer. The geometry of this path and the misalignments is

shown in Figure L-14, where the duplexer misalignment tolerance angle θ, and mixer lateral tolerance dr are indicated with their effect on phase-tilt angle. For these two components, the nutator adds a corrective bias to coalign the transmitter and receiver beams. A discussion of this is given in the acquisition and tracking subsystem.

6.3 LOSS IN SIGNAL CAUSED BY OUTER RING LOSS

The signal from the mixer, relative to the unblocked signal power incident on the mixer lens, P_{SD}/P_L, is given by

$$\frac{P_{sd}}{P_L} = \frac{P_{sd}}{P_{DO}} \frac{P_p}{P_{PO}}$$

where

P_{sd}/P_{DO} = ratio of power intercepted by mixer to that unblocked power incident on lens

P_p/P'_{PO} = ratio of signal from mixer with given phase tilt to that with zero phase tilt

As discussed previously, the first ratio is given by

$$\frac{P_{sd}}{P_{DO}} = \frac{2}{R_{SM}^2} \int_o^Z \left[R_{SM} J_1 (kR_{SM} Z) - R_{BR} J_1 (kR_{BR} Z) \right]^2 \frac{dZ}{Z}$$

where

R_{SM} = outer radius of annular incident signal beam

R_{BR} = inner radius of annular incident signal beam

$Z = R_a/F$

$k = 2\pi/\lambda$

6.4 LOSS IN SIGNAL RESULTING FROM PHASE TILT

The ratio of signal from the detector when there is no phase tilt to signal when there is a phase tilt is given by M. Ross, "Laser Receivers," Wiley, 1966, p. 119:

$$\frac{P(\theta)}{P(0)} = \left[\frac{\sin\left[\frac{2\pi}{\lambda} R_d \sin(\alpha)\right]}{\frac{2\pi}{\lambda} R_d \sin(\alpha)} \right]^2$$

where α is the angle of phase tilt at the detector. This formulation assumes that the decrease in signal due to a phase tilt over a circular detector of radius R_d can be approximated by that decrease in signal found over a square detector having a side of length 2 R_d. If small angles are assumed, then $\sin \alpha = \alpha = D/F$ where D is the beam displacement at the lens of focal length F. Therefore,

$$\frac{P(\theta)}{P(0)} = \left[\frac{\sin\left(\frac{2\pi}{\lambda} DZ\right)}{\frac{2\pi}{\lambda} DZ} \right]^2$$

where $Z = R_d/F$.

Figure L-15 shows the resulting signal loss P_{SD}/P_L as a function of R_d/F (= Z) for various values of D. Here, R_{SM} = 9.84 mm and $R_{BR} = R_I$ = 2.1 mm. Note that, as D increases, the optimum value of R_d/F decreases so that more of the central Airy disk overlaps the mixer. If $R_d/F = 7.7 \times 10^{-4}$, the Airy disk is matched to the mixer when R_{SM} = 9.842 mm and R_I = 2.1 mm. In this case, the signal loss is independent of focal length. In Figure L-16, signal loss is presented graphically as a function of D for this value of R_d/F.

6.5 NEP/HZ AS A FUNCTION OF LO BEAM MISALIGNMENT

The NEP of the mixer depends on the amount of local oscillator (LO) power impinging on it, as shown in Figure L-17. The amount of LO power falling on the mixer depends on (1) how much of the LO beam is intercepted by the injection mirror, and (2) how much of this intercepted energy falls on the mixer. In the first case, the amount of energy intercepted by the injection mirror is found as a function of D_1, the lateral displacement of the LO beam at the injection mirror. This displacement is dependent on the angular misalignment and position of the various mirrors directing the LO beam to the injection mirror. In the second case, the amount of energy falling on the mixer is found as a function of D_2, the lateral displacement of the LO beam

on the mixer. This displacement is dependent only on the angular misalignment of the beam passing through the mixer lens.

6.5.1 Loss at Injection Mirror

The amount of LO power, P_I, intercepted by the injection mirror, of semi-minor axis R_I, is given by

$$P_I = 2 \int_0^{R_I} \int_0^{\pi} E_L^2 \, r_I \, dr_1 \, d\theta$$

where

r_I, θ = polar coordinates of injection mirror

E_L = amplitude of Gaussian LO beam at the injection mirror

Here,

$$E_L = \frac{1}{\sigma_1} \sqrt{\frac{P_L}{2\pi}} \, e^{-\frac{r_L^2}{4\sigma_I^2}}$$

where

σ_I = standard derivation of intensity of LO beam at injection mirror

P_L = LO power at injection mirror

r_L = radial coordinate of beam

The radial coordinates of the beam and mirror are related by

$$r_L^2 = r_I^2 + D_1^2 - 2 \, r_I \, D_1 \cos \theta$$

where D_1 is the relative displacement of the beam and mirror.

Therefore, the fraction of LO power intercepted by the injection mirror is given by

$$\frac{P_I}{P_L} = \frac{1}{\pi \sigma_I^2} \int_0^{R_I} \int_0^{\pi} e^{-\frac{(r_I^2 + D_1^2 - 2r_I D_1 \cos\theta)}{2\sigma_I^2}} r_I \, dr_I \, d\theta$$

This expression is evaluated as a function of D_1 with a computer program for given values of R_I and σ_I. Figure L-18 shows how P_I/P_L varies with D_1.

6.5.2 Loss at Mixer

The amount of LO power intercepted by the mixer, P_{LD}, is given by

$$P_{LD} = 2 \int_0^{\pi} \int_0^{R_d} E_{Ld}^2 \, r_d \, dr_d \, d\alpha$$

where

r_d, α = polar coordinates of the mixer

R_d = radius of mixer

E_L = amplitude of the LO beam at the mixer

In order to determine E_{LD}, it is necessary to assume that the LO-beam is symmetric at the mixer lens. This will only be true if D_1 is zero. However, it is a good approximation for small D_1, so it will be used here. In this case,

$$E_{LD} = \frac{k}{f} \int_0^{R_{LM}} E_{LM} \, J_o \, (r_{LM} \, r_{Ld} \, k/f) \, r_{LM} \, dr_{LM}$$

where

$k = 2\pi/\lambda$

f = focal length of mixer lens

r_{LM} = radial coordinate of lens

r_{Ld} = radial coordinate of focused beam

R_{LM} = radius of LO beam at lens

E_{LM} = amplitude of LO beam at lens

It is assumed that $R_{LM} = R_I$ (i.e, that there is no divergence of the beam from the injection mirror), since the distance between mirror and lens is about 50 mm. Beam divergence for finite distances is given in paragraph 6.7.

The amplitude at the lens, E_{LM}, is given by

$$E_{LM} = E_{LO} \exp\left(-r_{LM}^2/4\sigma_I^2\right) \qquad r_{LM} < R_{LM}$$

$$= 0 \qquad r_{LM} > R_{LM}$$

Since the LO power from the injection mirror, P_I, is given by

$$P_I = 2\pi \int_0^{R_{LM}} E_{LM}^2 \; r_{LM} \, dr_{LM}$$

the constant, E_{LO}, is given by

$$E_{LO}^2 = \frac{P_I}{2\pi \sigma_I^2 \left[1 - \exp\left(-R_{LM}^2/2\sigma_I^2\right)\right]}$$

The relationship between the radial coordinate of the focused beam, r_{Ld}, and the mixer radial coordinate, r_d, is given in terms of their relative displacement, D_2, by

$$r_{Ld}^2 = r_d^2 + D_2^2 - 2 r_d D_2 \cos\alpha$$

The resulting ratio of power intercepted by the mixer to power incident on lens, is given by

$$\frac{P_{LO}}{P_I} = \frac{k^2}{\pi f^2} \frac{\int_0^{\pi} \int_0^{R_d} \left[\int_0^{R_{LM}} e^{-\frac{r_{LM}^2}{4\sigma_I^2}} J_o\left(b r_{LM}\right) r_{LM} \, dr_{LM} \right]^2 r_d \, dr_d \, d\alpha}{\sigma_I^2 \left[1 - \exp\left(-R_{LM}^2/2\sigma_I^2\right)\right]}$$

where

$$b^2 = \frac{k^2}{f^2}\left(r_d^2 + D_2^2 - 2\, r_d\, D_2 \cos\alpha\right)$$

This expression is evaluated with a computer program. Figure L-19 shows how P_{LD}/P_I depends on D_2.

6.5.3 Calculation of NEP/Hz

The noise equivalent power per cycle of bandwidth, NEP/Hz, is a function of the LO power intercepted by the mixer, P_{LD}, as is shown in Figure L-19. The power intercepted by the mixer is given by

$$P_{LD} = K\left(\frac{P_{LD}}{P_I}\right)\left(\frac{P_I}{P_L}\right)$$

where K is a constant of proportionality which accounts for the LO power produced at the LO laser and the efficiency of the optical train leading to the mixer. It is chosen so that P_{LD} is equal to a specified value (e.g., .015 watts) when the mirrors are properly aligned. Here, P_{LD}/P_I and P_I/P_L are functions of D_1 and D_2, respectively, as determined above. For a given angular misalignment, ϕ, of the i^{th} mirror in the train from the laser to the mixer, the displacements are given by

$$D_1 = 2\, Z_i \phi$$

$$D_2 = 2\, \phi f$$

where

Z_i = distance of i^{th} mirror from the injection mirror

f = focal length of mixer lens

Combining these parameters, the change in NEP/Hz as a function of misalignment angle, ϕ, is calculated with a computer program. The results of such a calculation are shown in Figure L-20. The vertical bars represent the effect of Z_i

on D_1; the closer the mirror is to the injection mirror (small Z_i), the less the NEP/Hz is affected for a given angular deviation. Note that, at these small angles, there is only a small dependence on which mirror is deviated. The location and corresponding values of Z_i used in the calculation are given in Figure L-21. The other parameters are listed below:

$$\sigma_I = .62 \text{ mm}$$

$$f = 130 \text{ mm}$$

$$R_I = 2.1 \text{ mm}$$

$$R_D = .1 \text{ mm}$$

6.6 SIGNAL AND LOCAL-OSCILLATOR POWER INTERCEPTED BY MIXER

This section determines the distribution and phase of the signal power and the local oscillator power at any radius in the focal plane of the mixer lens. It is assumed that the signal beam at the mixer lens is uniform in phase with a uniform annular amplitude of inner radius R_I and outer radius R_{SM}. The local oscillator beam at the mixer lens is uniform in phase with a truncated Gaussian amplitude profile given by

$$E_{LM} = E_{LO} \exp\left(-r_{LM}^2/4\sigma_I^2\right) \qquad 0 \le r_{LM} \le R_I$$

$$= 0 \qquad r_{LM} > R_I$$

where

r_{LM} = radial coordinate of lens

σ_I = standard deviation of LO beam intensity

E_{LO} = constant related to total LO power

The analysis determines the integrated power of the signal beam and LO beam within a given radius R_d in the focal plane of a lens of focal length F.

The parameters pertinent to our system are $R_{BR} = 2.14$ mm and $R_{SM} = 9.84$ mm. Nominally, $R_d = .1$ mm and $F = 130$ mm so that $R_d/F = 7.7 \times 10^{-4}$.

6.6.1 Net Signal Power Intercepted by Mixer of Radius R_d

The field, E_{sd}, os the annular amplitude, uniform phase, signal beam at a radius R_d in the focal plane of the mixer lens is given by

$$E_{sd}(r_d) = \frac{k}{F} E_{so} \left[R_{SM} J_1 (kR_{SM} Z) - R_{BR} J_1 (kR_{BR} Z) \right]$$

where

$k = 2\pi/\lambda$

$Z = r_d/F$

R_{SM} = outer radius of annular incident beam

R_{BR} = inner radius of annular incident beam ($=R_I$)

$E_{so} = \frac{1}{R_{SM}} \sqrt{\frac{P_{SO}}{\pi}}$ where P_{SO} = incident signal power if $R_{BR} = 0$

The phase of E_{sd} flips when $E_{sd} = 0$, i.e.,

$$R_{SM} J_1 (kR_{SM} Z) = R_{BR} J_1 (kR_{BR} Z)$$

A computer program is used to determine the values of Z where $E_{sd} = 0$.

The signal power intercepted by the mixer, E_{td}, is given by

$$P_S = E_{td} = 2\pi \int_0^{R_d} E_{sd}^2 \; r_d \, dr_d \qquad \frac{R_d}{F} < Z_1$$

$$= 2\pi \int_0^{Z_1 F} E_{sd}^2 \; r_d \, dr_d - 2\pi \int_0^{R_d} F_{sd}^2 \; r_d \, dr_d \quad Z_1 < \frac{R_d}{F} < Z_2$$

where

Z_1 corresponds to radius of 1st minimum of Airy pattern

Z_2 corresponds to radius of 2nd minimum of Airy pattern

Figure L-22 shows the ratio of P_s ($=E_{td}$) to P_o ($=P_{so}$) as a function of R_d/F ($=Z$) for R_I = 2.1 mm and R_{SM} = 9.8 mm as determined with a computer program. The ratio with R_i ($=R_{BR}$) = 0 is also shown for comparison.

From Figure L-22, the optimum imaging lens focal length can be chosen if the mixer size is given. Thus, the best transmissivity or coupling efficiency is .72 for the given blockage radius. This occurs at a focal length f = 161 mm if R_d = .1 mm.

6.6.2 LO Power Intercepted by Mixer

As determined previously the LO field in the focal plane is given by

$$E_{LO}(r_d) = \frac{k}{F} \int_o^{R_I} E_{LM}(r_{LM})\, J_o(r_{LM}\, r_d\, k/F)\, r_{LM}\, dr_{LM}$$

where

r_{LM} = radial coordinate of lens

E_{LM} = LO field at lens given by

$E_{LM} = E_{LO} \exp(-r_{LM}^2/4\sigma_I^2)$

where

$$E_{LO}^2 = \frac{P_I}{2\pi\sigma_I^2 (1 - \exp -R_I^2/2\sigma_I^2}$$

Here,

P_I = power incident on lens

σ_I = standard deviation of LO intensity at injection mirror

Since the LO power incident on the mixer, P_{LD}, is given by

$$P_{LD} = 2\pi \int_o^{R_d} E_{sd}^2 \, r_d \, dr_d$$

the ratio of P_{LD} to P_I is given by

$$\frac{P_{LD}}{P_I} = \frac{k}{\left[1 - \exp\left(-R_I^2/2\sigma_I^2\right)\right]} \int_o^Z \left[\int_o^{R_I} e^{-\frac{r_M^2}{4\sigma_I^2}} J_o\left(r_M Z k\right) r_M \, dr_M \right]^2 Z \, dZ$$

Figure L-23 shows the dependence of P_{LD}/P_I on Z ($=R_d/F$) for the case where R_i = 2.1 mm and σ_I = .62 mm, the values of the injection radius equal to the central blockage radius of the received beam (inner hole), and the specified collimated LO laser σ_I beamwidth.

From this graph, for a given focal length, F, the LO power on the mixer is shown to be a percentage of the total incident LO power on the imaging lens. A later analysis of mixer lateral tolerance requirements uses this graph also.

6.7 PROPERTIES OF LO BEAM FROM INJECTION MIRROR

The optimization analysis assumed that the radius, W, of the local oscillator beam at the lens equaled that at the injection mirror. It also assumed that the curvature of the phase front of the beam at the lens and at the mixer were negligible. A justification of these three assumptions is given here.

6.7.1 Basic Formalism

The amplitude, E, of a Gaussian beam can be represented by

$$E = \frac{w_o}{w} e^{-r^2/w^2}$$

where $w = 2\sigma_I'$, with σ_I being the standard deviation of the intensity profile and w_o is the beam waist at the LO laser output-end mirror, at which the beam

is perfectly collimated. The radius of curvature, R, of the beam's phase front and the radius of the beam, w, at a distance Z from the beam waist (LO output) are determined by the following relationships (see Figure L-24).

$$w^2 = w_o^2 \left[1 + \frac{2Z}{\pi w_o^2}\right]^2$$

$$Z = R/\left[1 + \frac{\pi w_o^2}{\lambda Z}\right]^2$$

Here R is > 0 if the phase front is convex when viewed from $Z = +\infty$. A beam parameter q is defined such that

$$\frac{1}{q} = \frac{1}{R} - \frac{i\lambda}{\pi w^2}$$

If q_1 and q_2 are measured at distances d_1 and d_2 from a lens, as indicated in Figure L-25, then the following relationship applies

$$q_2 = \frac{(1 - d_2/f)\, q_1 + (d_1 + d_2 - d_1\, d_2/f)}{-(q_1/f) + (1 - d_1/f)}$$

This expression, then, relates R_2 and w_2 to R_1 and w_1.

6.7.2 LO Radius at Lens Equals Radius at Injection Mirror

In order to show that the radius of the LO beam is the same at the mixer lens, w_2, as it is at the injection mirror, w_1, it is assumed that the phase front is plane at the injection mirror ($R_I = \infty$) and that the beam is essentially untruncated by the injection mirror, since R_I = 2.1 mm and σ_I = 0.62 mm. Using the relationship between q_1 and q_2 and letting $f = \infty$ (no lens) and $d_2 = 0$

$$q_2 = q_1 + d_1$$

Equating the imaginary parts of this expression, and solving for w_2

$$w_2^2 = w_1^2 \left[1 + \left(\frac{\lambda d_1}{\pi w_1^2}\right)^2\right]$$

Therefore

$$w_2 = w_1 \text{ if}$$
$$d_1 << \frac{\pi w_1^2}{\lambda}$$

In the case used during optimization

$$w_1 \mp 2\sigma_I = w\left(\frac{R_I}{2.22}\right)$$

where R_I is the radius of the injection mirror. Therefore, $w_2 = w_1$ if

$$d_1 << 241 R_I^2$$

This unequality is true for the parameters used for the optimization since, here, $d_1 = 104$ mm and $R_I = 2.1$ mm.

6.7.3 Radius of Curvature of LO Beam at Lens

The radius of curvature is found by equating the real parts of the expression found above, $q_2 = q_1 + d_1$.

Solving for R_2

$$R_2 = d_1 \left[1 + \frac{\pi w_1^2}{\lambda d_1}\right]^2$$

It is instructive to interpret this radius of curvature in terms of the number of wavelengths, N, between the phase front at the edge of the beam and a line tangent to that phase front at the center of the beam. If the radius of curvature is R_2 and the radius of the beam is R_I, then

$$N = \frac{1}{2}\left[\sqrt{R_2^2 + R_I^2} - R_2\right]$$

If $\left(\frac{R_I}{R_2}\right)^2 << 1$, then

$$N = \frac{R_I^2}{2R_2\lambda}$$

Returning to the expression for R_2, it can be shown that the minimum value of R_2 is when $d_1 = \frac{\pi w_1^2}{\lambda}$, so that $R_2(\text{min}) = \frac{2\pi w_1^2}{\lambda}$. Since $w_1 = 2\sigma_I = \frac{R_I}{1.11}$ $N\ (\text{min}) = \frac{1}{10}$ which is quite small.

The phase deviation is even smaller for the parameters assumed for the optimization. Here, $N = \frac{1}{93}$ which is negligible.

6.7.4 Radius of Curvature at Mixer

The radius of curvature at the mixer can be found by equating the real parts of the general expression relating q_2 and q_1 with $d_2 = F$, $R_1 = \infty$. Solving for R_2, the following is obtained

$$R_2 = \frac{F^2}{F - d_1}, \text{ an expression independent of } w_1.$$

With $F = 130$ mm and $d_1 = 104$ mm,

$$R_2 = 650 \text{ mm}.$$

Therefore, replacing R_I in the expression for N, with $R_d = 0.1$ mm, phase deviation parameter of $N = \frac{1}{1000}$, which is negligible, is obtained.

6.8 RECEIVER ANTENNA FIELD OF VIEW

The receiver field of view can be understood as the angular width to the 3-db points of a point source moving off the telescope optical axis. It is calculated by convolving the Airy disc of the point source signal with the mixer area as it moves laterally off the center of the mixer from moving off the telescope optical axis. This section first discusses the analysis of signal

loss caused by Airy disc/mixer mismatch, and then applies the mathematics in calculating the field of view of the designed telescope.

6.8 RECEIVER ANTENNA BEAMWIDTH

For each size of inner and outer radius of the annular received beam, there is an optimum ratio of detector radius to focal length (R_d/F), that maximizes the Airy disk energy on the mixer. The equations describing this optimization have been given previously. Since R_d is fixed at 0.1 mm, a smaller optimized R_d/F value, which results from increasing the primary mirror diameter, gives a larger focal length, F, for the mixer lens. However, for tracking the signal by using nutator error signals, a large angular beam shift caused by a relatively small beam displacement is desirable. Increasing the focal length, F, of the imaging lens decreases this angular beam displacement sensitivity.

Figure L-26 shows the receiver field of view for R_d/F. The field of view is defined as twice the half angle off the telescope optical axis, to the point of 3-db signal loss. For the given beam parameters, F = 161 mm is the optimum value maximizing Airy disk energy, as shown in Figure L-22.

Figure L-22 plots the fraction of signal power on the detector versus R_d/F, and for a central blockage radius R_I = 2.145 mm, the Airy disk energy is .73 at $R_d/F = 7.7 \times 10^{-4}$. A tradeoff of field of view and signal power is necessary, and possible, in order to have a field of view of 30 sec, since the loss in signal power is small for the necessary change in R_d/F. A value of $R_d/F = 7.7 \times 10^{-4}$ or F = 130 mm gives a 30-sec field of view, with a resultant fractional signal loss of .03 from the maximum. Consequently, the field of view is significantly increased over the value of 23 sec at the optimum value of F at 161 mm.

6.9 SIGNAL LOSS RESULTING FROM AIRY DISK - MIXER MISMATCH

This section discusses the effect of a relative displacement between the center of the Airy disk of the received beam and the center of the mixer for various values of the central blockage. The signal beam at the lens is taken to be of uniform phase and of uniform, annular amplitude, with an inner

radius of R_I and an outer radius of R_{SM}. The focal length of the mixer lens, F, is always chosen so that the mismatch corresponding to an external field of view of 30 seconds of arc gives a mismatch resulting in a 3 db signal loss. Under these conditions, the signal power, P_S, which is intercepted by the mixer of radius, R_d, is calculated as a function of the relative displacement, D, between the centers of the Airy disk and mixer, and is normalized to that power intercepted by the mixer when the displacement is zero. The signal power, P_S, is calculated with the phase change of alternate Airy rings considered; that is, the power in the first, third, fifth, etc., Airy rings which are intercepted by the mixer is subtracted from that power in the central disk and second, fourth, etc., Airy rings which are intercepted by the mixer. This is because alternate rings differ in phase from one another by π radians.

The amplitude, E_{sd}, of the optical field in the focal plane of the mixer lens is given by

$$E_{sd}(r) = \frac{E_{so}}{r}\left[R_{SM} J_1 (k R_{SM} r/F) - R_I J_1 (k R_I r)F\right]$$

with

$$E_{so}^2 = \frac{P_o}{\pi R_{SM}^2}$$

where

$k = 2\pi/\lambda$

P_o = incident power at lens if $R_I = 0$

r = radial coordinate centered at center of Airy pattern (maximum intensity)

The signal power, P_S, intercepted by the mixer is given by

$$P_S = 2 \int_0^{\pi} \int_0^{R_d} E_{sd}^2 (r)\, r_\alpha\, dr_\alpha\, d\alpha$$

where r_α, α = cylindrical coordinates centered with the center of the detector. Therefore, r_α, α and r are related through the expression

$$r_\alpha^2 = r_\alpha^2 + D^2 - 2r\ D \cos.$$

where D is the relative displacement between r = 0 and r_α = 0, i.e., the centers of the detector and Airy disk. Due to the phase sensitive detection E_{sd}^2 is taken as positive or negative depending on whether the quantity $\left[R_{SM}\ J_1\ (k\ R_{SM}\ r/f) - R_I\ J_1\ (k\ R_I\ r/f)\right]$ is positive or negative.

The quantity (P_S/P_0) is calculated and normalized to (P_S/P_0) when D = 0 with a computer program for various values of R_I. The results are shown in Figure L-27. Here, $(P_s/P_o)/(P_s/P_o)_{D\ =\ 0}$, in db, is plotted vs linear displacement and angular displacement, respectively, for various values of the radius of the central blockage. It must be remembered that the optimum focal length varies with R_I. Figure L-28 shows the relationship between the optimum focal length of the lens and the radius of the central blockage.

6.10 Mixer Axial, Lateral, and Tilt Tolerances

Some movement from the aligned position of the mixer location and the received signal beam is expected after launch. This section derives the axial, radial, and tilt tolerances of beam and mixer movement, and their effect on heterodyned signal output power.

6.10.1 Axial Tolerance of Mixer Position

The axial tolerance of mixer position is determined by the depth of focus of the received signal beam imaging lens. The depth of focus for a diffraction limited system is defined as the distance along the optical axis that the mixer can be moved for less than 1/4 λ deterioration of the wavefront (Rayleigh limit). Assuming the Rayleigh limit is applicable to a uniform intensity beam with central blockage, then the depth of focus is given by

$$\text{Depth of focus} = \frac{w}{n \sin^2 (U_m)}$$

where

w = wavelength

n = index of refraction of the medium (for vacuum or air, n = 1)

U_m = the angle defined in the sketch below:

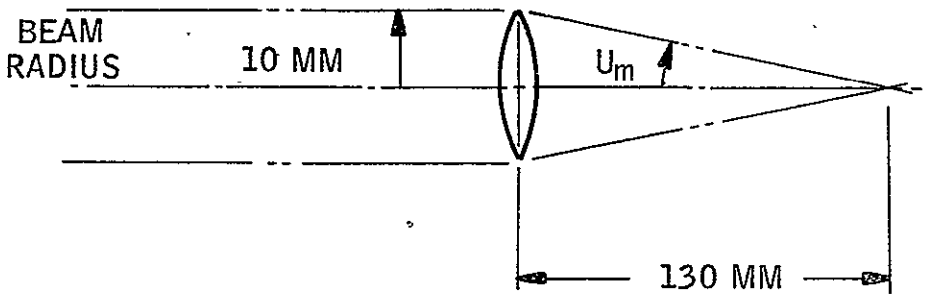

MIXER IMAGING LENS DEPTH OF FOCUS

Substituting in the values shown gives

Depth of focus = $\pm$ 1.80 mm ($\pm$ .070 in.)

A smaller tolerance than this depth of focus is necessary, since the desired wavefront should be plane to within $\lambda/10$ rather than $\lambda/4$. Hence, a tolerance of $\pm$ .010 inches would be a conservative axial tolerance, which would include the imaging-lens axial movement tolerance.

6.10.2 Lateral Mixer and Beam Position Tolerance

The lateral mixer and received-beam position tolerance is primarily limited by the movement of the mixer from the center of the local oscillator Airy disk and the consequent decrease in local oscillator power on the mixer. Figure L-29 shows the mixer size and the amplitude distribution of the local oscillator Airy disk, assuming 20 mw power on the mixer, when centered, and 80 mw total incident power. The recovered signal beam is automatically centered on the off-centered position of the mixer and adds only the phase-tilt loss described in paragraph 6.4, "Signal Loss if Received Signal Beam Tilts at the Mixer."

The local oscillator power intercepted by the mixer when the mixer is displaced off center is given by

$$P_s = 2 \int_0^{\pi} \int_0^{R_d} E^2 (r)\, r_a\, dr_a\, da$$

where

$E(r)$ = amplitude of local oscillator beam at distance r from center

r_a, a = cylindrical coordinates with center at the center of the mixer

and

$$r^2 = r_a^2 + D^2 - 2\, r_a\, D \cos (a)$$

where

D = relative displacement between r = 0 and r_a = 0 as shown on the sketch below.

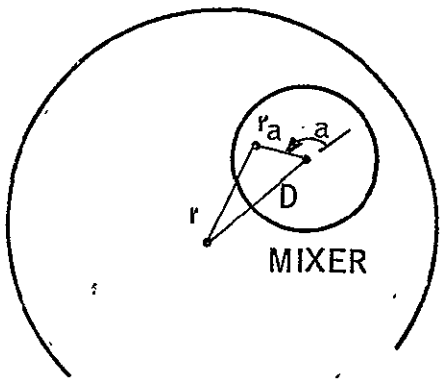

L. O. AIRY DISC

A computer program was used to find P_s for incremental values of displacement D. This graph is plotted in Figure L-30. From this figure, a lateral mixer movement of 0.2 mm shows a decrease of LO power to 3.8 mw. From Figure L-17, the resultant decrease in NEP for 3.8 mw incident power from 7 mw is less than .1 db.

6.10.3 Mixer Tilt Tolerance

The angle of tilt θ of the mixer with respect to the received beam and local oscillator beam is a non-critical tolerance, as shown by the following:

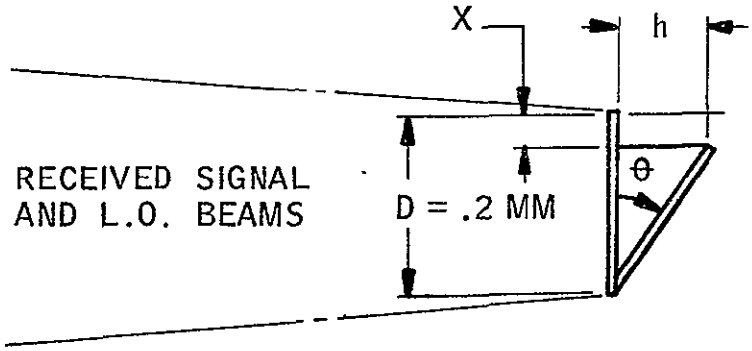

MIXER TILT

The mixer is illustrated by the two-plane phase beams which differ in frequency by 30 MHz. Any angular tilt between these beams results in phase changes of the 10.6 microns across the face of the mixer and a loss in intensity of the difference frequency of 30 MHz caused by the interference. If the two beams are collinear and the mixer face is tilted an angle θ as shown in the sketch above, then the phases of both beams will change many times over the tilted face as caused by the spatial lag. However, the relative difference between the two beam phases at any point will be small with respect to the difference frequency. The amount of phase shift at 30 MHz, to which the detector responds is proportional to the ratio of the distance n in the sketch to the wavelength of 30 MHz. This ratio is calculated as follows:

$$\lambda \text{ diff} = \frac{c}{f} = \frac{3 \times 10^{11} \text{ mm/sec}}{3 \times 10^{7} \text{ Hz}} = 10^{4} \text{ mm}$$

For $\theta = 5^{\circ}$, a liberal tolerance figure, h is calculated as

$$h = D \tan \theta = 9.2)\ (.087) = .017 \text{ mm}$$

Then

$$\frac{h}{\lambda_{diff}} = \frac{.017}{10,000}$$

Hence, the tilt θ has negligible effect on the difference frequency.

Another effect caused by tilt will be a decrease in effective area of the mixer. The face area will become elliptical to the vertical beams, having a semi-minor axis (D - x) as shown in the sketch. For $\theta = 5$ degrees,

$$x = h \tan \theta = (.017)\ (.087) = .0015 \text{ mm}$$

$$D = .2 \text{ mm}.$$

Then for θ less than 5 degrees, this area loss is negligible, since

$$(D - x) = (.2 - .0015) \approx .2.$$

7.0 ACQUISITION SIGNAL PATH OPTIMIZATION

In order to locate the transmitted beam initially, a relatively wide-angle beam is used in the search mode as compared with the beam width of the telescope. From the acquisition and tracking analysis of paragraph 5.1.5, an optimized specification for the angular width of the acquisition beam is determined to be 0.178 degree. Given the angle, the following analysis derives the optics necessary to spread the transmitter laser beam by far-field diffraction and calculates the resultant on-axis acquisition beam intensity.

7.1 ACQUISITION BEAM SPREADING OPTICS

The radial intensity distribution of the transmitted laser beam is essentially undisturbed Gaussian (untruncated and unblocked). Here, the beam from the laser is directed around the beam expanding optics and the transmitter telescope to the coarse pointing mirror. The only beam shaping optics in the path are those required to spread the beam to the required size at the receiver. These optics can be of three general forms: (1) A set of two lenses can be used to maintain the collimation, but increase the beam radius so that the beam diffracts to the required far field angle; (2) A set of two lenses can be used to diverge the beam to the required far field angle; and (3) A single lens can be used to diverge the beam. The advantage of (2) over (3) is that the effective focal length of the two-lens system can be varied easily, whereas the single lens has a fixed focal length.

7.1.1 Use of Recollimated Beam

The divergence of an undisturbed, collimated, Gaussian beam can be calculated in the following manner: The radial distribution of the initial beam amplitude E_i, can be represented by

$$E_i(r) = E_{oi} \exp\left(\frac{-r^2}{w_o^2}\right)$$

where r is the radial coordinate. Similarly, the far-field distribution is represented by

$$E_f(r) = E_{of} \exp\left(\frac{-r^2}{w^2}\right)$$

The far-field angle ϕ between the radial positions $r = 0$ and $r = w$ is given by

$$\phi = \frac{\lambda}{\pi w_o}$$

Since the intensity is the square of the amplitude, the full angle θ between the half-power (intensity) points is given by

$$\theta = \sqrt{2 \ln 2}\left(\frac{\lambda}{\pi w_o}\right)$$

Therefore, the w_o required is

$$w_o = \sqrt{2 \ln 2}\,\frac{\lambda}{\pi\theta}$$

From Section 5.1.5, it is specified that θ is required to be .178 deg. (3.11 mrad), which requires that w_o = 1.28 mm. Since the laser beam before recollimation has a w_o of 1.19 mm, then the beam diverges too much.

If the laser beam were directed to the coarse pointing mirror without any beam expanding and recollimating optics, then θ = .190 degree and the received acquisition mode power decreases by 0.82 db. These values assume that the transmitter laser output beam will be collimated with a tolerance that would not materially affect the beam spread. For the specified tolerance on the laser output dispersion angle of .1 mrad, the dispersion angle θ = .202 degree, which decreases received power an additional .48 db.

Since the acquisition field angle and power are critical, acquisition beam shaping optics with the following characteristics are used in order

to meet the requirements. The transmitter laser 3-sigma beamwidth is expanded to 2.48 mm and also adjustment is provided to recollimate any geometric dispersion from the laser output beam collimating lens. This adjustment is expected to provide for the maximum specified angular tolerance of 1 mrad.

7.1.2 Acquisition On-Axis Intensity

From the far-field equations discussed previously in Section 2.1, the on-axis intensity for a blocked and Gaussian beam is given by

$$I_T(o) = \frac{2\,\sigma_T^2\,k^2\,P_o}{\pi R^2}\left[e^{-\frac{R_B^2}{4\sigma_T^2}} - e^{-\frac{R_P^2}{4\sigma_T^2}}\right]^2$$

For the undisturbed beam, the on-axis intensity is given by

$$I_A(o) = \frac{2\,\sigma_A^2\,k^2\,P_o}{\pi R^2}\left(1 - e^{-\frac{R_A^2}{4\sigma_A^2}}\right)^2$$

Then, the ratio of the normalized telescope intensity to the undisturbed acquisition beam intensity reduces to

$$\frac{I_T(o)}{I_A(o)} = \frac{\sigma_T^2}{\sigma_A^2}\,\frac{\left(e^{-\frac{R_B^2}{4\sigma_T^2}} - e^{-\frac{R_P^2}{4\sigma_T^2}}\right)^2}{\left(1 - e^{-\frac{R_A^2}{4\sigma_A^2}}\right)^2}$$

The parameters are σ_T = 46.1 mm, σ_A = .71 mm, R_B = 21.45 mm, R_P = 98.425 mm, and R_A = 2.48 mm. Substituting these parameters into the equation,

$$\frac{I_T(o)}{I_A(o)} = 1820$$

The power ratio in dbm is

$$10 \log_{10}\left(\frac{I_T}{I_A}\right) = 32.60 \text{ db}$$

To this value, the telescope central blockage loss (1.33 db) and the transmitter-to-telescope path losses, which total 1.72 db, less the beam expander losses, are added to the on-axis acquisition intensity.

$$(32.60 - 1.33 - 1.72) = 29.55 \text{ db}$$

As shown in the equation for the ratio of far-field intensities, $I(\theta)/I(o)$, the attenuation below the telescope made in the ratio of squares of the dispersion $\left(\frac{\sigma_T^2}{\sigma_A^2}\right)$ times the ratio squared of the far-field diffraction functions.

This value is compared with the calculated telescope on-axis signal-to-noise ratio of 24.38 db achieved when in transmit mode, at the beginning of the experiment, and at the minimum operating temperature of 15°C. This acquisition carrier-to-noise ratio is then found by subtracting the difference between the two intensities from the operating carrier-to-noise ratio, as calculated in the previous section.

$$(C/N) \text{ acquisition} = 24.38 - 29.55 = -5.17 \text{ db}$$

Using the off-axis far-field equations discussed in Section 2.1, the following graph (See Figure L-30A) of the transmitter acquisition field of view was computed. The transmitter beam is redirected before the telescope through an appropriate power beam expander and directed to the coarse pointing mirror for this resultant far-field pattern.

8.0 SELF-CHECK CAPABILITY

The self-checks of the transmitter and local oscillator laser are included by arranging the optical paths layout so that a modification of the flip mirror used for selecting the backup laser mode of transmitter or local oscillator would also provide these two self-check modes.

The self checks are made by mixing a greatly attenuated portion of the backup laser beam at the appropriate P-line with either the local oscillator or transmitter laser supplying LO power at the detector. The backup laser power must be sufficiently attenuated to the operating range of -50 to -70 dbm.

Figure 5.2.1-1 of the text shows the optical paths layout. Flip mirror A is shown in Figure L-31. This layout also provides two primary operating modes without using movable mirrors. The table in Figure L-31 shows the corresponding operating modes and flip mirror operations.

To combine and attenuate the beams in the proper way and to maintain optical-axis alignment of the beams, the flip mirror is designed with the following characteristics: The two outer surfaces of flip mirror A are 100:1 beam splitters which reflect 99% of the impinging energy. The 1% of laser power that passes through the first beam splitter of flip mirror A is again attenuated by the blockage of the metal sheet between the two mirrors. The size of the central aperture in the metal sheet between the two mirror faces determines the amount of the Gaussian distributed power passing through and also the dispersion of the power caused by diffraction at the aperture. The second beam-splitter surface attenuates the passed power again by 100:1.

Thus, in Mode No. 4 the power from the backup laser is transmitted through the first beam splitter, through the aperture in the metal sheet, and through the second beam splitter. The attenuated beam then goes to the mixer. The total path attenuation of the backup laser power is summed up in the following table for an aperture diameter of .2 mm.

Backup Laser-to-Detector Path Losses

	dbm
Backup laser power (500 mw)	+27
First beam splitter (100:1)	-20
Blockage (aperture = .2 mm)	-19.8
Second beam splitter (100:1)	-20
Third beam splitter (5:1)	-7
Dispersion of beam at the detector lens and truncation loss	-11
Airy disk overlap at the mixer of the focused backup laser beam	-9
	-59.8

In Mode No. 4 part of the flip-mirror assembly is used to relocate the transmitter beam in the local oscillator-to-detector optical path. A germanium wedge enters the transmitter/telescope optical path and displaces the beam laterally while maintaining a plane phase front. The power from the backup laser is transmitted through the flip mirror and an attenuated signal goes to the mixer. Thus, both self-check modes will have output levels similar to the received signal output.

In order to meet the requirements of the self-check capabilities, certain factors must be taken into consideration in the construction of the flip mirror. The mirror material must be transparent at 10.6 microns, which requires the use of a material such as germanium. In order to reduce etalon effects, the inner surfaces of the two beam-splitter pieces require an anti-reflection coating. The metal must be coated with a paint that is highly absorbent to 10.6 microns so that the amount of power and the dispersion of power by diffraction depends only on the aperture.

The aperture must be located so that the center of the Gaussian distributed beam, which is the refracted optical axis, passes through the center of the aperture. Since the flip mirror is at an angle of 45° from the optical axis, the aperture must be drilled at an angle of 45° with respect to the metal surface.

The flip-mirror angular alignment tolerances must match the requirements of the other mirrors that colocate and align the transmitter and backup laser paths to within 3 $\widehat{\text{sec}}$ out of the telescope axis. This requires a flip-mirror alignment tolerance of .3 mrad, and so there is no exceptional alignment problem.

9.0 POWER METER SIGNAL PATH

At the output of each laser, there is a 99:1 beam-splitter mirror which passes 1% of the laser output power into a power meter signal path, as shown in Figure L-32. For the transmitter and backup laser outputs, this sampled energy illuminates a diffraction grating which is blazed to enhance the second order reflection of the 10.6 μ beam. For the local oscillator laser, the diffraction grating is included in the LO laser as the back-end mirror. The sampled output from the beam splitter is then reflected toward the power detector. In all three cases the second-order reflection is focused onto a power detector when the laser output is operating in the fundamental mode at the correct P-line. The detected energy then is amplified by a dc amplifier to 2.5 v,dc and fed into a feedback loop for laser frequency tuning and power measurement.

The following analysis considers three aspects of the power meter path.

Wavelength resolution of the diffraction gratings to an incident Gaussian distributed laser beam

Efficiency of the signal path

Transmitter power detector dc and ac outputs

9.1 WAVELENGTH RESOLUTION OF THE DIFFRACTION GRATINGS

Both the beam radius and Gaussian distribution affect the width of the second-order energy focused on the power detector. For power detectors that are smaller than this focused width there is consequently a power loss. For the backup laser which operates on two P-lines of the 10.6 μ wavelength, the resolution of the two lines also depends on the focused second-order beam width.

The effect of varying the beam radius involves the wavelength resolution of the wavelength monitoring diffraction gratings. In analyzing this effect, the diffraction properties pertaining to a uniform beam will first be discussed, followed by an analysis of the diffraction properties of a Gaussian beam. The goal is to determine how much energy at wavelength $\lambda + \Delta\lambda$ will overlap a detector used to observe energy at wavelength λ.

9.1.1 Uniform Beam

Using Figure L-33 to define geometric parameters, one has the following conditions which define the angular position of the principal maxima and minima for the case of a uniform beam:

$$\sin \beta_x = mN_o\lambda + \sin \alpha \qquad m = 0, \pm 1, \ldots \text{ maxima}$$

$$\sin \beta_N = 2N_o \left(m + \frac{n}{xN_o}\right) \qquad n = \pm 1, \pm 2, \ldots \text{ minima}$$

The blaze angle, θ, is given by

$$\theta = \frac{\alpha \pm \beta_x}{2}$$

where

λ = wavelength

x = beam width

N_o = total number of lines/unit length

The angular half-width of the mth order for a given wavelength is found by subtracting these two equations. Therefore,

$$\Delta\beta_\lambda = \frac{\lambda}{x \cos \beta_x}$$

To find the full angular separation, $\Delta\beta_x$, between two close wavelengths for the same diffraction order, one can differentiate the first equation and obtain

$$\Delta\beta_x = \frac{m N_o \Delta\lambda}{\cos \beta_x}$$

where $\Delta\lambda$ is the difference of the two wavelengths.

The parameters corresponding to our case are

$$\lambda = 1.06\mu$$

$$\Delta\lambda = .02\mu \text{ (P-line separation)}$$

$$x = .4 \text{ in.}$$

$$\alpha = -33^\circ$$

$$N_o = 1800 \text{ lines/in.}$$

Therefore, for $m = 2$, $\beta_x = 73^\circ$, and $\Delta\beta_x = 9.72$ mrad, independent of the width of the beam. However, the angular half-width of the diffracted beam at a single wavelength, $\Delta\beta_\lambda$, is dependent on the beam width, x. Here, $\Delta\beta_\lambda = 3.57$ mrad. Since $\Delta\beta_x = 9.72$ and since $2\Delta\beta_\lambda = 7.14$ mrad, the two wavelengths are clearly resolved.

9.1.2 Gaussian Beam

Because the energy of a Gaussian beam is peaked at its center, the effective width of a Gaussian beam is less than that of a uniform beam. Therefore, although the angular position of the maxima and minima will correspond to those for a uniform beam, the angular width of the principal maxima will always be greater for a Gaussian beam than for a uniform beam. The width of the principal maximum will be computed by summing up the field due to each slit of the grating.

The total amplitude, A, of the radiation at an angle β (see Figure L-33) is due to the sum of the fields from each grating slit with their relative phases accounted for.

Let the amplitude of the jth grating slit be a_j and its phase (relative to the j = 1 slit) be ζ_j. Then the total amplitude in the far field in a given direction is given by

$$A = \sum_{j=1}^{N} a_j \, e^{i\zeta_j}$$

where $i = \sqrt{-1}$ and N = total number of grating slits illuminated. The phase factor, ζ_j, can be expressed in terms of a constant phase difference, ζ, between slits as

$$\delta_j = (j - 1)\,\zeta$$

$$\zeta = \frac{2\pi}{\lambda} d \left| \sin \beta - \sin \alpha \right|$$

where

d = spacing of the grating slits

β = diffraction angle

α = incident angle

as defined in Figure L-33.

If the incident symmetric Gaussian beam is centered on a grating having an even number of slits, then there is a one-to-one correspondence between slits equidistant from the center of the grating. Therefore, the amplitude from the jth slit is equal to that from the (N + 1 - j) slit for $1 \leq j \leq \frac{N}{2}$.

The amplitude of the incident Gaussian beam, a, can be represented by

$$a = B\, e^{-\frac{r^2}{4\sigma_s^2}}$$

where B is a constant and r is the radial coordinate. Since the slits are very narrow, the incident beam can be considered of constant amplitude, though the jth slit can be approximated by

$$a_j = B\, e^{-\frac{1}{4\sigma_s^2}\left[\left(\frac{N}{2} - j + 1\right) d\right]^2} \qquad 1 \leq j \leq \frac{N}{2}$$

This amplitude applies to the field from two symmetrically placed slits. The phase factors corresponding to these slits are given by $e^{i(j-1)\zeta}$ and $e^{i(N-j)\zeta}$. Combining these expressions

$$A = B \sum_{j=1}^{N/2} \exp\left\{-\frac{1}{4\sigma_I^2}\left[\left(\frac{N}{2} - j + 1\right)d\right]^2\right\} \left(e^{i(j-1)\zeta} + e^{i(N-j)\delta}\right)$$

Therefore, the resulting intensity, I, at angle β is given by

$$I = A\, A^* = \left[\mathrm{Re}(A)\right]^2 + \left[\mathrm{Im}(A)\right]^2$$

With the exponential factors replaced by their trigonometric equivalents to facilitate computation, a computer program computes the angular width (to the minimum) of any desired principal maximum as well as the intensity I at any angle β.

Figure L-34 shows how the relative intensity about the second-order maximum varies with angle if the grating is .4 in. wide and has 1800 lines/in. Here, the radius to the 1/e point of the incident Gaussian beam, r 1/e is 1.19 mm (i.e., $1/e^2$ = 1.42 mm) and the wavelength is 10.6μ. The angular position of the maximum and the angular separation of two wavelengths are identical to those found for a uniform incident beam. Therefore, the second-order maximum is at $\beta = 73.28^\circ$ for $\alpha = 33^\circ$, and for a wavelength separation of .02μ, the angular separation is 9.85 mrad. The position of the minimum if r 1/e = 1.19 mm is also marked in the figure as is the angular width of the detector if it is .3 mm wide and the focal length of the lens is 2.98 in.

Thus, for this one-dimensional case, the power incident on the detector due to wavelength λ is some 12 times that power due to wavelength $\lambda + .02\mu$. This ratio gives the resolution requirement for distinguishing the separation of P-lines of operation of the backup laser, since the second detector is located at this offset to be centered on the second P-line mode.

9.2 POWER METER PATH EFFICIENCY

Besides the 99:1 beam splitter, there are other elements of the path that contribute to the path efficiency. The diffraction grating is designed to enhance the second-order reflection. Experimentally, this efficiency has been measured to be at least 40%. The efficiency of coupling this energy to the detector is a ratio of the energy falling on the detector to the total energy in the second-order reflection. From Figure L-34, this is 7.4/20 = 37%. Thus, the fractional amount of energy on the detector, compared with the laser output energy is the sum of the efficiencies, stated in dbm.

Beam splitter, 99:1	-20.0 db
Diffraction grating efficiency, 40%	-4.0 db
Detection coupling efficiency	-4.3 db
	-28.3 db

9.3 TRANSMITTER POWER DETECTOR AC AND DC OUTPUTS

The dc power output of the transmitter laser power detector corresponds to the power output of the laser at line center. The FM modulation of the laser also modulates the power amplitude.

The equation for power output can be written

$$P_1 = \frac{8GP_m f_d}{(\Delta f_{osc})^2} (f_a - f_c) \cos \omega t$$

where

G = tube dependent factor (approx. unity)

P_m = maximum power output

f_d = peak deviation of dither

(Δf_{osc}) = the range of frequencies that will allow oscillation

$(f_a - f_c)$ = deviation or displacement from line center

P_l = power output at frequency $(f_a - f_c)$ from line center

On the output of the power detector, the voltages V_s and V_m are directly proportional to input power P_l and P_m. The above equation may be rewritten as

$$V_s = \frac{8 V_m f_d}{(\Delta f_{osc})^2} (f_a - f_e)$$

However, the peak deviation can be referenced to the maximum, V_m, and for Δf_{osc} equal to 90 MHz, and the deviation of the dither is 300 kHz

$$\frac{V_s}{V_m} = \frac{8 \times 300 \times 10^3}{(90 \times 10^6)^2} (f_a - f_e)$$

$$= \frac{6 \times 10^6}{81 \times 10^{14}} = 7.4 \times 10^{-10} = 0.3 \times 10^{-9} (f_a - f_e)$$

If the displacement from line center is 1 MHz

$$\frac{V_s}{V_m} = 0.3 \times 10^{-9} \times 10^6 = 0.0003 \text{ or } 0.03\%$$

Hence, the relative amplitude of the modulation caused by dithering is 0.03%/MHz displacement, since it is seen that the modulation is directly proportional to the displacement.

The equation above may be written in yet another form

$$\frac{V_s}{V_m} = \frac{8}{(f_{osc})^2} f_d \, (f_a - f_c)$$

Differentiating

$$\frac{d\, V_s/V_m}{df_d} = \frac{8}{(\Delta f_{osc})^2} \cdot (f_a - f_e)$$

and the slope in percent per Hz at a displacement of $(f_a - f_e)$ may be found

$$\frac{d\, V_s/V_m}{df_d} = \frac{8}{81 \times 10^{-14}} (f_a - f_e) = 10^{-15} \, (f_a - f_e) \text{ percent/Hz}$$

This agrees with the previous result if the value of deviation is 300 kHz and the displacement is 1 MHz. The slope at 30 MHz is 3×10^{-8}%/Hz, and the allowable amplitude variation for 500 kHz is

$$3 \times 10^{-8}\%/\text{Hz} \times 5 \times 10^{5} \text{ Hz} = 15 \times 10^{-3} = 1.5\%$$

If the power detector has a sensitivity of 320 mv/mw and the incident power is 0.085 mw, then the dc output at line center is

$$V_m = 320 \times .085 = 27.2 \text{ mv}$$

and the allowable variation at 30 MHz for 500 kHz accuracy is 1.5% of 27.2 mv = $\pm$408 μv.

At the dither frequency, the frequency response of the detector is down about 4 db or about 0.63, and hence the amplitude of the dither at 30 MHz displacement will be

$$27.2 \times 0.03\% \times 30 \times 0.63 \text{ mv} = 0.154 \text{ mv} = 154 \text{ } \mu\text{v}$$

This is less than the 408 μv of the dc accuracy requirement because of the 4-db frequency response and because of the 300-kHz peak dither rather than the 500-kHz accuracy requirement.

The required dc gain must be

$$\frac{2.5 \text{ v}}{27.2 \text{ mv}} = 92 \text{ or } 39.2 \text{ db (voltage db)}$$

The dither amplitude at 1 MHz displacement is 0.03% x 27.2 mv x 0.63 = 5.1 μv. The gain of the a-c amplifier would have to be

$$\frac{55.5 \text{ mv}}{5.1 \text{ } \mu\text{v}} = 10{,}900 \text{ or } 80.7 \text{ db}$$

If the noise density of the power detector is 0.06 $\mu v/\sqrt{Hz}$, the noise level on the output of the a-c amplifier would be about 654 $\mu v/\sqrt{Hz}$. This exceeds the specification. However, if the beam splitter is modified to provide 1% to the power detector in the local oscillator instead of 0.1%, the required dc and ac gains drop by 20 db, and the noise density will be 65.4 $\mu v/\sqrt{Hz}$, well within the specifications.

10.0 ANGULAR MISALIGNMENT TOLERANCES FOR OPTICAL COMPONENTS

It is known that after launch of the spacecraft, there will be some misalignment of the optical components caused by vibration and shock of the launch, and varying temperatures of the LCE baseplate in space environment. In particular, the transmitter signal path will become misaligned from the receiver path. Some of the receiver path misalignment can be compensated for by biasing the nutator drive signals. This correction is discussed in the

receiver signal path optimization analysis, Section 6. For the transmitter signal path, however, the consequent misalignment cannot be corrected, and the transmit and receive beams separation must be minimized as much as possible. The misalignment loss can be read from Figure L-5, which gives the transmitter field of view, since the IMC will align the receiver optical axis in the direction of the incoming beam.

From the acquisition and tracking signal-to-noise requirements, it is estimated that the total transmitter/receiver beams misalignment will result in no more than 0.7 db additional loss. Thus, from the following analysis and experimental test data, the individual optical element tolerances will be derived so that the total loss is within the constraint. A list at the end of this section gives the tolerances for all components in the transmitter and receiver signal paths.

10.1 POWER LOSS DUE TO MISALIGNMENT OF TRANSMITTER LASER MIRRORS

A misalignment of the transmitter mirrors decreases the transmitted laser power for two reasons: First, because of vignetting within the laser cavity, a misalignment causes the losses within the cavity to increase. This additional cavity loss decreases the laser efficiency and output power. Second, a misalignment of the laser mirrors shifts the beam from the optic axis of the optical elements leading to the IMC mirror. The vignetting which then occurs results in a decrease of transmitted power. These two effects of XMTR mirror misalignment will be considered separately.

The ratio of laser power with mirror misalignment to that without misalignment is given by η_ϕ/η_o, where η_ϕ is the laser efficiency corresponding to a cavity loss of L_ϕ and η_o is the laser efficiency corresponding to the loss L_o when there is no misalignment. A curve of η_ϕ as a function of L_o is given in Figure L-35 for a laser discharge length of 16 cm. For $L_\phi > L_o = .11$, this curve is fit with the function $\eta_\phi = .14 - L_\phi$.

The loss, L_ϕ, for a given angular misalignment ϕ is determined from the following analysis: There are several effective apertures within the laser cavity which are formed by the laser mirrors, the two ends of the modulator crystal, and the two ends of the discharge tube. Figure L-36 depicts

the cavity geometry. The optical cavity length from the plane cavity mirror to the $i^{\underline{th}}$ aperture is given by Z_i where Z_1 and Z_2 correspond to the ends of the modulator crystal, Z_3 and Z_4 correspond to the discharge tube ends, and Z_5 corresponds to the output mirror of radius of curvature R_c. The beam in this cavity is Gaussian, with a standard deviation in intensity at location Z_i of $\sigma_I (Z_i)$. If the beam is displaced latterally an amount D_i at aperture i, then a reduction in the beam power will result as some of the beam falls outside the aperture. The fractional reduction of beam power is taken as an additional cavity loss. The loss, L_ϕ, is, therefore, given by

$$L_\phi = \left(1 - \frac{P_\phi}{P_o}\right) + L_o$$

where

P_ϕ = power through the limiting aperture

P_o = power through the limiting aperture when $\phi = o$

L_o = loss when $\phi = o$

The power, P_ϕ passing through a given aperture of radius R_M is given by

$$P_\phi = 2 \int_o^\pi \int_o^{R_M} E^2 (Z,r,\theta)\, r\, dr\, d\theta$$

where r and θ are the cylindrical coordinates of the aperture and $E(Z,r,\theta)$ is the field strength of the beam within the cavity at a distance Z from the plane cavity mirror. Here

$$E(Z,r,\theta) = \frac{1}{\sigma_I} \sqrt{\frac{P}{2\pi}}\, e^{-\frac{r^2}{4\sigma_I(Z)}}$$

where

P = beam power if there were no blockage

$\sigma_I(Z)$ = standard deviation of the beam intensity

r' = radial coordinate of beam

The relationship between r' and r depends on the lateral displacement, D, of the beam with respect to the aperture. Here,

$$r'^2 = r^2 + D^2 - 2rD \cos(\theta)$$

The power passing through the aperture is, therefore, given by

$$P_\phi = \frac{P}{\pi\sigma_I^2} \int_0^{\pi} \int_0^{R_M} e^{-\frac{r^2 + D^2 - 2rD\cos(\theta)}{2\sigma_I^2}} r \, dr \, d\theta$$

If $\phi = 0$, then

$$P_\phi = P_o = P\left[1 - \exp\left(\frac{-R_M^2}{2\sigma_I^2}\right)\right]$$

Therefore, the ratio of P_ϕ/P_o is given by

$$\frac{P_\phi}{P_o} = \frac{1}{\pi\sigma_I^2\left[1 - \exp\left(-R_M^2/2\sigma_I^2\right)\right]} \int_0^{\pi} \int_0^{R_M} \exp\left(-\frac{r^2+D^2-2rD\cos(\theta)}{2\sigma_I^2}\right) r \, dr \, d\theta$$

This integral is evaluated numerically using Simpson's method for any specified values of R_M and σ_I.

The blockage takes place at whichever aperture intercepts the most energy from the beam. Therefore, the radius R_M corresponds to the R_i which produces the minimum value of the expression $R_i/D_i + \sigma_I(Z_i)$. The displacement, D_i, and the standard deviation, $\sigma_I(Z_i)$, must be calculated at each aperture position Z_i.

The displacement at location Z_i depends on which mirror has an angular error. If the plane mirror has an angular error of ϕ_p, then $D_i = Z_i\phi_p$. If the curved mirror has an error ϕ_c, then $D_i = R_c\phi_c$, for in this case the beam is moved parallel to itself.

The standard deviation, $\sigma_I(Z_i)$ at position Z_i is given by

$$\sigma_I^2(Z_i) = \sigma_{Io}^2\left[1 + \left(\frac{\lambda Z_i}{4\pi\sigma_{Io}^2}\right)^2\right]$$

where

$$\sigma_{Io}^2 = \sigma_I^2(o) = \frac{\lambda Z_5}{4\pi}\sqrt{\frac{R_c}{Z_5} - 1}$$

Using the analysis above, the power loss as a function of mirror misalignment was calculated with computer programs for input parameters of

n = 3.3 (index of crystal)	R_c = 500 mm
d_1 = 13.5 mm	R_1 = 1.5 mm
d_2 = 55 mm	R_2 = 1.5 mm
d_3 = 26.2 mm	R_3 = 2.0 mm
d_4 = 185.0 mm	R_4 = 2.0 mm
d_5 = 18.2 mm	R_5 = 2.13 mm

The results are shown in Figure L-37.

10.2 MEASURED POWER LOSS INSIDE THE LASER

To substantiate the tolerance losses of the analysis based on an experimental curve given in Figure L-35, a test was conducted by the laser subcontractor to find the actual change in laser output power versus lateral changes in the laser tube and modulation positions with respect to the end mirrors. A vertical shift of the laser tube is equivalent to an angular change of the curved-end mirror for a given mirror radius of curvature. This test was presented earlier and the results plotted as dotted Curves A and B in Figure L-37, along with the analtyically derived curves.

As indicated in Figure L-37, the actual power loss for misalignments of the laser configuration is much less. The reasons for this overstatement are that the beam distribution within the laser is more centralized than a Gaussian distribution and the cavity loss for a given misalignment is consequently larger. Furthermore, the laser efficiency is less than the curve shown in Figure L-11, and so the changes in cavity loss have less effect on the laser efficiency. These data were not available in quantified form and the analysis relied on the earlier data shown in Figure L-11. Since the experimentally measured curves A and B reflect the actual angular misalignment losses, these curves will be used in determining the misalignment tolerances contributed by the transmitter power decrease.

The equations developed in the analysis are applicable to the next section.

10.3 POWER LOSS OUTSIDE LASER

The analysis for the power decrease due to vignetting outside the laser is similar to that given above. Figure L-21 is a schematic of the optical system. Here, since there is a lens which recollimates the beam at position Z_5, σ_{Io} must be replaced by $\sigma_I(Z_5)$ which is given by

$$\sigma_{Io}^2 = \sigma_I^2(Z_5) = \frac{\lambda Z_5}{4\pi} \sqrt{\frac{R_c^2}{Z_5(R_c - Z_5)}}$$

and for $6 \leq i \leq 8$

$$\sigma_I(Z_i) = \sigma_{Io} \sqrt{1 + \left[\frac{\lambda(Z_i - Z_5)}{4\pi\sigma_{Io}^2}\right]^2}$$

For $i = 9$,

$$\sigma_I(Z_9) = P_{B.E.}\ \sigma_I(Z_8)$$

where $P_{B.E.}$ is the power of the beam expander. For $12 \leq i \leq 14$,

$$\sigma_I(Z_i) = \sigma_I(Z_{i-1}) + \frac{d_i \theta_d}{2}$$

where $d_i = Z_i - Z_{i-1}$

$$\theta_d = \frac{\lambda}{2\pi\sigma_{Io} P_{B.E.}} = \text{divergence angle of the beam}$$

The displacement of the beam due to a misalignment of the plane mirror is given by

$$D_i = Z_i \phi_P \qquad 6 \leq i \leq 10$$

$$D_i = D_{i-1} + \frac{d_i \phi_P}{P_{B.E.}} \qquad 11 \leq i \leq 14$$

For the case of a misalignment of the curved laser mirror

$$D_i = R_c \phi_c \qquad 6 \leq i \leq 9$$

$$D_i = P_{B.E.}\ R_c \phi_c \qquad 10 \leq i \leq 14$$

The loss is now just given by $(1 - P_{\phi}/P_o)$ without being related to any laser efficiency. Here, P_o is the power passing through the smallest aperture (relative to σ_{Io}) when $\phi = 0$, and P_{ϕ} is the power passing through the confining aperture when $\phi \neq 0$.

The loss of transmitted power due to vignetting outside the laser is shown in Figure L-37. It is noted immediately that the loss within the laser far exceeds that outside the laser, which can generally be neglected. The parameters used were

i	D_i (mm)	R_i (mm)
6	67.2	2.13
7	255	2.13
8	94.2	2.13
9	89.2	14.1
10	18.2	14.1
11	32.7	14.1
12	93.5	14.1
13	125.0	14.1
14	101.3	14.1

10.4 POWER LOSS DUE TO LATERAL SHIFT OF CRYSTAL

Since the blockage occurs at Z_2, a lateral shift, D_M, of the position of the modulator crystal is equivalent to the case of an angular misalignment of the curved mirror. Thus, the power loss within the laser corresponds to that obtained with

$$\phi_c = \frac{D_M}{R_c}$$

For example, from Figure L-37, a .1-db loss occurs if $\phi_c = .2$ mrad; this corresponds to a displacement, D_M, of .1 mm since $R_c = 500$ mm.

10.5 TRANSMITTER/RECEIVER BEAMS, OPTICAL AXIS ALIGNMENT

Besides the power loss of the transmitter laser beam caused by vignetting of the beam, a more stringent alignment requirement is in aligning the transmitter and receiver optical axes to be colocal and collinear. The transmitter far-field beam pattern determines the degree of alignment necessary, as shown in Figure L-38. A 3 $\overset{\frown}{\text{sec}}$ misalignment of the two beams will reduce the received signal power by 0.7 db.

To achieve a 3 $\overset{\frown}{\text{sec}}$ collinearity of the transmit and receive beams, the angular misalignment between the two beams prior to the coupling mirror is required to be less than 30 $\overset{\frown}{\text{sec}}$, since the telescope power is 10. The two beams are joined at the duplexer, with the transmitter beam passing through the duplexer and the received beam being reflected. The misalignment tolerance of the duplexer therefore would be 30 $\overset{\frown}{\text{sec}}$, except that the nutator can correct for any static misalignment caused by launch vibration and shock or by a constant gravity force on the baseplate as long as it is constant in one direction. The nutator searches for the peak intensity of the received beam direction, and in doing so, the duplexer misalignment is corrected. Other misalignment changes, for instance those caused by bending of the baseplate from changes in temperature, are required to be less than 30 $\overset{\frown}{\text{sec}}$ to keep the signal-to-noise ratio loss to within 0.7 db.

To keep the nutator bias voltage small, this tolerance is reduced to .5 mrad.

Any static or dynamic misalignments, and those as caused by changing temperature in the image motion compensator (IMC), lens, or mirrors (elements 11-16 in Figure L-39) between the coupling mirror and the duplexer, affect both the transmit and receive beams. Hence, the IMC will correct for these misalignments. A vector sum of these angular misalignments should be within 1/10 of the maximum IMC off-axis tracking angle of .2 degrees external angle, or 1/10 x 2 degrees internal angle. The total tolerance is then .2 degrees = $\overset{\frown}{720}$ sec.

A total of 100 $\overset{\frown}{\text{sec}}$ for a correlated temperature tolerance leaves 620 $\overset{\frown}{\text{sec}}$ total random misalignment tolerance. Then the individual tolerances

for these five components are 20 $\widehat{\text{sec}}$ temperature misalignment tolerance and 370 $\widehat{\text{sec}}$ random misalignment tolerance, so that

$$\left(\sum_{i=1}^{5} \phi_{i_{temp}}\right) = 100 \ \widehat{\text{sec}}$$

$$\left(\sum_{i=1}^{5} \phi_{i_{random}}^{2}\right)^{1/2} = 620 \ \widehat{\text{sec}}$$

Thus, these values in comparison with other components are not critical and do not add a loss to the path transmissivity, because of the nutator angular compensation.

The optical elements before the duplexer in the transmitter/telescope path (elements 1-9 in Figure L-39) contribute to the power loss of the transmitter beam as already discussed and to the transmit/receive beam misalignment. The individual misalignments, as caused by chainging temperature of the baseplate, may not be considered as uncorrelated misalignments since a warped baseplate might bend the horizontal plane along the optical path. The misalignments would then add together to give a total misalignment.

To maintain collinearity of the transmitted and received beam out the telescope to within 3 $\widehat{\text{sec}}$, assuming they are initially aligned to within 2 $\widehat{\text{sec}}$, the total misalignment tolerance for elements preceding the duplexer is found by multiplying the external angular tolerance by the powers of the telescope and beam expander. The front lens of the beam expander is assumed to be rigidly housed with the back lens. For an additional 1 $\widehat{\text{sec}}$ misalignment angle

$$\phi_{total} = (1 \ \widehat{\text{sec}}) \times (10 \text{ telescope power}) \times (6.5 \text{ beam expander power})$$
$$= 65 \ \widehat{\text{sec}}$$

Considering misalignment of the 7 components as caused by independent effects, such as vibration shaking of the mounts to the Cervit baseplate and separation between the Cervit baseplate and the beryllium base on which the laser tube and modulator are mounted, then the root sum square of the random misalignments and the correlated temperature misalignments totals 65 $\widehat{\text{sec}}$.

$$k\left[\sum_{i=1}^{7} \phi_{i_{random}}^2 + \left(\sum_{j=1}^{7} \phi_{j_{temp}}\right)^2\right]^{1/2} = 65 \widehat{\text{sec}}$$

The misalignment angle of the laser tube and modulator is expected to be greater than the other components since these two units are mounted on a different base. An estimated tolerance of 50 $\widehat{\text{sec}}$ for this tolerance and total temperature tolerance of 20 $\widehat{\text{sec}}$ gives $\theta_{i_{random}} = 15 \widehat{\text{sec}}$ for all components other than the laser tube and modulator. Thus, the temperature variation tolerance is 20/5 = 4 $\widehat{\text{sec}}$ and the random misalignment tolerances are 15 $\widehat{\text{sec}}$, excepting the laser tube and modulator which are mounted on the beryllium base and are misaligned with respect to each other by less than 15 $\widehat{\text{sec}}$ tolerance.

To summarize these tolerances, Table L-2 lists the maximum angular variations permissible. The identifying numbers refer to those in Figure L-37. The mixer misalignment tolerances are discussed in a separate analysis.

Based on these tolerances, the combined effects of transmitter power decrease of -.3 db and transmitter/receiver optical axis misalignment loss of -.4 db for 1 $\widehat{\text{sec}}$ external telescope misalignment angle gives a total of -.7 db.

TABLE L-1

SYSTEM ABERRATIONS - CASSEGRAIN TELESCOPE/RELAY LENS

	Aberration microradians	Wavelengths
Single-Lens Relay		
On-axis beam		
Tangential	95	$\lambda/20$
Sagittal	95	$\lambda/20$
$.2^{o}$ off-axis beam		
Tangential	835	$\lambda/2$
Sagittal	411	$\lambda/5$
Doublet Relay		
On-axis beam		
Tangential	0	0
Sagittal	0	0
.2 off-axis beam		
Tangential	285	$\lambda/8$
Sagittal	245	$\lambda/8$

TABLE L-2

OPTICAL COMPONENT MISALIGNMENT TOLERANCES

No.	Component	Random Misalignment Tolerance $\widehat{sec}$	Temperature Misalignment Tolerance $\widehat{sec}$
	Flat laser and mirror	15	4
1-2	Modulator	50	4
3-4	Laser tube	50	4
5	Curved-end mirror	15	4
6-7	Reflecting mirrors	15	4
8-9	Beam expander	15	4
10	Duplexer	100	20
11	IMC	370	20
12,14	Reflecting mirrors	370	20
13	Filter relay lens	370	20
15	Nutator	370	20
16	Imaging lens	370	20

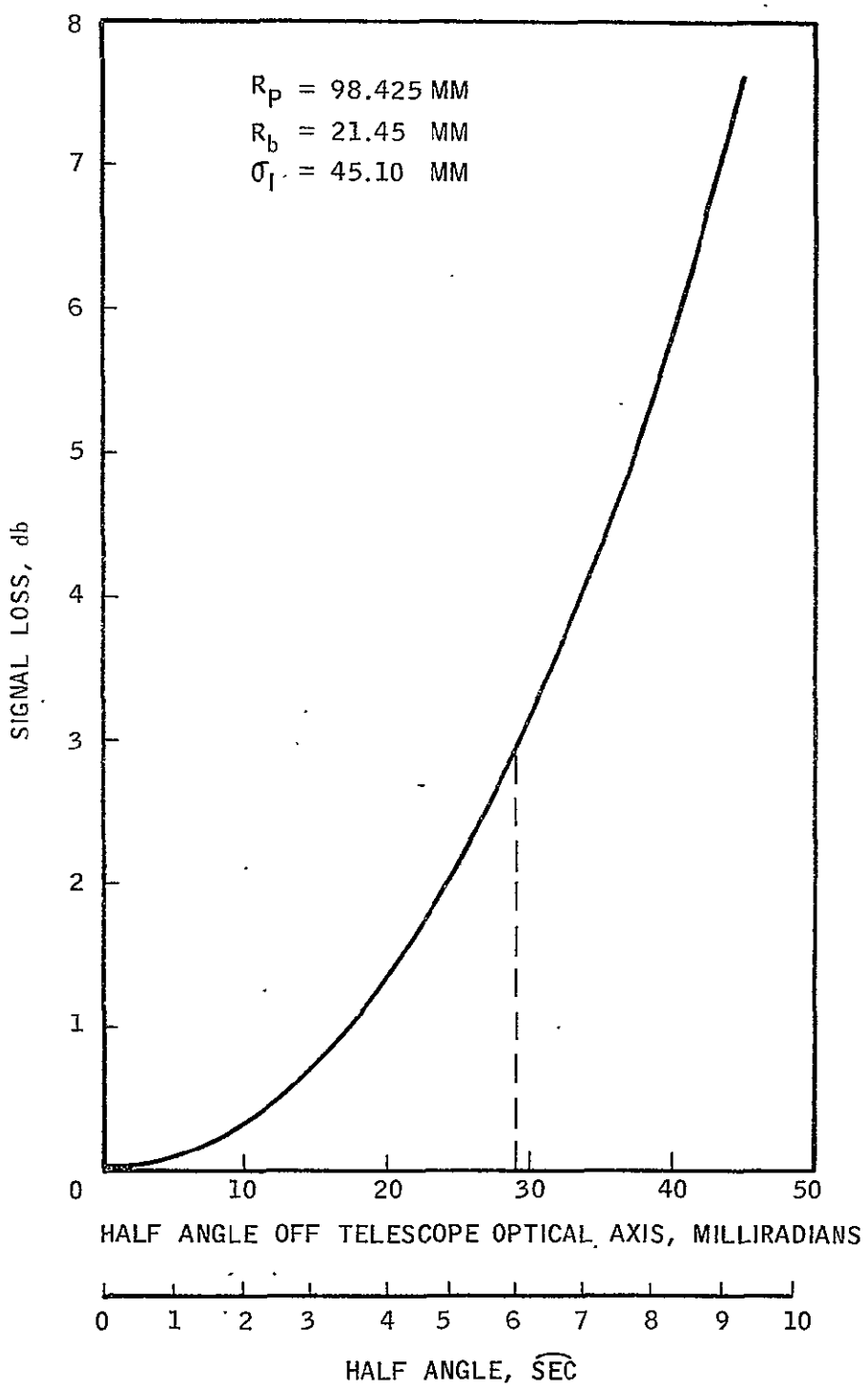

TRANSMITTER FIELD OF VIEW, σ_I = 46.10 MM

Figure L-5

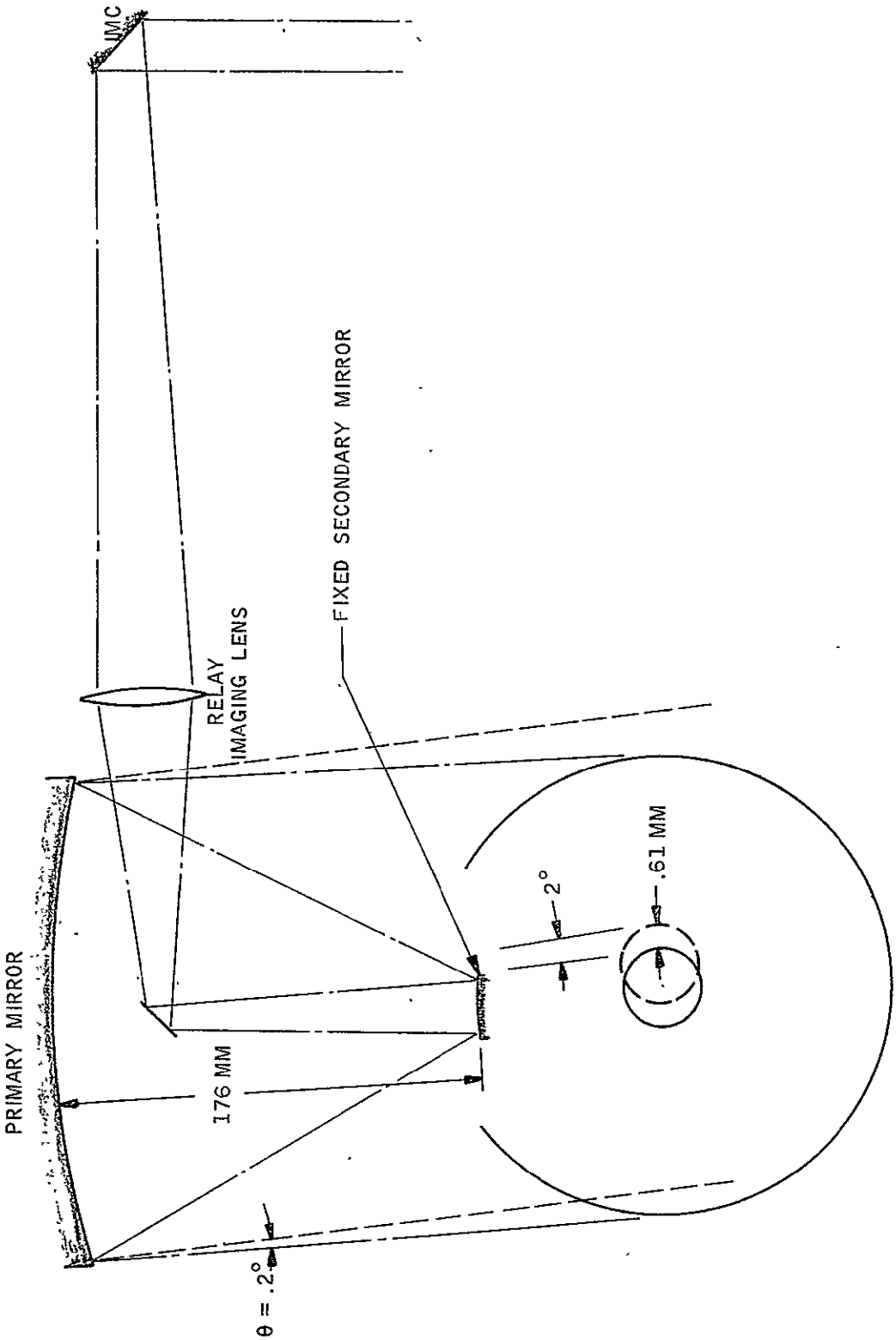

A .2° DISPLACED BEAM AS IT PASSES THE FIXED SECONDARY MIRROR

Figure L-6

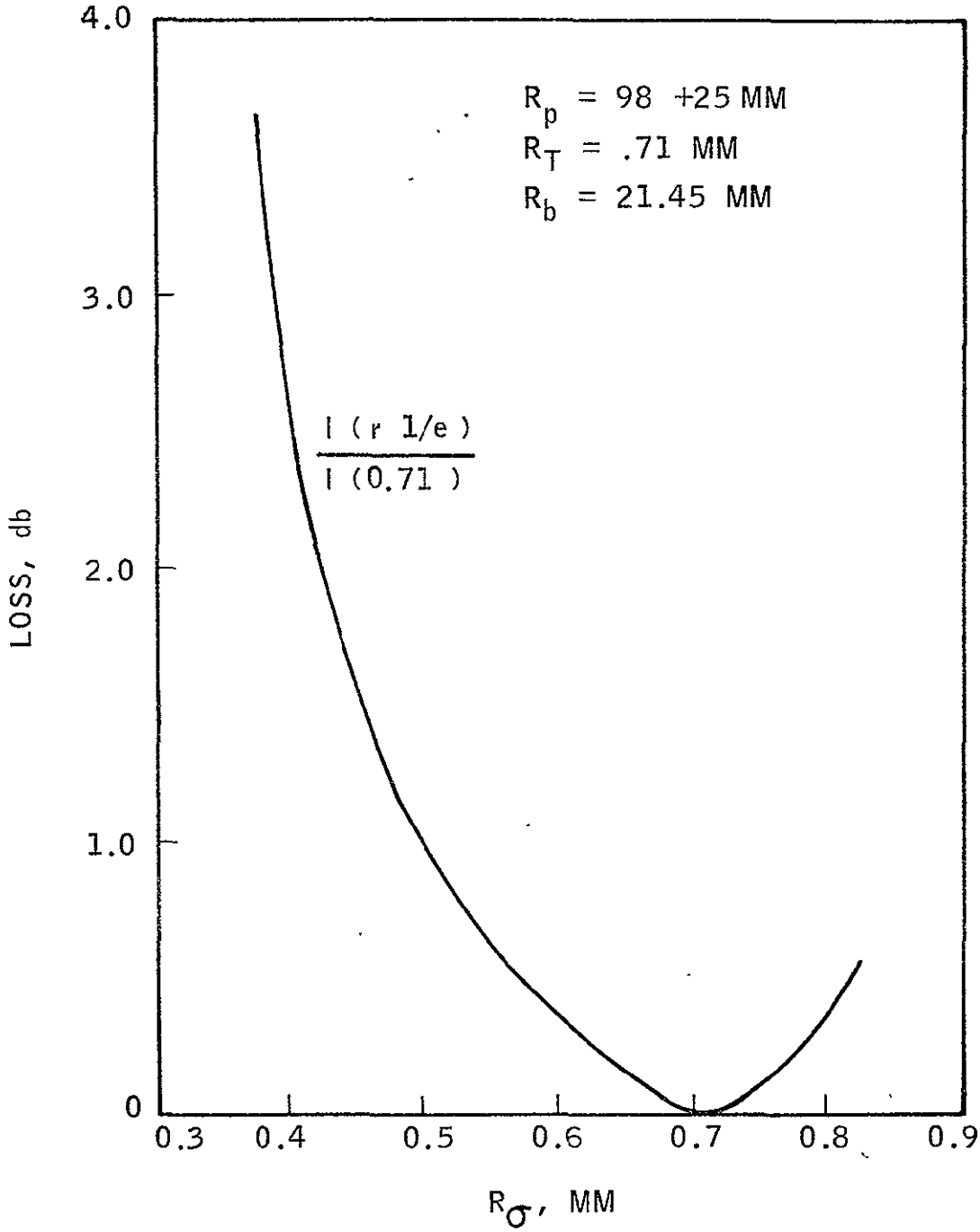

LOSS OF FAR FIELD AXIAL INTENSITY
AS BEAM RADIUS IS VARIED

Figure L-7

EFFECTS OF TELESCOPE CENTRAL BLOCKING

Figure I-8

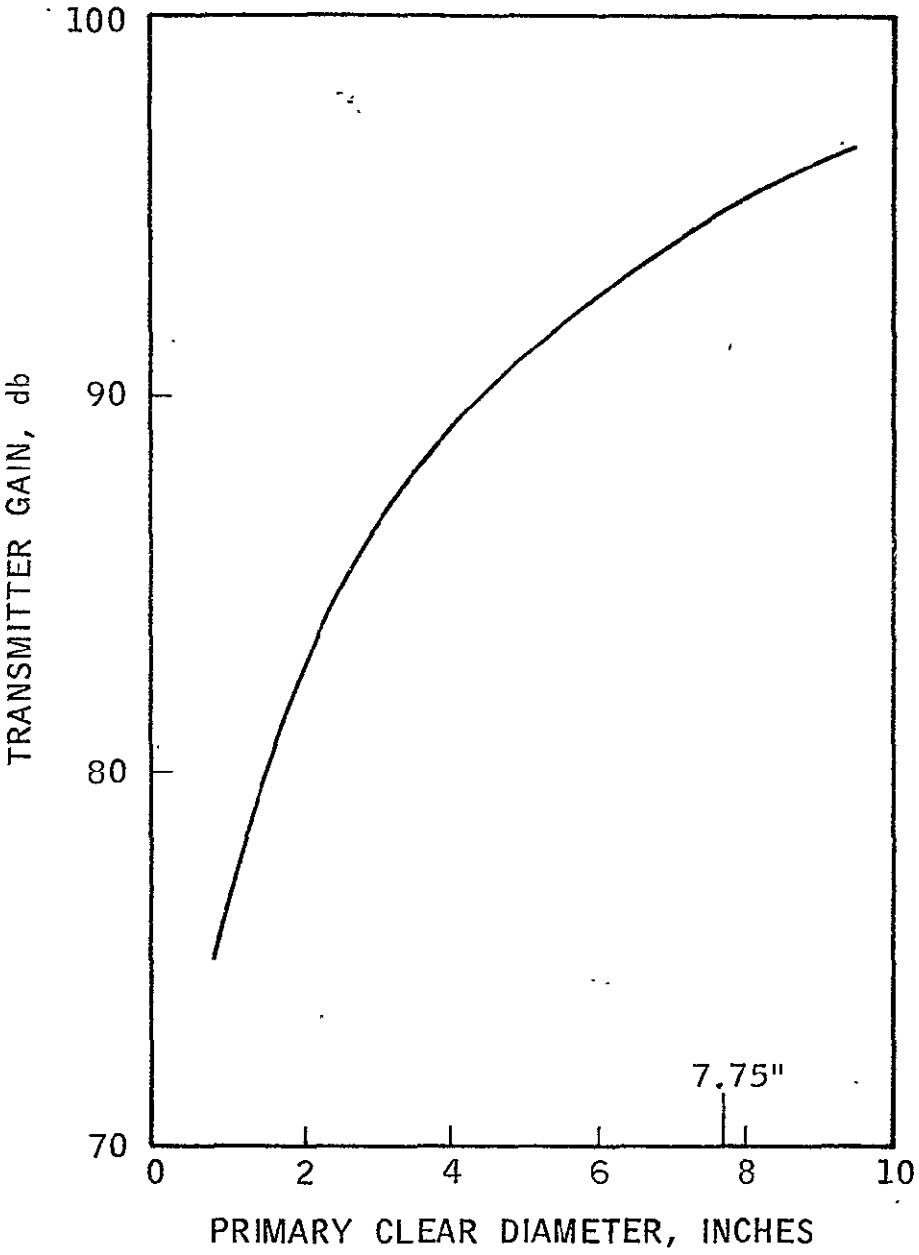

TRANSMITTER GAIN VS PRIMARY CLEAR DIAMETER

Figure L-9

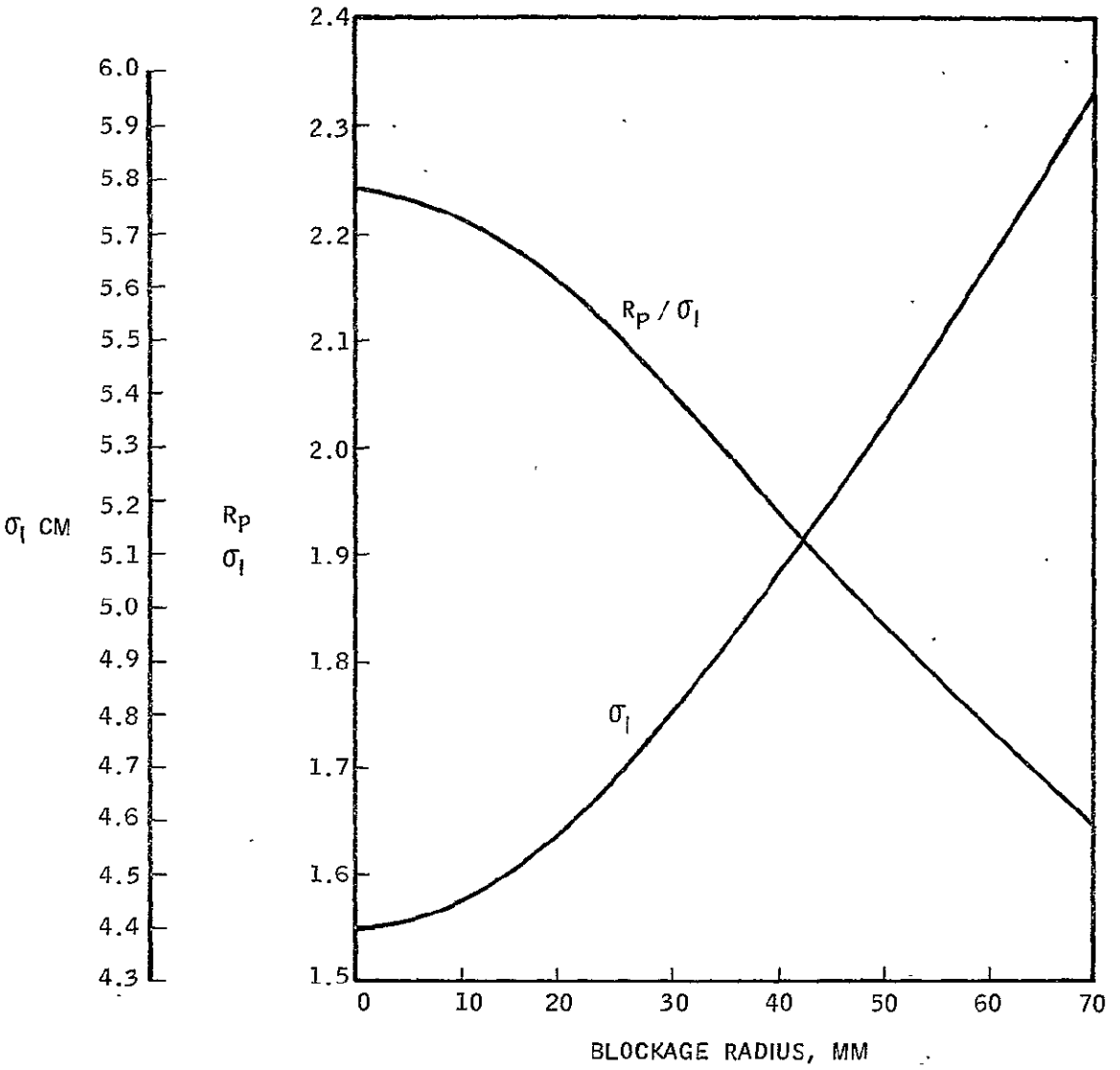

RATIO OF PRIMARY RADIUS TO σ_1 AT THE PRIMARY MIRROR FOR OPTIMUM FAR FIELD AXIAL INTENSITY AS A FUNCTION OF CENTRAL CLOCKAGE RADIUS (R_P = 98.425 MM) σ_1 VS CENTRAL BLOCKAGE RADIUS

Figure L-10

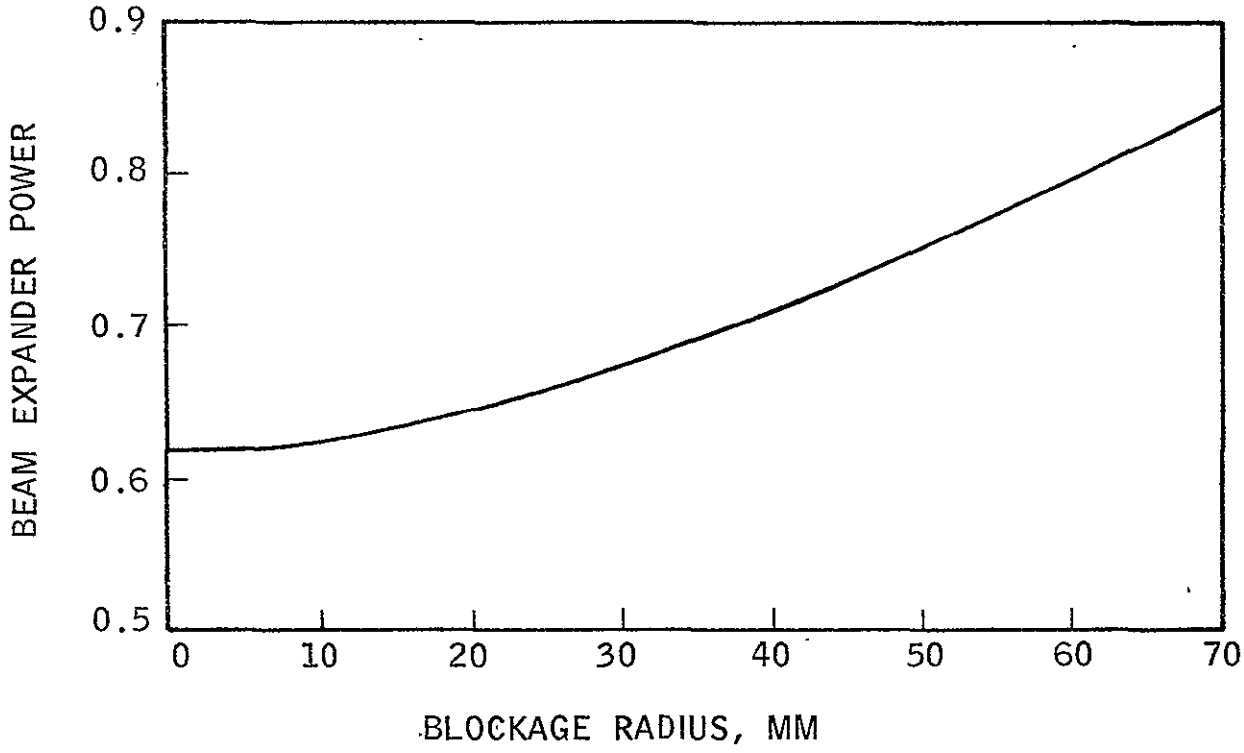

BEAM EXPANDER POWER VS
CENTRAL BLOCKAGE RADIUS

Figure L-11

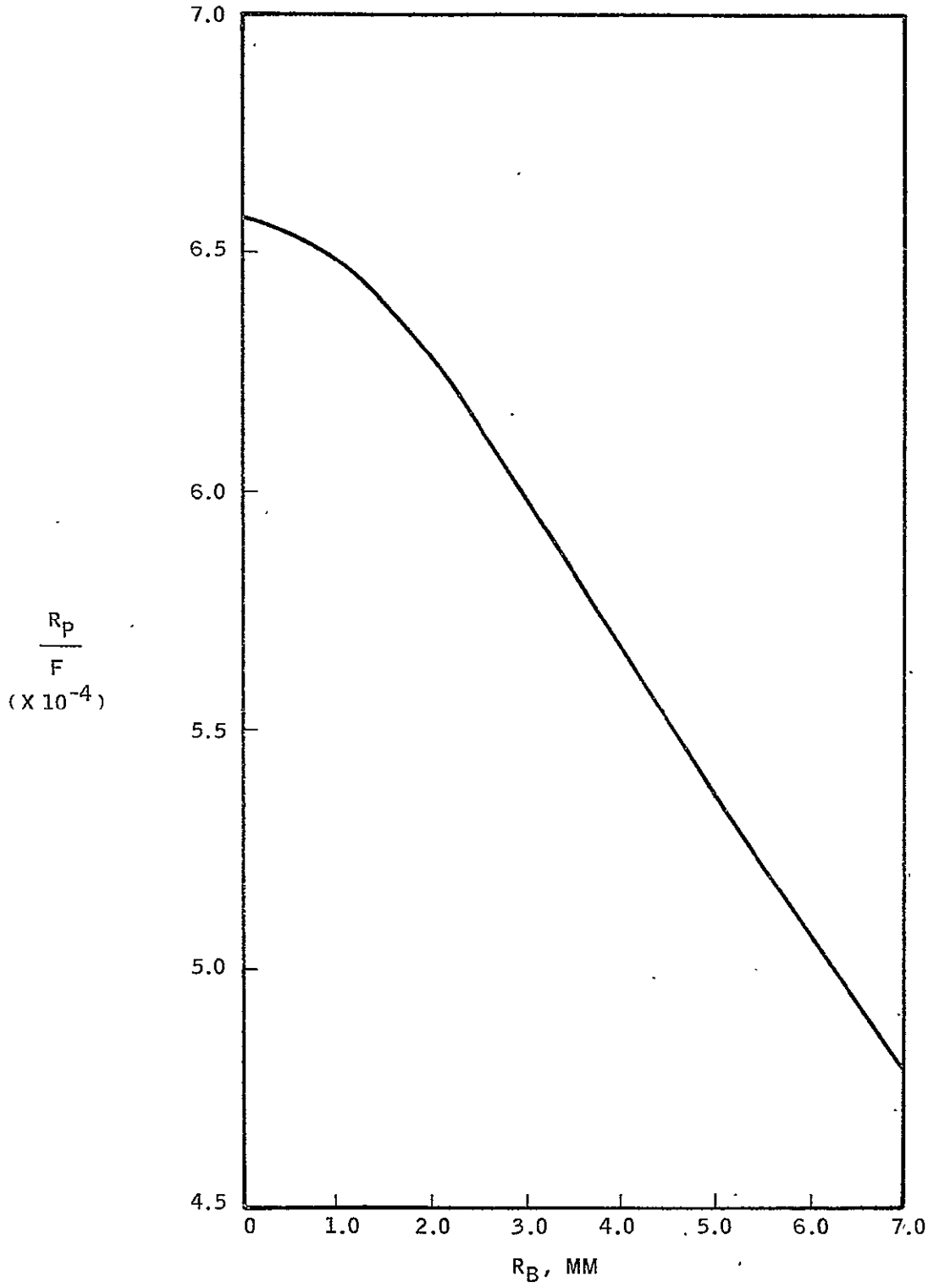

RATIO OF DETECTOR RADIUS TO FOCAL LENGTH WHICH MATCHES AIRY DISC TO DETECTOR AS A FUNCTION OF CENTRAL BLOCKAGE RADIUS

Figure L-12

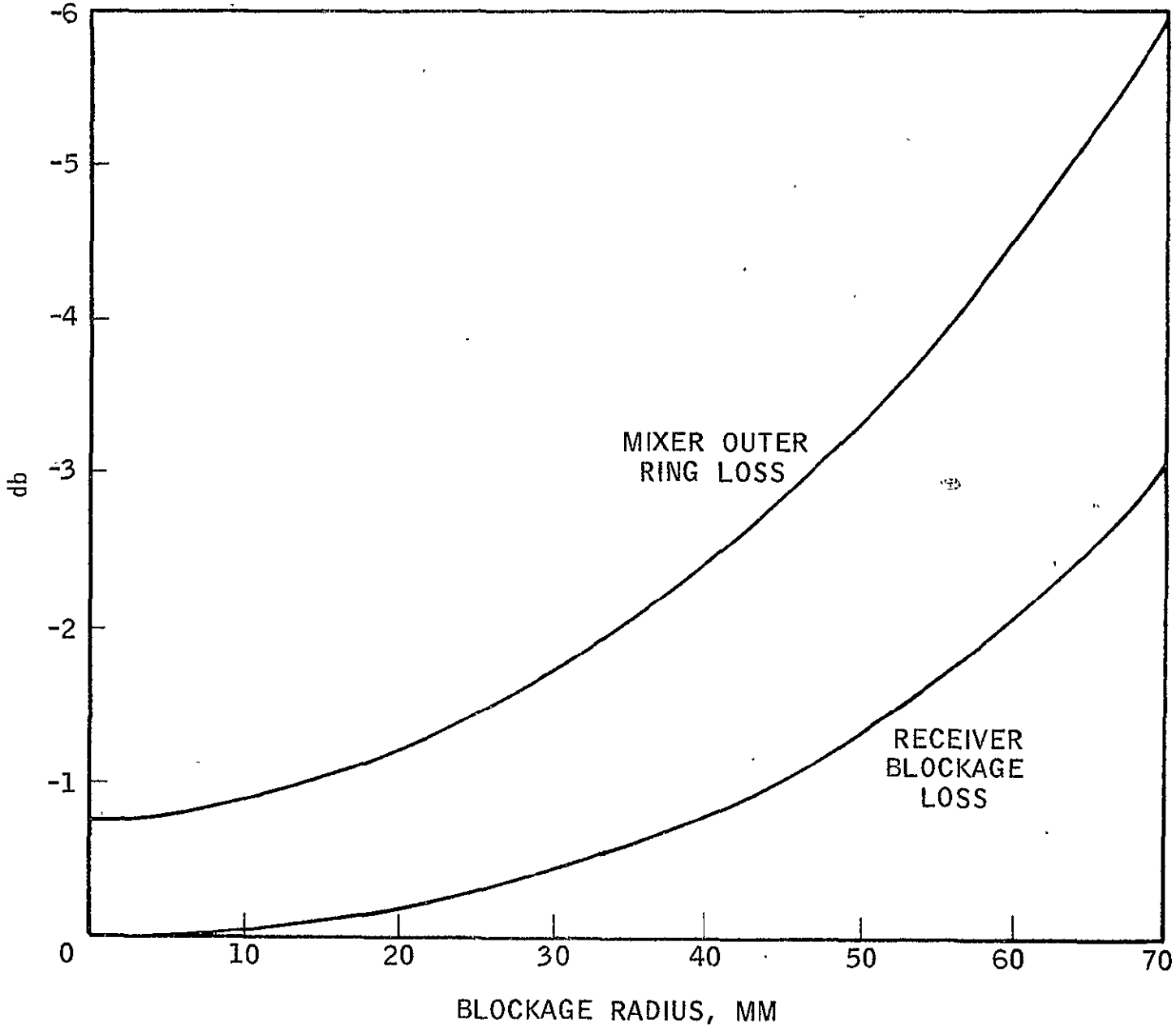

RECEIVER BLOCKAGE AND MIXER OUTER RING LOSSES VS BLOCKAGE RADIUS

Figure I-13

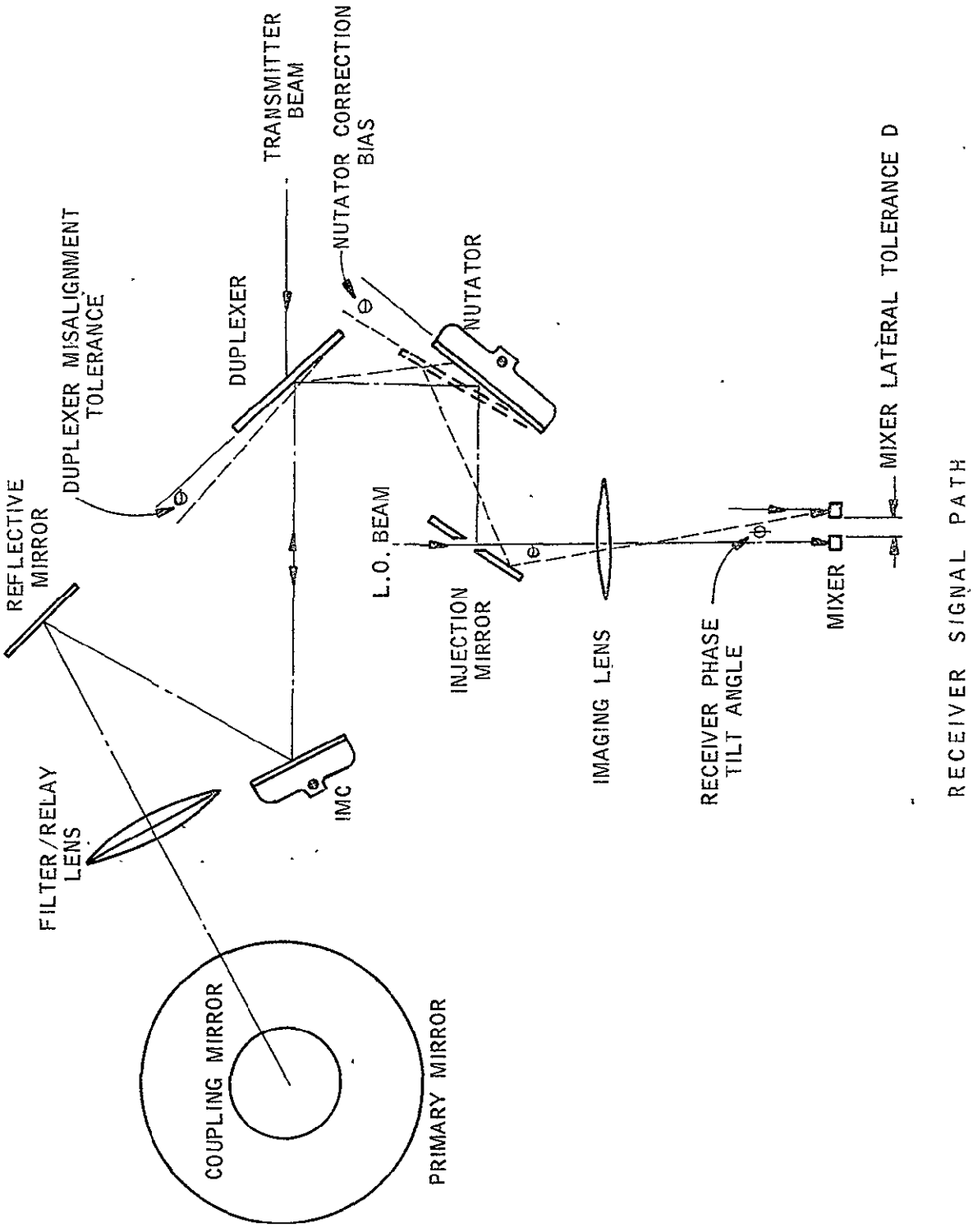
TRANSMITTER BEAM
NUTATOR CORRECTION BIAS
DUPLEXER MISALIGNMENT TOLERANCE
DUPLEXER
NUTATOR
REFLECTIVE MIRROR
L.O. BEAM
INJECTION MIRROR
IMAGING LENS
RECEIVER PHASE TILT ANGLE
MIXER
MIXER LATERAL TOLERANCE D
FILTER/RELAY LENS
IMC
COUPLING MIRROR
PRIMARY MIRROR
RECEIVER SIGNAL PATH

Figure L-14

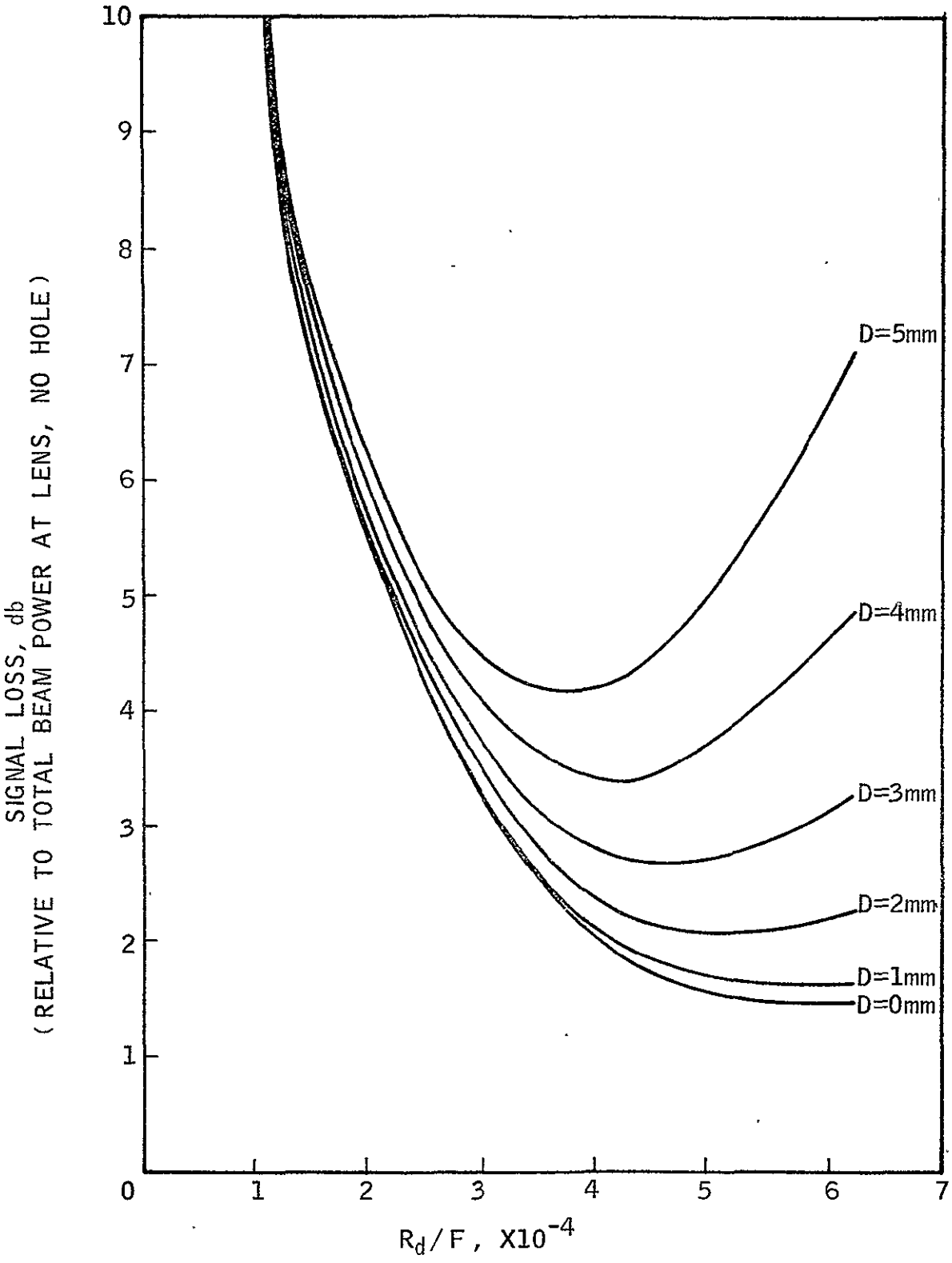

DECREASE IN OUTPUT AS
MIXER IS DISPLACED LATERALLY

Figure L-15

a. INDEPENDENT OF = DIAL LENGTH IF MIXER RADIUS IS MATCHED TO THE AIRY DISC.

b. RATE = 7.7×10^{-4}, R_{max} = 9.8 MM, R_{min} = 2.1 MM

c. TELESCOPE POWER = 10, DISPLACEMENT AT THE INC POSITIONED AT THE TELESCOPE TRANSFER MIRROR = 40∝

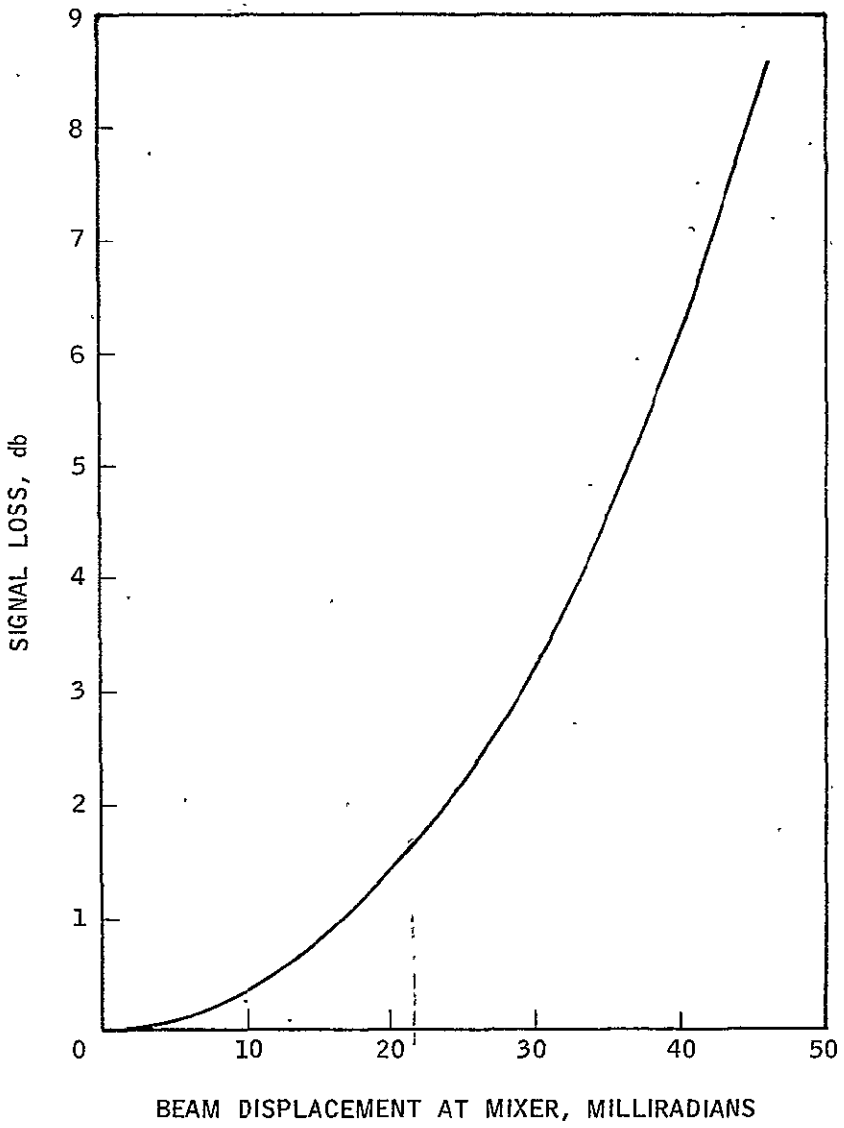

OR MIXER SIGNAL LOSS VS BEAM DISPLACEMENT

Figure L-16

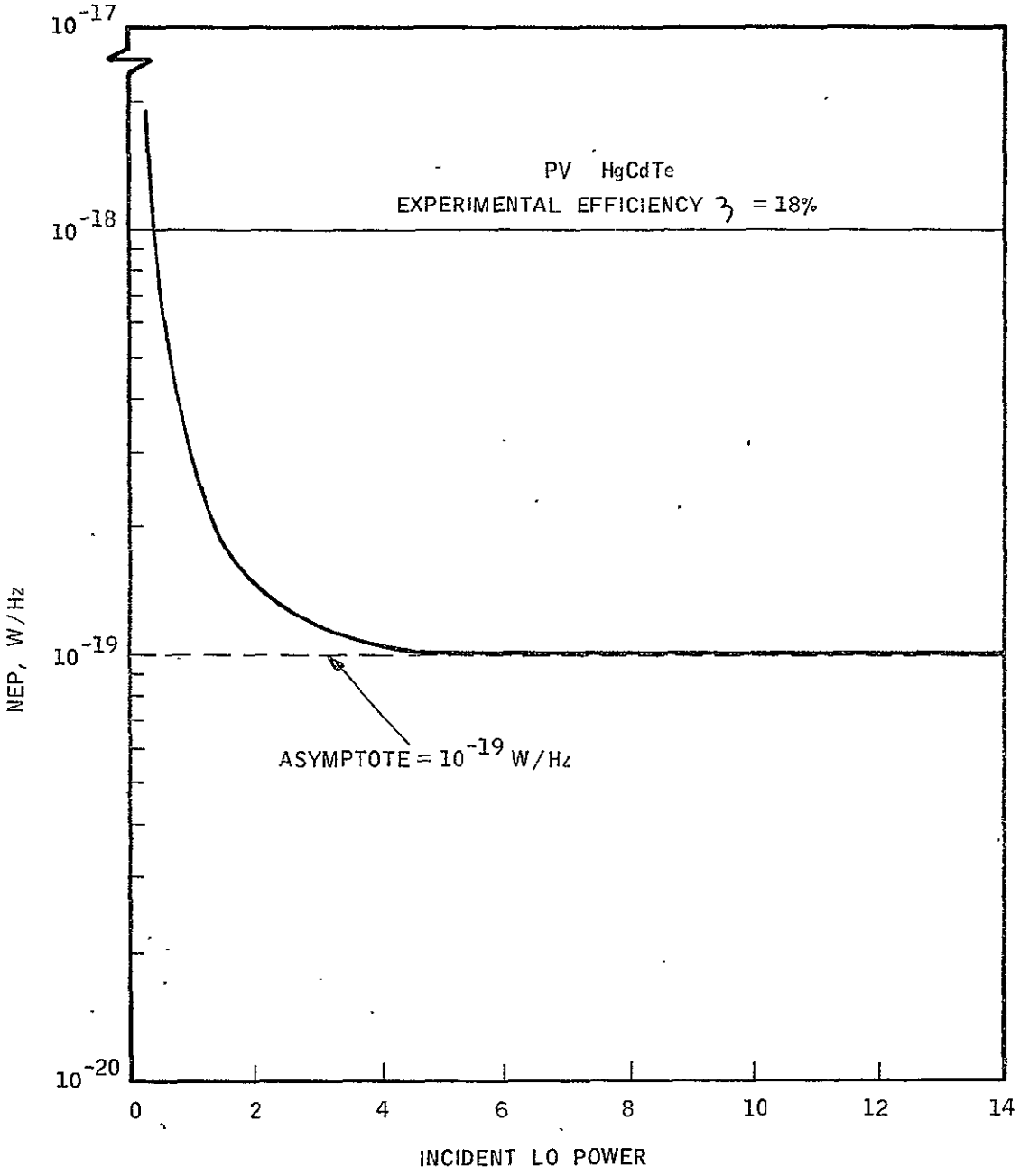

MIXER NEP AS A FUNCTION OF INTERCEPTED L/O POWER

Figure L-17

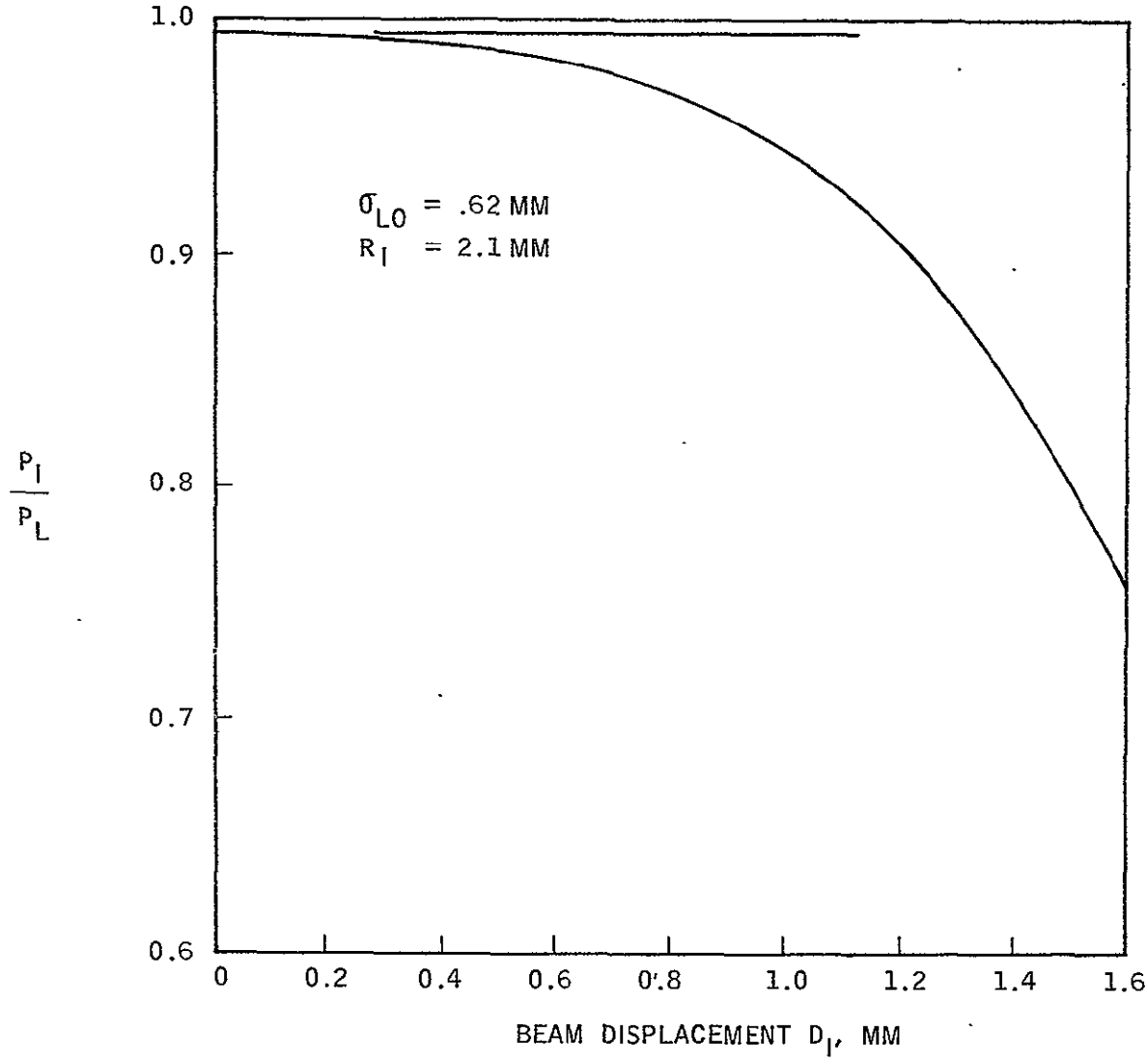

L/O POWER LOSS AT THE INFECTION MIRROR

Figure L-18

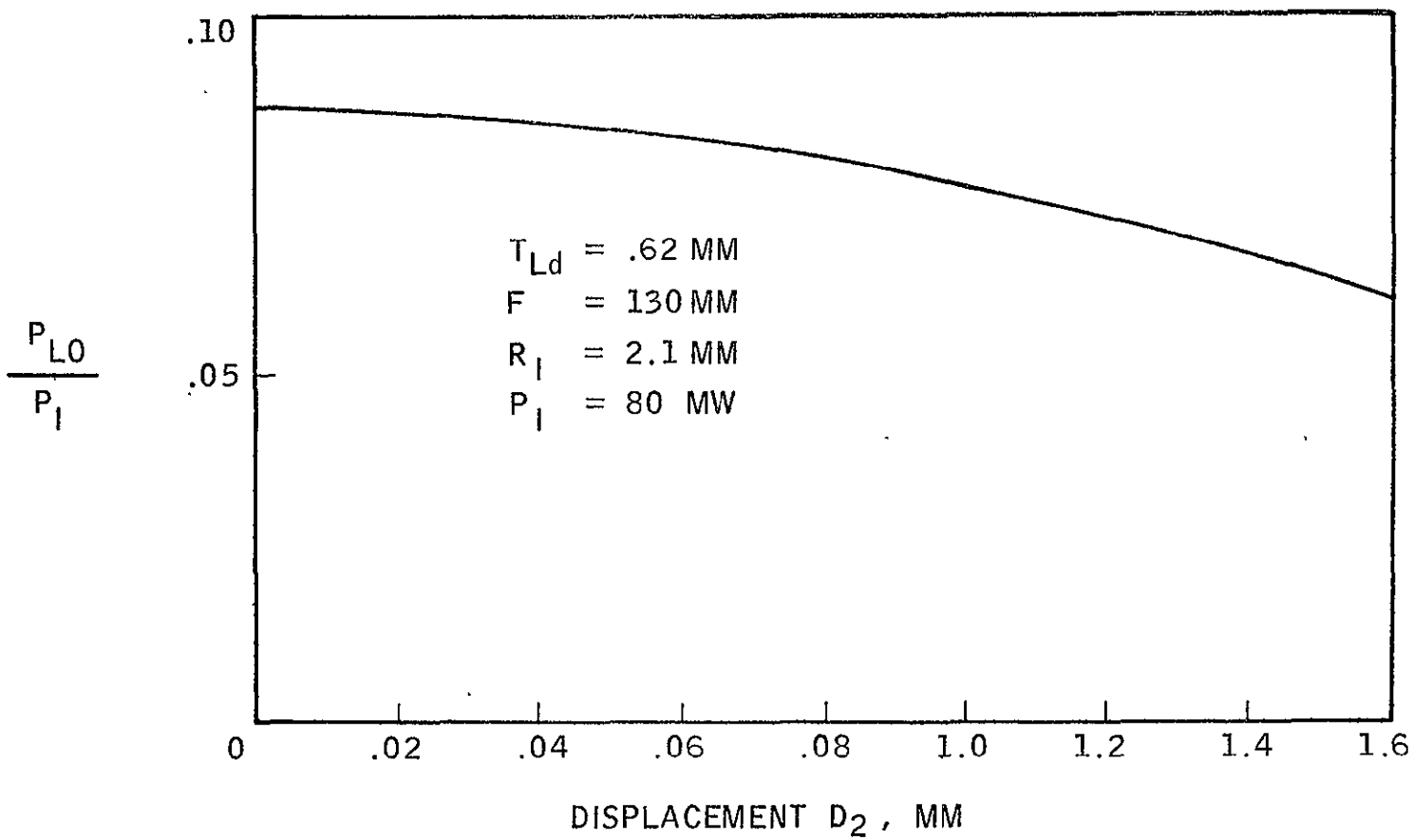

L.O. LOSS AT MIXER

Figure I-19

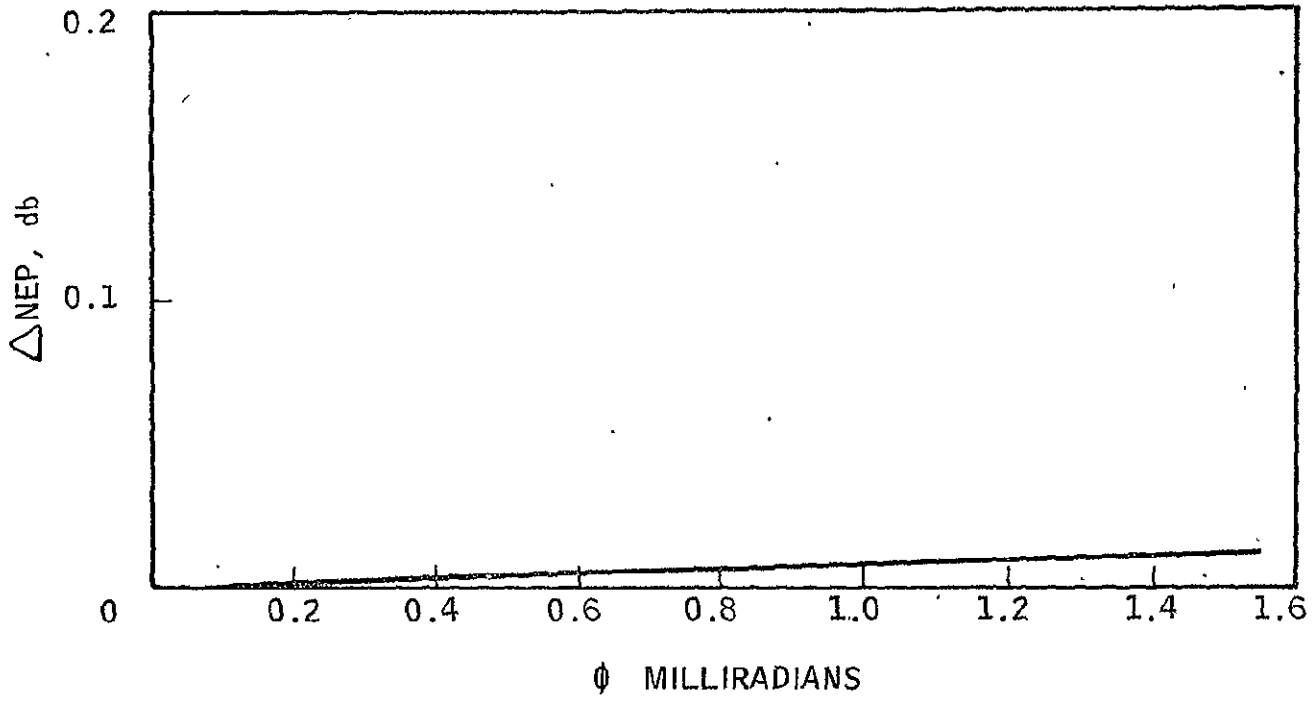

CHANGE IN NEP (W/Hz) AS L.O. MIRROR TRAIN IS MISALIGNED

Figure I-20

i	Zi (MM)
1	45
2	158
3	258
4	303
5	340
6	367

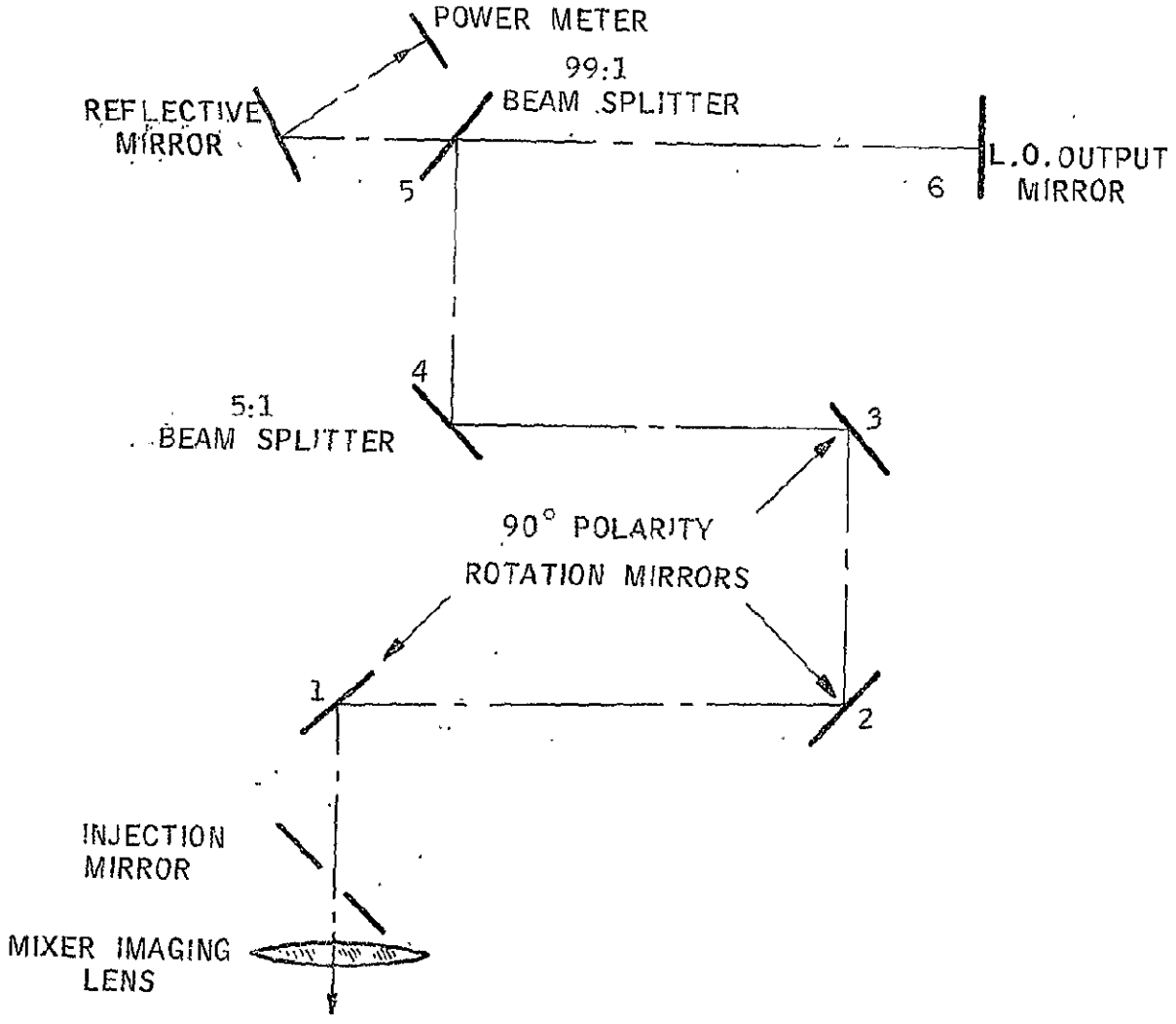

SCHEMATIC OF LOCAL OSCILLATOR OPTICAL TRAIN

Figure I-21

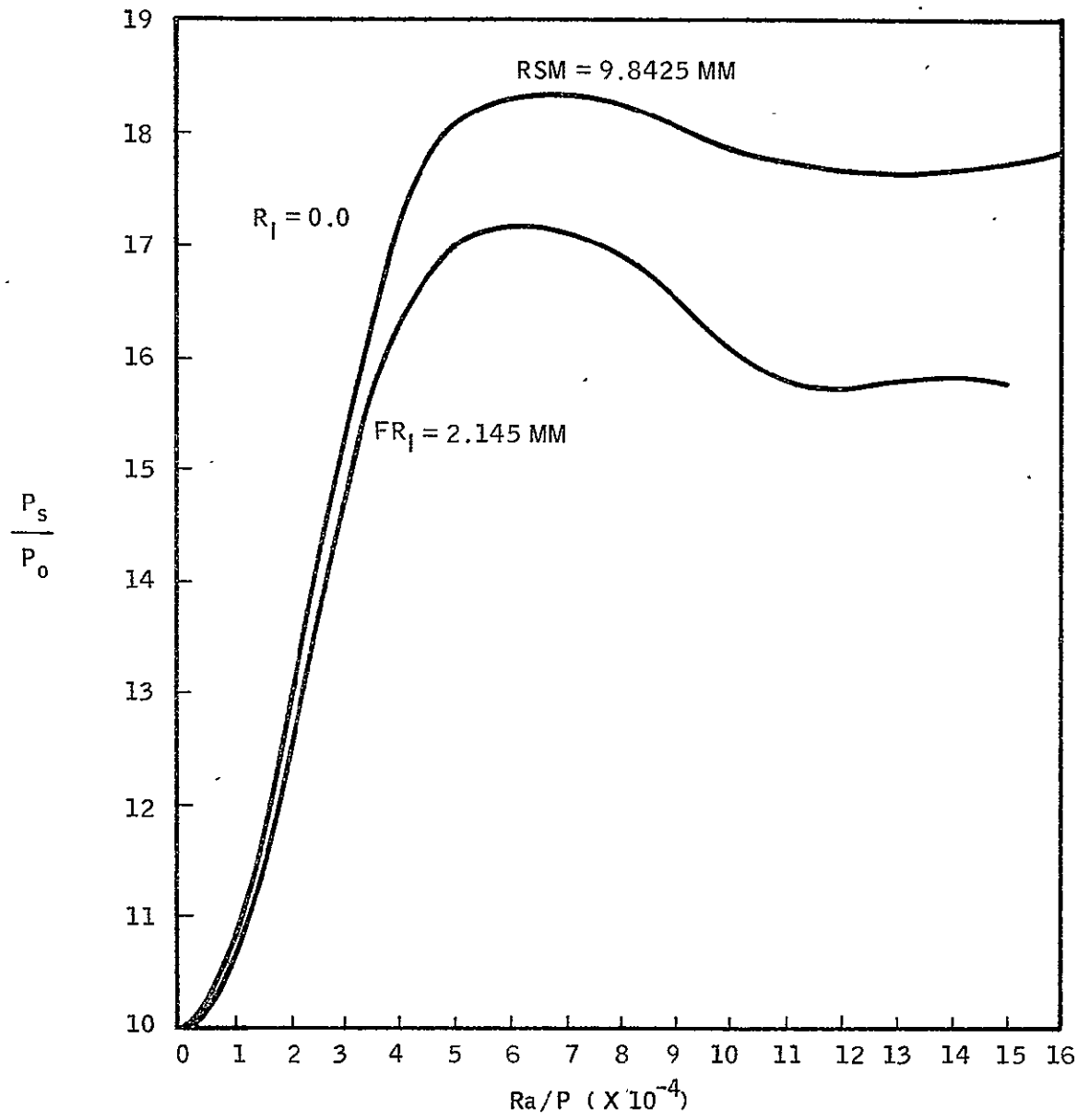

SIGNAL POWER WITHIN A CIRCLE OF RADIUS R_I IN THE FOCAL PLANE AS A FUNCTION OF Ra / P

Figure L-22

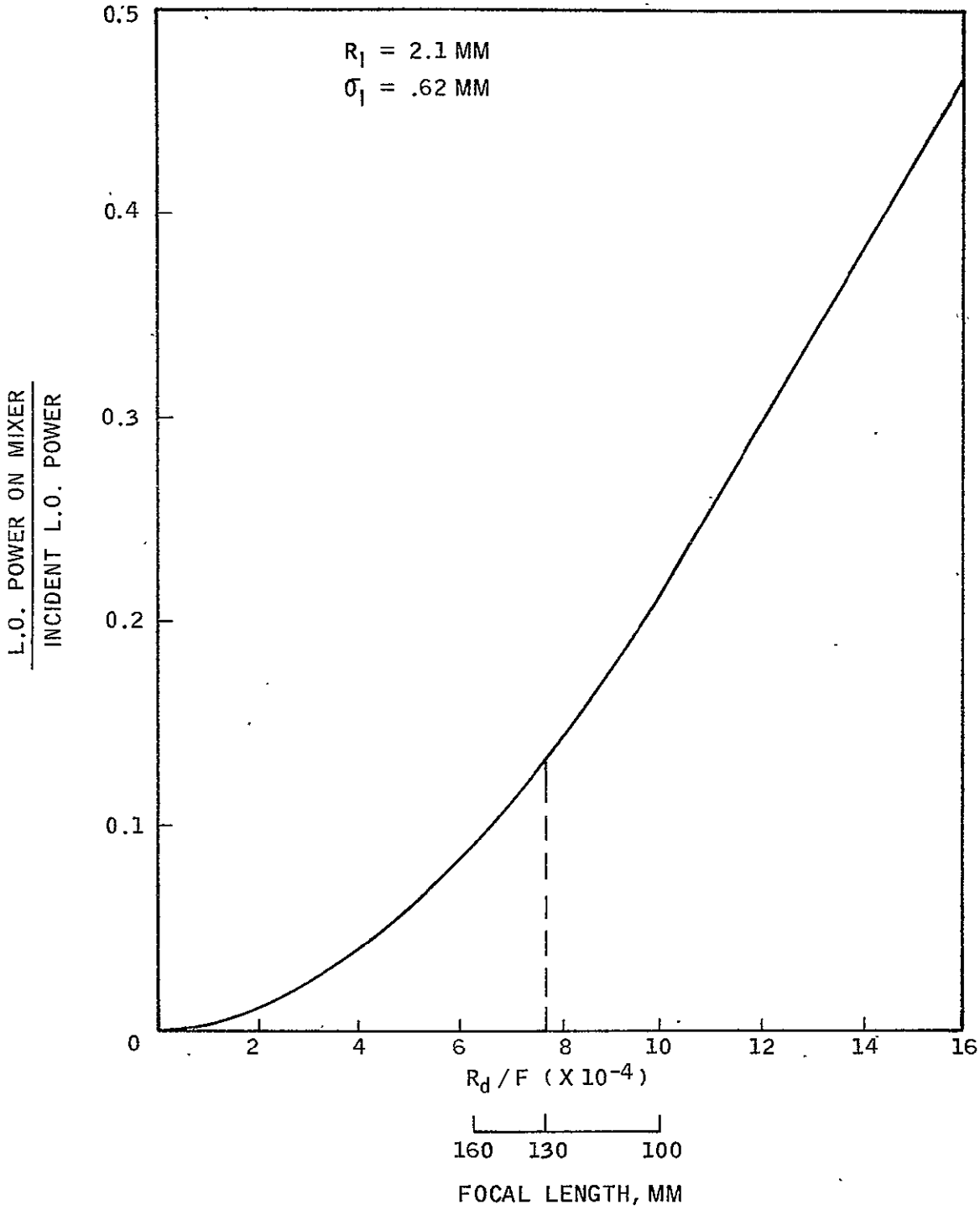

L/O POWER WITHIN RADIUS R_d IN FOCAL PLANE RELATIVE TO THAT INCIDENT ON LENS

Figure L-23

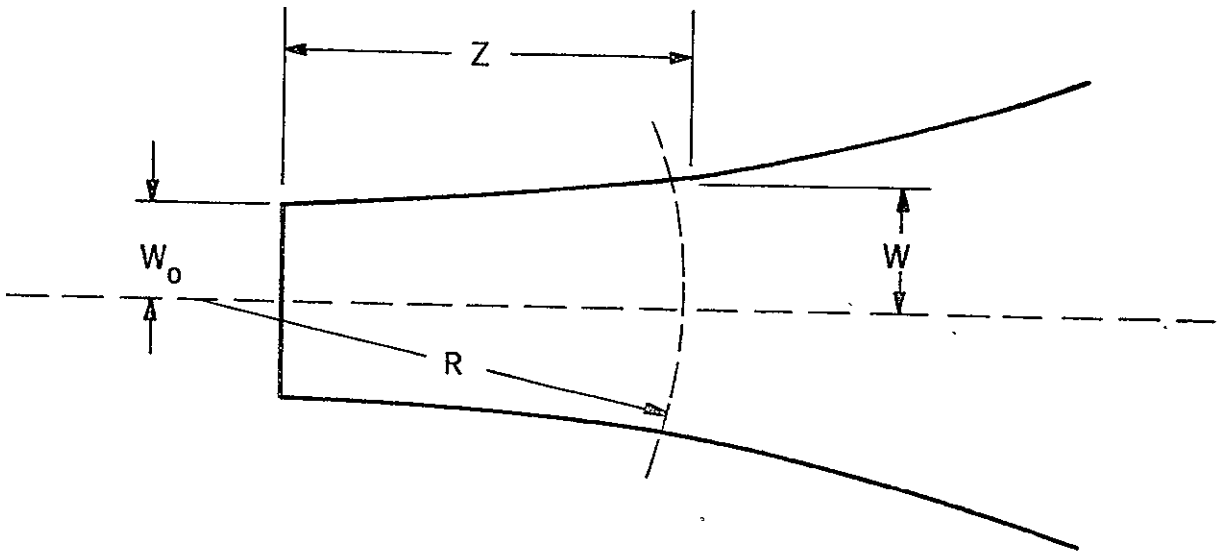

BEAM PARAMETERS

Figure L-24

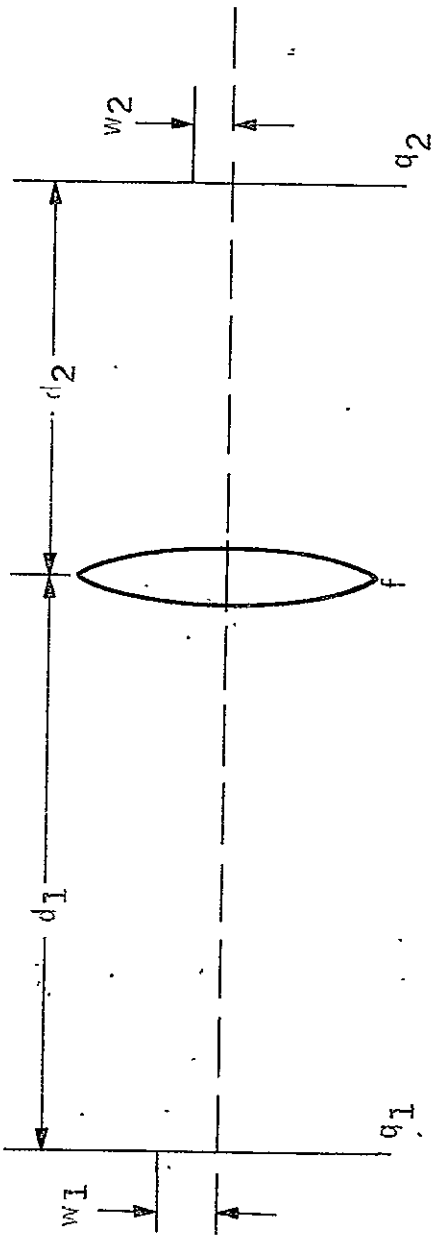

GEOMETRY OF MIXER LENS AND BEAMS

Figure L-25

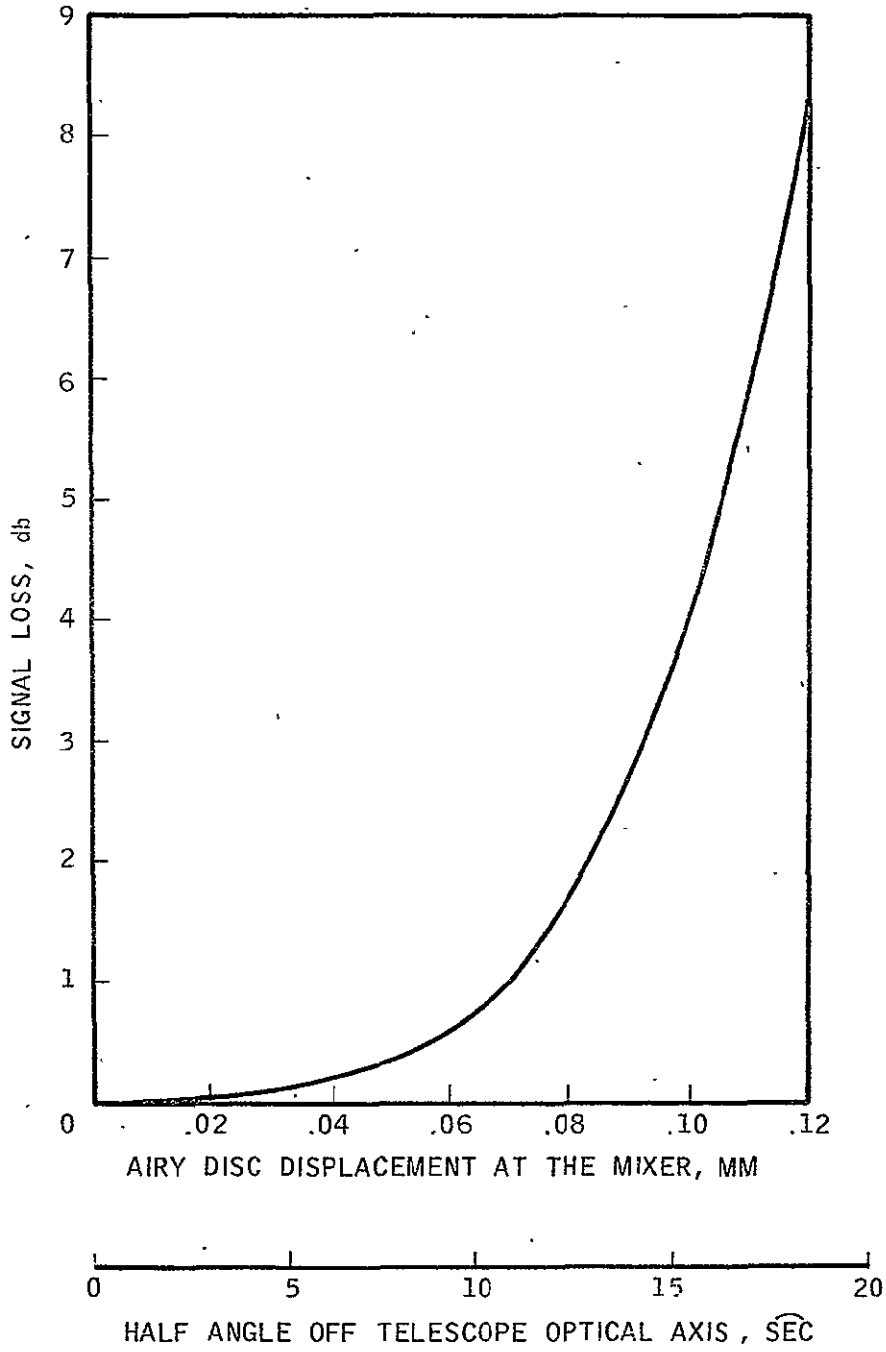

RECEIVER FIELD OF VIEW

Figure L-26

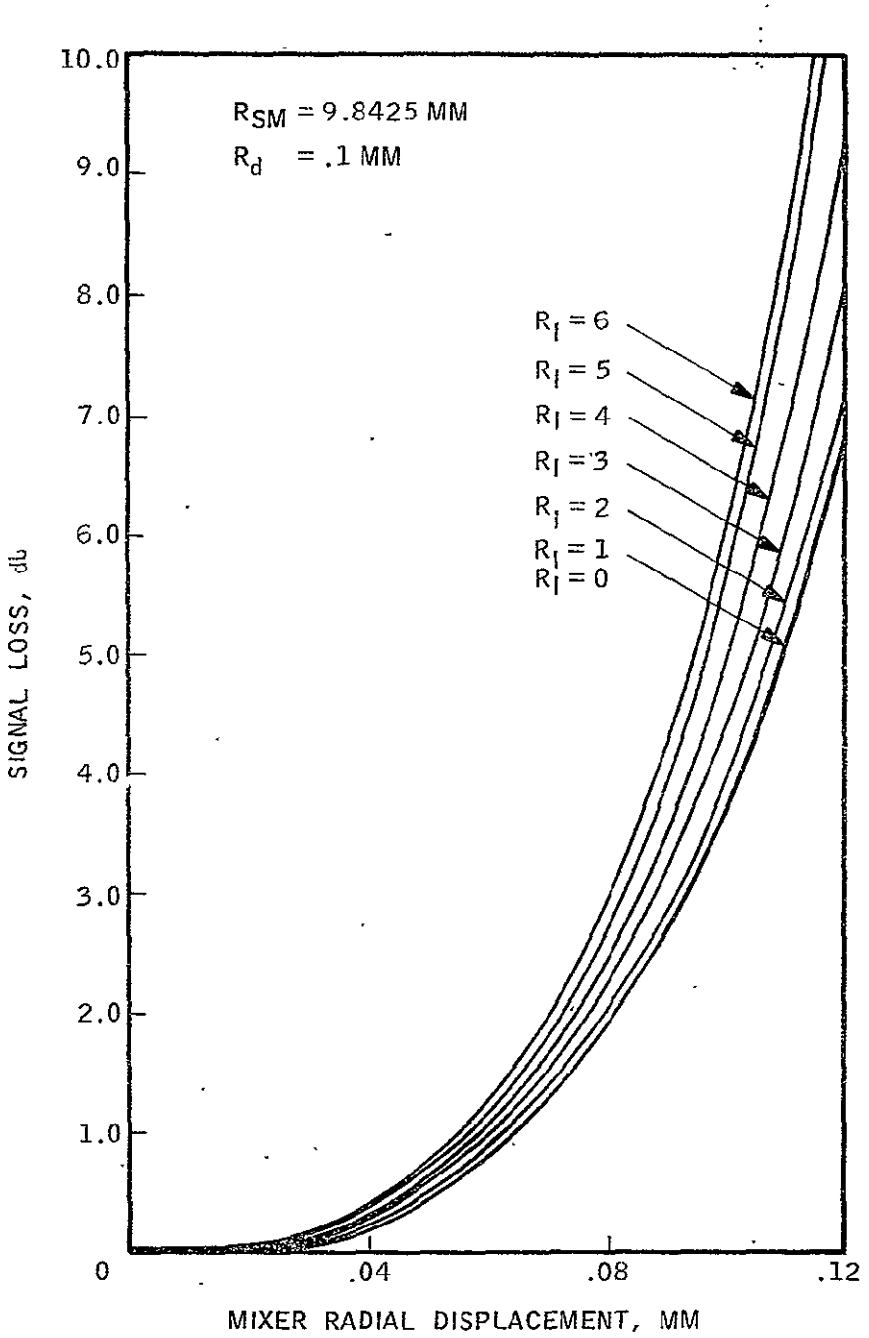

SIGNAL LOSS VS MIXER RADIAL DISPLACEMENT
FOR VARIOUS CENTRAL BLOCKAGE RADII
(OPTIMIZED FOCAL LENGTH)

Figure L-27

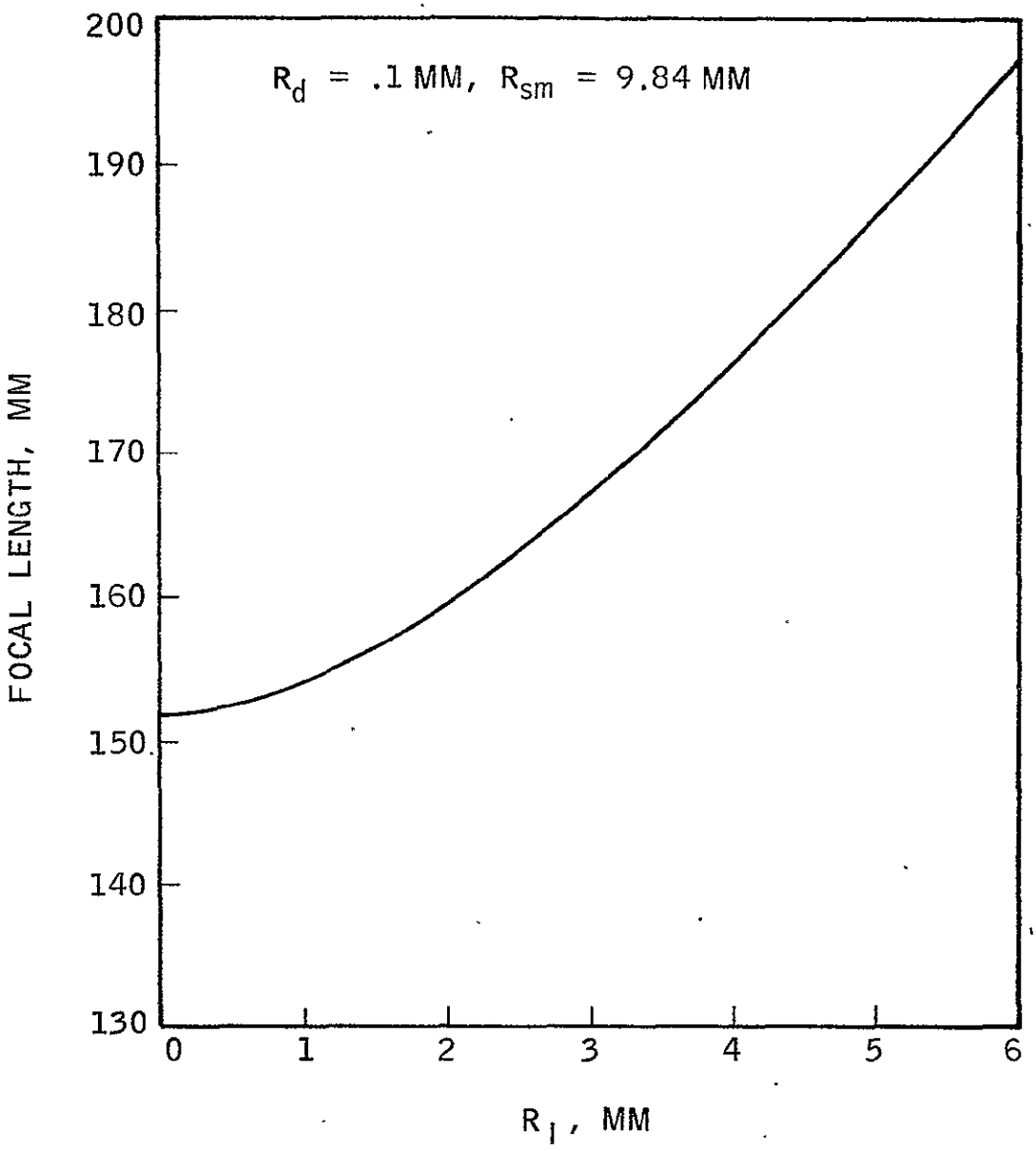

FOCAL LENGTH TO MATCH AIRY DISC WITH DETECTOR VS RADIUS OF CENTRAL BLOCKAGE

Figure L-28

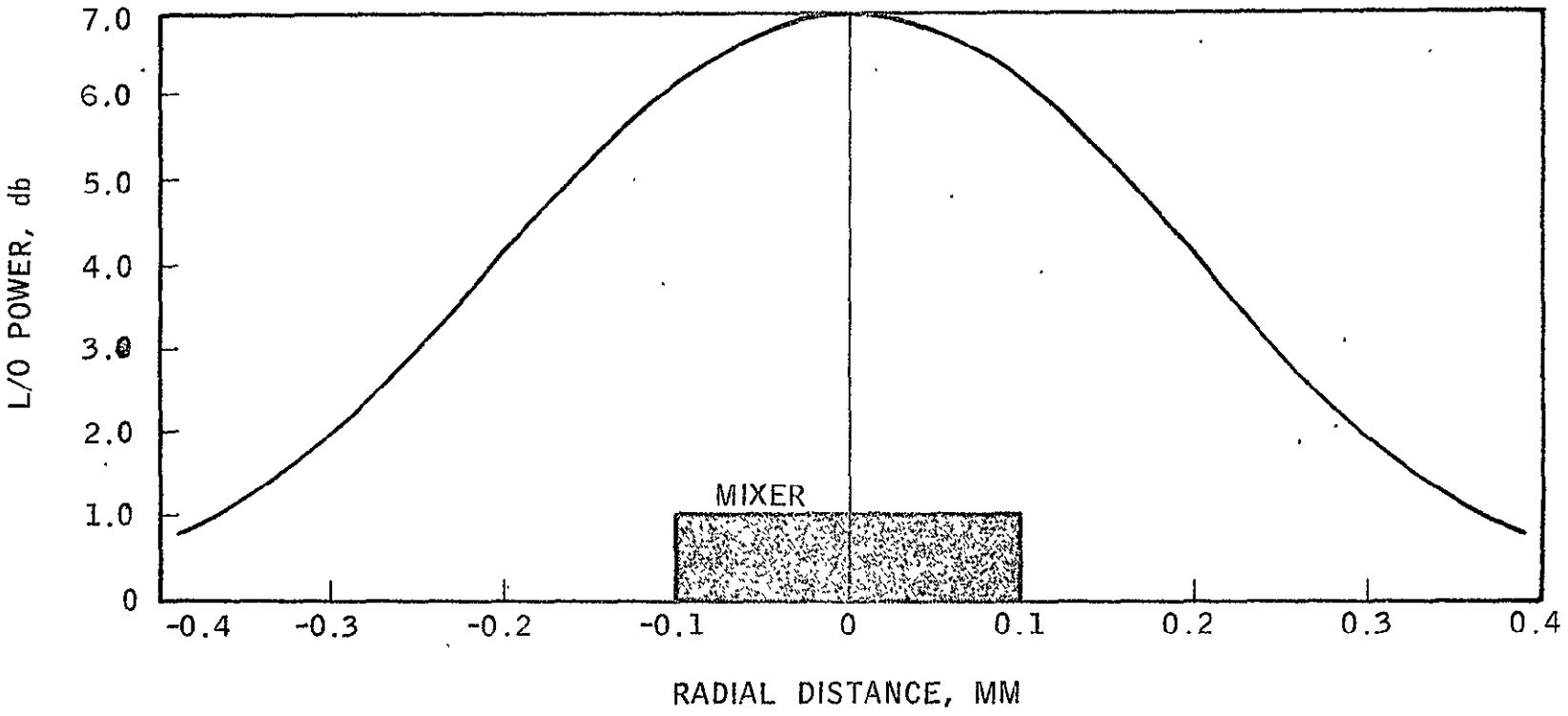

Figure I-29

CALCULATED L/O POWER DISTRIBUTION AT MIXER FOCAL PLANE, FOR P_o = 80 MW INCIDENT AND MIXER POWER = 7 MW

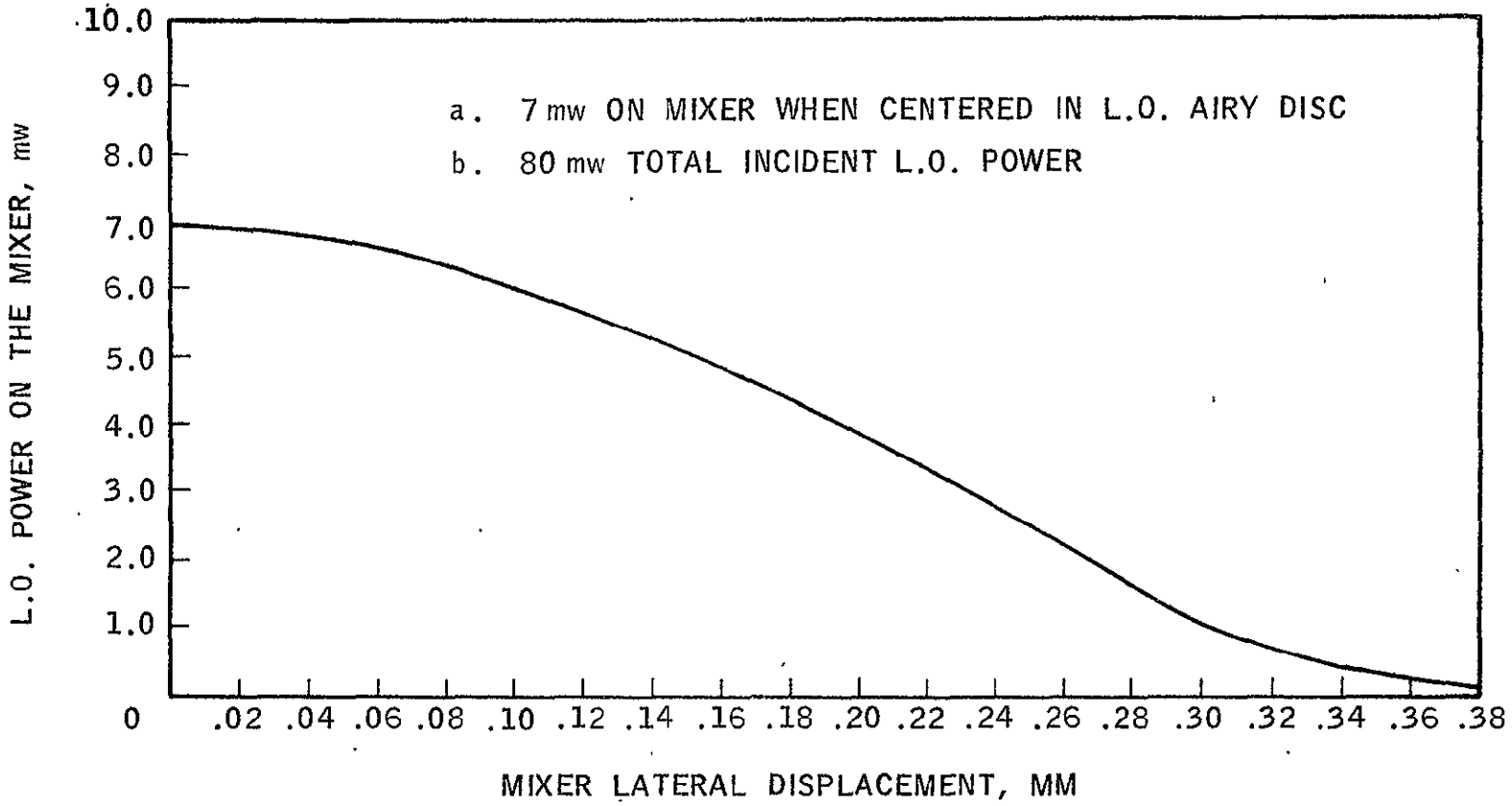

Figure L-30

L.O. POWER ON MIXER VS MIXER LATERAL DISPLACEMENT

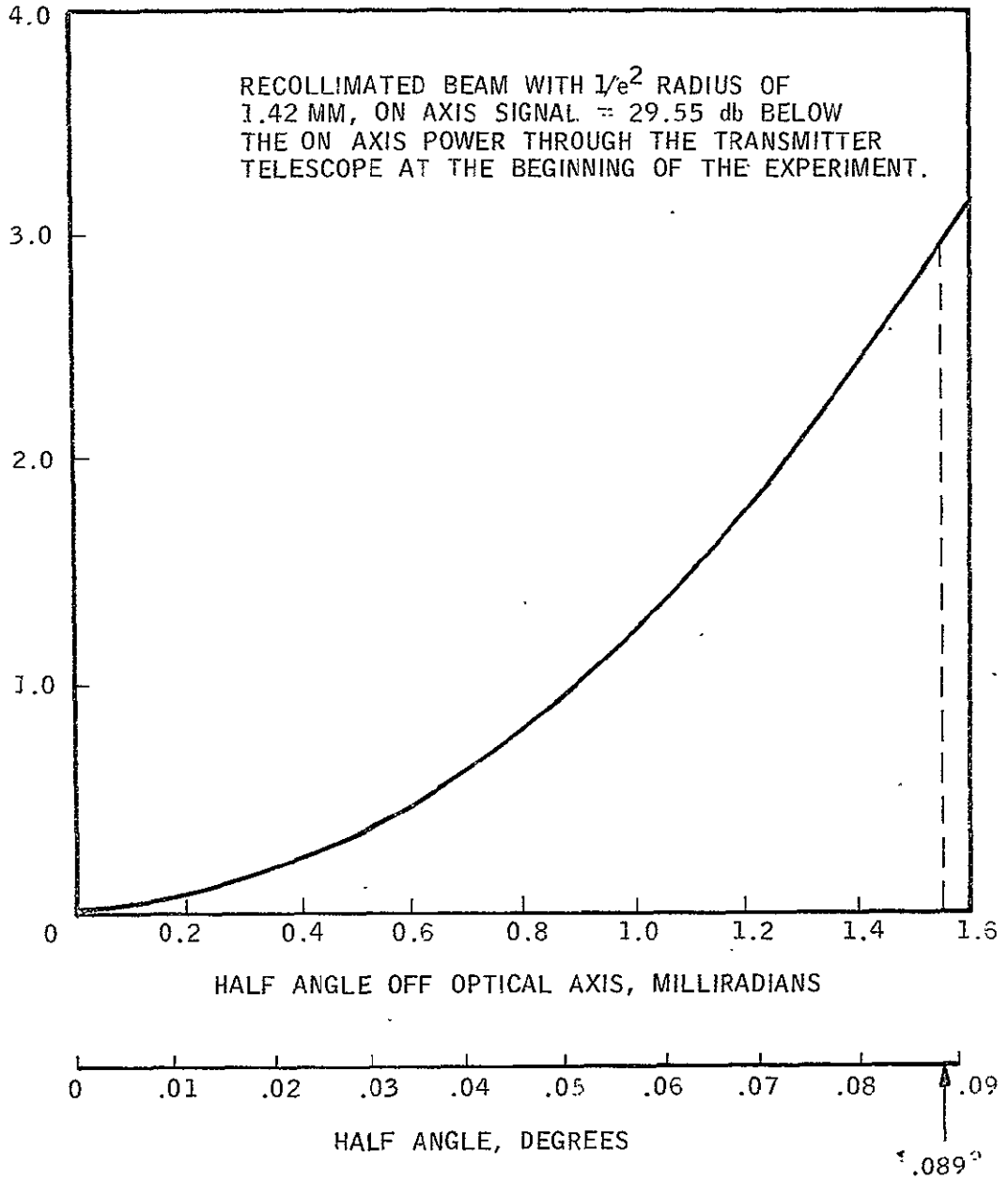

TRANSMITTER ACQUISITION FIELD OF VIEW

Figure L-30A

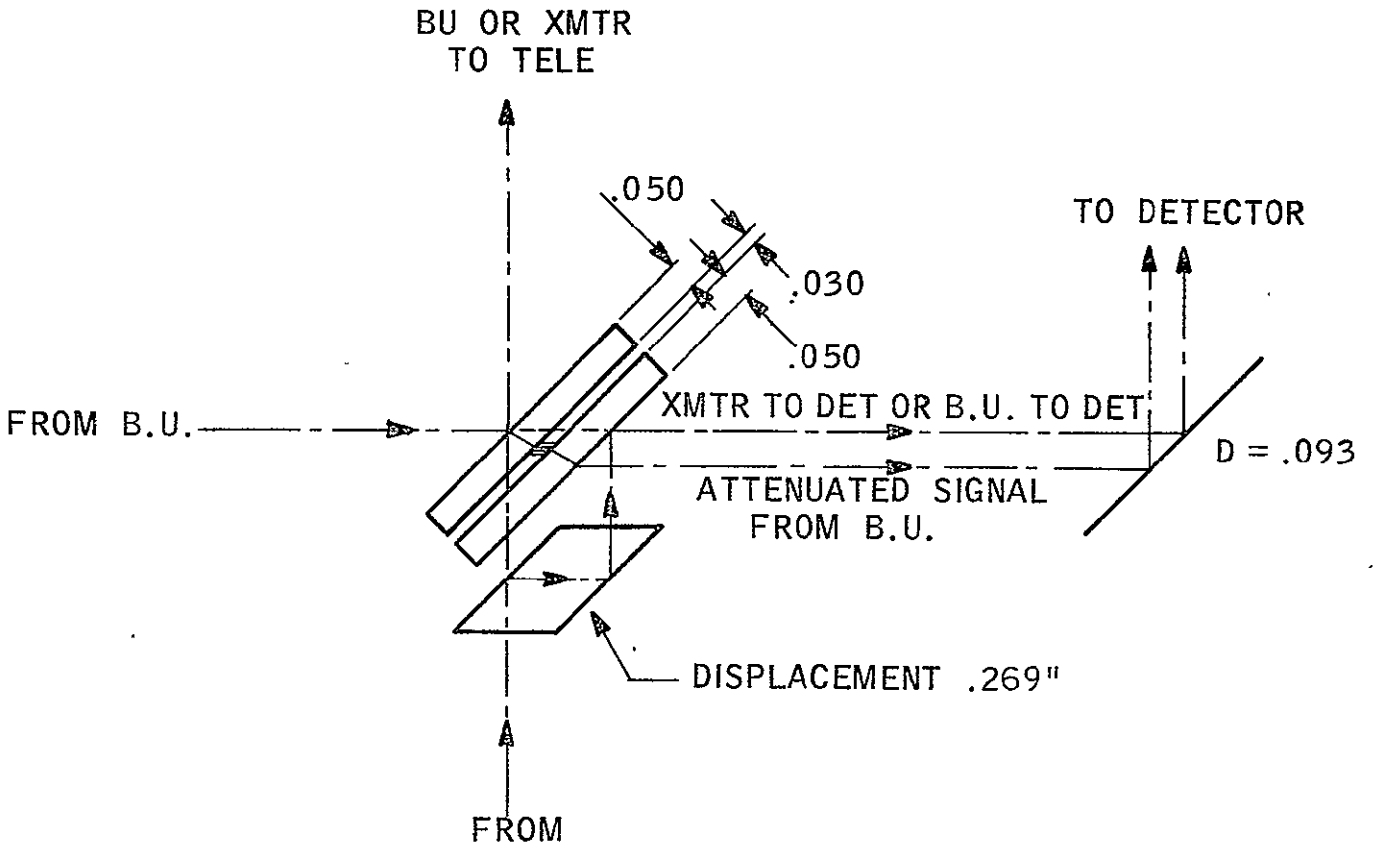

ATTENUATOR FLIP MIRROR

Figure L-31

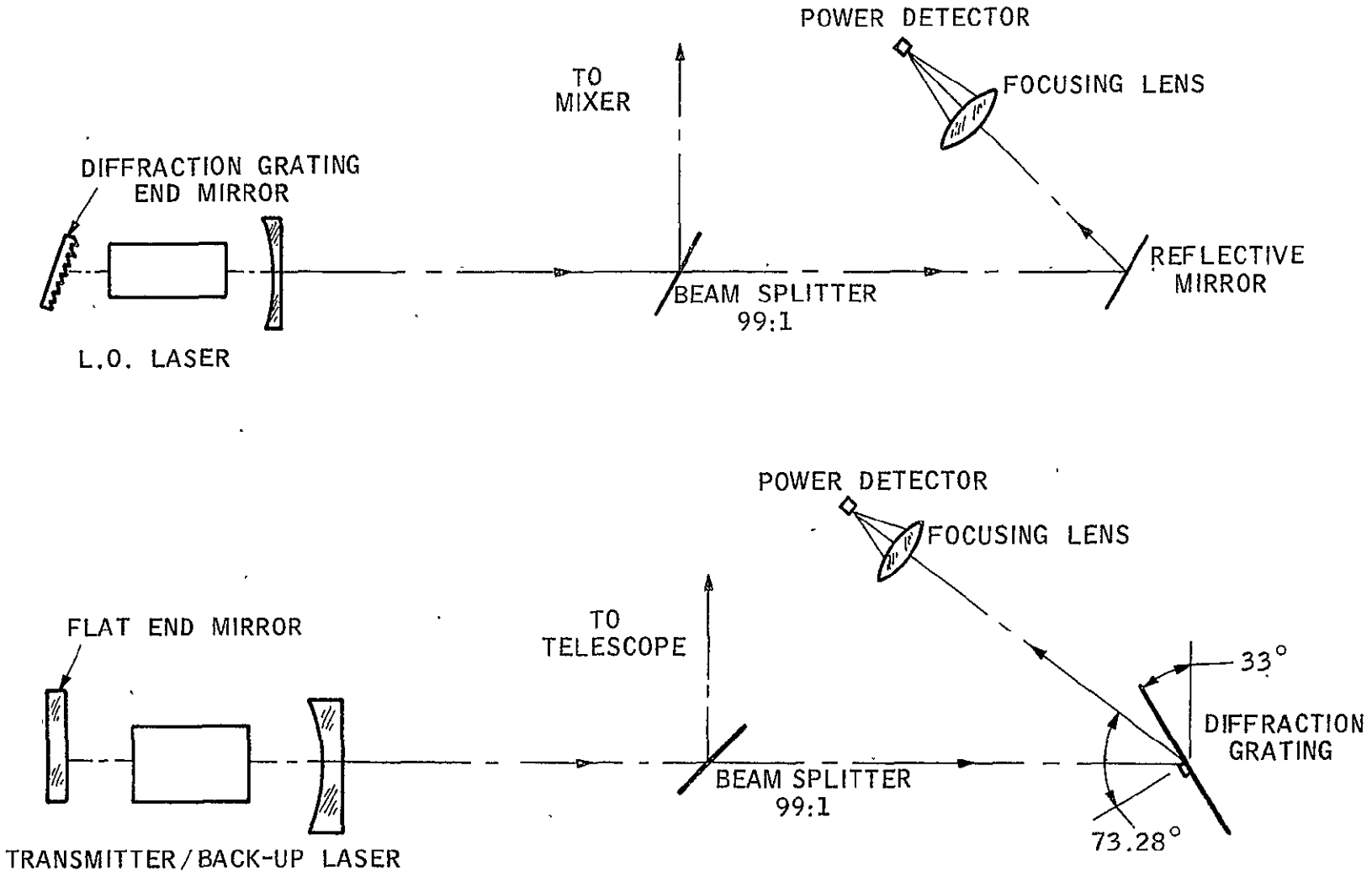

POWER METER SIGNAL PATH

Figure I-32

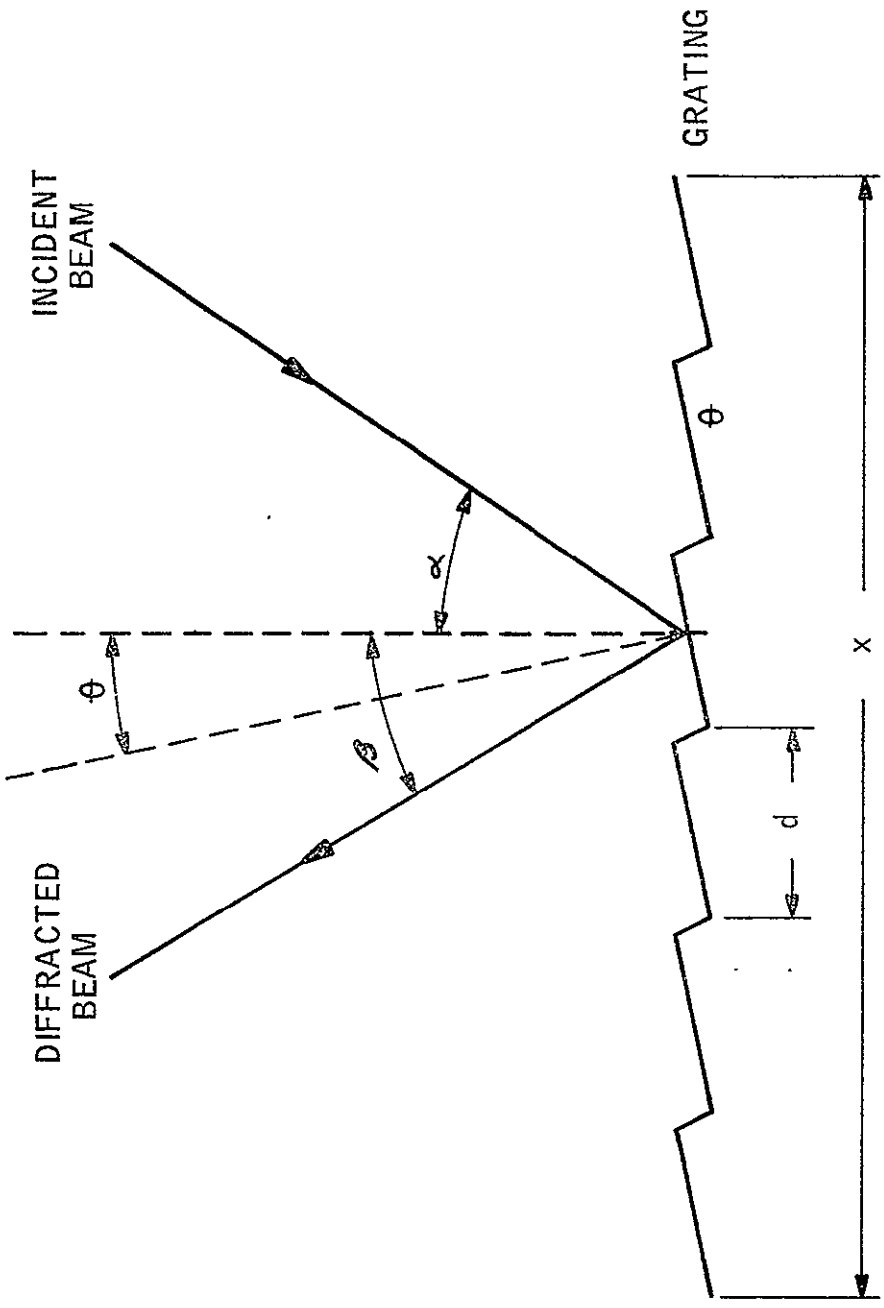

DIFFRACTION GRATING PARAMETERS

Figure L-33

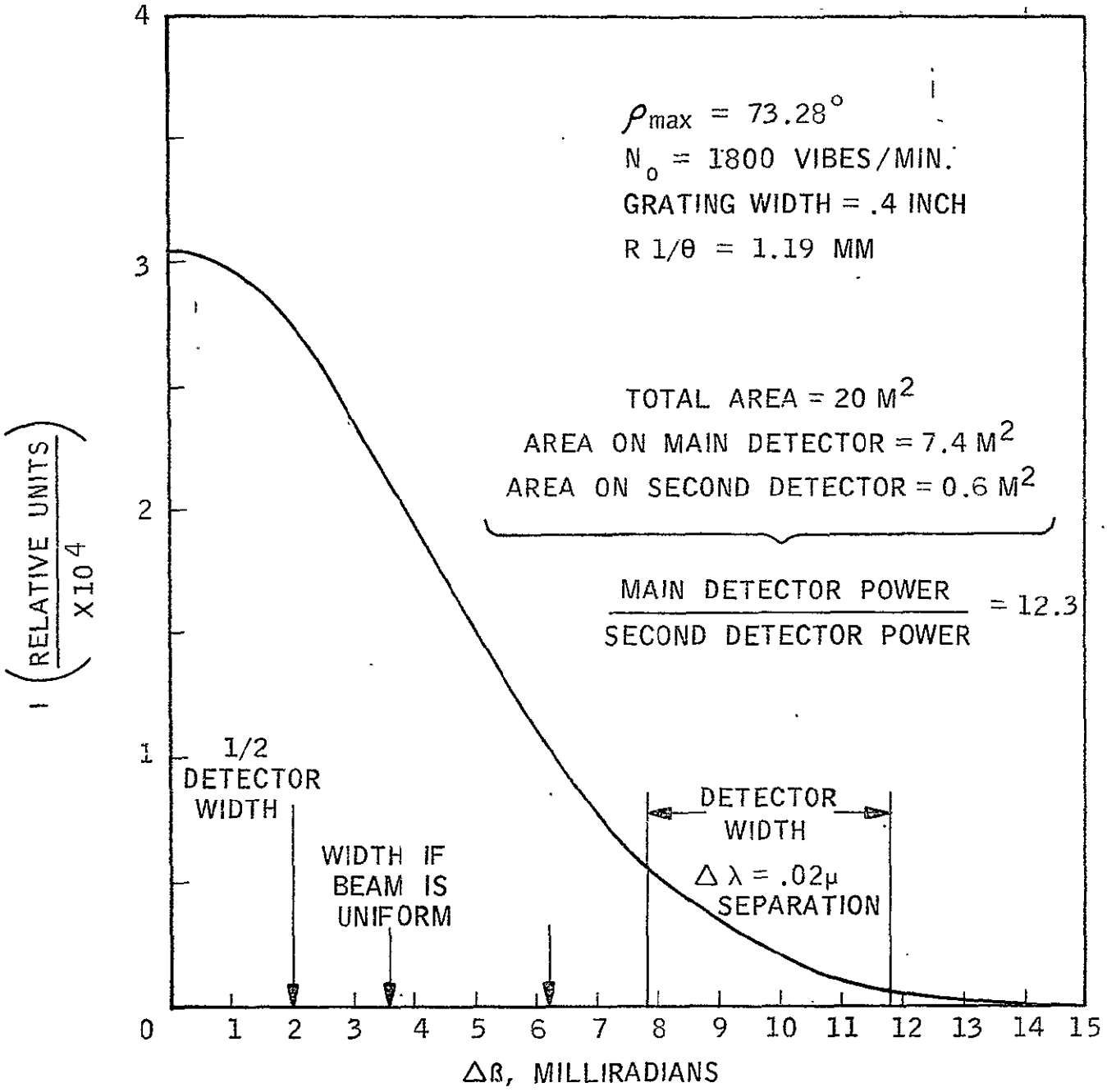

INTENSITY VS ANGLE AT SECOND ORDER MAXIMUM

Figure L-34

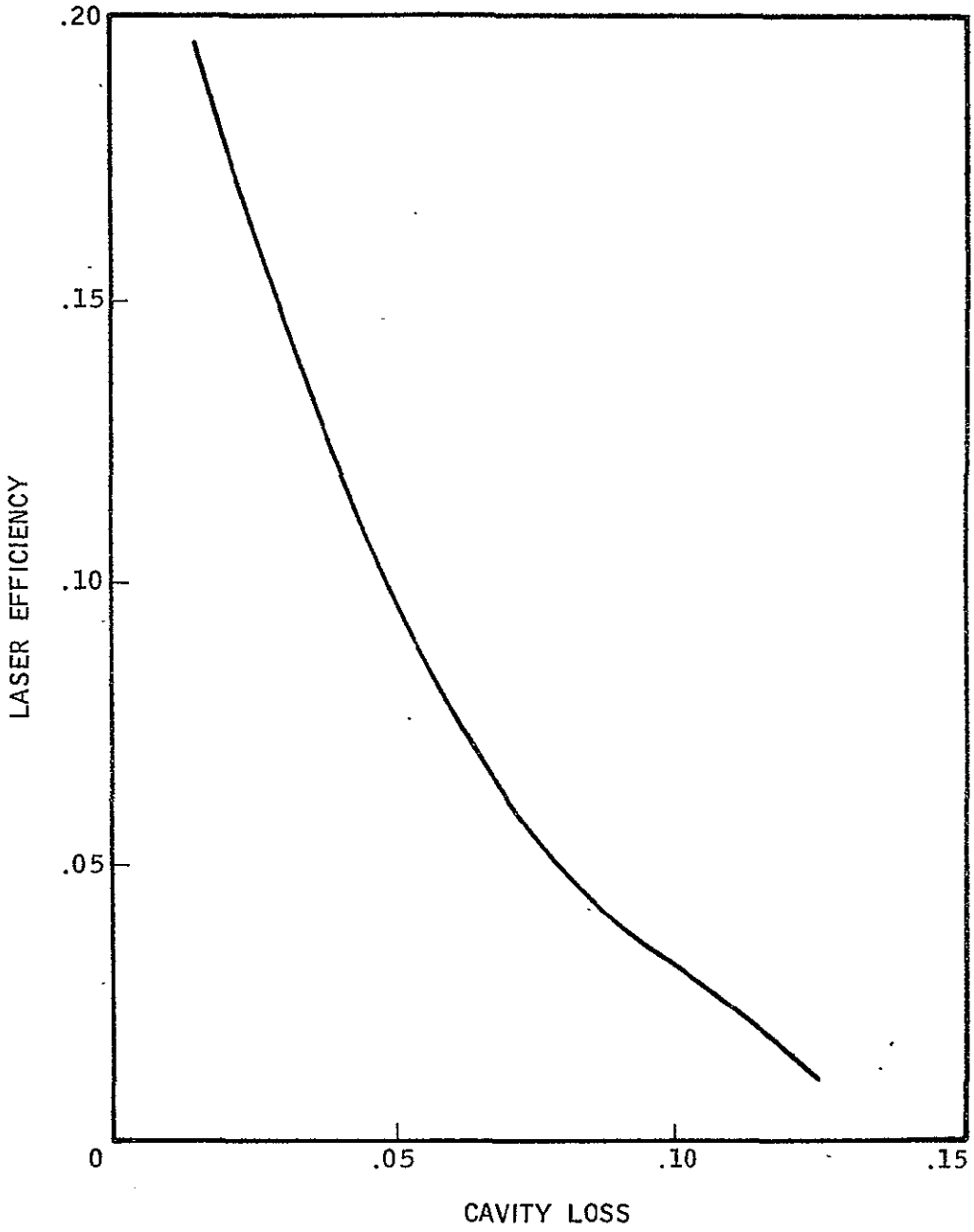

EXPERIMENTAL VALUES OF LASER EFFICIENCY VS CAVITY LOSS
(20 CM DISCHARGE)

Figure L-35

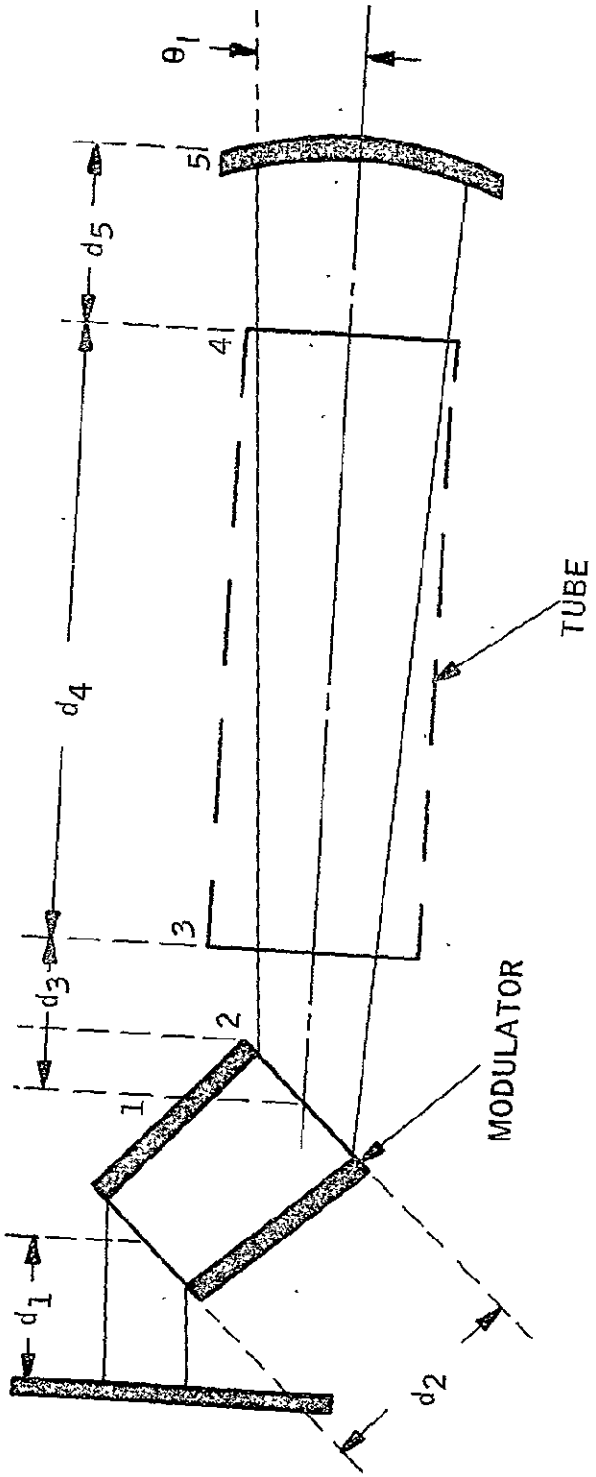

SCHEMATIC OF LASER CAVITY

Figure L-36

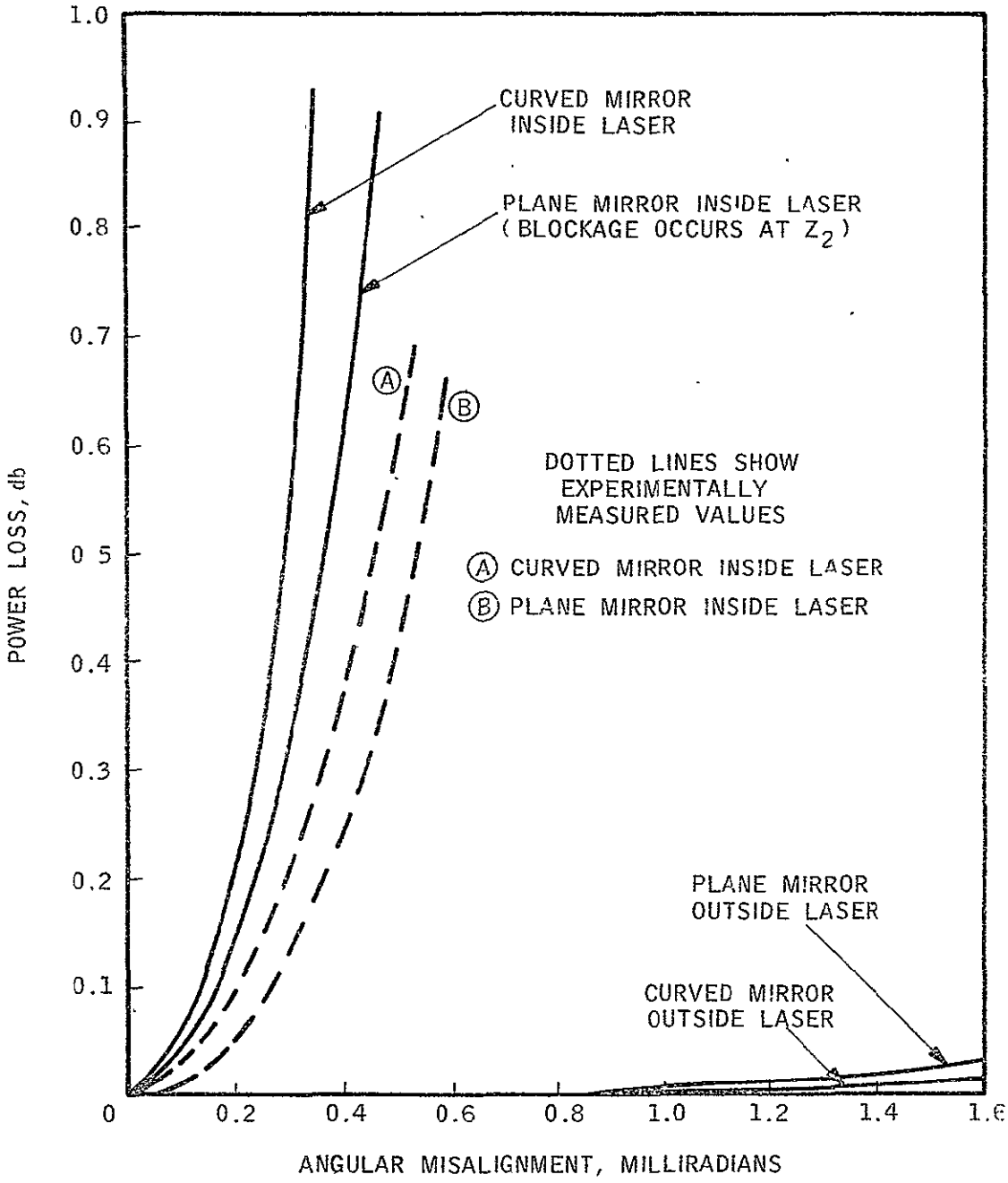

TRANSMITTER POWER DECREASE DUE TO OPTICAL ELEMENTS MISALIGNMENT

Figure L-37

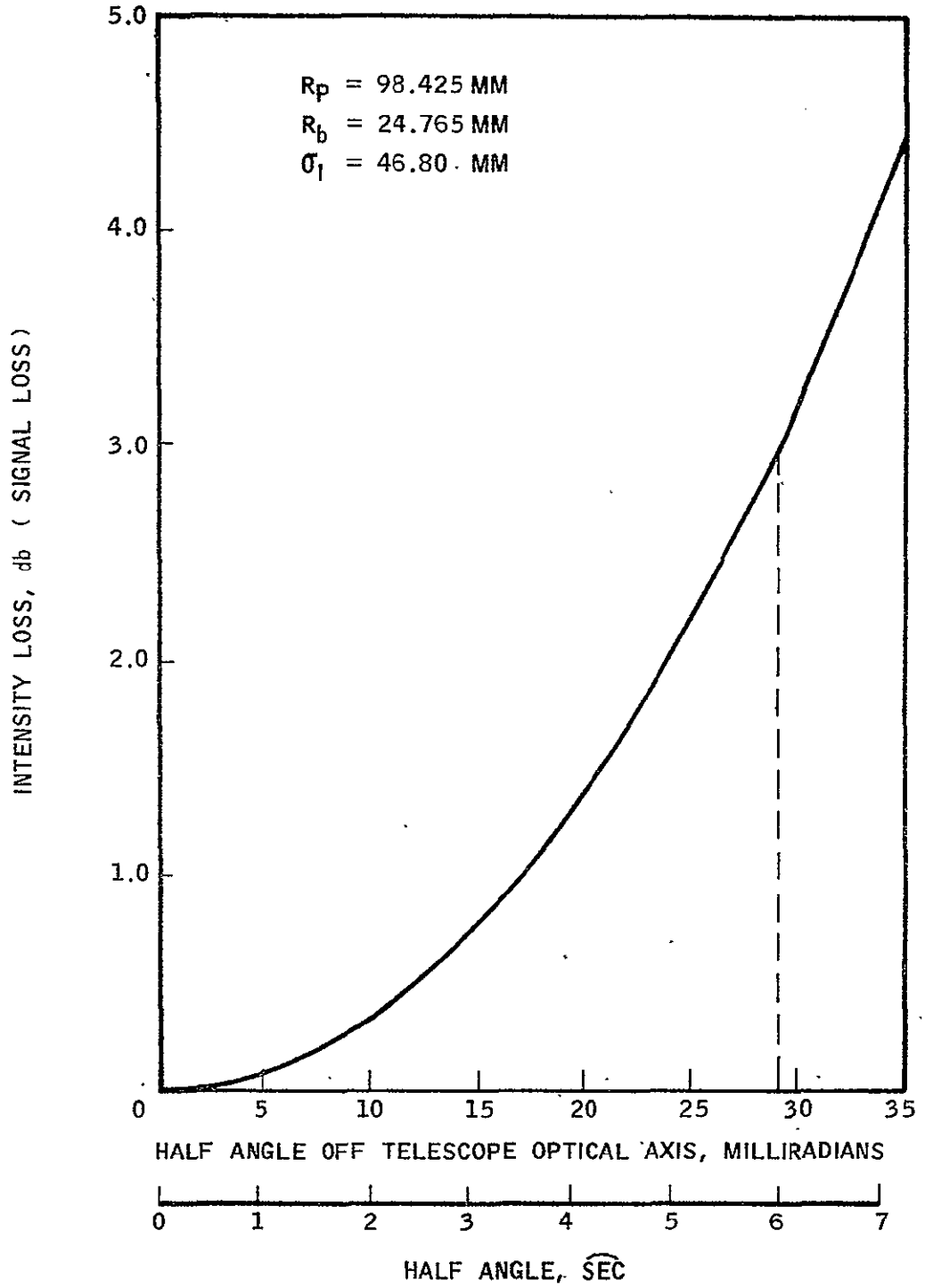

TRANSMITTER FIELD OF VIEW, σ_1 = 46.80

Figure L-38

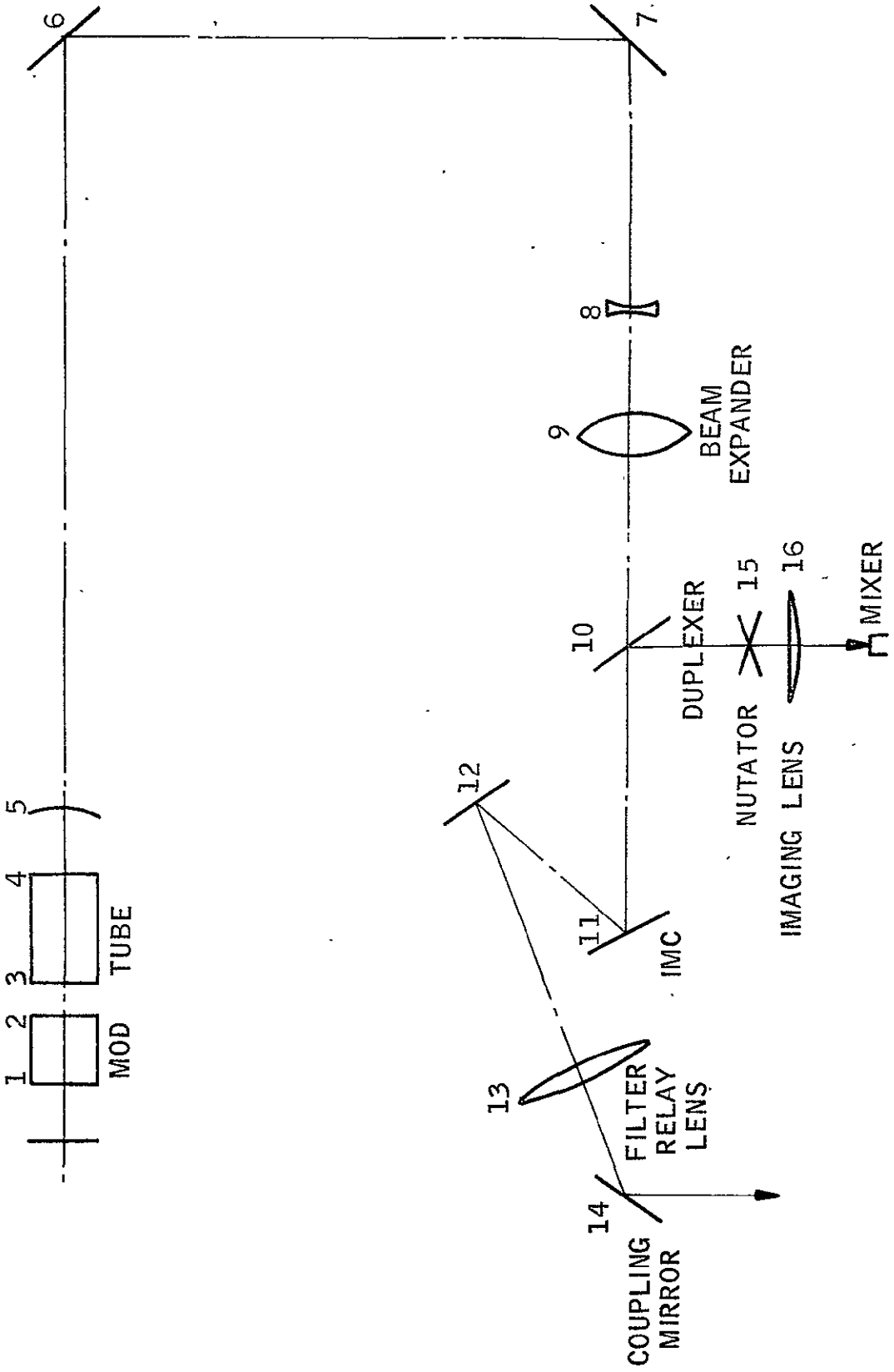

SCHEMATIC OF OPTICAL SYSTEM

Figure L-39

APPENDIX M

COARSE-POINTING-MIRROR LUBRICATION TECHNIQUES

The techniques that will be employed for lubricating the moving components of the LCE coarse pointing mirror subassembly are described below.

The areas that contain any moving parts should be sealed against the space environment by the use of Viton A elastomer ring seals between covers and housing and between components and housing.

The output shaft from the housing should be sealed by a rotary shaft seal of the garter type, using a graphite-filled Teflon material for the seal with a good finish on the shaft.

All components attached to the exterior of the case (stepper motor, encoder, potentiometers, etc.) should be hermetically sealed from the mounting flange outward. The mounting flange should have adequate flatness to seal to the O-ring seal in the housing.

All bearings used in the drives and components should be of a dry-lubricated type such as Barden Bartemp bearings. It is not sufficient merely to purchase and install these bearings. The bearings must be given a minimum 50-hour run-in at a minimum speed of 100 rpm, and then be thoroughly cleaned and reinspected to assure that they are still satisfactory and have low torque and noise. It is recommended that "Bearing Inspection" of Santa Fe Springs, California, be utilized for this run-in work. If the run-in is not performed, the initial buildup of debris in this type of bearings will result in increased torque and possibly in early failure.

An alternative to the use of Barden Bartemp bearings is the use of bearings processed by Ball Brothers Research Corporation, Boulder, Colorado, which specializes in liquid and dry lubrication for space applications.

All gears used in the subassembly should be dry-lubricated with Microseal and then be burnished to remove the residual dry-lubricant particles that could come off and cause trouble later. An alternative to Microseal would be the use of the Ball Brothers Research Dry Vac coating.

The lubricants recommended thus far are all dry and will operate in a vacuum environment. To provide additional lubrication, a coating of F-50 silicone oil should be applied to all gears and bearings that Aerojet designs and specifies. This oil will lower the torque of the gears and bearings and is compatible with the space environment (should a leak develop).

Because Aerojet is purchasing gear-reduced-stepper motors, encoders, and potentiometers, the vendors must be asked if they are using liquid lubricants in their components. If more than one liquid is utilized, they must be compatible. In purchased components employing dry lubricants, Aerojet must determine the base or primer for the dry lubricants to assure that a cadmium plating is not used under the lubricant or anywhere in the purchased components.

The housings should offer means of providing a perfectly sealed dry nitrogen purge after the subassembly is complete. An anlysis should be made to determine if a 15-psi difference between internal and external pressure will bulge the housing or cover sufficiently to affect the drive movement. If so, the housing should incorporate a one-way vent valve to reduce the internal pressure to some value greater than the external pressure. Aerojet has utilized a vent valve with a 2-psi pressure differential for such an application in previous space hardware.

The foregoing seals and lubricants will provide the necessary environment for the required operational life in space for the moving parts. The housing and shaft seals will maintain a positive pressure exceeding 1 psia in the housing and components. In itself, this is a deterent to cold welding, which could occur in a high-vacuum environment.

The above recommendations will result in a triply redundant lubrication system. The sealed liquid-lubricant system has been employed successfully in previous Aerojet space programs. The Microseal dry lubricant is presently employed in Aerojet-designed vacuum equipment and in newly designed flight hardware.